Development of next-generation 5G directive antennas at millimeter waves

Mohammad Reza Dehghani Kodnoeih

UNIVERSITE BRETAGNE LOIRE / MATHSTIC

UNIVERSITÉ DE NANTES

THESE DE DOCTORAT DE

L'UNIVERSITE DE NANTES

COMUE UNIVERSITE BRETAGNE LOIRE

ECOLE DOCTORALE N° 601
Mathématiques et Sciences et Technologies de l'Information et de la Communication
Spécialité : Electronique

Par

Mohammad Reza DEHGHANI KODNOEIH

Development of next-generation 5G directive antennas at millimeter waves

Thèse présentée et soutenue à Polytech Nantes, le 05 Novembre 2018
Unité de recherche : IETR UMR CNRS 6164

Rapporteurs avant soutenance :

George GOUSSETIS	Professeur, Heriot-Watt University, UK
Claire MIGLIACCIO	Professeur, Université de Nice-Sophia Antipolis, France

Composition du Jury :

Présidente :	Claire MIGLIACCIO	Professeur, Université de Nice-Sophia Antipolis, France
Examinateurs :	George GOUSSETIS	Professeur, Heriot-Watt University, UK
	Ashraf Uz ZAMAN	Professeur-Assistant, Chalmers University of Technology, Sweden
Dir. de thèse :	Eduardo MOTTA CRUZ	Directeur Chaire Télécom & Réseaux – HDR, Université de Nantes
Co-dir. de thèse :	Ronan SAULEAU	Professeur, Université de Rennes 1
Encadrant :	Yoann LETESTU	Responsable R&D, Radio Frequency Systems (RFS)
Invité :	André DOLL	Directeur Technique (CTO), Radio Frequency Systems (RFS)

To my life,

L'amour de ma vie,

Liebe meines Lebens,

Mia bellissima Golara !

“All things are difficult before they are easy.”

Dr. Thomas Fuller

Contents

Acknowledgements

First of all, I would like to express my sincere gratitude to my supervisors Dr. Eduardo MOTTA CRUZ, director of the Telecom and Network chair at University of Nantes, Prof. Ronan SAULEAU, Professor at the University of Rennes 1 and director of IETR, and Dr. Yoann LETESTU, R&D manager of Microwave Antenna Solutions unit at Radio Frequency Systems (RFS). I would like to thank them for providing me this extraordinary opportunity and allowing me to learn and grow during these three years, both scientifically and professionally. Their knowledge, wisdom and experience have been my main sources of inspiration.

I would like to give thanks to Prof. Claire MIGLIACCIO, Professor at the University of Nice Sophia-Antipolis, and Prof. George GOUSSETIS, Professor at Heriot-Watt University (UK), for having accepted to evaluate this thesis manuscript and to be part of the jury. Their comments have been very useful. I also express my gratitude to Prof. MIGLIACCIO for chairing the jury.

I would like to express my gratitude to Dr. Ashraf Uz ZAMAN, Assistance professor at Chalmers University of Technology, for accepting to participate at the defense and be part of the jury.

I express my gratitude to M. André DOLL, Chief Technology Officer at Radio Frequency Systems, for his interest and support of this thesis since the very beginning. His precise comments during the meetings, specially on the industrial aspects, and his professional discipline have been very precious and inspiring. I thank him for accepting to be part of the jury.

Acknowledgements

I would like to thank my dear colleagues at Microwave Antenna Solutions R&D department of RFS, M. Denis TUAU for his great technical support and brilliant propositions, Dr. Jose ENRIQUEZ GONZALEZ for his precious advices and interesting technical discussions, Dr. Armel LE BAYON for his support with the simulation softwares and, M. Daniel MORIN, M. Daniel NEDELEC and M. Ludovic METRIAU for the antenna measurements and, M. Patrice VAUTY and our industrial designers for their support with prototype realizations. I would like to thank the ensemble of RFS for welcoming me during these three years.

I would like to express gratitude to M. Arman AZADI, my supportive friend and brilliant comrade since we first started our bachelor's studies in Semnan, IRAN, for being always present by my side in difficult times, despite thousands of kilometers of distance.

A special thanks, to my parents, *Sakineh* and *Hassan*, to my little brother, *Milad*, for supporting and encouraging me since my day one. Words can not express my gratitude for them.

Finally, my deepest gratitude to my best friend, caring love and supportive life partner, my *Golara*. Thank you for being by my side all the time, in difficulties and in happiness. I would have not been able to overcome the challenges without your support and encouragement.

Frankfurt, December 2018

Mohammad Reza DEHGHANI KODNOEIH

List of Figures

List of Tables

Résumé en Français

La compacité, le faible coût, le gain et la compatibilité avec dépointage électronique sont les quatre principales caractéristiques requises pour les antennes directives point-à-point pour les futurs réseaux 5G dans la bande millimétrique. Cette bande a attiré beaucoup d'attention ces dernières années car elle est en mesure de fournir des communications à haut débit (jusqu'à 10 Gbits/s), en raison de leurs larges segments de bandes passantes. Dans la première étape de la thèse, les cahiers de charges pour les différents segments sont établis afin de définir les caractéristiques techniques requises pour des types d'antenne, en prenant en compte les normes et recommandations radio et mécanique de l'ETSI (European Telecommunications Standards Institute) et FCC (Federal Communications Commission).

Ensuite, dans le but de proposer la solution antennaire la plus adaptée pour l'application ciblée, une étude de l'état de l'art des différentes technologies d'antennes directives est faite en termes de performance, encombrement, complexité de fabrication et coût. Différentes technologies d'antennes sont proposées, avec leurs avantages et leurs inconvénients. Ce sont soit des solutions coûteuses, telles que des réseaux d'antennes directement alimentées (réseaux de cornets, réseaux de fentes, etc.), soit des solutions volumineuses telles que les antennes avec alimentation quasi-optique (lentilles, réseaux transmetteurs et réseaux réflecteurs).

L'ensemble des résultats de l'état de l'art et les cahiers de charges ont permis d'aboutir à une matrice de choix de technologie d'antenne. En utilisant cette matrice, les antennes avec alimentions quasi-optique sont retenues comme technologie de base d'antenne pour cette thèse. Une lentille plate, lentille de Fresnel, est sélectionnée grâce à sa compacité et à sa simplicité de réalisation.

Une antenne compacte, faible coût et directive basée sur des solutions quasi optiques est alors proposée pour la bande V (57-66 GHz). Une solution d'antenne à faisceau fixe optimisé avec une distance focale réduite est d'abord conçue puis validée par des mesures en champ lointain. Afin de réduire l'épaisseur totale de l'antenne, une structure repliée utilisée dans les antennes de type réflecteur est proposée. La Figure 1 présente les différents composants de la structure en vue en coupe et deux photos du prototype de cette solution, réalisé en bande V.

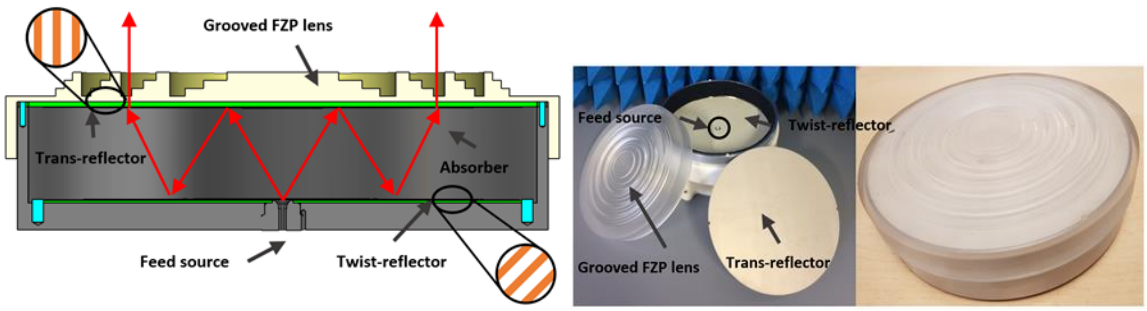

(a) (b)

Figure 1: Structure de la Lentille de Fresnel Replié :(a) vue en coupe, (b) photos du prototype réalisé en bande-V.

La structure repliée, constitué par deux grilles réflectrices (Trans-réflecteur et Twist-réflecteur), multiplie par trois le trajet électrique entre la source focale et la lentille Fresnel, se traduisant par une division par trois de la distance focale physique (épaisseur total de la structure d'antenne). Cette antenne a un diamètre total de 24.8 λ avec une épaisseur total de 9 λ (incluant la source focale), soit une distance focale physique entre la source focal et la lentille de seulement 5.6 λ, correspondant à un ratio focale à diamètre (*F/D*) très compact de 0.22.

L'ensemble de la structure d'antenne complète (Figure 1) est simulé en utilisant le logiciel *CST Microwave Studio* et les éléments de la structure repliée sont optimisés séparément à l'aide des portes Floquet du logiciel *ANSY HFSS*.

Les simulations et les mesures en bande V (57-66 GHz) de la lentille de Fresnel repliée sont illustrés dans la Figure 2. Les résultats des simulations et des mesures montrent, un gain supérieur à 30 dBi sur toute la bande passante et des diagrammes de rayonnement conformes au gabarit de l'ETSI dans les plans E (figure 2(a)) et H (figure 2(b)).

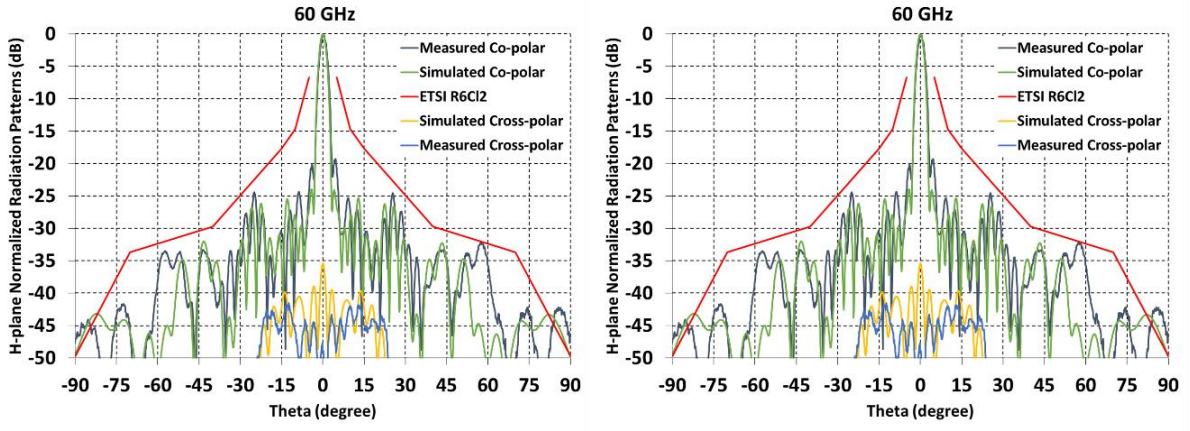

(a) (b)

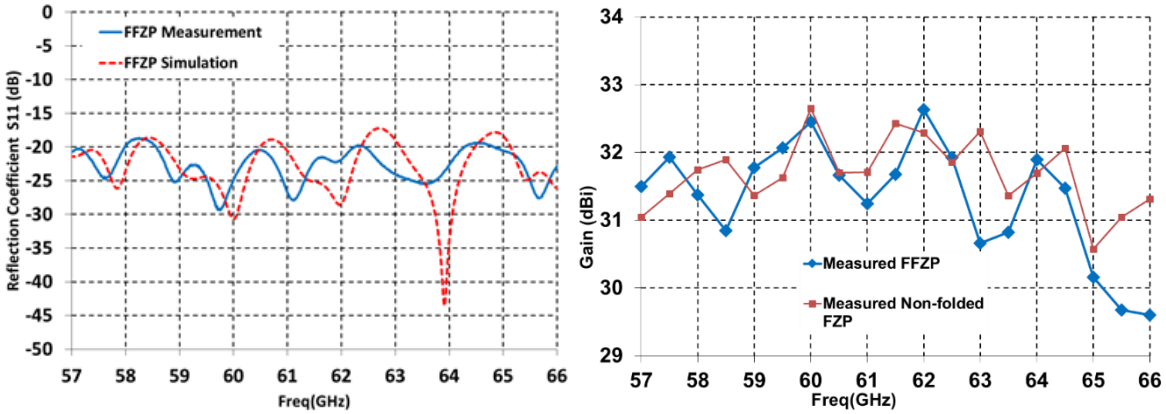

(c) (d)

Figure 2: Résultats simulé et mesuré de la lentille de Fresnel repliée (a) diagramme de rayonnement normalise dans plan-E, (b) diagramme de rayonnement normalise dans plan-H, (c) Coefficient de réflexion (S11), et (d) Variation du gain en fonction de la fréquence.

Un élément d'optimisation de ce type d'antenne basé sur des lentilles consiste à minimiser la perte de débordement, en utilisant des sources focales assez directives avec une pondération optimale. Une source focale optimale (cornet) munie d'une transition à guide d'ondes intégré standard WR15 est ensuite proposée pour atteindre cet objectif. Par ailleurs, la lentille de Fresnel peut servir comme de radome avec la partie corruguée tournée vers intérieur. La figure 3 présente la solution de la lentille Fresnel repliée avec radome intégré, alimenté par une source focal optimal. Cette solution offre un gain maximum mesuré de 33.5 dBi à 61.5 GHz, avec une variation de 2.3 dB dans la bande V (57-66 GHz). Les diagrammes de rayonnement de cette solution sont également conformes au gabarit de l'ETSI.

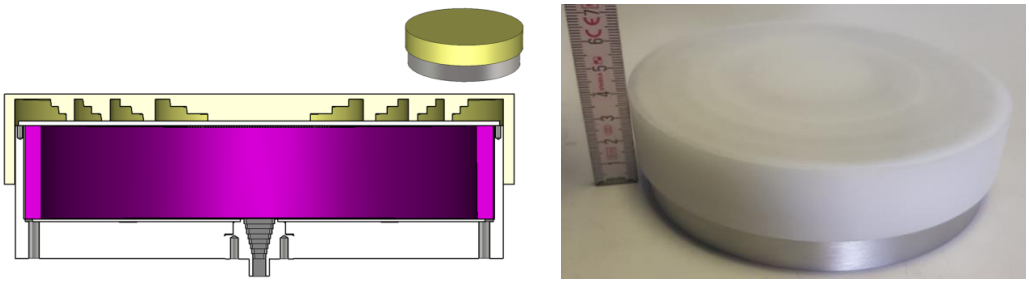

Figure 3: Lentille de Fresnel repliée avec radome intégré et source focal optimale.

En deuxième partie de la thèse la compatibilité de la lentille de Fresnel replié pour le dépointage électronique est étudiée, et deux solutions de dépointage sont proposées et caractérisées à la fois par des simulations et des mesures.

Pour obtenir un dépointage, la source cornet rayonnant est remplacée par un réseau des patches micro-ruban. Les patches s'avèrent plus compacts que les cornets et sont compatibles avec le dépôt des circuits RF sur un substrat, nécessaires pour obtenir un dépointage actif. Pour permettre de connecter la solution antennaire aux équipements radio, il est préférable que l'antenne puisse avoir un seul accès en guide d'onde standard pour bande V (WR15). Pour cela, une nouvelle transition directe de la ligne micro-ruban au guide d'ondes est proposée.

Cette transition a l'avantage d'utiliser une seule couche du substrat, celle de la ligne micro-ruban. La figure 4 présente en détail cette transition.

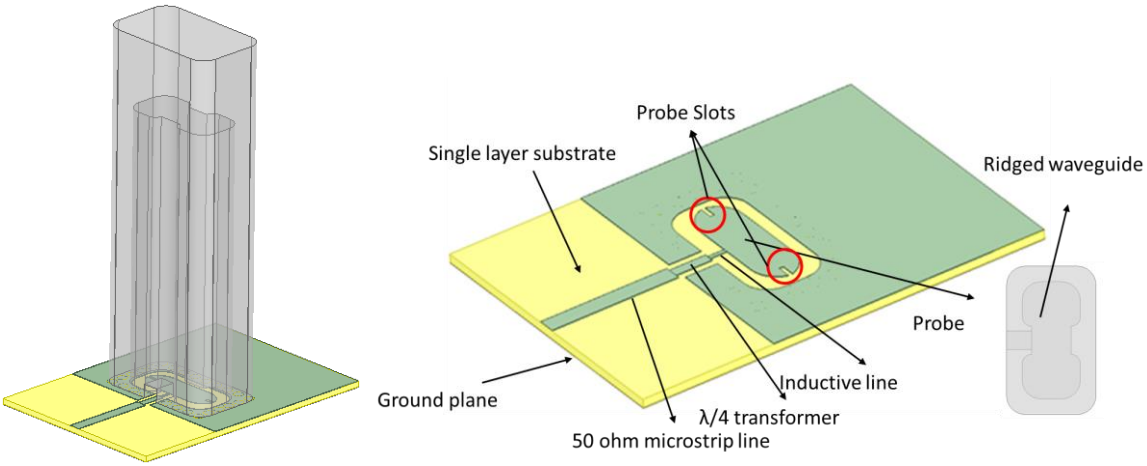

Figure 4:Transition intégré de la ligne micro-ruban à guide d'onde.

La première solution proposée pour dépointer le faisceau principal est du type commutation de faisceau (beam switching) : la source primaire est déplacée dans le plan focal de la lentille, où la commutation peut avoir lieu d'un patch à l'autre. La figure 5(a) présente un réseau focal planaire, où à chaque instant on n'excite qu'un élément. L'intégration de ce réseau focal dans la structure antennaire est montrée dans les Figures 5(b) et 5(c).

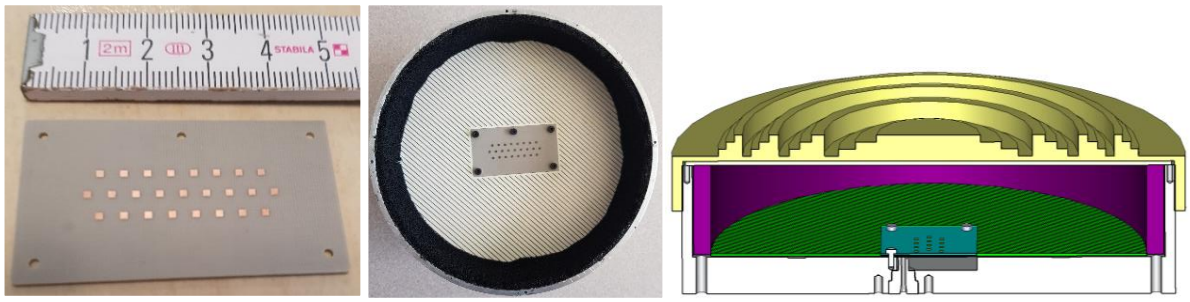

(a) (b) (c)

Figure 5: Prototype du réseau focal pour dépointage par commutation de faisceau (Beam Switching) : (a) réseau focal fabriqué, (b) intégration du réseau focal dans la structure antennaire (vue de dessus), et (c) Vue en coupe dans logiciel CST.

Afin de valider ce concept, des prototypes passifs du réseau focal présenté dans la Figure 5 sont réalisés, où dans chaque circuit un seul patch est excité par une ligne micro-ruban, reliée à une transition en guide d'ondes standard en bande V (WR15). Les résultats des simulations et des mesures de ces prototypes sont présentés dans la Figure 6. On observe bien que dans le cas d'excitation du patch central (BS N°1) on obtient un faisceau centré et pour les patchs déplacés, BS N°3 voisin de patch central et BS N°4 à l'extrémité du réseau focal, on produit des faisceaux dépointés à -2° et à -8° respectivement. L'inconvénient principal de ce type de solution est le dépointage non-continu, imposé par les dimensions physiques des patchs et leur distance inter-éléments, dans notre cas avec un pas de dépointage assez important, de l'ordre de 2°.

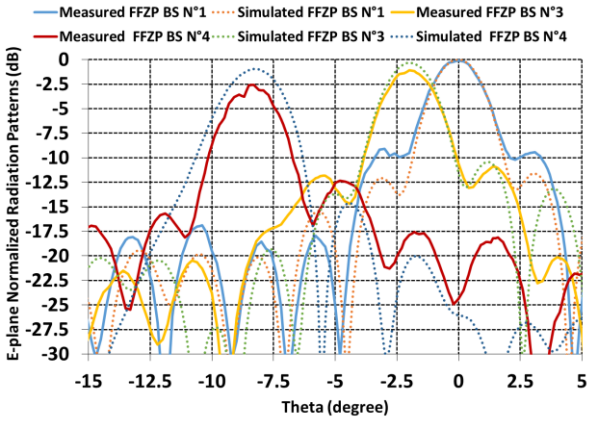

Figure 6: Diagrammes de rayonnement simulés et mesurés des prototypes de la solution dépointage par commutation de faisceau (Beam Swiching).

La deuxième solution de dépointage, qui offre des dépointages très fins (quasi-continus), de l'ordre de 0.3°, est basée sur le léger déplacement du centre de phase d'un sous-réseau 2×2 par pondération des ses éléments. En déplaçant le centre de phase dans le réseau focal, on contourne ainsi les contraintes imposées par les dimensions physiques des sources focales. Afin de valider ce concept, trois différents réseaux focaux (2×2 éléments) sont réalisés, où l'un est excité avec amplitude uniforme (N1), et les deux autres (N2 et N3) avec des amplitudes pondérées. Les photos de ces prototypes et leur intégration dans la solution antennaire lentille de Fresnel repliée sont présentés dans la Figure 7.

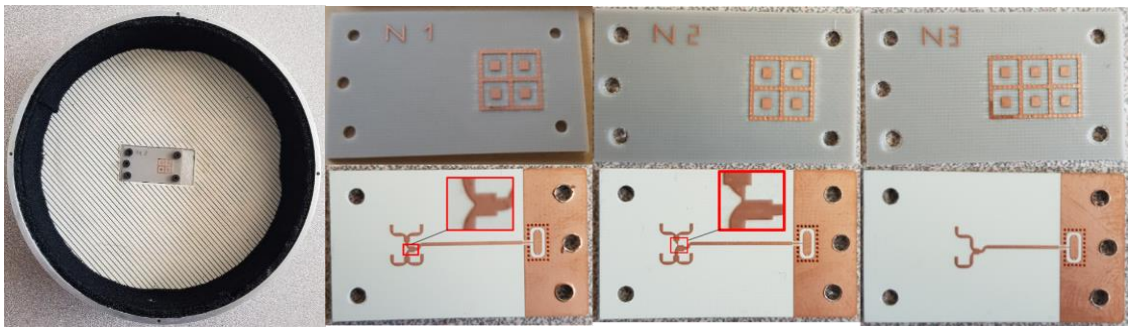

Figure 7: Prototypes des réseaux focaux pour des dépointages continus.

Le tableau 1 présente les coefficients d'amplitude de chaque réseau focal, la position du centre de phase associé et l'angle de dépointage obtenu (simulé et mesuré) lors que l'on illumine la lentille de Fresnel replié avec ces types de sources. Une solution de dépointage quasi-continu est démontrée à l'aide des prototypes passifs.

N° du circuit et ses coefficients d'amplitude $\begin{pmatrix} A_2 & A_3 \\ A_1 & A_4 \end{pmatrix}$	**Position du centre de phase-mm (x-axis / y-axis)**	**Direction du faisceau simulé (AZ / EL)**	**Direction du faisceau mesuré (AZ / EL)**
N1 $\begin{pmatrix} \mathbf{1} & \mathbf{1} \\ \mathbf{1} & \mathbf{1} \end{pmatrix}$	0/0	0° / +0.1°	0° / 0°
N2 $\begin{pmatrix} \mathbf{0.4} & \mathbf{0.4} \\ \mathbf{1} & \mathbf{1} \end{pmatrix}$	0/-0.8	0°/0.3°	-0.1° /+ 0.3°
N3 $\begin{pmatrix} \mathbf{1} & \mathbf{0} \\ \mathbf{1} & \mathbf{0} \end{pmatrix}$	-1.8/0	+1.1°/ 0 °	+1.1° / +0.3°

Tableau I: dépointage par réseau 2x2 pondéré.

Enfin, comme perspectives, des solutions possibles pour intégrer des propriétés telles que le fonctionnement bi-fréquence ou en double polarisation dans la lentille Fresnel repliée sont proposées. Ces deux solutions sont brevetées. Une solution alternative basée sur les structures triplement repliée est également proposé afin de rendre notre solution antennaire encore plus compacte.

1. Chapter 1 : Introduction on thesis framework and context

1.1. Thesis framework and partners

This thesis has been carried out in the frame of the French research program CIFRE (Convention Industrielle de Formation par la REcherche). The partners of this thesis project are:

- Industry: Radio Frequency Systems (RFS)
- Laboratory: Institut d'Électronique et de Télécommunications de Rennes (IETR)

1.2. Thesis context: 5G point-to-point communications

Since the introduction of the first generation of mobile networks (1G) in the 1980s, a new network generation was introduced each decade. As illustrated in the schematic presented in figure 1-1, each generation offered new features to the mobile network users. With the 1st generation (1G), users were able to have voice communications based on analogue signals. The 2nd generation (2G) used digital signals and enabled more users benefiting from this emerging technology. This generation offered more voice capacity and enable users to benefit from Short Message Services (SMS), and the introduction of GPRS and EDGE functionalities enabled TCP-IP data transmission (typically 80 Kps). The 3rd generation (3G), introduced in the 2000s, offered broadband communications enabling more data transfer flow (rates around 5 Mps). And the most recent generation, introduced in the 2010s, the 4G or known also as LTE (Long-Term Evolution), offers data transfer rates up to 10 times faster than the 3G with a peak of 50 Mbps.

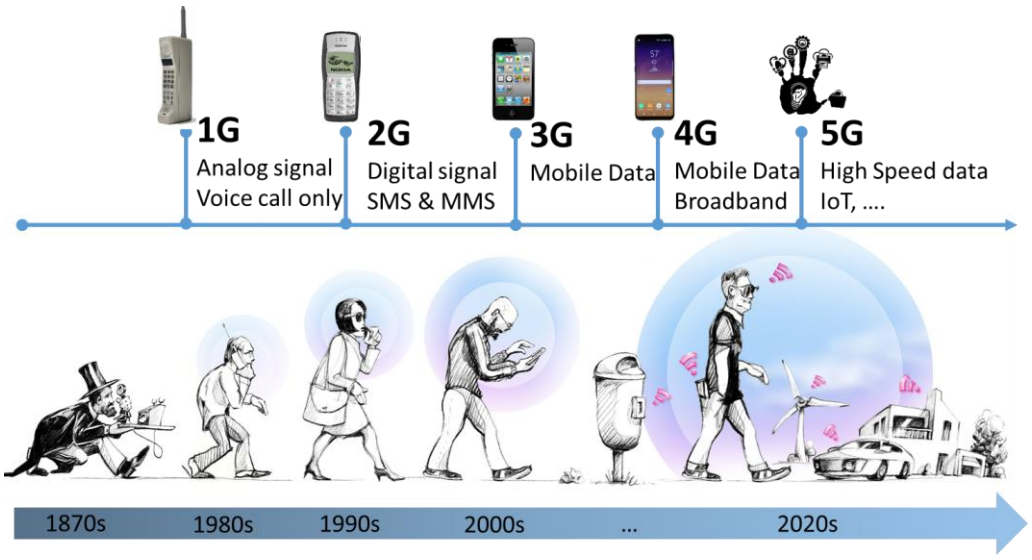

Figure 1-1: Mobile network generations evolution in time [1].

With approaching the end of 2010s, the market is expecting the next generation, the 5G. 5G, will not only be the fifth generation of mobile networks but everything network. For this generation, we expect high data transfer rate (up to 10 Gbps), no latency and robust communications independent from geographical position. Main application for 5G, not all of them known yet, are to be Internet of Things (IoT), smart cities, connected cars, e-Health and in other words, everything connected.

The 5G network layout is not yet completely standardized. However, based on current 4G network and following the discussions of the main academic, industrial and regulatory actors, a general network schematic can be anticipated. Figure 1-2 presents a simplified schematic of a possible 5G heterogeneous network. As presented in this figure, there are mainly two types of connections in a mobile network : Point-to-Multi-Point such as radio access between users and Remote Radio Units (RRU) of the base stations, fronthaul links between RRU and baseband units (BBU) of the base stations and Point-to-Point such as backhaul links between baseband units (BBU) and the Core Network and. This thesis is focused on new antenna technology development for 5G point-to-point (PtP) communications.

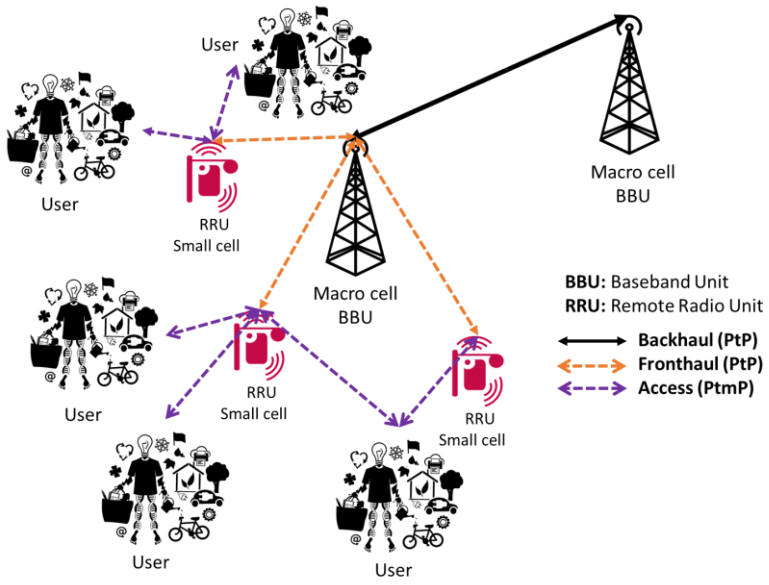

Figure 1-2: Possible 5G heterogeneous network.

In the following section, the potential frequency band candidates for 5G and their characteristics are detailed. Afterwards, the required antenna specifications for 5G backhaul links are defined and to summarize them, a primary datasheet per potential frequency band is proposed.

1.2.1. Frequency bands specifications for 5G point-to-point communications

Notwithstanding the definition of frequency bands below 6 GHz for 5G at the ITU World Radiocommunication Conference in 2015 (International Telecommunication Unions) until mid 2018, it was not known exactly which millimeter frequency bands will be allocated for 5G backhaul links, in order to fulfill the 5G expectations where large bandwidths are required. The frequency spectrum and mm-wave frequency bands are presented in figure 1-3.

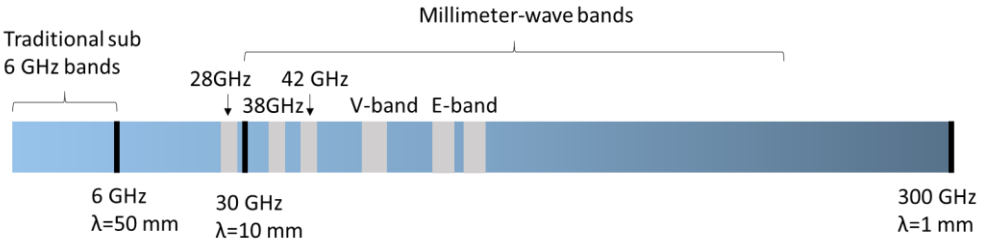

Figure 1-3: Frequency Spectrum.

In addition to large bandwidths, another advantage of mm-wave frequency bands is that some of them are not licensed or are light licensed, which is an important factor for the operators in terms of cost. Moreover, mm-wave frequency bands have higher atmospheric attenuation rate compared to sub-millimeter wave frequency bands, as presented in figure 1-4. This may look as a disadvantage, but as one of the mm-waves deployment scenarios is for dense urban

networks (small cells), high attenuation facilitates close frequency re-use while avoiding interferences.

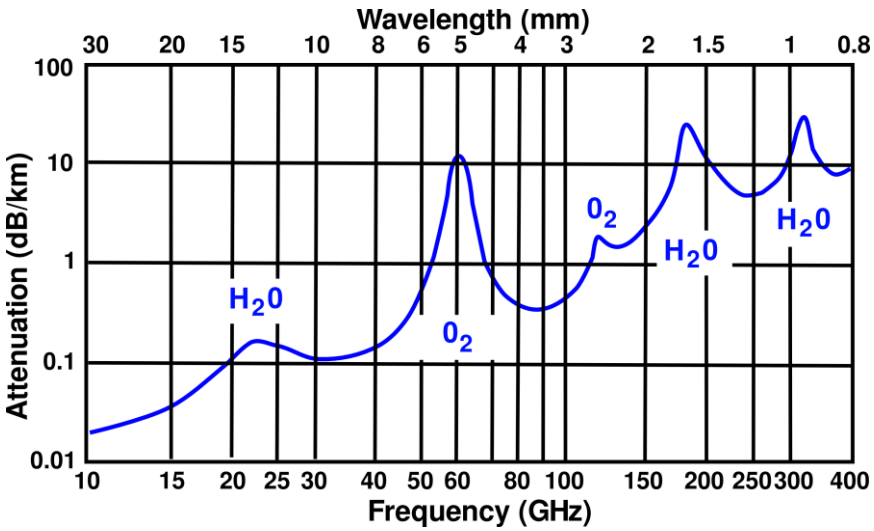

Figure 1-4: Sea level Atmospheric attenuation rate in function of frequency [2].

In recent years, the standardization regulatory bodies such as *European Telecommunications Standards Institute* (ETSI) and United States *Federal Communications Commission* (FCC), have directed their attention towards five mm-wave frequency bands as main candidates for 5G backhauling:

- 28 GHz (27.5-29.5 GHz)
- 38 GHz (37.5-40 GHz)
- 42 GHz (40.5-43.5 GHz)
- V-band (ETSI: 57-66 GHz , FCC: 57-71 GHz)
- E-band (71-76 GHz & 81-86 GHz)

In order to target the thesis scope, the focus for the antenna design was turned mainly on one of the highest frequency bands, the V-band. This is because V-band is one of the most constraint mm-wave frequency bands in terms of design and realization for two main reasons: 1- small wavelength, meaning small antenna elements dimensions which complicates the realization process, and 2- Requires the larger bandwidth comparing to other mm-wave frequency bands which further complicates the antenna design. Therefore, a solution suitable for this frequency band can be scaled easier to lower mm-wave frequencies such as 28 GHz and 38 GHz where the wavelength is bigger and the required bandwidth is smaller.

The V-band (57-66 GHz) provides large frequency bandwidth of 14.6%. Moreover it's unlicensed or light licensed in most countries meaning reduced deployment cost for operators. As presented in figure 1-4, the oxygen resonant frequency occurs at 60 GHz, which translates to an attenuation peak at this frequency. This characteristic makes V-band attractive for small cell applications as it helps to avoid interference and also enables high frequency re-use.

1.2.2. Antenna specifications for 5G point-to-point communications

In order to be authorized to use a frequency band, the antenna should be compliant with certain standards imposed by regulatory bodies such as *European Telecommunications Standards Institute* (ETSI) and United States *Federal Communications Commission* (FCC). These standards pose constraints on different characteristics of the antenna, such as its minimum gain and maximum Equivalent Isotopic Radiated Power (EIRP). Also the antenna radiation pattern should be compliant with a Radiation Pattern Envelope (RPE) of a certain class. The class of RPE to respect depends on the local regulators. The goal of these requirements is to avoid interferences within a network with respect to other networks operating in the near bands. Figure 1-5(a) presents an example of a class 2 RPE for V-band and figure 1-5(b) presents a class 3A RPE for V-band, defined by ETSI [3]. As illustrated in these figures, the main difference between two classes is the maximum side lobe levels acceptable which get more constraint for higher classes.

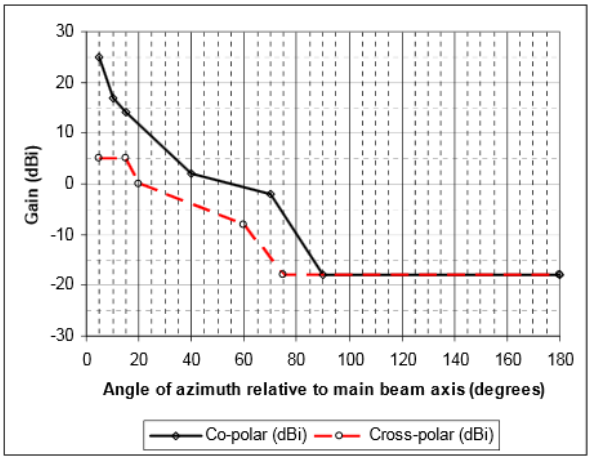

Angle (°)	Co-polar (dBi)	Angle (°)	Cross-polar (dBi)
5	25	5	5
10	17	15	5
15	14	20	0
40	2	60	-8
70	-2	75	-18
90	-18	180	-18
180	-18		

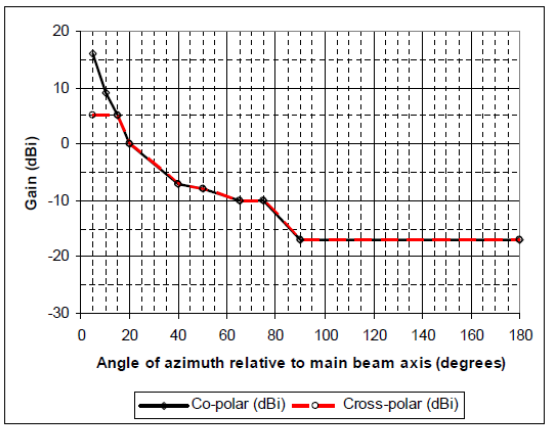

Angle (°)	Co-polar (dBi)	Angle (°)	Cross-polar (dBi)
5	16	5	5
10	9	15	5
15	5	20	0
20	0	40	-7
40	-7	50	-8
50	-8	65	-10
65	-10	75	-10
75	-10	90	-17
90	-17	180	-17
180	-17		

(a) (b)

Figure 1-5: Antenna Radiation Pattern Envelope for : (a) class 2, and (b) class 3A, for 47-66 GHz frequency rang.

The antennas intended for point-to-point communications, require very high gains in order to ensure an acceptable link range : more than 38 dBi for E-band and more than 32 dBi and 30 dBi for 28 GHz and V-band respectively [3]. Moreover, being high gain means having narrow beam radiation patterns and therefore the antenna can avoid interferences. However, the small beam width complicates the link alignment both in antenna installation phase and maintaining the link in operational phase. Therefore, another requirement for 5G backhaul/fronthaul antennas is their compatibility for electronic beam steering. As mentioned earlier and illustrated in figure 1-6, the beam steering feature is required for:

- Antenna installation phase: automatic link alignment to ensure fast and low cost installation;

- Antenna operational phase:
    - Compensating swift and sways of mounting structures to ensure continuous high quality link connection
    - Network re-configurability (reconfigurable backhauling/fronthauling)

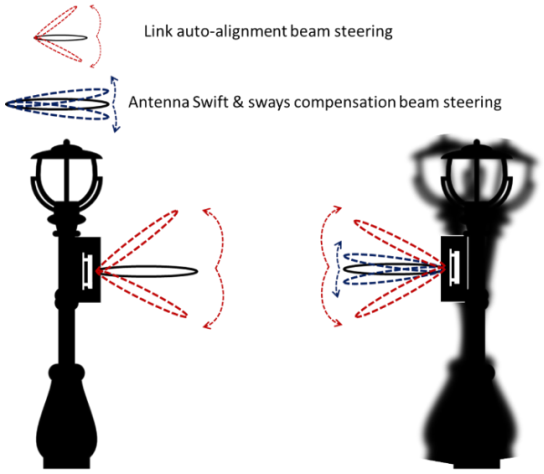

Figure 1-6: Backhaul antenna beam steering scenarios.

It was demonstrated in [4] that a beam steering of ±4° in both azimuthal and elevation planes will be sufficient to compensate swift and sways when the antenna is installed on fragile mounting structures such as lamp stand or bus stops. For the operational phase, in order to ensure an automatic link alignment, discussions with RFS clients concluded that a beam steering range of ±15° in both planes would be sufficient. For the network re-configurability, i.e. changing the network mesh layout there is no specific beam steering range defined and it will depend mostly on the network configuration and location of its different nodes (macro/small cells). However, larger beam steering range in azimuthal plane would be required comparing to elevation plane.

Beside of RF & Electronic specifications, as these antennas may be installed at street level in high numbers for small cell networks, low profile and low cost antennas are required to make them unobtrusive and agile in the urban areas and economically justifiable.

To summarize, main antenna requirements for 5G mm-wave backhaul are:

- High gain (>30 dBi)
- Compliancy with standards posed by regulators (ETSI & FCC)
- Electronic beam steering compatible (Min : ±4°, Max :±15°)
- Compact size
- Low cost

In order to have a reference for the antenna solution design, the following primary datasheets were constructed using the available standards and client expectations.

The following tables present the characteristics identified for the following bands: 28 GHz (table 1-I), 38 GHz (table 1-II), 42 GHz (Table 1-III), Band V (table 1-IV), and Band E (table 1-V)).

Table 1-I: Antenna specification for 28 GHz Point-to-Point links.

Frequency band	**28GHz**: 27.5-29.5 GHz **(7.4%)**
Product Type	Directive (pencil beam) antennas
MAX EIRP	85dBm
Antenna Gain	**Min : 32 dBi** Max : 60dBi
Max Power	25dBm
3dB beam width	4° Max (calculated)
Polarization	Single Linear (H or V)
Front to Back Ratio	~60 dB
Cross Polarization	27dB
Max VSWR (Return Loss)	~1.5(14 dB)
RPE class	ETSI EN 302 217-4 V2.1.1 (2017-05) **Class 3**
Beam steering range	Min : ±4°, Max :±15°
Input waveguide	WR-28
Temperature	Min : -45°C , Max : +85°C
Equivalent physical surface	17.2cm*17.2 with Maximum Height of 20mm

Table 1-II: Antenna specification for 38 GHz Point-to-Point links.

Frequency band	**38 GHz:** 37.5-40 GHz **(6.45%)**
Product Type	Directive (pencil beam) antennas
MAX EIRP	85dBm
Antenna Gain	**Min : 32dBi**, Max : 62dBi
Max Power	23dBm
3dB beam width	4° Max (calculated)
Polarization	Single Linear (H or V)
Front to Back Ratio	~60 dB
Cross Polarization	27dB
Max VSWR (Return Loss)	~1.5(14 dB)
RPE class	ETSI EN 302 217-4 V2.1.1 (2017-05) **Class 3b**
Beam steering range	Min : ±4°, Max :±15°
Input waveguide	WR-22
Temperature	Min : -45°,Max : +85°
Equivalent physical surface	12cm*12cm with Maximum Height of 20mm

Table 1-III: Antenna specification for 42 GHz Point-to-Point links.

Frequency band	**42GHz:** 40.5-43.5 GHz **(7.14%)**
Product Type	Directive (pencil beam) antennas
MAX EIRP	85dBm
Antenna Gain	**Min : 32dBi**, Max : 62dBi
Max Power	23dBm
3dB beam width	4° Max (calculated)
Polarization	Single Linear (H or V)
Front to Back Ratio	~60 dB
Cross Polarization	27dB
Max VSWR (Return Loss)	~1.5(14 dB)
RPE class	ETSI EN 302 217-4 V2.1.1 (2017-05) **Class 3b**
Beam steering range	Min : ±4°, Max :±15°
Input waveguide	WR-19
Temperature	Min : -45°,Max : +85°
Equivalent physical surface	12cm*12cm with Maximum Height of 20mm

Table 1-IV: Antenna specification for V-band Point-to-Point links.

Frequency band	**V-Band**: 57-66 GHz **(14.6%)**
Product Type	Directive (pencil beam) antennas
MAX EIRP	+55 dBm
Antenna Gain	**min: 30dBi**, MAX: 45 dBi
Max Power	10dBm
3dB beam width	4 degree Max (calculated)
Polarization	Single Linear (H or V)
Front to Back Ratio	~60 dB
Cross Polarization	Min 27 dB (Recommendation)
Max VSWR (Return Loss)	~1.5(14 dB)
RPE class	ETSI EN 302 217-4 V2.1.1 (2017-05) - **Class 2**
Beam steering range	Min : ±4°, Max :±15°
Input waveguide	WR-15
Temperature	Min : -45°,Max : +85°
Equivalent physical surface	7cm*7cm with Maximum Height of 20mm

Table 1-V: Antenna specification for E-band Point-to-Point links.

Frequency band	**E-Band**: 71-76 GHz & 81-86GHz **(19.1%)**
Product Type	Directive (pencil beam) antennas
MAX EIRP	+85 dBm
Antenna Gain	**min: 38dBi,** MAX: 55dBi
Max Power	30 dBm
3dB beam width	2 degree Max (calculated)
Polarization	Single Linear (H or V)
Front to Back Ratio	~60 dB
Cross Polarization	Min 27 dB(Recommendation)
Max VSWR (Return Loss)	~1.5(14 dB)
RPE class	ETSI EN 302 217-4 V2.1.1 (2017-05) - **Class 3**
Beam steering range	Min : ±4°, Max :±15°
Input waveguide	WR-12
Temperature	Min : -45°,Max : +85°
Equivalent physical surface	15cm*15cm with Maximum Height of 20mm

It should be noted that the ETSI requirements for V-band are optional but for E-band are obligatory. Even if it was decided to focus on V-band as the frequency band of interest for this thesis, the prepared datasheets of other potential frequency bands facilitate changing the frequency band and enable foreseeing required modifications in the antenna solution.

1.3. Conclusions

In this chapter, the context of the project, 5G mm-waves point-to-point communications was introduced. The mm-waves frequency bands characteristics, as they will be potentially used for 5G backhauling, were detailed. As the 5G frequency was not yet known at the time, it was decided to focus the antenna design on V-band (57-66 GHz). As this frequency band requires a comparatively large bandwidth and high gain antennas (see table 1-IV), it would be easier to scale a solution designed at this frequency to other frequency bands such as 28 GHz or 38 GHz. Also, because of the high absorption rate at 60 GHz, this frequency band is particularly interesting for small cell applications in dense networks.

The antenna specifications for this context were detailed as well. In terms of meeting customer expectations, it's required that the antenna solution must have a compact form factor and be a low cost solution. In order to be authorized to use these antennas in regulated frequency bands, these antenna need to respect some standards such as minimum gain (30 dBi for V-band) and low side lobe levels compliant with ETSI and/or FCC Radiation pattern envelopes. The goal of these standards is to avoid interferences in the network.

In the following chapter 2, a detailed study on different antenna technologies compatible for these requirements will be presented, based on the defined technical specifications defined above.

In Chapter 3, a fixed beam, compact, low cost and high gain antenna based on a quasi-optical solution with reduced focal distance is proposed in V-band (57-66 GHz). This antenna solution, Folded Fresnel Zone Plate (FFZP) antenna, is verified by both simulations and outdoor measurements.

In Chapter 4, a preliminary study on the FFZP antenna beam steering characteristics and its focal array design consideration is done.

In Chapter 5, twos beam steering solutions based on printed focal arrays are proposed for the FFZP antenna. These solutions are characterized by both simulations and measurements.

In Chapter 6, three perspective solutions to integrate properties such as more focal distance reduction, dual-frequency and dual-polarization into the FFZP antenna solution are proposed.

Finally general conclusions and perspectives are drawn at the end of the thesis.

1.4.References

[1] Deutsche Telekom https://www.telekom.com

[2] T. S. Rappaport, S. Sun, R. Mayzus, H. Zhao, Y. Azar, K. Wang, G. N. Wong, J. K. Schulz, M. Samimi and F. Gutierrez, "Millimeter Wave Mobile Communications for 5G Cellular: It Will Work!," *IEEE Access*, vol. 1, pp. 335-349, May 2013.

[3] ETSI EN 302 217-4- V2.1 (2017-05) -Fixed Radio Systems; Characteristics and requirements for point-to-point equipment and antennas; Part 4: Antennas, 2017.

[4] R. Kalimulin, A. Artemenko, R. Maslennikov, J. Putkonen and J. Salminen, "Impact of Mounting Structures Twists and Sways on Point-to-point Millimeter-Wave Backhaul Links," *IEEE International Conference on Communications (ICC)*, June 8-12, 2015, London, UK.

2. Chapter 2 : State of the art on antenna technologies for mm-waves point-to-point communications

2.1. Introduction

In the previous chapter, the context of the thesis was detailed. As discussed, the objective of this thesis is to introduce a new highly directive antenna solution for 5G mm-waves Point-to-Point (PtP) communications. In this chapter, a state of the art analysis on antenna technologies are presented in order to evaluate different antenna technologies in terms of :

- Gain performance: ensure a minimum gain required (30 dBi for V-band) and provide large 3-dB gain bandwidth corresponding to the impedance bandwidth (14.6% for V-band).
- Side lobe levels: should be compliant with ETI Radiation Pattern Envelope (class 2 for V-band) [1].
- Form factor (compactness): especially in terms of antenna height as flat antennas are the market trend for 5G.
- Low cost: as these antennas will be deployed in high numbers in small cell solutions for dense networks they should be economically justifiable.
- Compatible with electronic beam steering: enable a maximum beam steering range of ±15° in both planes while being compliant with datasheet requirements such as minimum gain and RPE.

In order the study the state of the art on different antenna technologies, we divide them into two main families: 1-directly fed antenna arrays, such as waveguide based slot arrays, horn arrays, Continuous Transverse Stub (CST) arrays and microstrip arrays, and 2- quasi-optical antenna solutions, such as lens antennas, transmit-arrays and reflect-arrays.

In the following sections 2 and 3, each antenna family is first studied in details taking into account the latest progress in the literature. Then an analysis on available commercial antenna

solutions potentially compatible for our application is presented in section 4. Afterwards, a decision matrix is constructed in section 5, taking into account the detailed state of the art. The objective of this decision matrix is to facilitate the choice of an antenna technology for our application by comparing each antenna technology with the datasheets developed in first chapter. Finally this chapter is concluded in section 6.

2.2. Directly fed antenna arrays

Directly fed antenna array, means that there is no optical path between the radiating element(s) and the feeding network and they are either directly connected (such as inset or coaxial fed microstrip patch antenna) or coupled using an aperture/slot (such as aperture coupled microstrip patch antenna or slot arrays). Figure 2-1 shows the schematic presentation of different sub-families of direct radiation antennas for high gain solutions.

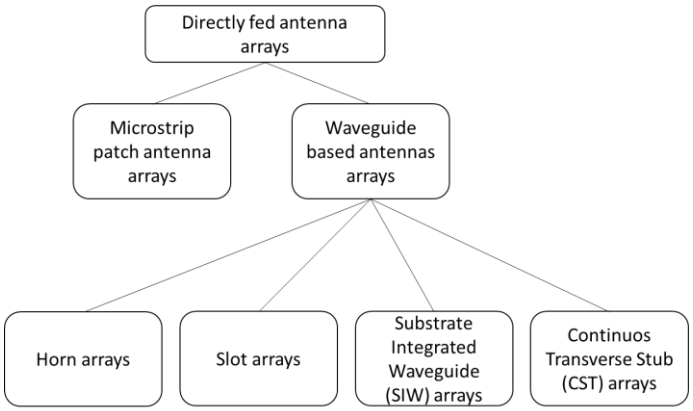

Figure 2-1: Schematic representation of different types of directly fed antenna arrays for high gain solutions.

In order to have high gain antenna solutions, these antenna technologies are used in form of arrays. Therefore, before going into detail for each of these antenna array technologies, an analytical study based on array factor calculations is presented. The goal of this study is to determine the array phase shifting and the amplitude tapering requirements of the antenna in order to be compliant with the defined datasheets in chapter 1.

2.2.1. Planar Array requirements for 5G mm-waves Point-to-Point communications

In this section a brief resume on an analytical study on array amplitude tapering and phase shifting requirements for our application is presented. This study is carried out to determine array antennas requirements for mm-waves high gain point-to-point links in terms of: 1- amplitude tapering in order to have side lobe levels compliant with ETSI masks. For this, tapering sensitivity per element and per sub array was determined. 2- phase shifting for electronic beam steering and meanwhile being compliant to datasheet. For this, quantized phase shifting impact is studied and the phase shifting required per element and per sub-array is determined.

These calculation were done by simply using array factor equations. The V-band (57-66 GHz) frequency band was chosen as reference, and as the most constrained frequency band in mm-

waves. Minimum required gain for this frequency band is 30 dBi and the antenna radiation patterns should be compliant with class 2 ETSI Radiation Pattern Envelope (RPE).

Figure 2-2 compares the calculated radiation patterns of 32×32 elements array with uniform amplitude, tapered amplitude per element, tapered amplitude per 4×4 sub-array and tapered amplitude per 16×16 sub-array. It should be noted tapering per *n*×*m* sub-array mean that the elements of each sub-arrays have equivalent amplitude coefficients and the tapering law, Taylor in our case, is applied to the ensemble of the sub-arrays and each sub-array is seen as one element. As in our case the array has 32×32 elements, 4×4 sub-arrays means each sub array has 8×8 elements and 16×16 sub-array means each sub arrays 2×2 elements. The inter-element spacing of the array was chosen the 0.7 λ practical value. The radiating elements are assumed to be point sources. We can conclude from figure 2-2 that, tapering per element or very small sub-arrays is required so the antenna side lobe levels be compliant with ETSI RPE. By tapering the array elements, we observed almost 5 dB total gain reduction and to compensate it, it is required to increase yet array elements numbers and this means more complicated tapering.

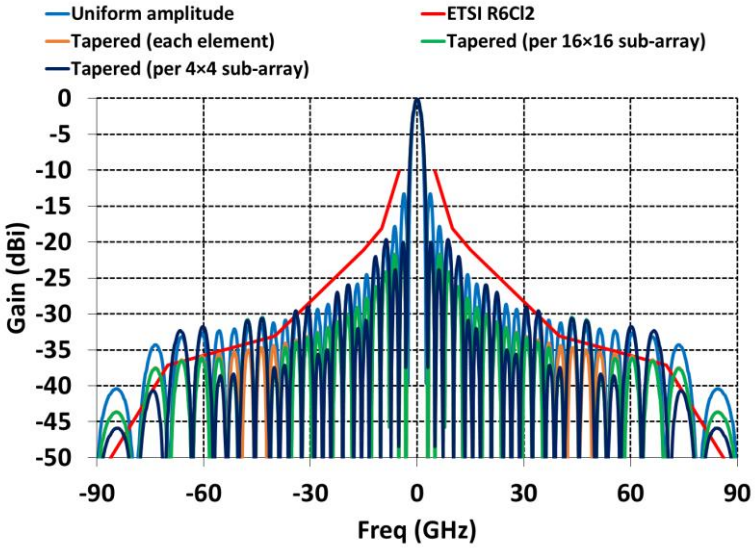

Figure 2-2: Superimposed normalized radiation patterns of 32×32 elements array at 60 GHz, illustrating the impact of amplitude tapering per element and per sub-array.

The amplitude tapering coefficients of the cases of figure 2-2 are presented in figure 2-3. The *x*- and *y*-axes represent the array elements and sub-arrays. The *z*-axis represent the amplitude coefficient of each element or sub-array normalized to one. It can be observed that amplitude coefficients per element and per 2×2 elements (16×16 sub-array) have minimum deltas in order of 0.02 and 0.03 respectively. These coefficients are obtained using a Taylor tapering law with a target of obtaining side lobe levels of 20 dB. This high precision tapering required for an array to be compliant with ETSI RPE, class 2 here which is the less constrained class, requires very challenging and costly high precision realization technologies.

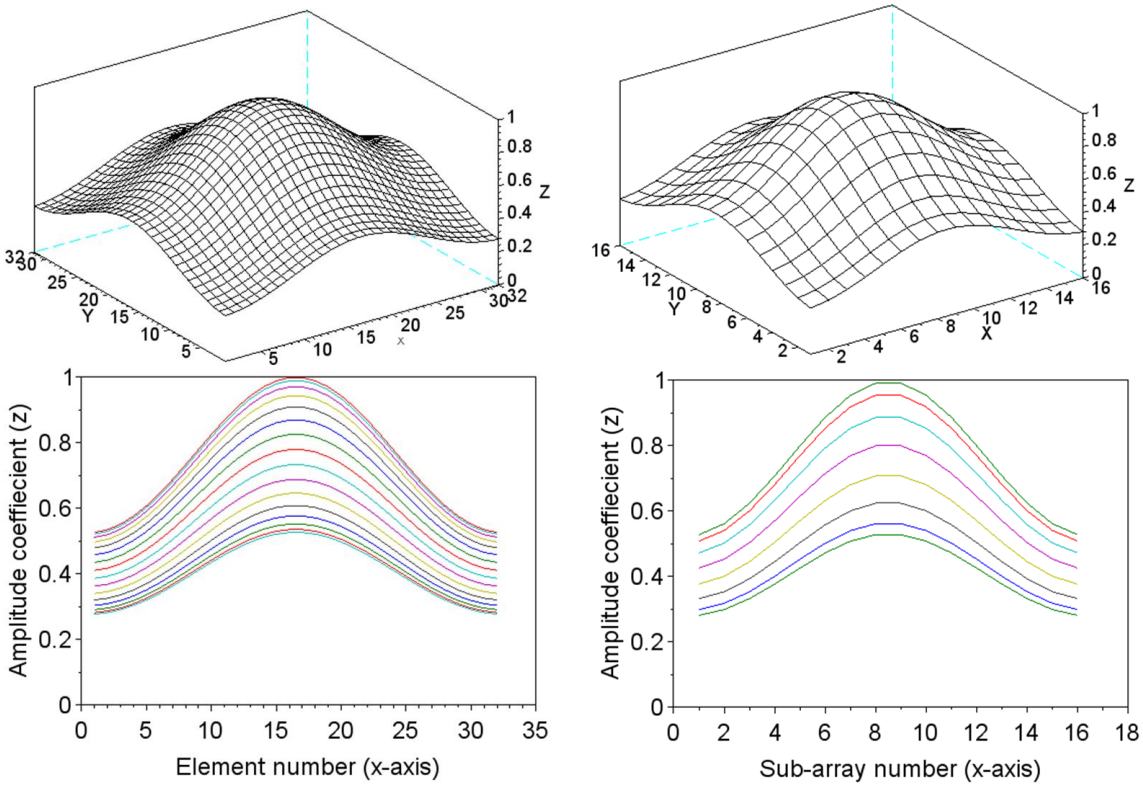

(a) (b)

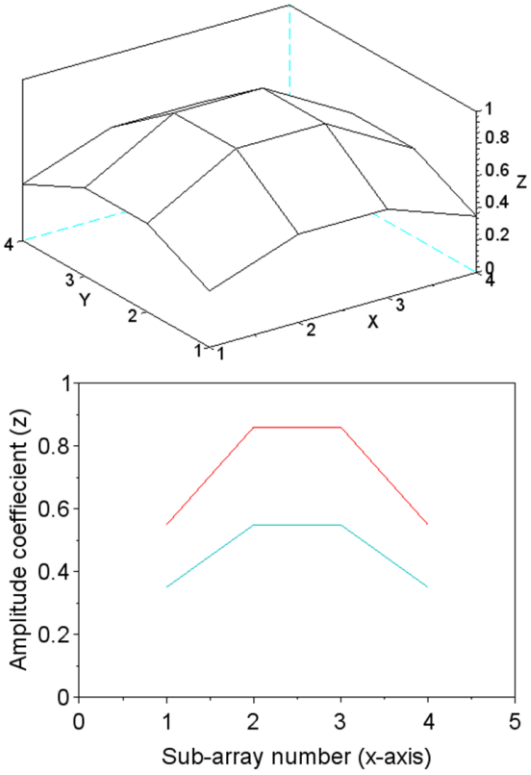

(c)

Figure 2-3: 3D view (top) and cut-view (bottom) of amplitude coefficients distribution (Taylor tapering) of : (a) each element of the 32x32 elements array, (b) each sub-array of 16×16 sub-arrays, and (c) each sub-array of 4×4 sub-array.

Figure 2-4 presents the superimposed radiation patterns of the 32×32 elements array with uniform amplitude for 15° beam steering where a perfect (non-quantized) phase shifting is applied to each element of the 32×32 elements array, to each sub-array of the16×16 sub-array and to each sub-array of 4×4 sub-array. Applying a phase shift to sub-arrays, means that there is a phase delta between the sub-arrays and the elements of each sub-array have the same phase level. It can be observed that, by applying phase shifting to sub-arrays instead of each element, the antenna radiation pattern will have grating lobes because each sub-array is larger element the inter-element spacing is larger than λ.

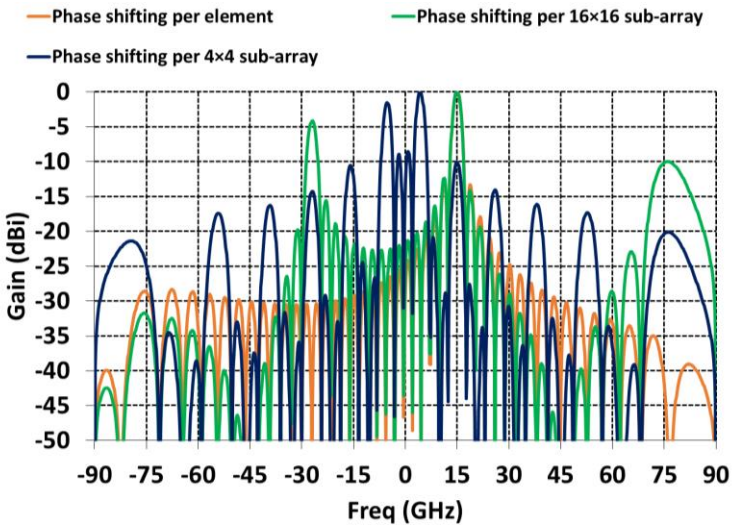

Figure 2-4: Superimposed normalized radiation patterns of 32×32 elements array at 60 GHz illustrating the impact of phase shifting per element and per sub-array for beam steering angle of 15°.

The progressive phase shift value applied in each case is presented in figure 2-5. As the beam steering is only in one plane, the phase shifting is applied only in one direction (*x*-axis).

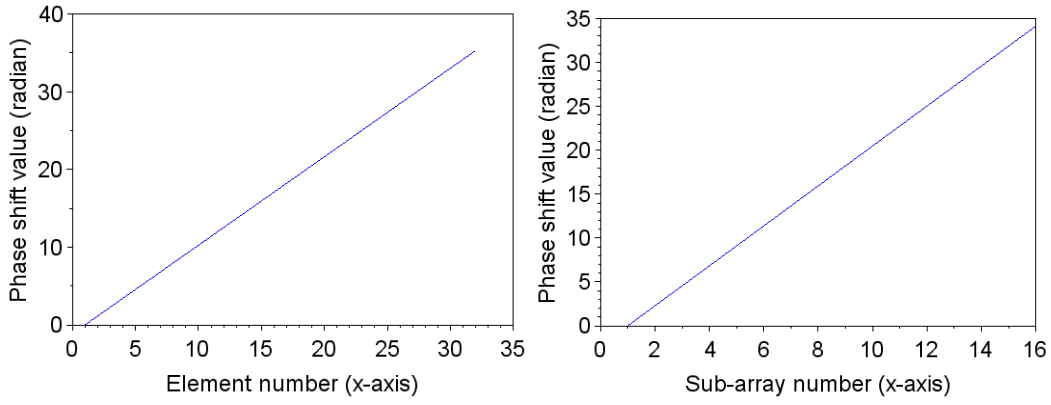

(a) (b)

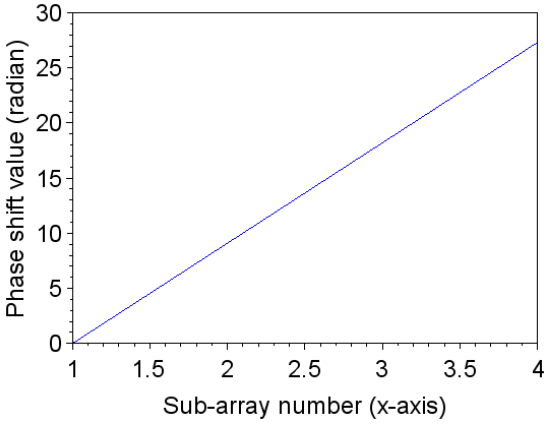

(c)

Figure 2-5: Phase shift value (radian) applied to : (a) each element of the 32x32 elements array, (b) each sub-array of 16×16 sub-arrays, and (c) each sub-array of 4×4 sub-array.

Moreover, it should be noted that the phase shifting applied per element in figure 2-4 and illustrated in figure 2-5 is an ideal phase shifting. In reality, the phase shifters have quantized phase levels depending on their resolution. For example, a 5-bit resolution phase shifter can offer 32 phase states. Applying quantized phase shifting results in increased side lobe levels. Other important point to consider for real life phase shifters is their phase and amplitude error. Amplitude error means a phase shifter will not have the same output amplitude (S21) out for all of its states. Phase error is when the phase shifter, shifts the phase with a deviation (usually in order of 5 to -6°) comparing to the expected phase shifting value. Moreover, these phase and amplitude errors are variable in function of frequency. The manufactures give this information in form of Root Mean square values as a function of frequency.

Overall, it can be concluded, having an array at mm-waves for high gain PtP communications with beam steering capability requires very high precision amplitude tapering and phase shifting per element (1024 phase shifters for the 32×32 elements array) which is very challenging and costly for realization with current available technologies.

2.2.2. Microstrip antenna arrays

Microstrip antenna arrays may seem suitable for 5G Point-to-Point communications at first, because of their beam steering compatibility and side lobe level control due to the array theory phase shifting and amplitude tapering capability. But considering that the working frequency range of the antenna will be at mm-waves, these antennas will be out of scope mainly because the high dielectric substrate loss reduces the antenna efficiency significantly [2]. In other words, large number of small array elements are required to ensure a minimum high gain which results in large antenna aperture and therefore it leads to high dielectric and microstrip line losses in mm-waves. Figure 2-6 from [3] presents the gain variation of an array of *N* elements taking into account the microstrip transmission loss (dB/λ) and compares it with the ideal directivity of an array (zero loss). It can be observed that microstrip array gain start to drop after a certain number of elements because of the increased dielectric loss.

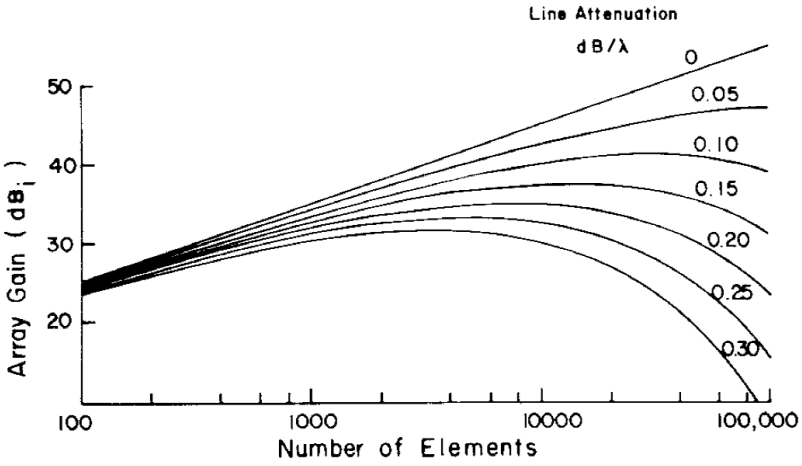

Figure 2-6: Microstrip antenna array gain in function of number of elements for different microstrip line losses [3].

Other concern of microstrip antennas are surface waves who generate spurious radiations and leakage. This will also result in antenna gain and efficiency reduction.

Figure 2-7 presents the layout of a 256 elements microstrip patch array fed by corporate feeding network [2]. This type of feeding network offers higher bandwidth comparing to series fed arrays.

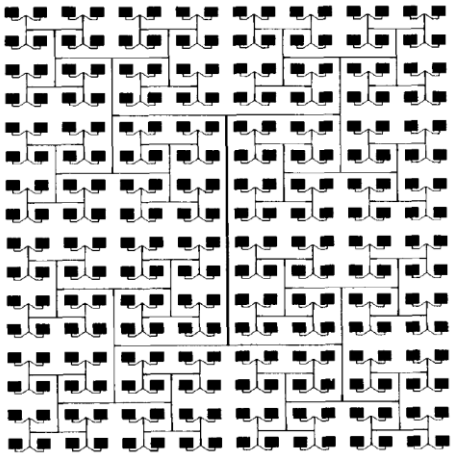

Figure 2-7: Layout of 256 elements microstrip array with corporate feeding network [2].

For example, in reference [4], the author compares, for a 256 elements microstrip antenna array designed for Ka-band, the calculated gain (theory) and real gain taking into account microstrip line loss, radiation loss and mismatch loss, leading to a total of 5.5 dB of microstrip and dielectric loss for this array. Also, reference [5] presents 0.9 dB/cm measured loss for microstrip feed line at 73 GHz, meaning for a 60 mm long microstrip line there is almost 5.4 dB loss.

Furthermore, in the previous section dedicated to numerical study of array tapering and phase shifting requirements we saw that a phase shifter per element and a tapering precision in order of 0.02 is required which is challenging and costly to obtain in manufacturing.

2.2.3. Waveguide based antenna arrays

Waveguide based antenna arrays main advantage comparing to microstrip patch antenna arrays is that they don't suffer from high losses due to the wave propagation inside dielectric substrates, but within the waveguide structures. Generally, waveguide based arrays offer very good efficiency performance.

As presented previously in figure 2-1, main types of waveguide based arrays are:

- Horn Arrays,
- Slot Arrays,
- Substrate Integrated Waveguide (SIW) arrays,
- Continuous Transverse Stub (CTS) arrays.

In the following each type is be presented in details.

2.2.3.1. Horn arrays

Horn arrays are one of the antenna solutions proposed for mm-wave PtP communications in recent years. The horn array presented in reference [6], offers a directivity of 40.9 dBi for an array of 32×32 stepped horn elements (physical radiating aperture of 120mm × 120mm). This antenna can only be compliant with the ETSI class 3 RPE on the 45° plane (diamond position) as presented in figure 2-8.

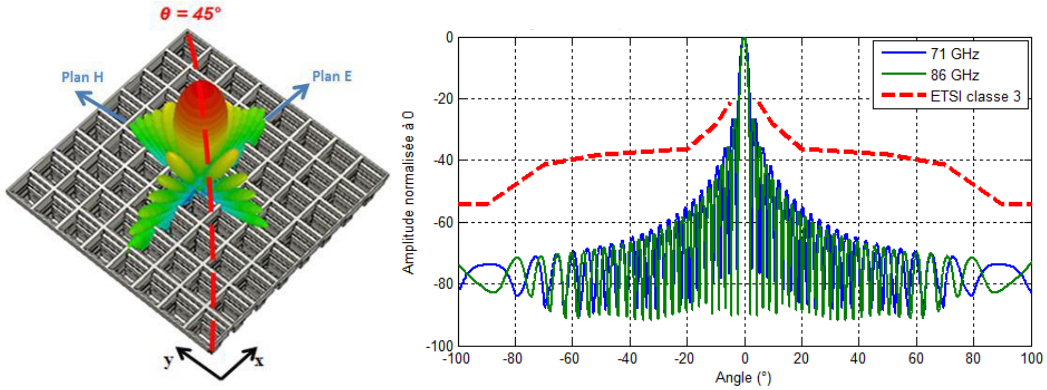

(a) (b)

Figure 2-8: 32×32 stepped horn elements array : (a) 3D schematic and radiation pattern, and (b) normalized 45° plane radiation patterns at 71 GHz and 86 GHZ superimposed by ETSI class 3 RPE [6].

Figure 2-9 present the 3D view of the stepped horn unit cell. As presented the dimension of the steps are in order of 0.2-0.3 mm which means the realization of this antenna will be challenging and costly [6].

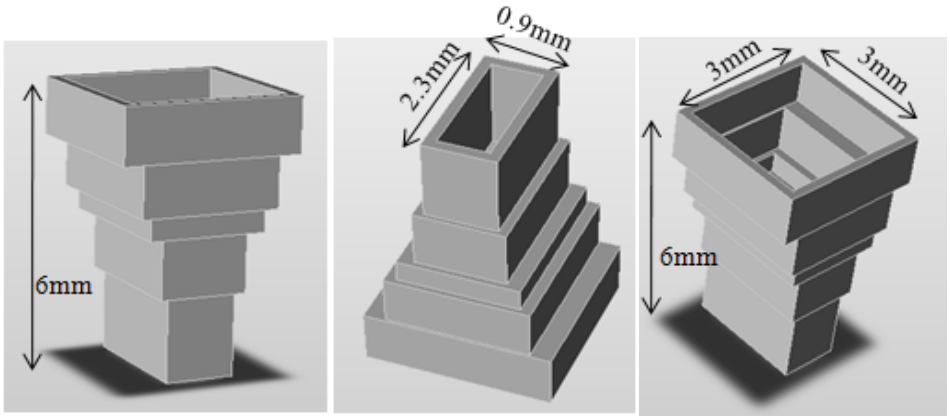

Figure 2-9: Stepped horn unit cell designed for E-band 3D View and dimensions [6].

Not only the radiating element, but the feeding network has miniature dimensions which will also complicate the realization and make it costly. The complete structure and dimensions of the stepped horn unit cell and its vertical feeding network is presented in figure 2-10 [6].

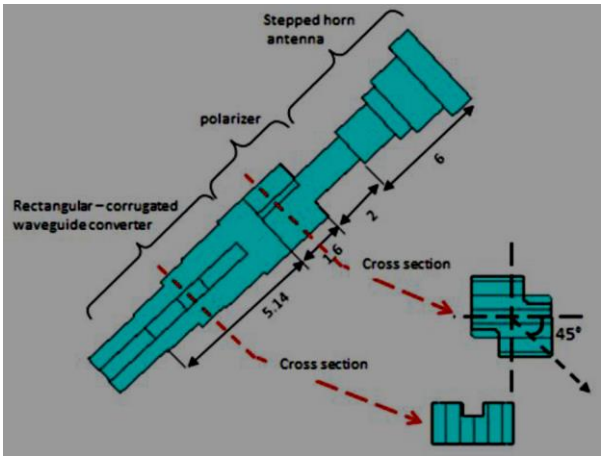

Figure 2-10: Structure and dimensions of the designed stepped horn unit cell and its feeding network components [6].

These kind of antennas are commercialized and available in the market. As an example, HUBER+SUHNER propose horn arrays for E-band and V-band [7-8]. Their products will studied in detail in the section dedicated to commercialized solutions. Figure 2-11 shows a photo of the E-band antenna taken from reference [7].

Figure 2-11: HUBER+SUHNER Horn array antenna at E-band [7].

In order to have a horn-array compliant with ETSI RPE in both elevation and horizontal planes, as demonstrated in section 2.1 of this chapter, the array elements need to be tapered which is technologically challenging and costly. This is the main reason why, to the knowledge of the author, a tapered horn-array at mm-waves compliant with ETSI RPE at both main planes does not exist.

Moreover, to the knowledge of the author, there exist no active beam steerable horn-array solution up to today. This is mainly because having a phase shifter per array element (horn) and integrating it within the waveguide feeding network is technologically challenging and costly.

2.2.3.2. Waveguide Slot arrays

Same as horn arrays, waveguide slot arrays benefit from high efficiency and low loss grace to absence of dielectric substrates. But due to the resonance nature of the slots these antennas suffer from limited gain bandwidth.

Generally waveguide slot arrays can have two types of feeding: End feed (serial feeding) or Center feed (parallel feeding). Figure 2-12 presents an example of a series-fed single layer waveguide slot array [9].

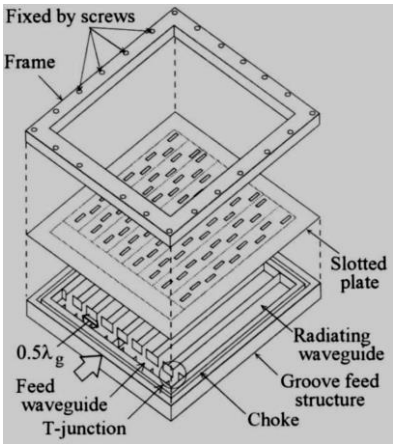

Figure 2-12: End feed waveguide slot array antenna example [9].

Figure 2-13 presents the gain variation over frequency of an end feed waveguide slot array [9]. As can be seen the antenna has 3-dB gain bandwidth of only 3%.

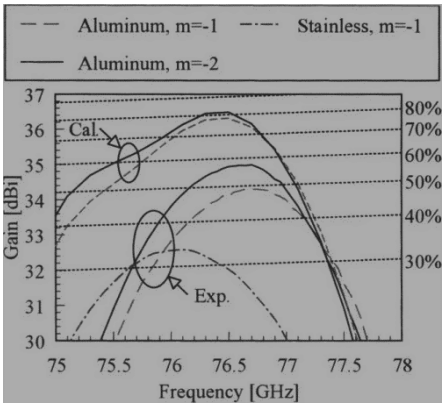

Figure 2-13: Measured and calculated gain and efficiency variation over frequency of an End feed waveguide slot array [9].

Figure 2-14 shows frequency dependent main beam squinting of a conventional end feed waveguide slot array [10].

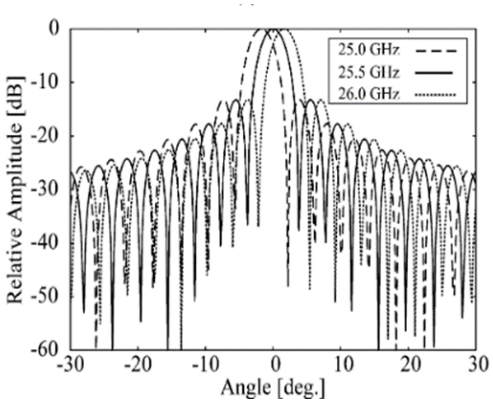

Figure 2-14: Typical beam squinting in end feed waveguide slot arrays in function of frequency [10].

From figures 2-13 and 2-14, we can conclude that end feed slot arrays, have two main disadvantages regarding our application due to the long-line effect when the array size becomes large (i.e., different delays to each element): 1- limited gain bandwidth and 2- beam squinting in function of frequency.

Beside end-fed waveguide slot arrays, there exists center feed, partially-corporate feed and full-corporate feed waveguide slot arrays. The center feed type [11] halves the long-line effect by arranging the feed waveguide at the center of the antenna in the comparison with the end feed type. The partially corporate feed type [12] quartered the long-line effect by dividing the antenna into four subarrays. However, the aperture efficiency of both the models was degraded by grating-lobes due to no-slot areas in the aperture just above the feed waveguide newly introduced. Figure 2-15 shows an example of a center-fed waveguide slot arrays and its gain and efficiency performance over frequency from [11]. The efficiency reduction of the center feed waveguide slot array comparing to end feed waveguide slot array is visible in this figure.

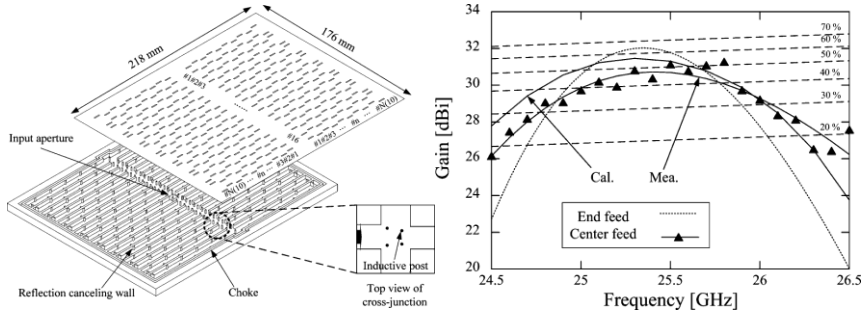

Figure 2-15: Center feed waveguide slot array (left) and its gain and efficiency variation over frequency (right) [11].

A wideband and high efficiency Full-corporate feed antenna was reported in V-band in [13]. As shown in figure 2-16(a), this structure is double-layer in order to keep the element spacing smaller than one wavelength to avoid grating lobes. As presented in figure 2-16(b), this double layer full-corporate waveguide slot array offers a high efficiency of 83.6% and a wide 3-dB gain bandwidth better than 14%. Moreover it can be observed in figure 2-16(c) that the antenna is not suffering from beam squinting over frequency in contrary to end feed slot arrays. Other advantage of this solution is high cross polarization discrimination of 46.3 dB at 58 GHz and 48.6 dB at 64 GHz. Due to the mentioned advantages, the concept of full-corporate feeding network introduced here, is further used in many other type of waveguide based antenna arrays.

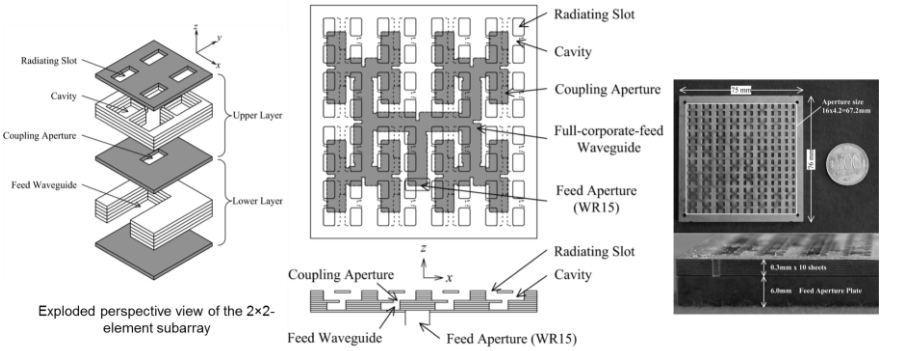

(a)

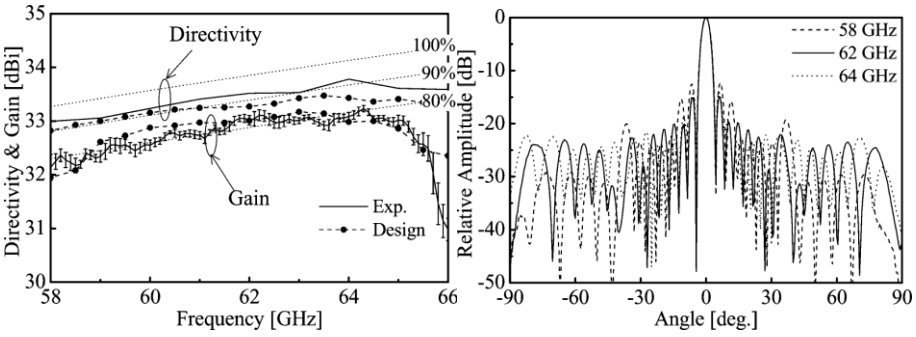

(b) (c)

Figure 2-16: (a) Photo of the fabricated antenna, its layout and exploded perspective view of the 2×2-element subarray, (b) directivity, gain and efficiency variation of the antenna over frequency, and (c) E-plane radiation patterns [13].

Other interesting waveguide slot array solution proposed by the team managed by Professor *Hirokawa* and Professor *Ando* is a filter-antenna for E-band point-to-point communications

[14]. As E-band is composed of two separate frequency segments, 71-76 GHz and 81-86 GHz, this solution integrates bandstop filters to stop radiation at 76-81 GHz frequency range and bandpass filters to allow radiation at E-band. This 16×16 element slot array fed by corporate feeding network demonstrates a 33 dBi directivity, a 32.7 dBi realized gain, and an 82.7% total efficiency. Diffusion bonding technology is used to realize this solution. Moreover, this solution offers low side lobe levels of -24 dB.

The full-corporate center feed waveguide slot array promises very good efficiency and wide bandwidth performances comparing to other waveguide slot arrays introduced previously. But, this type of antenna requires near perfect electric contact between the feeding layer and the radiating layer. Ensuring this contact in manufacturing and mass production is tricky and challenging. To overcome this issue, an alternative solution based on gap waveguide was proposed [15]. By using a gap waveguide, the perfect electrical contact is no longer necessary and thus the manufacturing process becomes more routine and technics such as molding or die-sink Electrical Discharge Machining (EDM) can be used. This solution is based on a parallel-plate waveguide configuration and using soft/hard boundary conditions to control the propagation of waves in desired directions between the two plates. In fact, the gap waveguide technology, uses the basic cut-off of Perfect Electrical Conductor – Perfect Magnetic Conductor (PEC-PMC) parallel plate waveguide to create a stopband. This stopband can be obtained using periodic structures such as metallic pins [16]. By having a guiding structure in-between the periodic structure, the electromagnetic wave can propagate within them without leaking in any other direction. The guiding structure can be ridge, groove or microstrip waveguide [15]. Figure 2-17 presents four different types of gap waveguide technologies: ridge gap waveguide [17], groove gap waveguide [18], inverted microstrip-ridge gap waveguide [19], and microstrip-ridge gap waveguide [20].

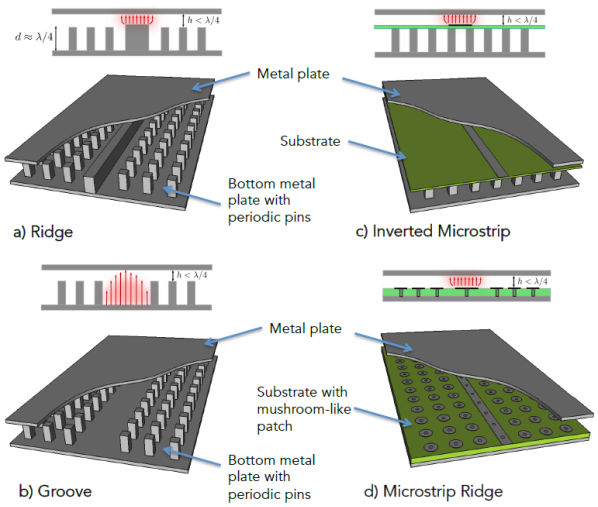

Figure 2-17: Different types of gap waveguide structures [15], (a) Ridge gap waveguide, (b) Groove gap waveguide, c) Inverted- microstrip gap waveguide, and (d) Microstrip-ridge gap waveguide.

As an example, figure 2-18 shows a multi-layer ridge gap waveguide slot array with corporate feed network designed for V-band [21].

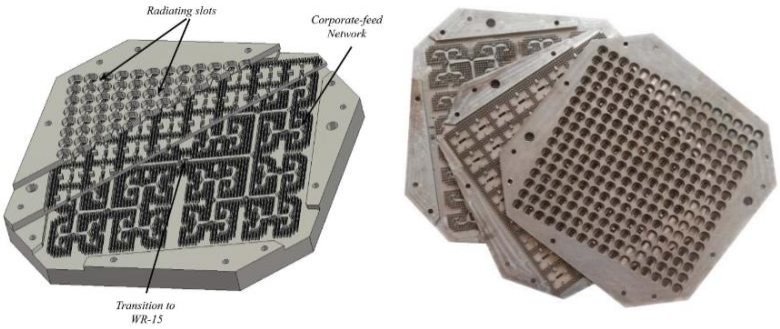

Figure 2-18: Multi-layer Ridge gap waveguide 16×16 slot array with corporate feed network designed for V-band [21].

This 16×16 slot array offers an efficiency higher than 80% and a 1-dB gain bandwidth of 18% for 58-70 GHz frequency range. The simulated reflection coefficient is below -10 dB from 56-67 GHz. These results are shown in figure 2-19.

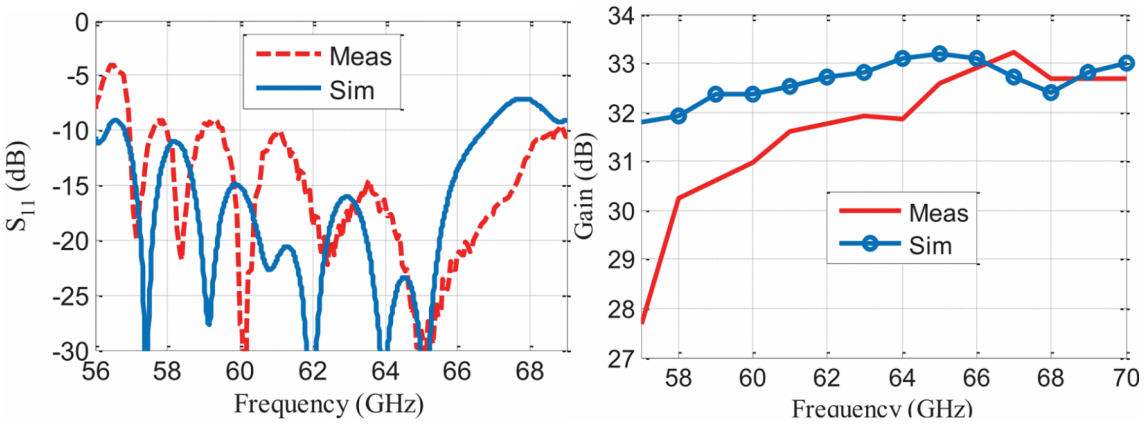

Figure 2-19: Ridge gap waveguide slot array Reflection coefficient (left) and gain variation over frequency (right) [21].

In terms of radiation pattern, in order to be compliant with ETSI class 2 RPE in E-plane and H-plane, the author of reference [21] uses tilted slot as presented in figure 2-18. Figure 2-20 presents the radiation patterns of the antenna in both conventional E/H-planes and also principal E/H-planes taking into account the slot tilting angle. It can be observed that the antenna is not compatible with ETSI RPE in principal E/H plane.

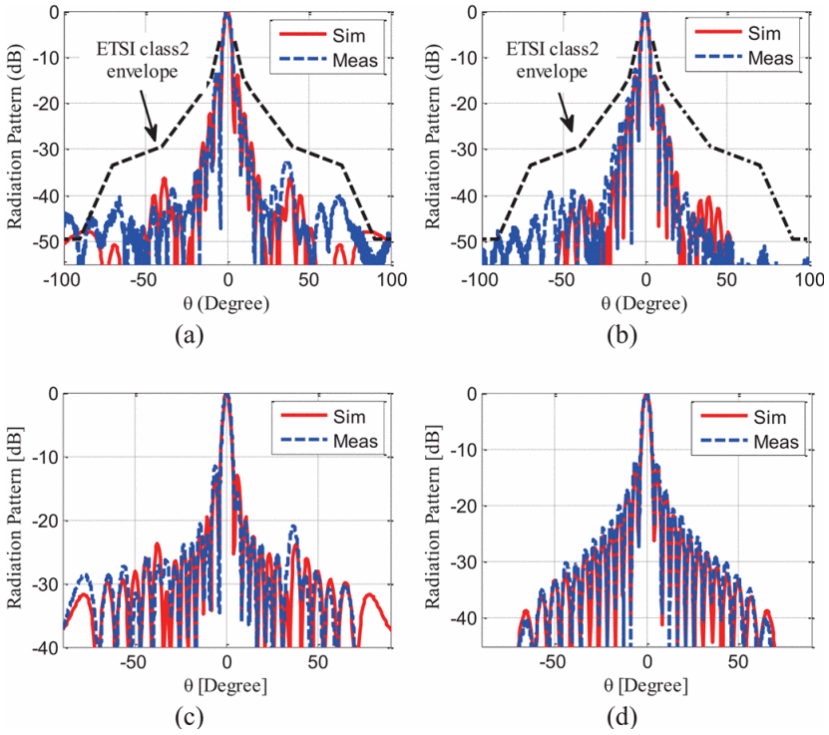

Figure 2-20: Simulated and measured radiation patterns of the proposed ridge gap waveguide slot array antenna at 64 GHz. (a) E-plane, (b) H-plane, (c) principal E-plane, and (d) principal H-plane [21].

It's interesting to note this technology introduced by Prof. Kildal was further industrialized and commercialized with a company named *GAPWAVES* [22]. Their product will studied in detail in the section dedicated to commercialized solutions.

In brief, proposed waveguide slot arrays are in good accordance with our datasheets in terms of high gain and efficiency (more than 80%), large bandwidth and small form factor. However, as discussed in section 2.1, large antenna arrays at mm-waves, require a phase shifter per element in order to obtain beam steering features compatible with datasheet requirements which is both costly and complicated in terms of realizations. Moreover, to really be compliant with ETSI RPE in principal E/H planes they require amplitude tapering which is challenging to obtain in mm-waves.

2.2.3.3. Substrate Integrated Waveguide arrays

An alternative low cost solution to waveguide slot arrays can be Substrate Integrated Waveguide (SIW) slot arrays. SIW slot arrays, also called post-wall waveguide or laminated waveguide slot arrays, have a functionality similar to waveguide slot arrays introduced in the previous section. As presented in figure 2-21, their difference is that for the SIW slot arrays, the waveguide is filled with dielectric and its walls are created using metallic pins (via-holes). This makes the fabrication of these antennas easier and cheaper comparing to waveguide slot arrays. Also the slots and their feeding network can be fabricated on a single substrate which offers size reduction as well [23]. These antennas have less loss comparing to microstrip antennas due to the fact that wave is guided through a cavity with much less leakage comparing to microstrip transmission lines. Yet, the presence of dielectric will be a concern for losses

(comparing to waveguide slot arrays) especially for large-aperture high gain (more than 30 dBi) antennas in mm-waves frequencies [24, 25].

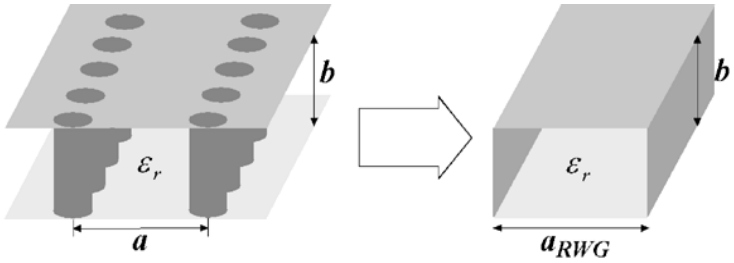

Figure 2-21: Substrate integrated waveguide (left) and the equivalent rectangular waveguide (right) [23].

Similar to waveguide slot arrays, in order to achieve a wide gain bandwidth, the SIW slot array should use corporate feeding networks. Moreover, in order to further increase the antenna bandwidth, the radiating element can in addition to slots can be microstrip patches [26] or cylindrical cavities [27]. For example, authors in [27] propose a SIW array with corporate feeding network at E-band (71-76 and 81-86 GHz) frequency band. The radiating elements in this case are cylindrical metallic via-holes (filled with air) in order to increase the antenna bandwidth. Figure 2-22 shows the antenna schematic, radiation pattern at 7.35 GHz and gain variation over frequency. The measured gain contains the reflection loss, the conductor loss and the dielectric loss, i.e., the realized gain. The grating lobes in the H-plane radiation patterns (right side pattern) are due to inter-element spacing larger than λ forced by the feeding network dimensions.

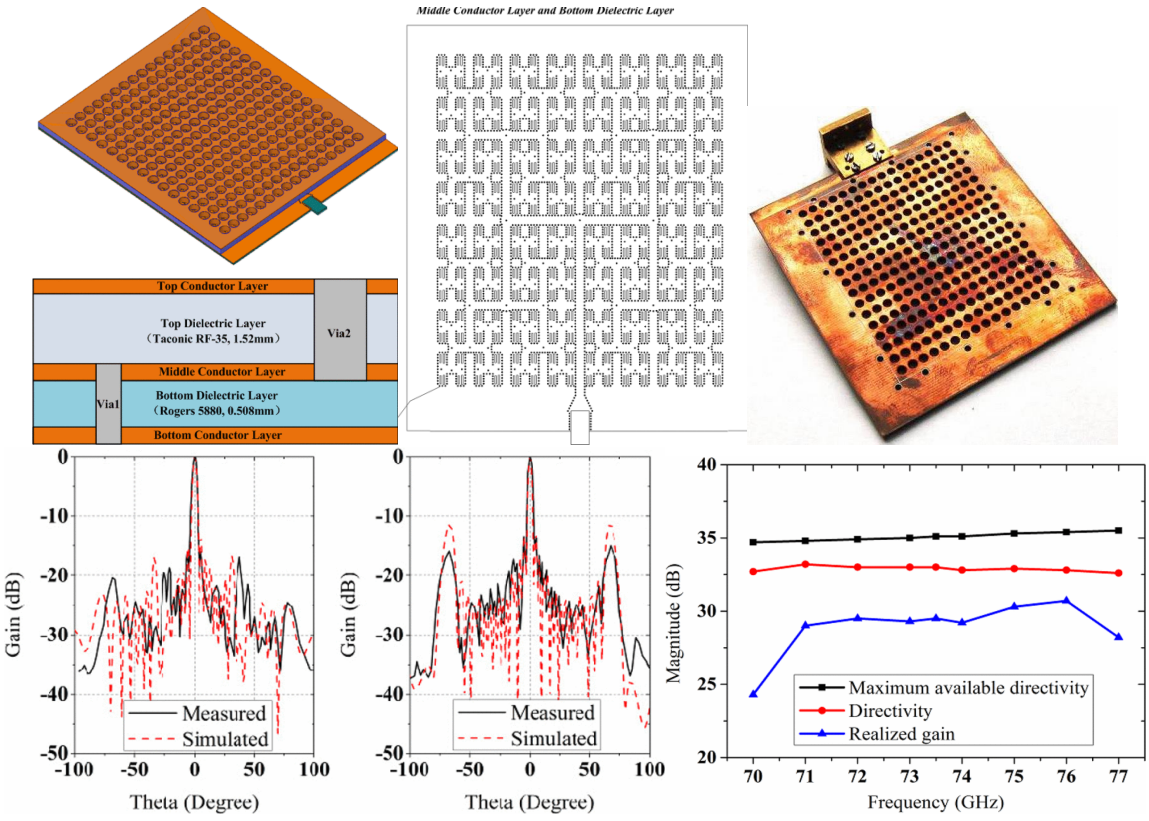

Figure 2-22: 16x16 SIW antenna array for E-band [27].

To conclude, the SIW antennas have similar performance to waveguide antennas but offer less complicated realization process. Moreover, they are more compatible for integrating active RF components for beam steering purposes. However, as in mm-waves the antenna elements dimensions become very small and also the dielectric loss is increased, this solution remains challenging in terms of realization technology and dielectric material loss. Also, same as any mm-wave large array, tapering each element (to control side lobes and be compliant with ETSI RPE) and integrating a phase shifter per element (for beam steering purposes) remains challenging and costly for SIW arrays as well.

2.2.3.4. Continuous Transverse Stub (CTS) arrays

These antennas are constituted of an array of *N*-elements instead of *N*×*M* elements which make their feeding network design easier comparing to typical planar arrays such as horn arrays and waveguide slot arrays. As presented in figure 2-23, these elements are long stubs with limited height fed by parallel plate waveguide [28]. Because of absence of dielectric, this antennas have much better efficiency comparing to microstrip antennas arrays or SIW slot arrays. These antennas have naturally a linear polarization based on their propagation structure but circular polarization can be achieved using classical polarizers. Furthermore, because of the parallel plate waveguide they don't need a ground plane to improve the Front-to-Back (F/B) ratio [29].

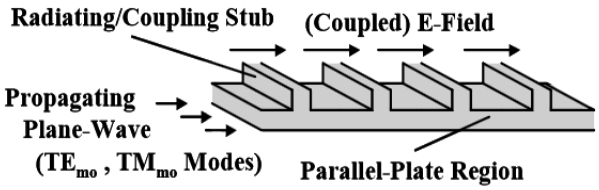

Figure 2-23: Coplanar CTS.

Similar to waveguide based slot arrays, we can have either a series feeding network or parallel feeding network. To have a wideband antenna solution, parallel feeding network is required. In general there exists different feeding systems for a CTS array:

- Sectoral (H-plane) horn,
- Pillbox launcher,
- Rotman lenses:
    - Needs transition structure,
- Slotted waveguide array:
    - Substrate integrated waveguide (SIW) structure,
    - Coplanar waveguide (CPW) transmission line based structure.

An example of a parallel feeding network with pillbox launcher is presented in Reference [29]. As shown in figure 2-24, the CTS array is excited in parallel with corporate feeding network. The transition between the input horn to the corporate feed network is achieved using a pillbox.

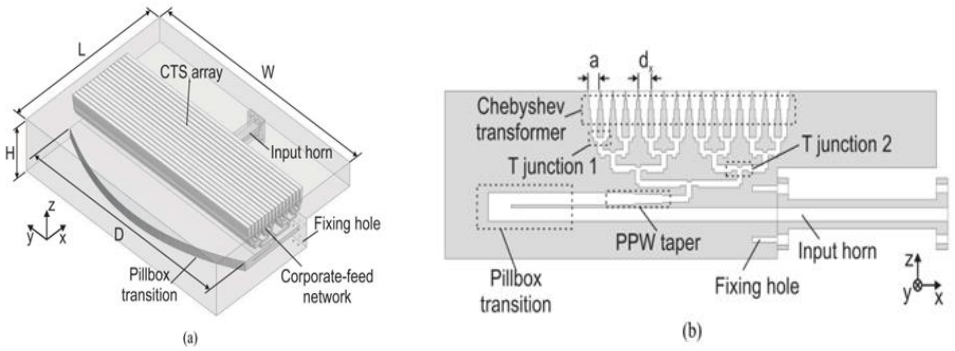

Figure 2-24: CTS antenna fed using a pillbox: (a) 3D perspective view, (b) side view [29].

The radiation patterns of the reference [29] are presented in figure 2-25. As can be seen the antenna radiation pattern has low level of side lobes in H-plane (*x-z* plane in figure 2-24). But, in E-plane (*y-z* plane in figure 2-24), due to the uniform excitation, side lobe levels are high (13 dB) and not compliant with the ETSI RPE. This antenna has an efficiency better than 80% and a gain higher than 27.6 dBi in the frequency range of 27.5-31 GHz.

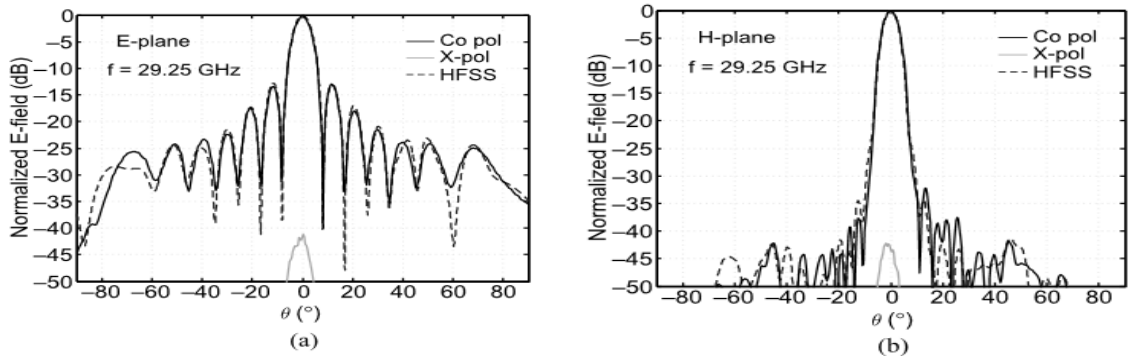

Figure 2-25: CTS antenna parallel-fed using a pillbox normalized radiation patterns: (a) E-plane, (b) H-plane [29].

Having two-dimensional beam steering for CTS antennas is complicated due to their nature (longitude slot in E-plane). One can achieve H-plane beam steering by moving the pillbox input source along elevation plane (y-axis regarding to figure 2-23), as shown in figure 2-26. The SLLs are lower than − 18.6 dB within the ± 27° scan range at 29.2 GHz with scan losses lower than 0.35 dB, whereas the SLL and the scan losses reduce to ≈ − 11 and − 2 dB, respectively, for θ = 40°.

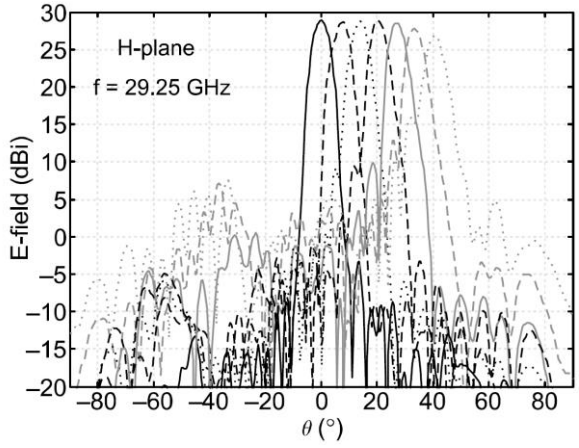

Figure 2-26: Measured H-plane Radiation pattern for different scanning angles [29].

In order to obtain E-plane electronic beam steering, controlled variation of the propagation constant within the parallel-plate region is required [29]. Various methods exist to obtain this variation, such as non-linear voltage variable dielectrics (metamaterials, ferroelectric materials) and varactor devices (such as varactor diodes) [30-37]. However, the main drawbacks of these solutions are that they are either frequency dependent or narrow-band solutions and therefore not compatible for large band antenna solutions required for 5G point-to-point communications.

This antenna technology is highly patented (about 65+ patents) because of its simple structure and high efficiency (more than 90%). These antennas have been commercialized for P-t-P mm-wave communications as well [38]. Similar to the commercialized horn arrays, these antennas should be in diamond position (45° rotation) in order to be compliant with ETSI RPE.

To conclude, main advantages of CTS antennas are high efficiency (more than 90%) and simpler feeding network comparing to planar arrays (N elements instead of N×M elements). Their main drawbacks are challenging amplitude tapering and phase shifting specifically in their E-plane due to their nature. Moreover, as the targeted application is at mm-waves meaning very small antenna components dimensions, manufacturing process becomes more challenging in terms of complexity and cost.

2.2.4. Conclusions on directly fed antenna arrays

Different types of directly fed antenna arrays, an array of radiating elements fed directly by a feeding network, were presented in section 2 of this chapter. Using array factor calculation in section 2.1, it was demonstrated that any type of directly fed array intended for mm-waves high gain applications will require high precision amplitude tapering to have low side lobe levels compliant with ETSI RPE. Moreover to have beam steering feature, the arrays will require a phase shifter per element. Taking into account these requirements, different directly fed antenna array technologies were studied in detail.

It was demonstrated that for microstrip arrays main drawbacks are very low efficiency, less than 30% for large arrays at mm-waves, and limited bandwidth. In addition to low form factor and easy fabrication for mass production, microstrip antenna arrays are one of the most compatible for integrating phase shifters and applying amplitude tapering among other array technologies. However, as they have limited obtainable maximum efficiency (see figure 2-6), they are not suitable for high frequency and high gain applications.

In contrary to microstrip arrays, waveguide based arrays offer very good efficiency and low losses as the wave transmission is done within the air. There exists different types of waveguide based arrays such as horn arrays, slot arrays, SIW arrays and CTS arrays. These antennas require complicated corporate feeding networks in order to ensure wide bandwidth. Moreover, integrating active RF components, such as phase shifters for beam steering purposes, is more complicated comparing to microstrip arrays. Also, as in mm-waves the antenna components become very small, the realization of these type antennas is challenging and costly for mass productions. In addition, obtaining high precision amplitude tapering within their feeding network will increase the realization complexity, and somehow impossible to achieve.

Main advantage of directly fed array antennas is their very compact form factor comparing to other type of antennas such as lens and reflector antennas.

A performance comparison between different directly fed antenna array technologies is presented in table 2-1.

Table 2-I: Directly fed antenna array technologies performance comparison.

Antenna solution		Efficiency	bandwidth	Beam steering compatible	Compactness	Realization simplicity & low cost
Microstrip arrays		*	*	***	****	***
Waveguide based arrays	Horn arrays	****	****	**	***	*
	Slot arrays	****	**	**	****	*
	SIW arrays	***	**	**	****	**
	CST arrays	****	****	**	***	*

2.3. Quasi-optical antenna solutions

Quasi-optical antenna solutions or in other words, aperture antennas with non-direct (quasi-optical) space-fed systems, are also good candidates for directive antennas. These antennas are constituted from a phase correcting aperture illuminated by a focal source (primary source) at the aperture's focal point. In contrast to directly-fed antenna arrays, the simplicity of their feeding network simplifies the side lobe level control as well as the beam steering process. In order to steer the beam of any quasi-optical antenna solutions, the focal source needs to be displaced from the focal point in lateral directions. For an active beam steering, beam switching solutions can be deployed, but these solutions require a focal array with RF circuits. Their main drawback is their large form factor because of the needed focal distance between the antenna primary source and its phase correcting aperture [39].

In this section a summary on different types of quasi-optical antenna solutions such as lens antennas, parabolic antennas, reflect arrays and transmit arrays is presented.

2.3.1. Lens antennas

Lenses have been used in microwave applications decades ago but they were abandoned because of their bulky form factor and expensive manufacturing when being used in low frequencies. Moreover, larger lens dimensions mean more dielectric losses for dielectric lenses. Recently, with emerging application at mm-waves and THz frequencies where the wavelength become very small, and thus smaller lens dimension, lens antennas are attracting more attentions. For microwave applications, lenses can either be used as imaging systems or as antennas.

As presented in figure 2-27, the lens transfers the spherical incident wave-fronts from the focal source to plane wave-fronts by correcting their phase differences. In fact, lenses collimate the incident divergent energy. The lenses can transform various type of divergent energies into plane waves if their geometrical configuration is properly shaped and appropriate material is chosen for them [40].

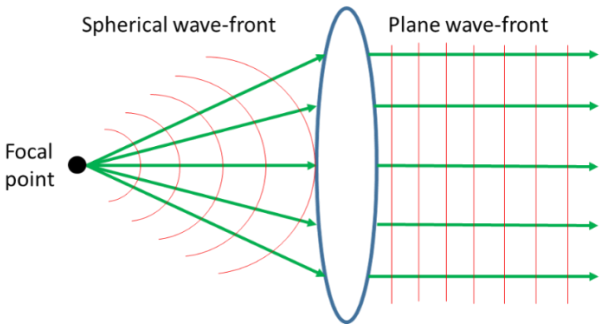

Figure 2-27: Lens principal functionality as a transmission antenna.

The material of the lens can either be dielectric or metal. Main difference between these two materials is in the way that they correct the phase difference between the incident spherical wave-front rays:

- Dielectric lens delays the outgoing electromagnetic rays and collimates them,
- Metal lens converts spherical wave-fronts into plane wave-fronts by speeding up the outgoing electromagnetic rays.

The lens is constituted either from homogeneous or non-homogeneous materials [42]. A homogeneous material lens can have different geometrical forms such as canonical profile (spherical [43], extended hemispherical [44]-[46], elliptical [47] or shaped profile [48]-[54]). For the non-homogeneous material lenses, like Fresnel Zone Plates (FZP) [55] or Luneburg lenses [56]-[58], several materials with different refraction index are assembled. The refraction index variation can also be achieved using same material but with properly modified profile (for example corrugated FZP lenses). In the following, different types of homogeneous and non-homogeneous lenses are presented with more details.

2.3.1.1. Homogeneous lens

Figure 2-28, presents various forms of homogeneous spherical lenses in function of refractive index n [41]. Depending on their refractive index n, a lens can be diverging ($n < 1$) or converging ($n > 1$).

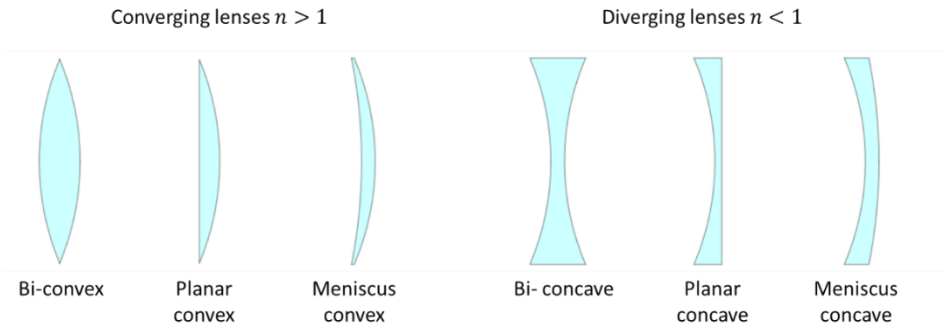

Figure 2-28: Different types of homogeneous spherical lenses in function their refractive index n.

In first steps of the design, simple equations based on ray optics, available in [41] for different shapes, can be used. As an example, figure 2-29 presents the ray tracing for convergent (Bi-convex) and divergent (Bi-concave) lens with their design equations in the inset.

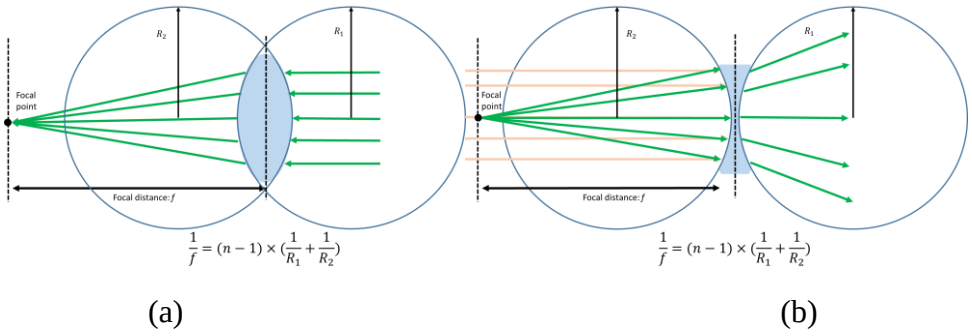

Figure 2-29: Ray tracing and design equations for a homogenous spherical : (a) Convergent Bi-convex lens, and (b) Divergent Bi-concave lens.

Different types of non-spherical homogeneous lenses are presented in figure 2-30. Their optical design equations are also presented in their inset.

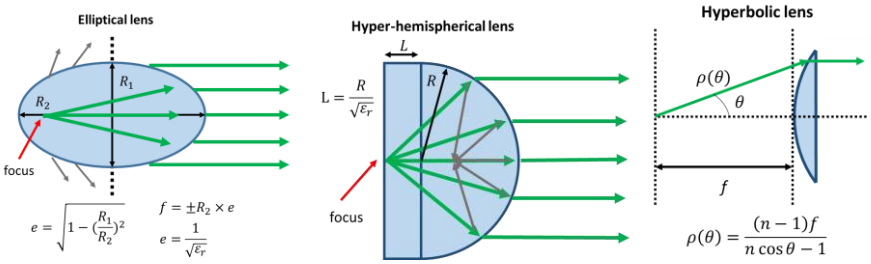

Figure 2-30:Different types of non-spherical homogeneous lenses.

As presented in figure 2-30, an elliptical lens produces plane wave-front radiation at the other side of its focus. Manufacturing of this type of lenses may be challenging at high frequencies. The hyper-hemispherical lens is in fact a hemispherical dielectric with extended cylindrical base. Manufacturing of this type of lens is easier comparing to elliptical lens. Hyperbolic lens is actually a special case of homogeneous convex lens which is optimal to reduce spherical aberration.

Lens antennas have some limitations due to their nature [59]. One type of these limitations is aberrations which are mainly due to imperfections in the design and their consequence is having several focal points which leads to side lobe levels increase and directivity decrease in antenna point of view. These aberration are either independent from frequency (monochromatic) or frequency dependent (chromatic). Monochromatic aberrations are either due to the spherical shape of the lens or asymmetry in the lens shape. Chromatic aberration results in different focal points as a function of frequency. Other limitation of lenses is reflections between material transition, such as air-dielectric and different dielectrics transitions. These reflections become more important when the difference of materials refractive index is larger. For normal incidence, typical solution to reduce these reflections is to use matching layers between two materials.

As an example of homogenous lens antennas developed for mm-waves point-to-point communications, the authors of [60] propose an Integrated Lens Antenna (ILA) at E-band (71-76/81-86 GHz) with beam steering feature. This ILA is in fact a hyper-hemielliptical lens with similar concept to hyper-hemispherical lens. The focal source of this antenna is a network of multiple single radiating elements (microstrip patches) distributed on the lens focal plane, called focal array. By exciting the sources displaced from the focal point, the antenna main beam is steered. The lens is made from a thermoplastic material and has an aperture size (diameter) of 260 mm ensuring a half power beam width below 1° and a minimum measured gain of 33.7 dBi. Figure 2-31 shows the antenna prototype structure as well as its radiation patterns at 76 and 81 GHz. This antenna offers a gain variation of 2.1 dB over the 71-86 GHz with a reflection loss better than 10 dB over 70-88 GHz frequency. This performance confirms the lens antenna large band (both gain and impedance) and high gain characteristics. However as visible in the antenna photo, lens antennas have larger form factor comparing to the array antennas presented in the previous section.

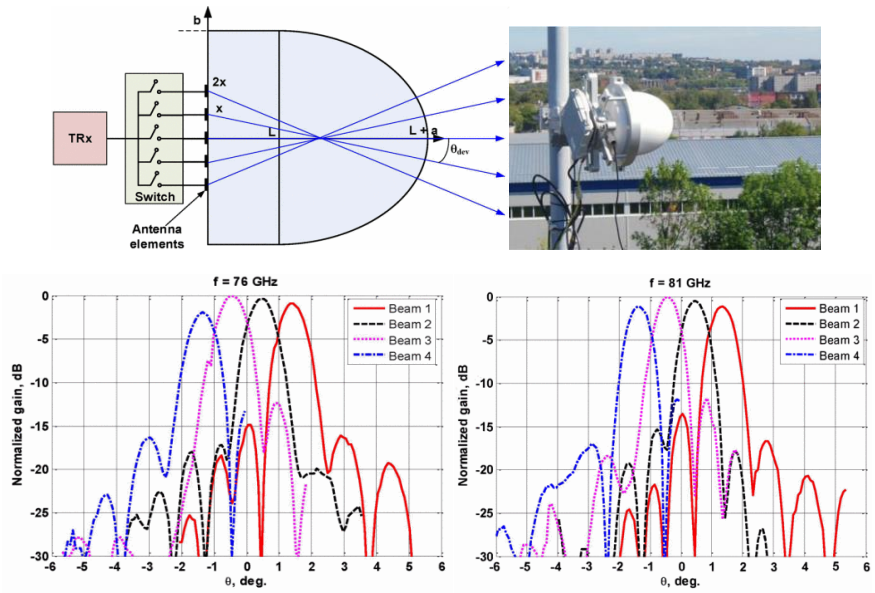

Figure 2-31: Homogeneous lens antenna example developed for E-band (71-76/81-86 GHz) [60].

Figure 2-32 presents another homogeneous lens antenna fed by a focal plane array for 2-D beam steering purposes [61]. This antenna is designed for E-band (71-86 GHz) as well. As presented in figure 2-32, the lens used here is a hyper-hemispherical lens with shaped extension to minimize the air-dielectric reflections. The focal array is constituted of 4 rows of 16 elements producing beam steering range of ±4° in elevation and ±17° in azimuth. MMIC SP4T switches are used to switch between different elements of the focal plane array (microstrip patch antennas). This antenna offers a maximum measured directivity of 36.7 dBi and maximum measured gain of 15 dBi. This huge losses is mainly due to the switch network losses. Other than RF performances, the bulky size of the lens antenna (almost 25 λ height) is to be noted.

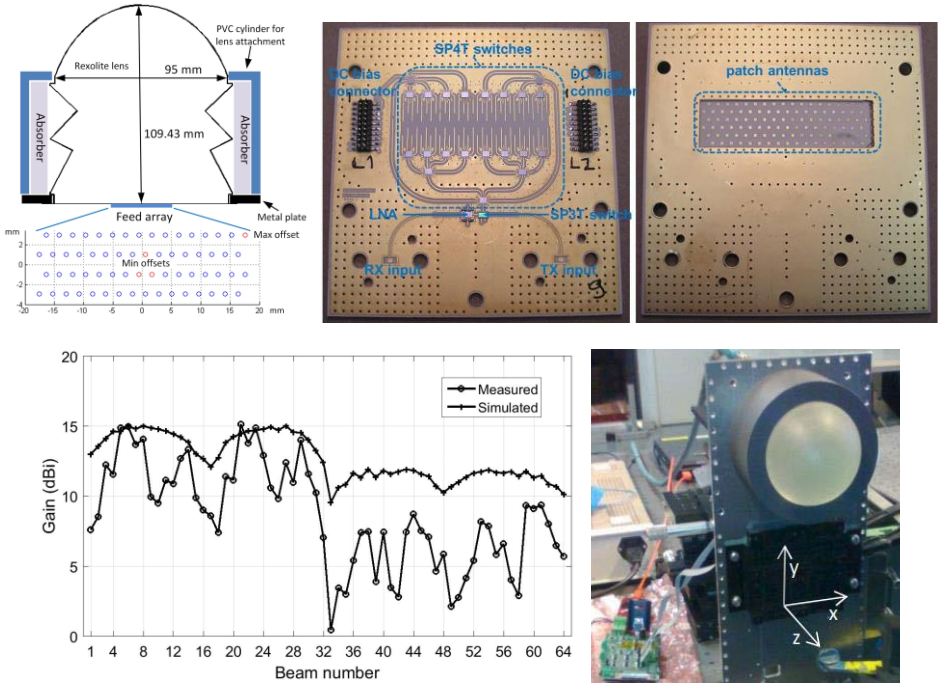

Figure 2-32: 2-D beam steerable lens antenna realized at E-band [61].

2.3.1.2. Non-Homogeneous lens

Non-homogeneous lenses, also known as graded index lenses use a combination of different materials, or a homogeneous material with locally varied refractive index. Their refractive index varies from the center to the surface of the lens according to a radial refractive index. Figure 2-33 shows the most famous laws of gradient index variation along the lens radial dimension [62]. The design of these lenses is based on geometric optics and more specifically Fermat's principle [63].

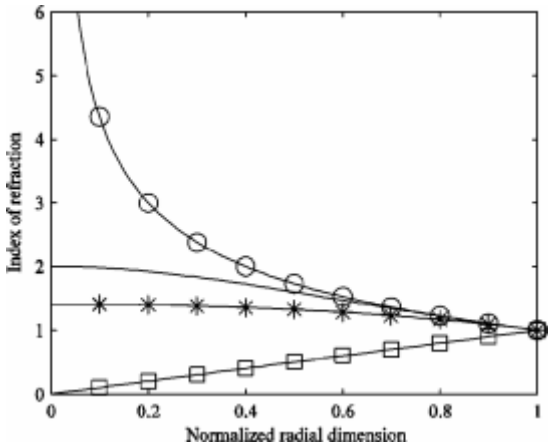

Figure 2-33: Graded index lenses: Index distribution along the normalized lens radius in the case of: Maxwell fish-eye (–), Eaton (□), Eeaton-lippman (O), and Luneburg (*) [62].

Non-homogeneous lenses are attracting a lot of attention recently mainly because of their broadband behavior, high gain and ability to form multiple beams [64].

Main examples of graded index lenses are Half Maxwell fish-eye and Luneburg lenses. Figure 2-34 presents ray tracing of these two lenses and compares them with full Maxwell fish-eye lens. It should be noted that in all three lenses presented in figure 2-34, the color degradation from center to border corresponds to decrease of their dielectric permittivity.

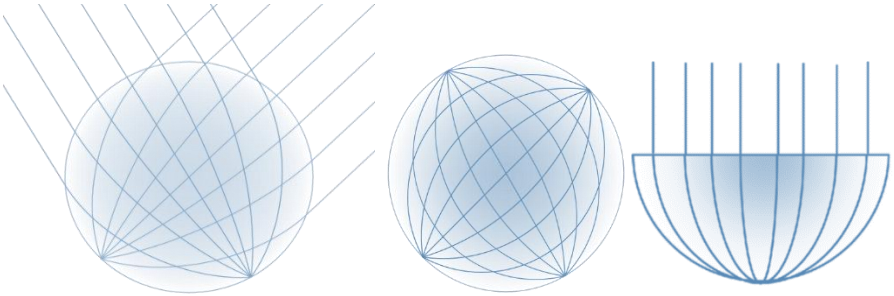

(a) (b) (c)

Figure 2-34: Ray tracing of an incoming plane wave to illustrate the focusing properties inside (a) Luneburg lens, (b) full Maxwell fish-eye lens, and(c) half Maxwell fish-eye lenses.

Half Maxwell fish-eye lens is actually half of a full Maxwell fish-eye spherical lens. Its advantage compared to the full lens is that it can transfer an Omni-directional source to a directive antenna, whereas the full Maxwell fish-eye cannot achieve this because of its spherical shape. However, the reflections at the transitions between the lens and free space will reduce the antenna efficiency [65].

Because of it rotationally symmetry, Luneburg lens can steer the antenna beam by displacing the focal source and it does not have reflections at its borders [67]. Contrary to a full Maxwell fish-eye lens, when a Luneburg lens is fed by a source, a highly directive pattern will be radiated by the lens. Luneburg lens has a very large frequency band response, but its main limitations are its bulky size at low frequencies and high dialectic losses at high frequencies [66].

One of the main problems of these graded index lenses is their form which requires circular feedings for beam steering and/or multi beam solutions. To address this problem, transformation optics can be used to shape the lens and enable planar feeding. The optical transformation can be used to obtain conformal mapping [68]. Conformal mapping approximates the original solution and is always worse in terms of performance.

Other type of flat graded index lenses is Fresnel Zone plate (FZP) lens which doesn't have the spherical lenses issues [55]. This lens was first deployed in light houses to focus and magnify the light. Their main advantage is that they are very thin comparing to other types of lenses but in contrary they have narrower bandwidth. The FZP lens can be either single material, where its refractive index is locally varied by properly modifying its profile, or multi-material where different materials with different refraction indexes are assembled.

Authors in [69] propose a thin graded index lens. As presented in figure 2-35, the proposed lens is much more compact comparing typical bulky hyperbolic lenses. This lens concept is a hybrid sub-λ lens based on Fresnel zone lenses where the lens refractive index is varied by spatially varying the fractions in the lens material. This lens antenna is excited using 2×2 patch array and offers 3-dB gain bandwidth of 10% with maximum measured gain value of 32.8 dBi. This antenna has a diameter of 150mm (20 λ) and a focal distance of 80 mm (11 λ) offering a focal to diameter (F/D) ratio of 0.53. It was demonstrated that main inconvenient of thin graded index lenses is narrower bandwidth comparing to typical bulky homogeneous lenses.

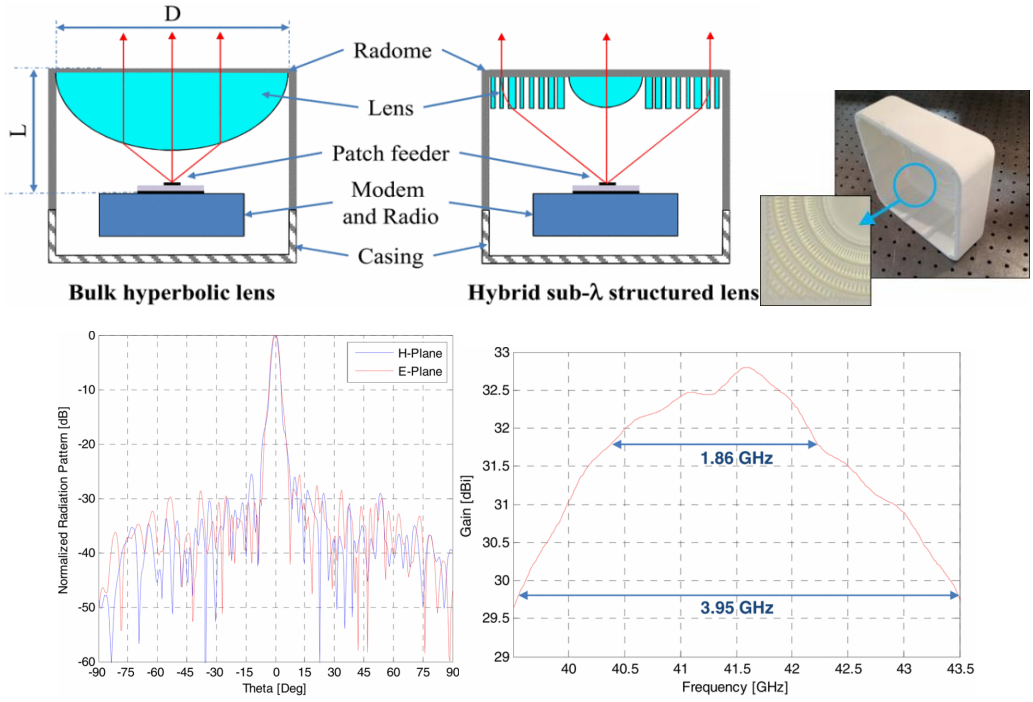

Figure 2-35: Q-band lens antenna for backhaul Point-to-Pint communications [69].

Authors in [70] propose a new technological process in order to realize compact graded index lenses using a single material. In this work they realize a compact Fresnel zone plate lens. They use a special foam material (Airex PXc 320 with ε_r=1.4) to realize the lens with locally varied refraction indexes (figure 2-36(a)) and then press the foam to obtain a more compact form factor (figure 2-36(b)). The lens has a diameter of 30 λ_0 and the primary source is a waveguide aperture at focal distance of 26.4 λ_0. The thickness of the lens before and after pressing are 6.25 mm and 2.8 mm respectively. This antenna offers low side lobe levels of -22 dB (compliant with ETSI class 2 RPE) with high gain of 33.3 dBi but with not so good aperture efficiency of 31%. It's main inconvenient, common between all quasi-optical antenna solutions, is the not so compact overall form factor because of the focal distance between the lens and its focal source.

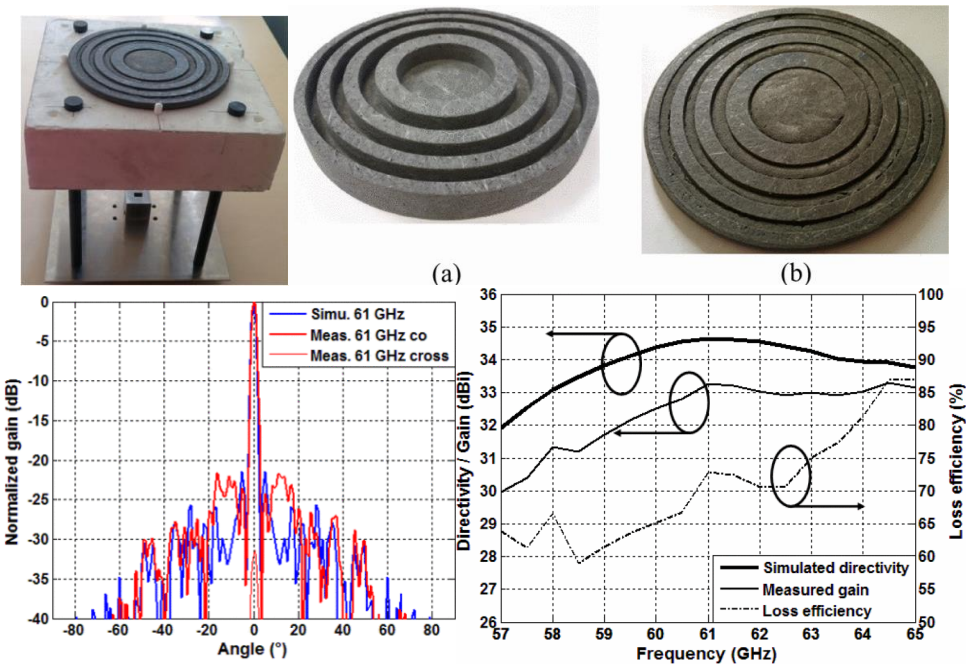

Figure 2-36: V-band Fresnel Zone plate lens antenna with foam technological process [70].

2.3.2. Parabolic antennas

Parabolic antennas, or reflector antennas, firstly introduced by Henrich Hertz in 1888 are constituted of a parabolic reflector and focal source(s). As presented in figure 2-37, depending on the focal source position, we can have different type of parabolic antennas. The parabolic reflector focalizes the radiated field of the focal source by correcting its phase in reflection using the parabolic shape of the reflector.

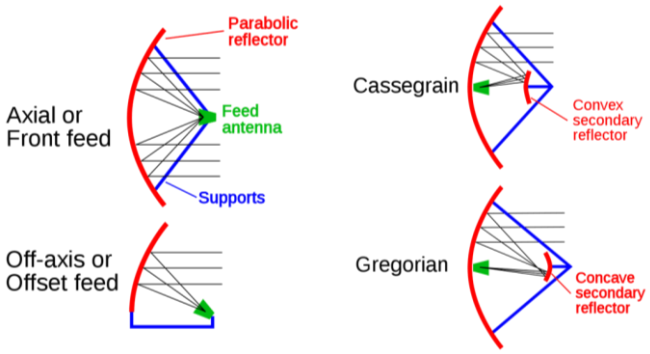

Figure 2-37: Parabolic antennas different configurations depending the focal feed position.

Generally, parabolic antennas offer a very high gain and efficiency because of their very low radiation losses. These antennas are very broadband as well, in fact their bandwidth is mainly limited by the focal feed and not the phase correcting aperture (the metallic parabolic reflector). By using wide band focal feeds such as waveguides and horns, very large band solution are obtainable. One of the main limiting point of reflector antennas is the shadow effect of the feed source in front of the reflector reflections that will result in antenna efficiency reduction. Other loss associated to these antennas is spillover loss which correspond the focal feed illuminating outside the reflector surface.

Regarding to our application (5G Point-to-Point links), where compactness and beam steering features are required, these antennas become problematic. Their form factor is quite bulky because of the parabolic reflector comparing to directly fed antenna arrays such as horn arrays. In order to steer the beam of the parabolic antenna, similar to all quasi-optical antenna solutions, the focal source needs to be displaced from the focal point in lateral directions. For an active beam steering, beam switching solutions can be deployed, but these solutions require a focal array with RF circuits and thus the masking effect of the focal feed on reflector will increase.

Industrially speaking, parabolic antennas are the most used antennas for fix (no beam steering) Point-to-Point links where very high gain antennas with low side lobe levels are required. As an example, figure 2-38 presents an E-band (71-86 GHz) Cassegrain parabolic antenna which is compliant with class 3 ETSI RPE. This antenna is developed at *Radio Frequency Systems (RFS)* [71]. The parabola has a diameter of 362 mm offering a gain more than 43 dBi with 2 dB variation over the 71-86 GHz frequency range.

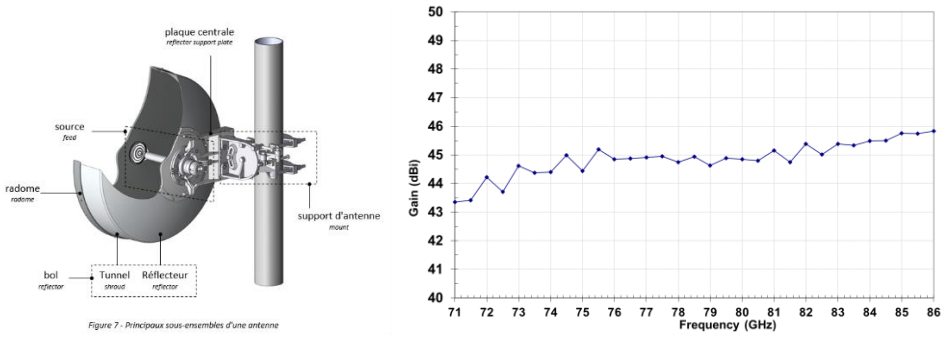

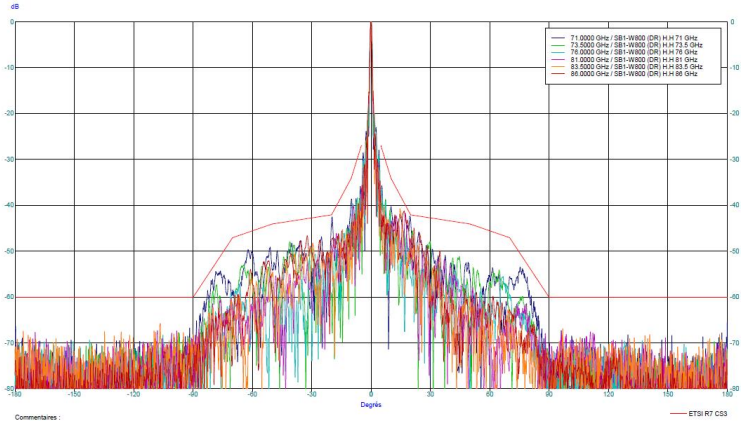

Figure 2-38: Parabolic antenna at E-band, product of Radio Frequency Systems [71].

Parabolic antennas offer the best quality in terms of RF performances such as efficiency, band width and low side lobe levels among any other antenna technology for point-to-point communications. For this reason, they are the dominant antenna technology for microwave applications market. However, as more compact and also beam steerable solutions are expected for 5G applications, major antenna manufactures such as *RFS* are focusing on developing other antenna technologies compatible with the new requirements.

2.3.3. Reflect-array antennas

Reflect-array antennas are the low profile and lighter version of parabolic reflector antennas where a planar reflector is used to focus the reflected field instead of a parabolic shape reflector. These antennas became a replacement of parabolic antennas especially for satellite applications. The first reflect-array antenna was introduced in 1963 where a variable length shorted waveguide array was used as the reflector [72]. But more compact versions where introduce in late 1980s where printed microstrip arrays were used as reflectors [73-75].

Conventional microstrip reflect-arrays, use microstrip patch antennas with variable dimensions to reflect the incident field from a primary source while correcting its phase and focusing it. In fact, the size variation of the patches results in reflection phase variation, which provide a phase shift that emulates the path of each ray reflected in a parabola [76]. Because of quasi-optical feeding system, reflect-arrays avoid the complexity and losses of microstrip feeding networks comparing to directly fed microstrip arrays. Figure 2-39 shows a microstrip reflect-array. It can be observed that similar to parabolic reflectors, these antennas also suffer from focal source masking effect, as it blocks some part of the reflect-array radiations.

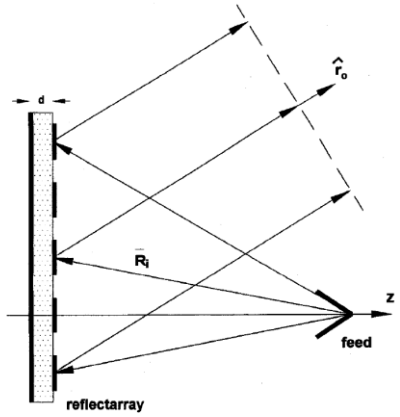

Figure 2-39: Geometry of the microstrip reflect-array [76].

The fact of using planar printed reflect-arrays allows benefiting from re-configurability features of printed technology structures. In recent years, different reflect-array configurations such as dual-polarized [77], dual-band [78], conformal [79], reflection phase reconfigurable (beam steerable) [80] and etc. have been proposed. Because of these re-configurability properties, reflect arrays are the dominant antenna technology for satellite application where high gain antennas with contoured beams are required.

One of the main limitations of reflect-arrays is their limited bandwidth due to the resonance nature of printed radiating elements which limits their bandwidth around 3-6% [81]. Other bandwidth limiting factor is frequency dependence of the phase delay of the incident field which become more critical in large reflect-arrays where its array elements should be able to compensate different phase delays at different operating frequencies. However, much wider bandwidth solutions based on multi-layer stacked structures [82] or using non-conventional shape patches [83] have been proposed.

Other drawback of reflect-arrays is their form factor forced by the primary source focal distance from the reflect-array. A solution based on folded structure was proposed by *W. Menzel* to reduce the physical focal distance by a factor of two [84]. As presented in figure 2-40, the folded structure doubles the electrical path of the radiated field between primary source and the reflect-array and therefore one can reduce the focal distance by a factor of two. This is done by having a parallel linear polarized wave, illuminated by a primary source and propagated to a polarizing grid (trans-reflector), which reflects to the twisting and focusing array. This one reflects, twists and focuses the wave with a perpendicular linear polarization to pass through the trans-reflector. Main inconvenient of this solution is that's a single polarization solution. Due to the polarizing grid the will always block one polarization, one cannot have a dual-polarization folded reflect-array.

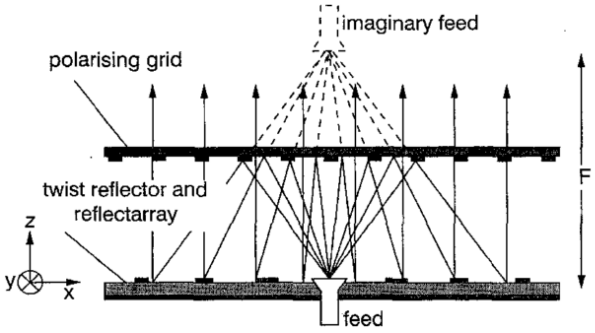

Figure 2-40: Principle of the folded Reflect-array antenna [84].

As an example, a folded reflect-array designed at mm-waves 94 GHz frequency band is presented in figure 2-41 [85]. This antenna offers -3 dB gain bandwidth of 10% with a measured gain of 36.5 dB for an aperture diameter of $40\lambda_0$ and a focal distance of 10.6 λ_0. This solution offers very low side lobe levels of -30 dB.

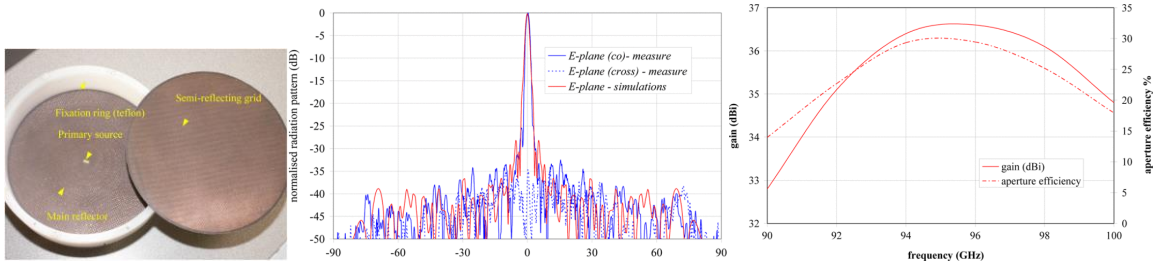

Figure 2-41: Folded reflect array at 94 GHz [85].

2.3.4. Transmit-array antennas

Transmit-array antennas functionality is similar to lens antennas, where a radiated field from a focal source is focused in transmission. Figure 2-42 presents the principal of a transmit-array [86]. As presented, the transmit-array plate is constituted of planar arrays on both sides, receiving layer and transmitting layer. The radiated field form the primary source at the focal point is received by the receiving layer, then it's transmitted to the transmitting layer through passive/active phase shifters. These coupling phase shifters, correct the receiving spherical fields phase (by delaying them) and transfer them to plane waves (i.e. focus them), similar to lenses functionality.

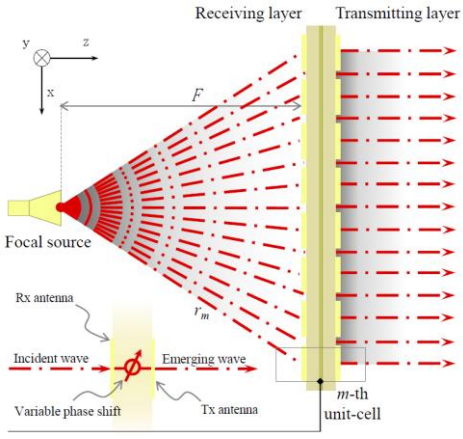

Figure 2-42: Principal of Transmit-array [86].

Transmit-arrays are similar to reflect-arrays regarding their quasi-optical feeding system and the fact of using planar microstrip arrays for focusing purposes. By comparing figure 2-42 and figure 2-39, we can see that their main difference is that transmit-arrays focus the primary source field in transmission (e.g. lenses) and reflect-arrays focus the primary source field in reflection (e.g. parabolic reflectors). This gives transmit-arrays the advantage of not having focal source masking effect, and thus be able to deploy focal plane arrays for beam steering purposes [87] or even reducing the focal distance [88].

Similar to reflect-arrays there are two related factors that limit the bandwidth of transmit-arrays. First is the limited bandwidth of the microstrip technology based unit-cells which can be overcome by using multi-layer structures [89] or multi resonances motifs [90]. Second bandwidth limiting factor is phase variation in function of frequency which will result in antenna gain bandwidth reduction over the frequency band.

Figure 2-43 presents a transmit-array designed at 60 GHz [91]. This antenna offers a minimum gain of 23 dBi with 1-dB gain bandwidth of 6.5%. This antenna's focal to diameter ratio is 0.5, meaning for a diameter of 10 λ, it requires a focal distance of 5 λ. The side lobe levels of this solutions are around 15 dB and therefore not compliant with ETSI RPE. The 5 λ focal distance may seem quite small at 60 GHz, but it should be noted this is for a diameter of 10 λ offering only 23 dBi gain. Minimum required gain at 60 GHz by ETSI is 30 dBi, meaning larger aperture is required which leads to larger focal distance.

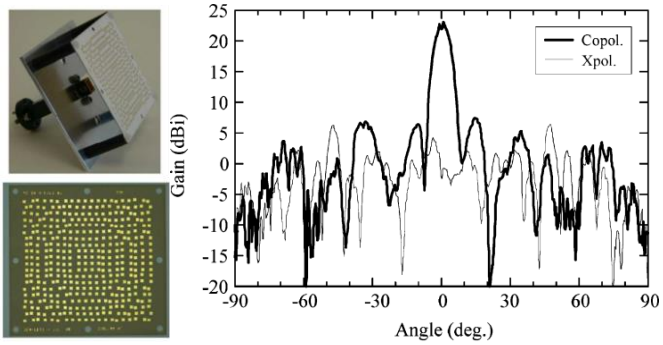

Figure 2-43: Transmit-array designed at V-band [91].

One of the advantages of transmit-arrays comparing to other quasi-optical antenna solutions such as lenses is that beam steering feature can be obtain by other means than changing the position of the focal source or exciting displaced focal sources[91]. By using variable phase shifters, reconfigurable transmit-arrays with beam steering/shaping features can be obtained [86]. There are several technics to obtain reconfigurable beam steerable transmit-array, such as implementing active device on the resonating elements which enables an electronic control or using Tunable materials [92-96]. Main concerns of using active devices or tunable materials, is their RF loss and also limited bandwidth.

As an example of reconfigurable transmit-arrays, authors in [97] propose a 2-bit unit cell (meaning it can have 4 phase states) for electronically reconfigurable transmit-array at Ka-band. As presented in figure 2-44, the phase shifting control is achieved using two PIN diodes in both the reception transmission side of the unit-cell. This unit-cell is used to design a 196-element transmit-array which exhibits a maximum gain of 22.9 dBi, an aperture efficiency of 32.3%, and a side-lobe level equal to 18.1 dB at broadside. The beam scanning capabilities have been studied up to-40°, and a maximum gain of 20.2 dBi is obtained. The transmit-array

is illuminated by a standard WR-34 waveguide horn with a nominal gain of 10-dBi placed at the optimal focal distance (F=50 mm). This corresponds to a focal ratio (F/D) equal to 0.7 where D is the length of the array side (71.4 mm).

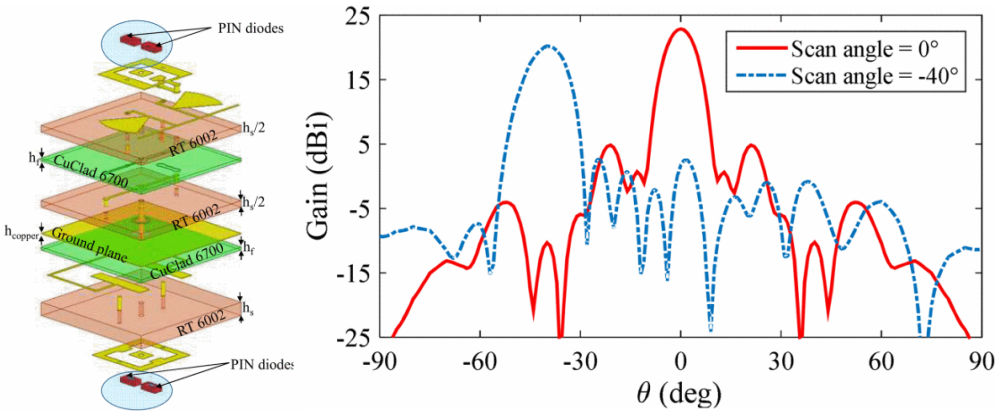

Figure 2-44: Ka-band re-configurable transmit-array [97].

To conclude, transmit-array antennas main advantage comparing to other quasi-optical antenna solutions such as typical lens antennas is that they offer different options to obtain electronic beam steering. However, as multi-layer structures are required to obtain wide-band solutions, they have more complicated realization processes and therefore are more costly.

2.3.5. Conclusions on quasi-optical antenna solutions

In the context of mm-waves point-to-point communications, Quasi-optical antenna solutions have different advantages and disadvantages. Overall, comparing to waveguide based arrays, these antennas have lower efficiency (with the exception of parabolic reflectors) and larger form factor. But their feeding network simplicity enables obtaining beam steerable solutions and ETSI RPE compatible radiation patterns with lower complexity and cost comparing to directly fed array antennas. Moreover, these antennas offer a great degree of freedom in their design to have different type of solutions such as dual-band, dual-polarized, beam forming/shaping and etc.

Table 2-2, presents a comparative evaluation of the main characteristics of different quasi-optical antenna solutions.

Table 2-II: Quasi-optical antenna solutions performance comparison.

Antenna solution		Efficiency	bandwidth	Re-configurability	Compactness	Realization simplicity & low cost
Lenses	Homogeneous	***	****	**	*	***
	Non-homogeneous	**	***	***	**	**
Parabolic reflectors		****	****	**	*	****
Reflect-arrays		**	**	***	**	**
Transmit-arrays		**	**	***	**	**

2.4. Commercialized antenna products for mm-waves point-to-point communications

In this section, a brief summary of commercialized antenna solutions for mm-waves point-to-point communications is presented. The goal is to have a clear idea of current industrial solutions and determine their advantages and disadvantages with respect to our defined datasheets in first chapter.

In the following, commercialized solutions per antenna technology are presented. It should be noted that some of these solutions are based on new technologies proposed by startup companies and are still in development phase, and therefore because of confidentiality the companies did not provide much information on their websites. However it was tried to comment these solutions based on their core technology and available information in corresponding literature.

2.4.1. Commercialized antennas based on directly fed antenna arrays

The solutions based on directly fed antenna arrays offer very compact form factor as it can be expected from the state of the art studies. Current relevant solution, to the knowledge of author, are:

- Slot arrays based on gap waveguide by *GAPWAVES* © [22]:

This company offers antenna solutions at E-band (71-86 GHz) and V-band (57-66 GHz) for fixed beam point-to-point communications. Their E-band solution (figure 2-45(a)), with total size of 118×118×8.2 mm offers a gain of 38.5 dBi (mid band) and is compliant with class 3 ETSI RPE. The V-band solution (figure 2-45(b)) has a total size of 93×93×15.8mm with a gain of 32.5 dBi. However, in their datasheet they have not noted if the V-band antenna radiation pattern is compliant with ETSI RPE.

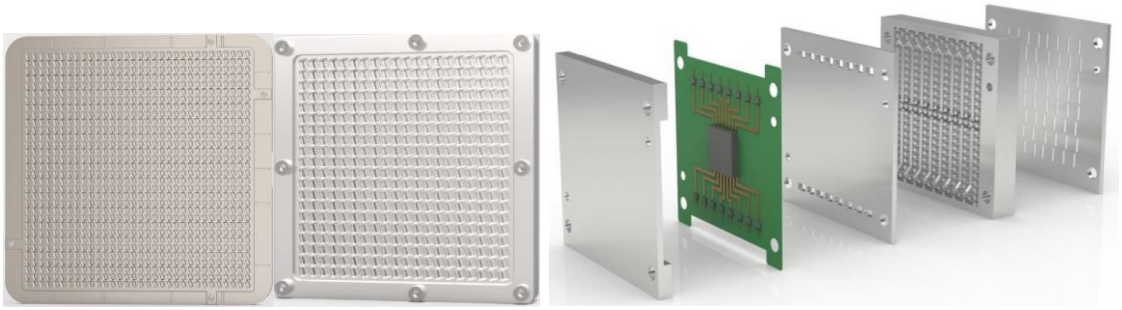

(a) (b) (c)

Figure 2-45: GAPWAVES slot array antennas for (a) E-band fixed beam, (b) V-band fixed beam, and (c) 28 GHz beam steerable [22].

GAPWAVES uses different high volume production methods such as plastic injection molding with metallization, Die-casting in Aluminum and Dies casting in Zinc. They are also working on a beam steerable solution (phased array) at 28 GHz (figure 2-45(c)), but no datasheet of this solution is available yet. This phased array solution is intended for point-to-multi point links.

- Horn array by *HUBER+SUHNER* © [7-8]:

The proposed antenna for E-band has an aperture of 106mm×102mm with a thin thickness of 7.5mm. According to the datasheet this antenna offers a minimum gain of 38.2 dBi and is compliant with ETSI class 2 RPE only for 45° rotated installation. This means for typical vertical or horizontal planes the antenna will not be compliant with ETSI RPE, as same as Ref [6]. Same for the V-band antenna which has dimension of 9.5 mm × 135 mm × 130 mm (Height × Width × Depth) with a gain of 38 dBi and is compliant with ETSI class 2 only for 45° rotated installation. Figure 2-46 shows a photo of the E-band antenna taken from reference [7].

Figure 2-46: HUBER+SUHNER Horn array antenna at E-band [7].

This antenna is manufactured out of metalized plastic parts produced by high precision injection molding.

- CTS antenna by *ThinKom Solutions* © [38]:

This company offers a fixed beam antenna solution based on CTS technology at E-band (71-86 GHz) with a minimum gain of 44.2 dBi. This antenna claims to be compliant with FCC RPE. However, similar to the commercialized horn arrays, these antennas should be in diamond position (45° rotation) in order to be compliant with ETSI and FCC RPE. No information on antenna size are available but from photos one can tell that they are thicker comparing to slot and horns arrays.

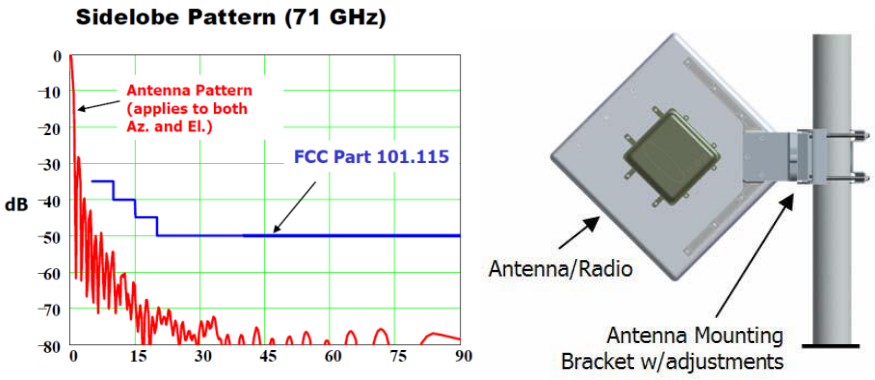

Figure 2-47: ThinKom CTS antenna solution at E-band [38].

- Beam steerable microstrip antenna arrays based on holographic beam forming by *PIVOTAL COMMWARE* © and *KYMETA* ©

PIVOTAL COMMWARE proposes a beam steerable microstrip based antenna array solution. However, instead of using phase shifters per element to steer the antenna beam, they use a technic called Holographic Beam Forming which only requires biased control components like a reactor or transistor per element [98]. There are no detailed information available on the antenna performances such as efficiency and bandwidth. The company claims their antenna can be used for different application where beam steerable antennas are required such as satellite communications and 5G. However, the antenna performance can be estimated by analyzing its functionality principles [99-102]. Holographic beamforming is achieved using modulated surface-impedance metamaterials. The modulation function, known also as the holographic function, transfers a reference field (obtained by illuminating the antenna surface by point source at a certain distance) to the desired field distribution. The modulation function is complex (amplitude and phase), but one can use only one part (amplitude or phase) depending on the application objective. We can map this modulation function by modifying the constituting properties of each radiating element, either physically using variable element size or orientation, or electronically, using electronically controlled modules or materials within each element (meta-surfaces or metamaterials).

Figure 2-48 shows an example of reconfigurable holographic antenna [102]. As can be seen, in fact the holographic beam forming antenna, or metamaterial surface antenna, is a reconfigurable leaky-wave antenna.

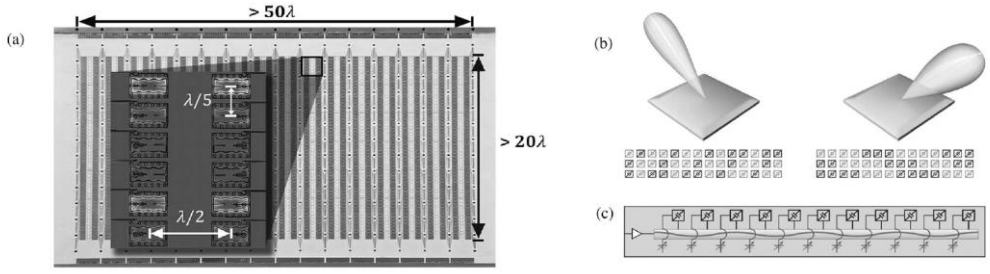

Figure 2-48: (a) Example of a reconfigurable holographic metamaterial antenna (b) Holographic images on the surface of the array, when illuminated by an underlying feed wave, produce a coherent beam. (c) The physics of the metamaterial antenna. [102].

KYMETA © proposes a similar approach by using Liquide Crystal (LC) as its base metamaterial [103]. With applying an AC voltage to the LC molecules, they will rotate and change the slot RF permittivity which will result in the radiating element resonance frequency shift. The main market target for this company is satellite applications at Ka/Ku frequency bands. A product datasheet for Ku satellite band says the antenna offers a minimum gain of 33 dBi at 12 GHz for an aperture of 823×823 mm which translated into an aperture efficiency of 14.7 %. This company claims that it uses a glass structure similar to Liquid-Crystal Displays (LCD) as its main material, therefore it can benefit from existing LCD mass production lines.

Figure 2-49 shows photos of the products proposed by these two companies.

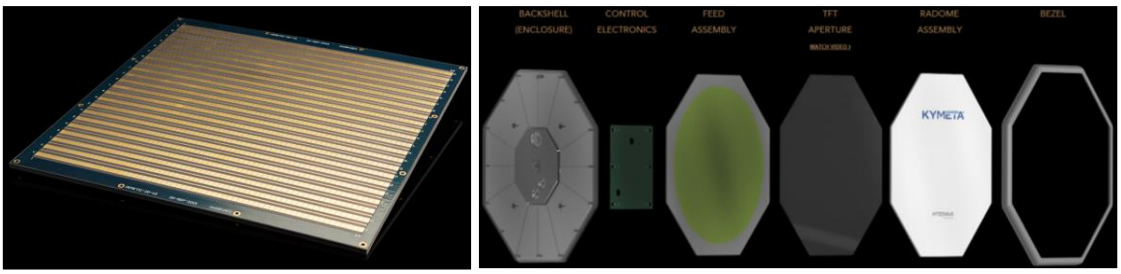

(a) (b)

Figure 2-49: Holographic beam forming based antennas from (a) PIVOTAL COMMWARE [102], (b) KYMETA [103].

Other than low efficiency, one of main drawbacks of these solutions for mm-wave point-to-point communications is limited bandwidth due to the metamaterials resonant nature. Moreover, the modulation function which defines the unit-cells configuration is a function of frequency on its own. This will also result in a limited bandwidth. Other concern is their side lobe levels, which may not be compliant with ETSI as no information was communicated on these aspects. It appears that, one can control either the elements amplitude or phase by the modulation function, meaning it will be challenging to obtain a low side lobe level beam steerable solution.

- Beam steerable Microstrip phased array antenna from *ALCAN SYSTEMS* © [104]:

ALCAN SYSTEMS proposes active phased array antenna using Liquide Crystal (LC) instead of conventional dielectric substrates. By doing so, they are able to shift the array elements phase by applying bias voltages instead of using conventional phase shifters which leads to considerable cost reduction. Due to the LC properties, mainly high losses at lower frequencies, they can offer solutions starting from 10 GHz up to mm-waves. Their main targeted market is satellite communications for digital satellite reception on the move applications. This solution seems to offer wider bandwidth comparing to holographic beam forming antennas as it is not dependent to frequency-dependent modulation functions and beam steering is done by conventional phase shifting technics. As this solution is still in development phase, there is no product datasheet available to assess its compliance with our datasheets.

Figure 2-50: ALCAN SYSTEMS Liquide Crystal based phased array antenna [104].

ALCAN SYSTEMS says it will be using Liquid-Crystal Display Televisions (LCD TV) existing manufacturing lines in order to offer a low cost product.

2.4.2. Commercialized antennas based on quasi-optical antenna solutions

As discussed in the state of the art section, antenna solutions based on quasi-optical solutions have simpler feeding network and overall antenna structure but they suffer from large form factors imposed by the focal distance. Current commercialized solutions, to the knowledge of author, are:

- Parabolic antenna by *Radio Frequency Systems (RFS)* © [71]:

RFS proposes a novel fixed beam parabolic antenna for V-band (57-64 GHz) targeted for small cell backhauling. This antenna offers a minimum gain of 31.5 dBi for a diameter of 120mm. This solution has a very low weight of only 0.5 Kg. The antenna radiation patterns compliant with class 2 ETSI RPE. By changing the primary source of the same parabola, the solution can be scaled to E-band (71-86 GHz) offering a minimum gain of 38 dBi for the same diameter and compliant with class 3 ETSI RPE. This antenna is perfect in terms of RF performances, but it lacks beam steering functionality and it doesn't have a flat form.

Figure 2-51: RFS small cell compact antenna for V and E frequency bands [71].

The parabolic part of the antenna is manufactured using plastic injection molding with metallization technology and the metallic feed is fabricated using machining technology.

- Lens antennas by *Radio Gigabit* © [105]

This company develops antenna solutions for V-band and E-band point-to-point communications based on Integrated Lens Antennas (ILA). Products proposed by this company are mainly fixed beam solutions but they have demonstrated activities on developing beam steerable solutions via scientific publications [60]. Figure 2-52 shows pictures of some of their products and their gain for different frequency bands. As it can be observed in the table presented in figure 2-52, this antenna has a bulky size comparing to the directly fed array antenna examples. These lens antennas benefit from low cost milling manufacturing.

#	Band, GHz	Antenna Outline, mm	Midband Gain, dBi	Weight, kg
1	57-66	75(diam)x83	32.3	0.3
2	57-66	80(diam)x88	32.7	0.34
3	57-66	100(diam)x110	34.7	0.6
4	57-66	110(diam)x121	35.2	0.7
5	71-76/81-86	120(diam)x132	38.1	0.85
6	71-76/81-86	130(diam)x143	38.7	1.1
7	71-76/81-86	220(diam)x243	43.0	7.1
8	71-76/81-86	240(diam)x265	43.7	9

Figure 2-52: Lens antennas by Radio Gigabit [105].

- Graded Index Lens Antenna by *Isotropic Systems* © [106]:

Isotropic Systems proposes Multi Beam wide band antennas based on optical beam former modules at Ku- and Ka-band frequencies for satellite industry claiming 70% lower cost than phased array and flat panel technology. This technology is actually based on a special kind of flattened graded index lenses, obtainable by transformation optics [107]. It's claimed that novel calculations methods based on [108] are used to optimized these antenna and achieve low focal solutions. As presented in figure 2-53, the antenna is constructed of an array of hexagonal dielectric lenses. The dielectric lenses are in fact discretized graded index lenses. For the antenna operating at Ku-band (10.7-12.75/13.75-14.5 GHz), the diameter of each lens is 130 mm and its optical focal length is to be 50 mm offering a small focal to diameter ratio of 0.38 [108]. The thickness of the lens itself is only 15 mm. Each lens in the array has independent feeds placed behind the lens at the focal distance, from which a subset of feeds are selected to produce a directive pattern, and then independently controlled and phased to allow for scanning the combined beam across the entire field of regard of the individual lenses using the standard principles of phased arrays. However in case of phased array, because of the large dimension of the lenses, there will be grating lobes. Moreover, the impact of couplings between lenses on the directive radiation pattern side lobe levels should be taken into account. There is no product datasheet available for this solution yet, therefore it's not evident if their solution is applicable for 5G mm-wave point-to-point communications and if it's compliant with our determined antenna requirements especially in terms of ETSI RPE.

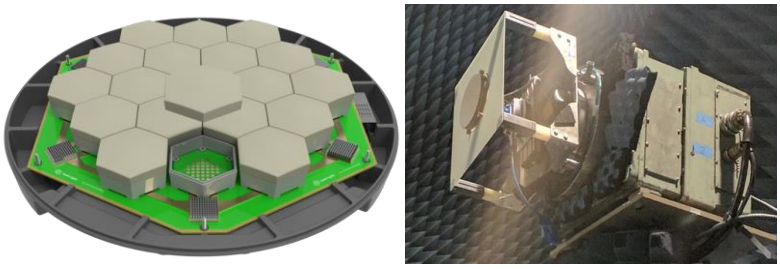

Figure 2-53: Isotropic Systems antenna solution based on transformation optics [106].

The focal source and the Digital Signal Processing (DSP) unit of this antenna are based on PCB technology and the lens part can be manufactured by conventional milling technology or 3D additive printing.

- Transmit-array antenna by *Radiall* © [109]

Transmit-arrays have attracted the attention of industrial antenna manufacturers as well. Figure 2-54 presents the photo of a commercial transmit-array developed for V-band (57-66 GHz) fixed (no beam steering feature) point-to-point communications by *Radiall*. The characteristics table extracted from their online datasheet presented in figure 2-54 claims that this antenna is compliant with class 2 ETSI RPE and offers a minimum gain of 31 dBi over 57-66 GHz frequency range. However, this antenna has quite large form factor by having a diameter of 24 λ_0 and a total length of 17.2 λ_0.

Test/Characteristics	Values/Remarks
ELECTRICAL CHARACTERISTICS	
Frequency range (GHz)	57-66 GHz
V.S.W.R. (max)	< 1.5
Gain (typical)	32 dBi
Gain (min full band)	31 dBi
3dB beamwidth	3.5° x 3.5°
Side lobe level	ETSI Class 2
Polarization	Linear
Compliance standard	ETSI Class 2
Flange type	WR15 (UG-385/U)
Diameter	121 mm
Length	86.2 mm

Figure 2-54: Commercialized V-band transmit-array (Radiall) [109].

The transmit-array aperture is fabricated using conventional PCB technology manufacturing methods and the metallic primary source and the conical support are fabricated using existing machining techniques.

2.4.3. Conclusions on commercialized mm-wave antennas

Different commercialized antenna solution based on various antenna technologies where presented. Some of these antennas were particularly designed for 5G point-to-point communication and some were for satellite communication that may be used for 5G applications as well. It was demonstrated that there exist no perfect solution. Each solution lacks one of our datasheet specifications. They are either expensive, bulky, lack beam steering capability or not-compliant with ETSI RPE.

2.5.Decision Matrix

After defining the antenna requirements for 5G mm-waves Point-to-Pint communications and performing a state of the art research on different antenna technologies potentially compatible with the defined datasheets, a decision matrix was defined with the following criteria:

- Antenna technology dominant efficiency,
- Antenna technology typical bandwidth,
- Antenna technology form factor, especially its height,
- Electronic beam steering compatibility,
- Realization complexity and cost.

This decision matrix is used to determine the choice of the antenna technology for this project by comparing it with the developed 5G potential frequency bands datasheets

Technology Facmily	Technology	Surface efficiency ($\frac{D_{Max-antenna}}{D_{Unifrome}}$)	Radiation efficiency ($\frac{G_{measured}}{D_{measured}}$)	Bandwidth%- (ΔG=+/- 0.5 dB)	Height (en λ)	Return loss (bandwidth)	Beam steering (operational ±3°)	Beam steering (deployment ±15°)	Realization technology	Inconvenient/ Advantage
Quasi-optical antenna solutions	Homogeneous lenses	28%	55%	7%	27 λ	15dB (15%)	Yes Focal plane array	Yes Focal plane array	Dielectric ; Additive fabrication	Important volume / simple structure
	Non-homogeneous lenses	25%	55%	7%	15 λ	15dB (8%)	Yes-Aperture phase shifting or focal plane array	Yes-Aperture phase shifting or focal plane array	Dielectric ; Additive fabrication	Important volume / simple structure
	Parabolic reflector	70%	70%	7.5%	12λ (F/D=0.36)	15dB (10%)	Yes Focal plane array BUT Masking effect	Yes Focal plane array BUT Masking effect	Metallic parabola's-stamping/spinning	Important volume-feed masking/ efficiency
	Reflect-arrays	30%	50%	7.5%	10λ (F/D=0.5)	15dB (10%)	Yes Focal plane array BUT Masking effect	Yes Focal plane array BUT Masking effect	PCB printing ; Additive fabrication	Important height-feed masking/ Beam steering
	Transmit-arrays	30%	50%	7.5%	10λ (F/D=0.5)	15dB (10%)	Yes-Aperture phase shifting or focal plane array	Yes-Aperture phase shifting or focal plane array	PCB printing	Important height/ Beam steering
Direct fed antennas-Waveguide based antenna arrays with parallel feeding networks	Slot array	70%	80%	11%	2 λ	15dB (8.5%)	Yes-inter sub-array phase shifting	Challenging-requires inter-element phase shifting	Injected plastic and metalized ; Machining; (Additive fabrication)	Beam steering & tapering / Thickness & efficiency
	Horn array	70%	80%	12% (20% pour 2dB du gain)	6 λ	15dB (8%) (dual band for E-band)	Yes-inter sub-array phase shifting	Challenging-requires inter-element phase shifting	Injected plastic and metalized ; Machining; (Additive fabrication)	Beam steering & tapering / Thickness & efficiency
	CTS	40%	80%	11.8%	6λ	15dB (13%)	Yes-inter sub-array phase shifting	Complicated in both planes (Multi source possible in H-plane)	Injected plastic and metalized ; Machining; (Additive fabrication)	Beam steering & tapering in E-plane / Thickness & efficiency

2.6. Conclusions

In this chapter, different antenna technologies potentially compatible with the defined datasheets in first chapter, were studied in detail using the recent state of the art. Moreover, as a complementary to the state of the art research, array factor based calculations were used to determine any type of directly fed arrays (planar arrays) requirements in terms of amplitude tapering and phase shifting in order to be compliant with our datasheets.

For the directly fed antenna arrays, it was demonstrated that they offer the lowest form factor. However, controlling the array elements amplitude and phase, was proven to be challenging and very costly for large mm-waves arrays where high number of small array elements are used to fulfill the gain requirements.

Quasi-optical antenna solutions, contrary to directly fed antennas arrays, offer more simple feeding network structure which enables obtaining beam steerable and low side lobe level solutions with much less complexity and cost. But, these antennas have form factors at least 8 times bigger than directly fed arrays. However there exist some solutions such as folded structures to reduce these antennas form factor which has a drawback of being only a single polarization solution.

In the addition to the state of the art on different antenna technologies, main commercialized antenna solution were also analyzed. It was demonstrated that up to this day, there is no perfect solution fulfilling all the requirements defined in first chapter.

A decision matrix was proposed to summarize different antenna technologies characteristics and determine their compatibility with the defined datasheets in first chapter.

Using the decision matrix proposed in the previous section, and taking into account industrial constraints such as cost, it was decided to choose quasi-optical antenna solutions as the base antenna technology for this thesis. The goal is to propose a low cost, compact, directive, ETSI/FCC compliant and beam steerable antenna solution for 5G point-to-point communications such as small cell backhauling. Evidently, some compromises are needed between these different requirements. Main reasons that quasi-optical antenna solution was chosen as base this technology, in comparison with directly fed antenna arrays are:

- They are generally a low cost and easy to manufacture technology.
- They have simple feeding network which facilitates integrating beam steering features.
- The side lobe levels can be controlled by the phase correcting aperture profile and/or the primary source illumination which facilitate being compliant with ETSI RPE.
- There are high gain and large bandwidth solutions available in this technology.

The phase correcting aperture of our quasi-optical solution was chosen to be a dielectric Fresnel Zone Plate lens. As presented previously in this chapter, this lens offers very compact from factor and also a low cost fabrication. In following chapter 3, a fix (non-steerable) antenna solution based on a Fresnel Zone Plate lens is proposed.

2.7.References

[1] ETSI EN 302 217-4- V2.1 (2017-05) -Fixed Radio Systems; Characteristics and requirements for point-to-point equipment and antennas; Part 4: Antennas, 2017.

[2] E. Levine, G. Malamud, S. Shtrikman, and D. Treves, "A study of microstrip array antennas with the feed network," *IEEE Trans. Antennas Propag.*, vol. 37, no. 4, pp. 426–434, Apr. 1989.

[3] Robert J. Mailloux, "Phased Array Antenna Handbook" library of congress cataloging in publication data, 1993

[4] A. Saban, "Ka Band Microstrip Antenna Arrays With High Efficiency," *IEEE International Symposium on Antennas and Propagation*, pp. 2740-2743, Orlando, FL, 1999.

[5] J. Ala-Laurinaho, J. Aurinsalo, A. Karttunen, M. Kaunisto, A. Lamminen, J. Nurliharju, A. V. Räisänen, J. Säily, and P. Wainio, "2-D beam-steerable integrated lens antenna system for 5G E-band access and backhauk*," IEEE Trans. Microw. Theory Tech*., vol. 64, pp. 2244-2255, Jun. 2016.

[6] M. B. Gueye, "Définition, Conception et Réalisation d'une Antenne Compacte en Ondes Millimétriques (71GHz -86 GHz) pour des Liaisons Haut Débit Numérique," *Ph.D thesis*, Université Paris Ouest Nanterre La Defense, 2014.

[7] "SENCITY®Matrix 70/80 GHz Antenna 38 dBi," *Product Data sheet,* HUBER+SUHNER, 2017.

[8] "SENCITY®Matrix 60 GHz Antenna 38 dBi," *Product Data sheet,* HUBER+SUHNER, 2017.

[9] Y. Kimura, M. Takahashi and M. Haneishi, "76 GHz alternating-phase fed single-layer slotted waveguide arrays with maximum gain and sidelobe suppression," *Antennas and Propagation Society International Symposium*, vol. 3, , pp. 1042-1045, Jun. 2005.

[10] Y. Kimura, Y. Miura, T. Shirosaki, T. Taniguchi, Y. Kazama, J. Hirokawa, and M. Ando, "A low-cost and very compact wireless terminal integrated on the back of a waveguide planar array for 26 GHz band fixed wireless access (FWA) systems," *IEEE Trans. Antennas Propag.*, vol. 53, no. 8, pp. 2456–2463, Aug. 2005.

[11] S. Park, Y. Tsunemitsu, J. Hirokawa, and M. Ando, "Center feed single layer slotted waveguide array," *IEEE Trans. Antennas Propag.*, vol. 54, no. 5, pp. 1474–1480, May 2006.

[12] S. Fujii, Y. Tsunemitsu, G. Yoshida, N. Goto, M. Zhang, J. Hirokawa, and M. Ando, "A wideband single-layer slotted waveguide array with an embedded partially corporate feed," in *Proc. Int. Symp. Antennas Propag., TP-C27-5*, Oct. 2008.

[13] Y. Miura, J. Hirokawa, M. Ando, Y. Shibuya, and G. Yoshida, "Doublelayer full-corporate-feed hollow-waveguide slot array antenna in the 60- GHz Band," *IEEE Trans. Antennas Propag.*, vol. 59, no. 8, pp. 2844–2851, Aug. 2011.

[14] Xu, M. Zhang, J. Hirokawa and M. Ando, "E-Band Plate-Laminated Waveguide Filters and Their Integration Into a Corporate-Feed Slot Array Antenna With Diffusion Bonding Technology," in *IEEE Transactions on Microwave Theory and Techniques*, vol. 64, no. 11, pp. 3592-3603, Nov. 2016.

[15] E. Rajo-Iglesias, M. Ferrando-Rocher and A. U. Zaman, "Gap Waveguide Technology for Millimeter-Wave Antenna Systems," in *IEEE Communications Magazine*, vol. 56, no. 7, pp. 14-20, JULY 2018.

[16] E. Rajo-Iglesias and P.-S. Kildal, "Numerical studies of bandwidth of parallel plate cut-off realized by bed of nails, corrugations and mushroom-type EBG for use in gap waveguides," *IET Microw., Antennas Propag*., vol. 5, no. 3, pp. 282–289, Mar. 2011.

[17] D. Zarifi, A. Farahbakhsh, A. U. Zaman and P. Kildal, "Design and Fabrication of a High-Gain 60-GHz Corrugated Slot Antenna Array With Ridge Gap Waveguide Distribution Layer," in *IEEE Transactions on Antennas and Propagation*, vol. 64, no. 7, pp. 2905-2913, July 2016.

[18] E. Rajo-Iglesias and P.-S. Kildal, "Groove gap waveguide: A rectangular waveguide between contactless metal plates enabled by parallel-plate cut-off", *4th European Conference on Antennas and Propagation EuCAP 2010*, Barcelona, Spain, 12-16 April 2010.

[19] J. Liu, A. Vosoogh, A. U. Zaman and J. Yang, "Design and Fabrication of a High-Gain 60-GHz Cavity-Backed Slot Antenna Array Fed by Inverted Microstrip Gap Waveguide", *IEEE Transactions on Antennas and Propagation*, vol. 65, no. 4, pp. 2117-2122, April 2017.

[20] S. A. Razavi, P. Kildal, L. Xiang, H. Chen and E. Alfonso, "Design of 60GHz planar array antennas using PCB-based microstrip-ridge gap waveguide and SIW," *The 8th European Conference on Antennas and Propagation (EuCAP 2014)*, The Hague, 2014, pp. 1825-1828.

[21] A. Vosoogh, P. Kildal, and V. Vassilev, "A Multi-Layer Gap Waveguide Array Antenna Suitable for Manufactured by Die-Sink EDM," *10th European Conference on Antennas and Propagation (EUCAP)*, 2016.

[22] GAPWAVES AB, Information avalable on http://www.gapwaves.com.

[23] L. Yan, W. Hong, G. Hua, J. Chen, K. Wu, and T. J. Cui, "Simulation and experiment on SIW slot array antennas," *IEEE Microw. Wireless Comp. Lett*., vol. 14, no. 9, pp. 446–448, 2004.

[24] M. Bozzi, M. Pasian, L. Perregrini, and K.Wu, "On the losses in substrate integrated waveguides and cavities," *Int. J. Microw. Wireless Tech.*, vol. 5, no. 1, pp. 395–401, 2009.

[25] J. Hirokawa and M. Ando, "Efficiency of 76-GHz post-wall waveguide-fed parallel-plate slot arrays," *IEEE Trans. Antenna Propag.*, vol. 48, no. 11, pp. 1742–1745, Nov. 2000.

[26] J. Wu, Y. J. Cheng, Y. Fan, "A wideband high-gain high-efficiency hybrid integrated plate array antenna for V-band inter-satellite links", *IEEE Transactions on Antennas and Propagation*, vol. 63, no. 4, pp. 1225-1233, Apr. 2015.

[27] L. Wang, Y. J. Cheng, D. Ma and C. X. Weng, "Wideband and dual-band high-gain substrate integrated antenna array for E-band multi-gigahertz capacity wireless communication systems", IEEE Trans. Antennas Propag., vol. 62, no. 9, pp. 4602-4611, Sep. 2014.

[28] W. H. Henderson and W. W. Milroy, "Wireless Communication Applications of the Continuous Transverse Stub (CTS) Array at Microwave and Millimeter Wave Frequencies," *IEEE/ACES Int Conf Wirel. Commun. Appl. Comput. Electromagn.* 2005., pp. 253–256, 2005.

[29] M. Ettorre, F. F. Manzillo, M. Casaletti, R. Sauleau, L. Le Coq, and N. Capet, "Continuous Transverse Stub Array for Ka-Band Applications," *IEEE Transactions on Antennas and Propagation*, vol. 63, no. 11, pp. 4792–4800, Nov 2015.

[30] W. W. Milroy, "Continuous Transverse Stub element antenna arrays using voltage-variable dielectric material," United States Patent 5,583,524.

[31] T. W. Bradley, W. W. Chen, J. R. Chow, S .B. Coppedge, T. K. Dougherty, S..A. Gabelich, N. H. Harris, N. T. Hrobak, R. T. Lewis, J. F. Linder, W. W. Milroy, B. M. Pierce, and R .J Wittmond, "Development of a Voltage Variable Dielectric (VVD), Electronic Scan Antenna (ESA)," 43rd Annual Tri-Service Radar Symposium (1997), Edinburgh, Scotland.

[32] M. Iskander, Z. Zhang, Z Yun, R. Isom, M. Hawkins, R. Emrick, B. Bosco, J. Synowczynski, B. Gersten, "New phase shifters and phased antenna array designs based on ferroelectric materials and CTS technologies," 2001 *IEEE International Microwave Theory and Techniques Symposium*, May 20-25, Phoenix, AZ, USA.

[33] Magdy Iskander, Zhijun Zhang, Zhengqing Yun, "Low cost low loss antenna array with beam steering capability," United States Patent application submitted.

[34] R. Robertson, "Electronically-Scanned semiconductor antenna," United States Patent 6,064,349

[35] W. W. Milroy, "Planar antenna radiating structure having quasi-scan, frequency-independent driving-point impedance," United States Patent 5,995,055.

[36] W. W. Milroy, "Compact, ultra-wideband matched E-plane power divider," United States Patent 5,926,077.

[37] W. W. Milroy, "Compact, ultra-wideband, antenna feed architecture comprising a multistage, multilevel network of constant reflection-coefficient components," United States Patent 6,075,494.

[38] ThinLine by ThinKom Solutions, datasheet available at http://www.thinkom.com/antenna-products/thinline/

[39] "Aperture antennas for millimeter and sub-millimeter wave applications," Springer, A. V. Boriskin and R. Sauleau Ed., Sep. 2017.

[40] C. Balanis Antenna theory: "Analysis and design", third edition; Wiley-Interscience Apri 4, 2005 Title: Antenna Theory: Analysis And Design, 3rd

[41] L. V. Blake, "Antennas", Wiley, New York, 1966.

[42] R. Sauleau, C. A. Fernandes, and J. R. Costa, "Review of lens antenna design and technologies for mm-wave shaped-beam applications," *presented at the 11th Int. Symp. Antenna Technology and Applied Electromagnetics*, Saint Malo, France, June 15–17, 2005.

[43] B. Schoenlinner, X. Wu, J. P. Ebling, G. V. Eleftheriades, G. M. Rebeiz, "Wide-scan spherical-lens antennas for automotive radars", *IEEE Trans. Microwave Theory Tech*., vol. 50, n°9, pp. 2166-2175, Sept. 2002

[44] X. Wu, G. V. Eleftheriades, T. E. van Deventer-Perkins, "Design and characterization of single- and multiple-beam mm-wave circularly polarized substrate lens antennas for wireless communications", *IEEE Trans. Microwave Theory Tech*., vol. 49, n°3, pp. 431-441, March 2001

[45] D. F. Filipovic, S. S. Gearhart, G. M. Rebeiz, "Double-slot antennas on extended hemispherical and elliptical silicon dielectric lenses", *IEEE Trans. Microwave Theory Tech*., vol. 41, n°10, pp. 1738-1749, Oct. 1993

[46] M. J. M. van der Vorst, P. J. I. de Maagt, A. Neto, A. L. Reynolds, R. M. Heeres, W. Luingue, M. H. A. J. Herben, "Effect of internal reflections on the radiation properties and input impedance of integrated lens antennas – Comparison between theory and measurements", *IEEE Trans. Microwave Theory Tech*., vol. 49, n°6, pp. 1118-1125, June 2001

[47] A. Skalare, Th. de Graauw, H. van de Stadt, "A planar dipole array antenna with an elliptical lens", *Microwave and Optical Technology Letters*, vol. 4, n°1, pp. 9-12, Jan. 1991

[48] J. Thornton, "A low sidelobe asymmetric beam antenna for high altitude platform communications", I*EEE Microwave and Wireless Comp. Letters*, vol. 14, n°2, pp. 59-61, Feb. 2004.

[49] C. A. Fernandes, "Shaped-beam antennas", Chapter 15 in "Handbook of Antennas in Wireless Communications", Lal Godara, *CRC Press*, New York, 2002

[50] C. A. Fernandes, "Shaped dielectric lenses for wireless millimeter-wave communications", *IEEE Antennas and Propag. Magazine*, vol. 41, n°5, pp. 141-150, Oct. 1999

[51] C. A. Fernandes, L. M. Anunciada, "Constant flux illumination of square cells for mm-wave wireless communications", *IEEE Trans. Microwave Theory and Tech*., vol. 49, n°11, pp. 2137-2141, Nov. 2001

[52] C. A. Fernandes, P. Francês, A. Barbosa, "Shaped coverage of elongated cells at millimetre waves using a dielectric lens antenna", *Proc. 25th European Microwave Conference 1995*, Bologna, Italy, pp. 66-70, Sept. 1995

[53] B. Chantraine-Barès, R. Sauleau, J.-P. Daniel, K. Mahdjoubi, "Analysis and design of non-axis symmetric shaped dielectric lens fed by arrays of patch antennas", *12th Int. Symp. on Antennas, JINA '2002*, Nice, France, vol. 1, pp. 443-446, 12-14 Nov. 2002

[54] B. Barès, R. Sauleau, L. Le Coq, K. Mahdjoubi, "A new accurate design method for millimeter-wave homogeneous dielectric substrate lens antennas of arbitrary shape", *IEEE Trans. Antennas and Propag*., in press

[55] H. D. Hristov, "Fresnel zones in wireless links, zone plate lenses and antennas", London, Artech House, 2000

[56] H. Mosallaei, Y. Rahmat-Samii, "Non-uniform luneburg and two-shell lens antennas: radiation characteristics and design optimization", *IEEE Trans. Antennas Propagat*., vol. 49, n°1, pp. 60-69, Jan. 2001

[57] A. D. Greenwood, J. Jian-Ming, "A field picture of wave propagation in inhomogeneous dielectric lenses", *IEEE Antennas and Propag. Magazine*, vol. 41, n°5, pp. 9-18, Oct. 1999

[58] S. Rondineau, M. Himdi, J. Sorieux, "A sliced spherical Lüneburg lens", *IEEE Antennas and Wireless Propag. Letters*, vol. 2, pp. 163-166, 2003

[59] Dr. Oscar Quevedo-Teruel online course, available at http://www.etk.ee.kth.se/personal/oscarqt/index.html.

[60] A. Artemenko, A. Mozharovskiy, A. Sevastyanov, V. Ssorin and R. Maslennikov, "Electronically beam steerable lens antenna for 71–76/81–86 GHz backhaul applications," *2015 IEEE MTT-S International Microwave Symposium*, Phoenix, AZ, 2015.

[61] J. Ala-Laurinaho et al., "2-D beam-steerable integrated lens antenna system for 5G E-band access and backhaul*," IEEE Trans. Microw. Theory Techn.*, vol. 64, no. 7, pp. 2244–2255, Jul. 2016.

[62] B. Fuchs, O. Lafond, S. Rondineau, and M. Himdi, "Design and characterization of half Maxwell fish-eye lens antennas in millimeter-waves," *IEEE Trans. Microw. Theory Tech*., vol. 54, pp. 2292–2300, Jun. 2006.

[63] R. K. Luneburg, Mathematical Theory of Optics. Providence, Rhode Island: Brown Univ. Press, 1944.

[64] B. Fuchs, O. Lafond, S. Palud, L. Le Coq, M. Himdi, M.C. Buck, S. Rondineau : 'Comparative Design and Analysis of Luneburg and Half Maxwell Fish-Eye Lens Antennas', *IEEE Transactions on Antennas and Propagation*, vol. 56, n°9 , pp. 3058-3062, 2008.

[65] A. D. Greenwood and J. Jian-Ming, "A field picture PF wave propagation in inhomogeneous dielectric lenses," *IEEE Antennas Propag Mag.*, vol. 41, no. 5, pp. 9–18, Oct. 1999.

[66] J. C. Maxwell, *Scientific Papers, I*, New York, Dover Publications, 1860.

[67] R. K. Luneburg, *Mathematical Theory of Optics*. Providence, Rhode Island: Brown Univ. Press, 1944.

[68] Kundtz, N. & Smith, D. R., "Extreme-angle broadband metamaterial lens," Nature *Materials*, vol. 9 , pp. 129-132, 2010.

[69] R. Czarny et al., "Q-band high gain radome integrated lens antenna for compact backhaul terminal*", 11th Euoropean Conference on Antenna and Propagation (EuCAP)*, Paris, France, 2017.

[70] A. Jouadé, J. Bor, O. Lafond and M. Himdi, "Millimeter-wave fresnel zone plate lens based on foam gradient index technological process," *2016 10th European Conference on Antennas and Propagation (EuCAP)*, Davos, 2016.

[71] Radio Frequency Systmes, Information available on https://www.rfsworld.com/

[72] D. G. Berry, R. G. Malech, and W. A. Kennedy, "The reflectarray antenna," in *IEEE Transactions on Antennas and Propagation*, vol. 11, pp. 645–651, 1963.

[73] C. S. Malagisi, "Microstrip disc element reflect array," in *Proceedings of the Electronics and Aerospace Systems Convention (EASCON '78)*, pp. 186–192, 1978.

[74] J. P.Montgomery, "A microstrip reflectarray antenna element," in *Proceedings of the Antenna Applications Symposium*, Urbana, Ohio, USA, 1978.

[75] J. Huang, "Microstrip reflectarray," *in Proceedings of the Antennas and Propagation Society International Symposium Digest*, vol. 2, pp. 612–615, Ontario, Canada, 1991.

[76] D. M. Pozar, Stephen D. Targonski, and H. D. Syrigos,." Design of millimeter wave microstrip refbctarrays," *IEEE Transactions on Antennas and Propagation*, 45(2):287-295, February 1997.

[77] J. Perruisseau-Carrier, "Dual-polarized and polarization-flexible reflective cells with dynamic phase control," *IEEE Transactions on Antennas and Propagation*, vol. 58,p p. 1494-1502,M ay 2010.

[78] C. Guclu, J. Perruisseau-Carrier, and O. Aydin Civi, "Proof of Concept of a Dual-band Circularly-polarized RF MEMS Beam-Switching Reflectarray" *IEEE Transactions on Antennas and Propagation*, vol. 60, pp. 5451-5455, 2012.

[79] P. Nayeri, F. Yang, and A.Z. Elsherbeni, "Radiation characteristics of conformal retlectarray antennas, " Proc. *IEEE Antennas and Propagation Soc. Int. Symp*., pp. 365 - 368, Spokane, WA, USA, June 201l.

[80] S. Hum and J. Perruisseau-Carrier, "Reconfigurable reflectarrays and array lenses for dynamic antenna beam control: A review," *IEEE Transactions on Antennas and Propagation*, vol. 62, no. 1, pp. 183–198, Jan. 2014.

[81] D. M. Pozar, "Bandwidth of reflectarrays," *Electronics Letters*, vol. 39, no. 21, pp. 1490–1491, 2003.

[82] L. Moustafa, R. Gillard, F. Peris, R. Loison, H. Legay, and E. Girard, "The phoenix cell: a new reflectarray cell with large bandwidth and rebirth capabilities," *IEEE Antennas and Wireless Propagation Letters*, vol. 10, pp. 71–74, 2011.

[83] P. de Vita, A. Freni, G. L. Dassano, P. Pirinoli, and R. E. Zich, "Broadband element for high-gain single-layer printed reflectarray antenna," *Electronics Letters*, vol. 43, no. 23, pp. 1247–1249, 2007.

[84] W. Menzel, D. Pliz, and M. Al-Tikriti, "Millimeter-wave folded reflector antennas with high gain low loss and low profile," *IEEE Antennas Propag. Mag*., vol. 44, pp. 24-29, Jun. 2002.

[85] B. D. Nguyen, J. Lanteri, J. Y. Dauvignac, C. Pichot, and C. Migliaccio, "94 GHz folded Fresnel reflector using C-patch elements," *IEEE Antennas and Wireless Propagation Letters*, vol. 56, no. 11, pp. 3373–3381, 2008.

[86] L.D. Palma, "Antennes Réseaux Transmetteurs Reconfigurables aux Fréquences Millimétriques, " *Thesis manuscript*, Université de Rennes 1, 2015.

[87] A. Moknache, L. Dussopt, J. Saily, A. Lamminen et al. "A Switched-Beam Linearly-Polarized Transmitarray Antenna for V-Band Backhaul Applications", *10th European Conference on Antennas and Propagation (EUCAP)*, 2016.

[88] L. Di Palma, A. Clemente, L. Dussopt, R. Sauleau, P. Potier, P. Pouliguen," Experimental Characterization of Reconfigurable Transmitarray with Reduced Focal Distance in X-Band", *IEEE AP-S International Symposium on Antennas and Propagation*, Vancouver, Canada, July 2015.

[89] Nematollahi, H., Laurin, J.-J., Page, J.E., Encinar, J.A., "Design of Broadband Transmitarray Unit Cells With Comparative Study of Different Numbers of Layers", *IEEE Transaction on Antennas and Propagation*, Vol. 63, No. 4, pp. 1473-1481, Apr. 2015.

[90] C. G. M. Ryan, M. R. Chaharmir, J. Shaker, J. R. Bray, Y. M. M. Antar, and A. Ittipiboon, "A wideband transmitarray using dual-resonant double square rings," *IEEE Transaction Antennas and Propagation*, vol. 58, no. 5, pp. 1486 –1493, 2010.

[91] H. Kaouach, L. Dussopt, J. Lantéri, T. Koleck, and R. Sauleau, "Wideband Low-Loss Linear and Circular Polarization Transmit-Arrays in V-Band," *IEEE Transactions on Antennas and Propagation,* vol. 59, no. 7, pp. 2513–2523, 2011.

[92] M. Sazegar, Y. Zheng, C. Kohler, H. Maune, M. Nikfalazar, J. Binder, and R. Jakoby, "Beam steering transmitarray using tunable frequency selective surface with integrated ferroelectric varactors," , *IEEE Transactions on Antennas and Propagation*, vol. 60, pp. 5690–5699, Dec 2012.

[93] E. Erdil, K. Topalli, N. Esmaeilzad, O. Zorlu, H. Kulah, and O. Aydin Civi, "Reconfigurable nested ring-split ring transmitarray unit cell employing the element rotation method by microfluidics," *IEEE Transactions on Antennas and Propagation*, vol. 63, pp. 1163–1167, March 2015.

[94] C. Cheng, B. Lakshminarayanan, and A. Abbaspour-Tamijani, "A programmable lens-array antenna with monolithically integrated mems switches," *IEEE Transactions on Microwave Theory and Techniques*, vol. 57, pp. 1874–1884, Aug 2009.

[95] T. Chaloun, C. Hillebrand, C. Waldschmidt, and W. Menzel, "Active transmitarray submodule for k/ka band satcom applications," *German Microwave Conference (GeMiC)*, 2015, pp. 198–201, March 2015.

[96] A. Clemente, L. Dussopt, R. Sauleau, P. Potier, and P. Pouliguen, "1-bit reconfigurable unit cell based on pin diodes for transmit-array applications in x -band," *IEEE Transactions on Antennas and Propagation*, vol. 60, pp. 2260–2269, May 2012.

[97] F. Diaby et al., "Design of a 2-bit unit-cell for electronically reconfigurable transmitarrays at Ka-band," *2017 European Radar Conference (EURAD)*, Nuremberg, 2017.

[98] *PIVOTAL COMMWARE*, Information available on https://pivotalcommware.com/ .

[99] R. Stevenson, M. Sazegar, et al. "Metamaterial Surface Antenna Technology: Commercialization through Diffractive Metamaterials and Liquid Crystal Display Manufacturing" *international Congress on Advanced Electromagnetic Materials in Microwaves and Optics – Metamaterials* Crete, Greece, 17-22 September 2016.

[100] B. H. Fong, J. S. Colburn, J. J. Ottusch, J. L. Visher, and D. F. Sievenpiper, ''Scalar and tensor holographic artificial impedance surfaces,'' *IEEE Trans. Antennas Propag*., vol. 58, no. 10, pp. 3212-3221, Oct.

[101] M.C. Johnson, S.L. Brunton, N.B. Kundtz, J.N. Kutz, "Sidelobe Canceling for Reconfigurable Holographic Metamaterial Antenna," *IEEE Trans. Ant. Prop*., Vol. 63, No. 4, pp. 1881-1886, 2015.

[102] M. C. Johnson, P. T. Bowen, N. Kundtz, and A. Bily, "A discrete dipole approximation model for control and optimization of a holographic metamaterial antenna," *Appl. Opt*., vol. 53, no. 25, pp. 5791–5799, 2014.

[103] *KYMETA*, Information available on https://www.kymetacorp.com/ .

[104] *ALCAN SYSTEMS*, Information available on https://www.alcansystems.com/ .

[105] *Radio Gigabit*, Information available on http://radiogigabit.com/ .

[106] *Isotropic Systems*, Information available on https://www.isotropicsystems.com/ .

[107] Q. Wu et al., "Flat transformation optics graded-index (TO-GRIN) lenses," *2012 6th European Conference on Antennas and Propagation (EUCAP)*, Prague, 2012.

[108] Isotropic Systems LTD. (London, GB), 'System And Method For Providing A Compact, Flat, Microwave Lens With Wide Angular Field Of Regard And Wideband Operation', WO/2018/116258, 2018.

[109] *Radiall*, Information available on www.radiall.com .

3. Chapter 3 : Folded Fresnel Zone Plate Lens Antenna (Fixed beam Solution)

3.1. Introduction

In the previous chapter an analytical study on existing directive antenna solutions compatible with the requirements defined in chapter 1 was developed. These studies lead to the design of an antenna based on quasi-optical antenna solutions with a grooved Fresnel Zone Plate (FZP) lens as its phase correcting aperture [1]. In order to overcome the major drawback of quasi-optical antenna solution, large form factor due to the focal distance of the primary source from the phase correcting aperture, a folded structure is applied to the FZP lens [2]. This folded structure, as presented in figure 3-1, consists of a Trans-reflector and a Twist-reflector which are made of printed metallic strips on dielectric substrates. The folded structure triples the path of the electrical field between the lens and its focal source and so allows reducing the focal distance by a factor of three.

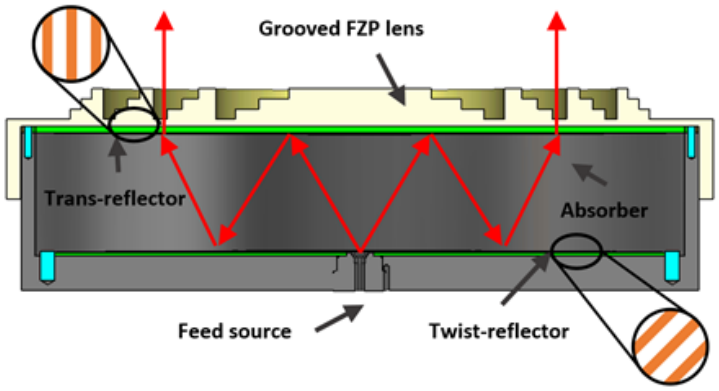

Figure 3-1: Cross-section of the Folded FZP lens antenna structure.

In section 2 of this chapter, the main building blocks of the FFZP antenna are presented, namely:

- Detailed studies on the FZP lens different characteristics and parameters and also the design parameters of the final FZP lens.
- The primary source (focal source) design parameters.

- The folder structure and its assembled blocks, Trans-reflector and Twist-reflector, design and simulation methods.

In section 3, we will proceed with the complete antenna simulation and measurement results of the assembled prototype.

Finally, in section 4, the presented antenna is modified and optimized to offer a lower cost, compact structure and a high gain for fixed point-to-point communications.

3.2.FFZP building blocks

3.2.1. Fresnel Zone Plate lens

Fresnel zone plate (FZP) lenses, briefly introduced in the first chapter, benefit form thin profile comparing to typical hemispherical lenses. FZP lens functions based on diffraction and constructive interference between zones (*N*) composing the lens. This zones act as phase shifters and each are consisted of sub-zones (*p*) performing a step wise phase correcting. The maximum phase error of each zone is defined by the number of its sub zones (*p*) and corresponds to $2\pi/p$. Two adjacent zones have a phase shift of 2π.

In general, the Fresnel lens reflective index is varied locally. Depending on how this variation is achieved, we have 3 main types of FZP lenses:

- Grooved FZP lens : refractive index variation using corrugations in single dielectric → [3-4], see figure 3-2.

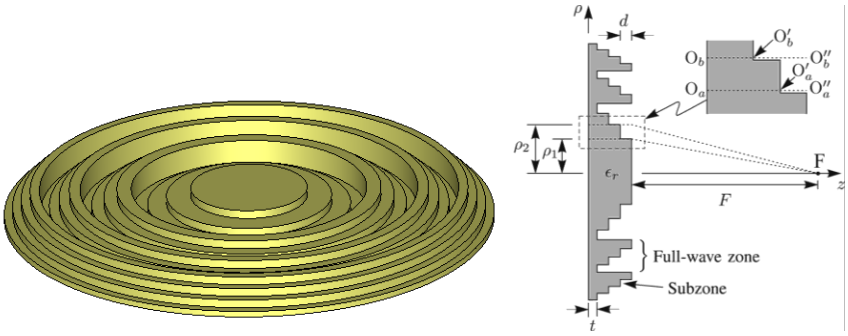

Figure 3-2: Grooved FZP lens.

- Perforated FZP lens : refractive index variation using perforation in single dielectric → [5-6], see figure 3-3.

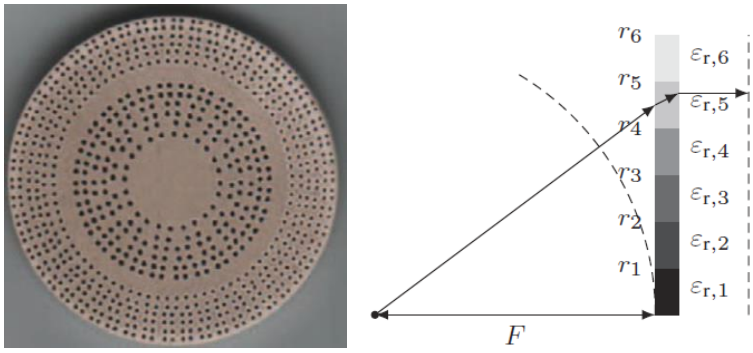

Figure 3-3: Perforated FZP lens.

- Multi-dielectric FZP lens : refractive index variation using different dielectrics → [7], see figure 3-4.

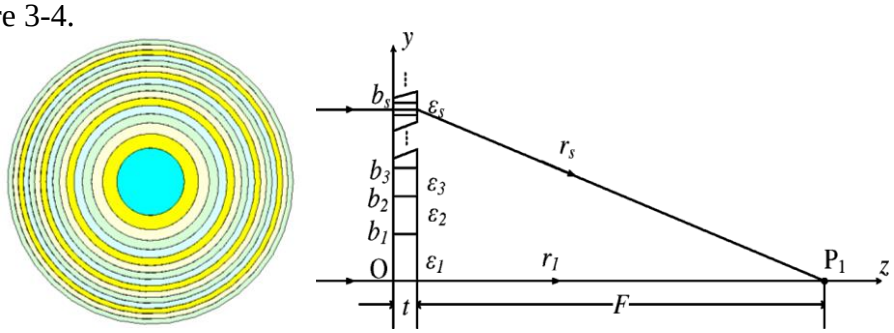

Figure 3-4: Multi-dielectric FZP lens.

The main drawback of grooved FZP lens is the corrugation shadow blockage effect [8] as presented in Figure 3-5. This shadows reduces the antenna aperture efficiency and is a function of Focal to Diameter (*F/D*) ratio.

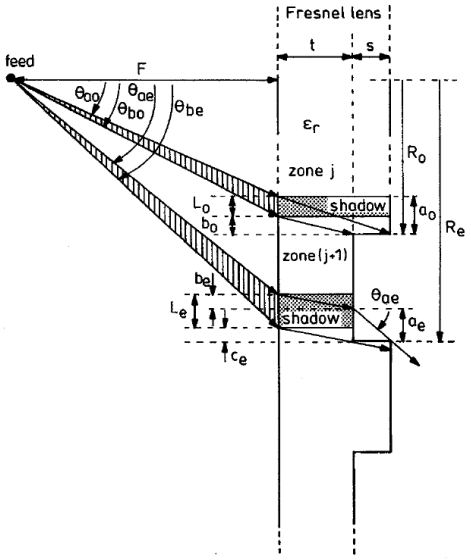

Figure 3-5: Grooved FZP lens corrugations shadow effect.

By using more planar structures, such as multi-dielectric FZP or perforated FZP, the shadow effect can be avoided. The latter, requires holes, with quite small dimensions in order of 0.1 λ, which becomes challenging in realization at mm-waves. Also the multi-dielectric structures require assembling different dielectric rings, with small dimensions around 0.4 λ, which increases the manufacturing complexity at mm-waves. For reasons of simplicity of manufacture and cost, it was decided to use a grooved FZP lens as the radiating aperture of the proposed antenna structure, as it's low cost and easy to manufacture.

In order to obtain an optimal grooved FZP lens for the antenna structure, different parametric studies are developed using full-wave simulations. The goal is to quantify the impact of different designed parameters on the FZP lens. Studied parameters are:

- Base dielectric thickness (for grooved FZP lens)
- Number of zones, as a function of *(F/D)*
- Number of sub-zones
- Primary source optimal edge taper

In the following the parametric studies on the grooved FZP lens is presented. It should be noted that the simulations are performed at V-band (57-66 GHz). Also, all the FZP lens simulations are done using *CST Microwave Studio* Time domain solver.

3.2.1.1. Grooved Fresnel Zone Plate lens parametric study

A grooved FZP lens is designed as the reference for parametric studies (figure 3-6). A typical single-dielectric (with ε_r=2.3) grooved FZP lens was designed using the following equations. The dielectric circular grooves, referred to as zones, act as phase shifters, each zone radius R_z being calculated by (1)

$$R_z = \sqrt{2n\lambda_0 F + (n\lambda_0)^2}\,, \quad n = 1,2,\dots,N \tag{1}$$

where F is the focal distance of the FZP lens antenna, N is the total number of zones and λ_0 is the wavelength in free space at the center frequency (60 GHz).

Each Full-Wave Grooved (FWG) zone is made of step corrugations, referred as sub-zones (p), performing a step wise phase correction. The maximum phase error of each FWG zone is defined by the number of sub-zones p and corresponds to $2\pi/p$. The radius of each sub-zone R_s is calculated using (2)

$$R_s = \sqrt{\frac{2s\lambda_0 F}{p} + \left(\frac{s\lambda_0}{p}\right)^2}, \quad s = 1,2,\dots,N \times p \tag{2}$$

where $s=N\times p$ is the total number of the sub-zones.

The thickness of corrugation steps t_c is calculated as follows

$$t_c = \frac{\lambda_0}{p(\sqrt{\varepsilon_r}-1)}\,. \tag{3}$$

The thickness t_b of the supporting dielectric layer is optimized in order to reduce the interface mismatch between the grooved FZP lens and the air as shown in figure 3-6.

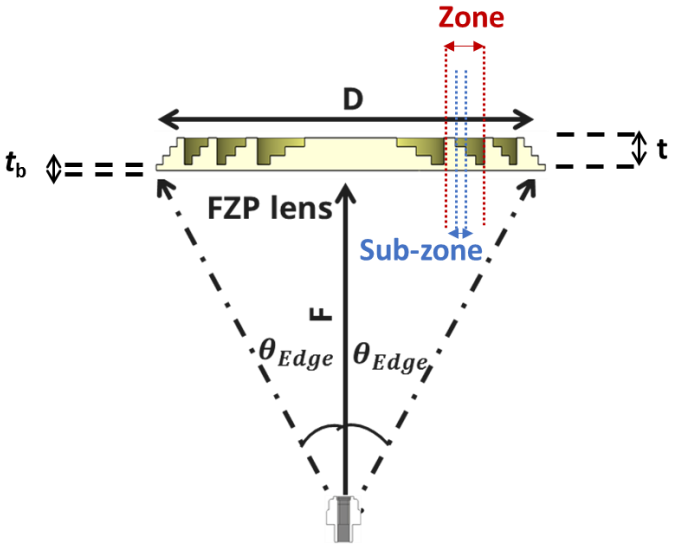

Figure 3-6: Corrugated FZP lens design parameters.

The main characteristics of the designed corrugated FZP lens, also presented in figure 3-6, are the followings:

- Diameter D = 120mm
- Focal distance F = 80 mm
- F/D=0.66
- 4 sub-zones → max phase error: π/2 → Quarter-wavelength Fresnel
- Material: Polypropylene (PP) with $\varepsilon_r = 2.3$
- Base dielectric thickness t_b = 0.1 λ = 0.5 mm
- FZP lens thickness t = 7.85 mm
- Edge illumination angle θ_{Edge}= 36.9°

The designed corrugated FZP lens is excited by a simple waveguide aperture with dimensions of 4.5 mm × 3.5 mm.

Figure 3-7 presents the simulated normalized radiation patterns of the primary source at 60 GHz. The edge taper of this primary source is 5 dB in both planes which will result in symmetrical radiation patterns for the circular FZP lens. We will see further that the 5 dB edge taper is not the optimal value and we can achieve better antenna performance (in terms of efficiency) by using more directive primary source which will minimizes spillover losses.

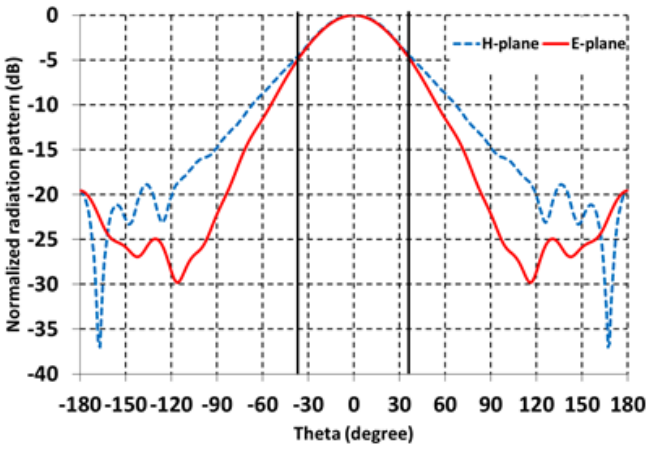

Figure 3-7: Normalized radiation simulated pattern of FZP lens primary source at 60 GHz.

Figure 3-8 shows the corrugated FZP lens simulated gain variation over frequency range of 57-70 GHz. We can observe a maximum gain of 32.9 dBi at 66 GHz with an aperture efficiency of 34.3 % (maximum directivity of surface with 120 mm diameter is 37.5 dB). The gain variation over the V-band (57-66 GHz) is 3 dB. As can be seen, the maximum is not centralized in 57-66 GHz frequency for the current FZP design. Further in this chapter, we will optimize it and move the maximum gain to 60 GHz instead of 66 GHz.

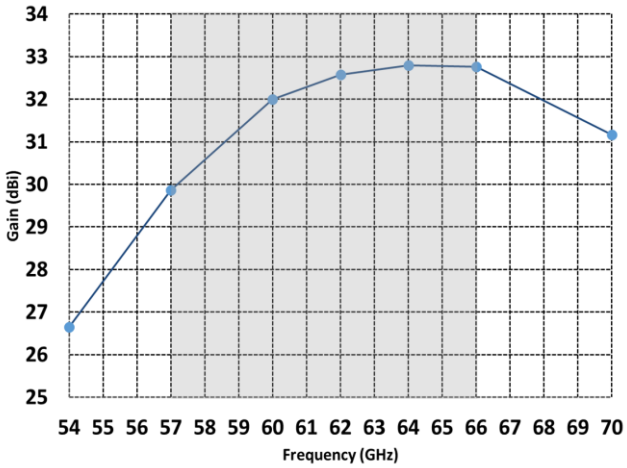

Figure 3-8: Basic Grooved FZP lens simulated gain variation over frequency (before optimization).

The simulated radiation patterns of the basic grooved FZP lens fed by the waveguide aperture at 57, 60 and 66 GHz are presented in figure 3-9. In coherence with the gain versus frequency curve, it's noticeable that the radiation pattern at 66 GHz is most focused one, with lower side lobe levels (SLL). Also the class 2 ETSI RPE has been superimposed on the patterns. We can see that the diagrams are not entirely compliant, namely for thetas larger than the illumination angle (36.9°). This is mainly because of the primary source spillover, and can be attenuated by using an absorber around the antenna structure, between the focal source and the lens. This is demonstrated in section 3 where the folded FZP antenna is simulated and measured with an absorber around the antenna structure.

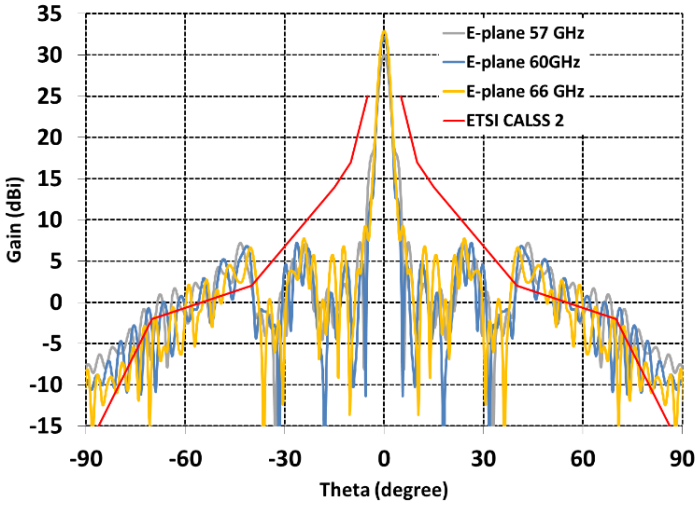

Figure 3-9: Basic grooved FZP lens simulated radiation patterns (before optimization).

In order to optimize the design of the grooved FZP, different parametric studies were performed and their results are presented in the following sub-sections.

3.2.1.1.1. Parametric study on base dielectric thickness

The first parameter to be optimized is the thickness of the base dielectric (t_b) of the grooved FZP lens in order to reduce the air-dielectric interface reflections. As presented in figure 3-10, the gain and efficiency of the antenna continues to increase up to 33.9 dBi and 47.3% respectively by increasing the base dielectric thickness until t_b = *5.5 mm*. Afterwards we observe that the antennas performance degrades. This degradation is explained by the increased transmission loss due to the dielectric material loss. As it can be observed, there are periodic gain drops (at 1.75 mm and 3.25 mm for example) which are mainly due to the increased reflection loss at these thicknesses because of not adapted dielectric-air interference. Typically, to minimize the reflection loss the base thickness should be a function of $\lambda_g/4$ (0.84 mm in our case), where λ_g is the guided wavelength in the substrate at the center frequency (60 GHz).

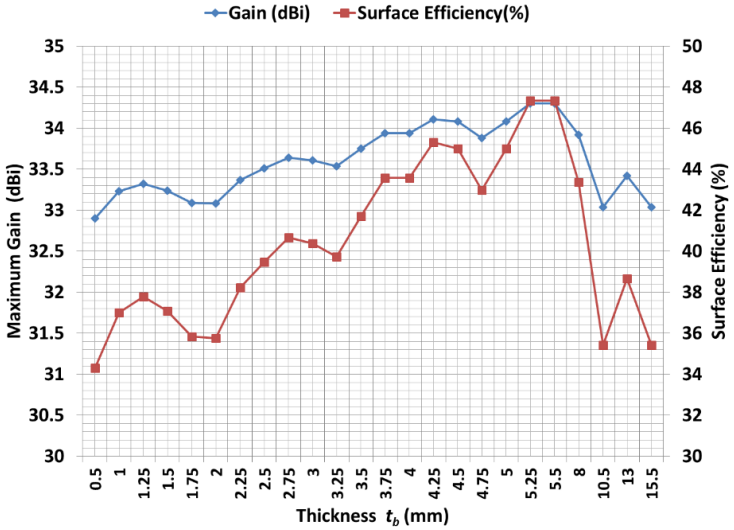

Figure 3-10: Parametric study on grooved FZP lens base dielectric thickness.

For this study, the focal distance between the primary source and the FZP lens is kept constant at *F=80 mm*. The compromise to make is between the FZP lens form factor and its efficiency, therefore the base thickness of t_b*=1.25 mm* (which is the first peak in figure 3-10) is chosen to fulfill this objective.

3.2.1.1.2. Parametric study on number of sub-zones

The number of sub-zones defines the FZP lens phase correction resolution. As demonstrated in the equation (4), by adding the number of sub-zones, finer phase correcting is achieved.

$$Phase\ correction\ resolution = {}^{2\pi}/_{p} \tag{4}$$

where *p* is number of the FZP lens sub-zones.

Figure 3-11 presents the simulations of the isotropic gain of the grooved FZP lens in function of number of sub-zones. The number of sub-zones also impact the corrugations steps thickness (t_c, see equation (3)) and as well the overall FZP lens thickness. This impact is also illustrated in figure 3-11. The numerical values of these curves are also presented in table 3-1.

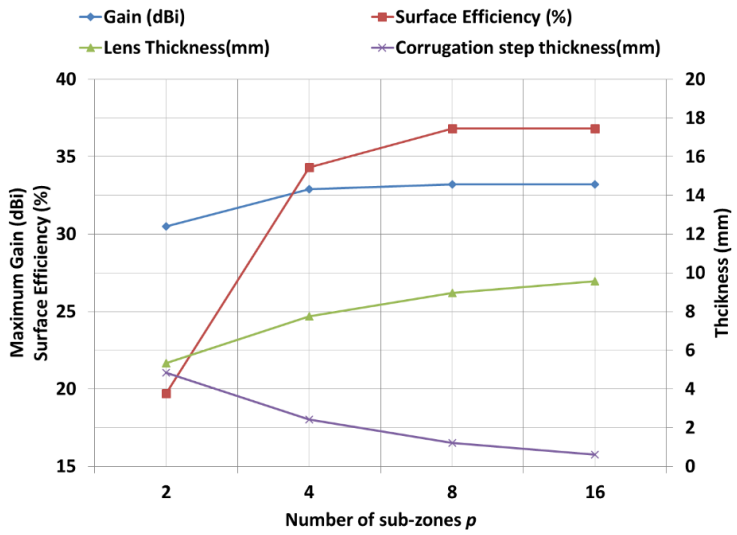

Figure 3-11: Parametric study on grooved FZP lens number of sub-zones.

As illustrated in figure 11, the gain and efficiency of the antenna increase by adding the number of sub-zones for an asymptotic behavior beyond 8 sub-zones, leading us to an optimum choice of 8 sub-zones.

As mentioned before and presented in the figure 3-11 and table 3-1, the number of sub-zones impacts as well the corrugations step thicknesses as the lens overall thickness. For example, for 8 sub-zones corrugations step is 1.2 mm with an overall thickness of 8.96 mm for the lens, and for 4 sub-zones these values are 2.42 mm and 7.75 mm respectively. The simulated gain difference between 4 and 8 sub-zones is only 0.3 dB while the 4 sub-zone FZP lens has less overall thickness and also larger corrugation steps which makes its realization easier. So the 4 sub-zone configuration is chosen for our grooved FZP lens.

Table 3-I: Parametric study on the number of sub-zones of the grooved FZP lens.

Number of sub-zones	Gain (dBi)	Surface Efficiency (%)	Lens thickness (mm)	Corrugation steps Thickness (mm)
2	30.5	19.7	5.34	4.84
4	32.9	34.3	7.759	2.42
8	33.2	36.8	8.969	1.21
16	33.2	36.8	9.574	0.605
90	33.2	36.8	10.072	0.108

3.2.1.1.3. Parametric study on number of zones (F/D)

For this study, the dimeter of the antenna is remained constant and therefore the Focal to Diameter ratio (*F/D*) is varied with the variation of the number of zones. For each number of zones, or each *F/D* value, we adapt the primary source in order to have equivalent edge taper for all cases when the focal distance and therefore illumination angle (θ_{Edge}) are varied. In addition to gain and efficiency variation for different number of zones, the variation of 2 dB gain bandwidth is also studied. These parameters variations in function of *F/D* are presented in

figure 3-12. Numerical values in function of number of zones and *F/D* are shown in Table 3-2.

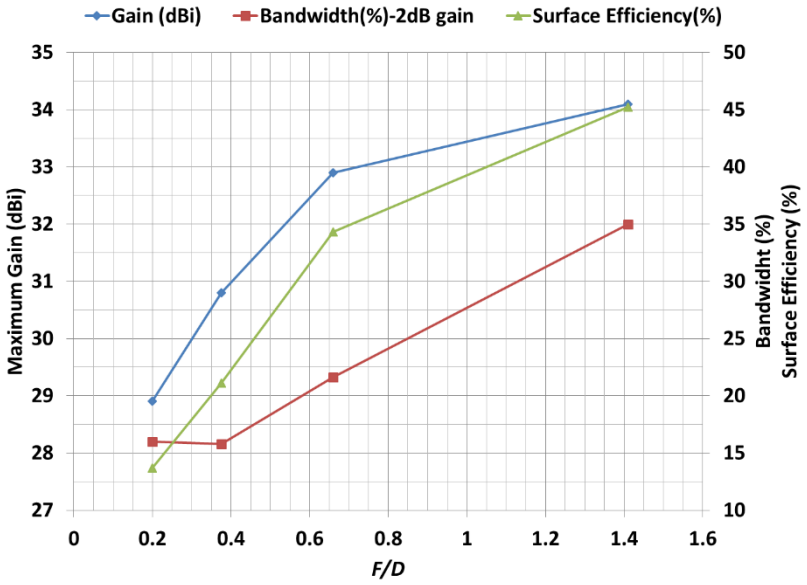

Figure 3-12: Parametric study on grooved FZP lens number of zones (F/D).

As mentioned, with increasing the number of zones for a constant diameter (*D*), the focal distance (*F*) will reduce and therefore we're in fact decreasing the *F/D* value. As illustrated in figure 3-12 and table 3-2, with the increase of *F/D*, the gain, efficiency and bandwidth of the antenna will increase until a certain point *(F/D=0.66*) where its increasing rate becomes slower (specially for the gain). It should be noted that for the case of *F/D*=0.2, same primary source designed for the case of *F/D*=0.375 is being used, meaning the feed has higher edge taper for the primary case. This means that the gain obtained for the *F/D*=0.2 is even lower if a feed with the same edge taper was used. One of the reasons of the antenna efficiency reduction for smaller *F/D* values is the shadow blockage effect. The FZP lens corrugations shadows become more important for smaller *F/D* values. As the bigger *F/D* means bulkier and larger antenna form factor, a compromise between the antenna performance and its form factor is required. For this FZP lens, *F/D=0.66* seems to be the optimal value both in terms of performance and also form factor.

Table 3-II: Parametric study on the number of zones and F/D of the grooved FZP lens.

Number of zones	Focal (F) (mm)	*F/D*	Gain (dBi)	Surface Efficiency (%)	θ_{Edge}	Edge taper (dB)	Gain bandwidth(%)-2dB	Feed dimensions	Feed max gain (dBi)
2	170 (35λ)	1.41	34.1	45.5	19.4°	-5	35%	11×10 mm	15
4	80(16λ)	0.66	32.9	34.3	36.9°	-4.12	21.6	6.5×5.5 mm	9
6	45(9λ)	0.375	30.8	21.1	53.1°	-4.93	15.8	5×4 mm	7.52
8	25(5λ)	0.2	28.9	13.7	67.4°	-7.4	16	5×4 mm	7.52

3.2.1.1.4. Parametric study on primary source optimal edge taper

For the FZP lens, as same as for any other aperture excited by a primary source, there is an optimal edge taper to minimize spillover losses and concentrate the feed energy uniformly on the aperture surface. As presented in figure 3-13, the ideal would be to have a feed source that uniformly illuminates the lens surface and moreover has zero spillover, but such a source is impossible in reality. The goal of this parametric study is to find the optimal edge taper with the best compromise between spillover and illumination efficiencies. In order to find this value, five horn antennas with different apertures and consequently different edge tapers are designed and simulated with the corrugated FZP lens. Figure 3-13 shows the radiation patterns of these horns and a simple standard WR15 waveguide aperture at 60 GHz.

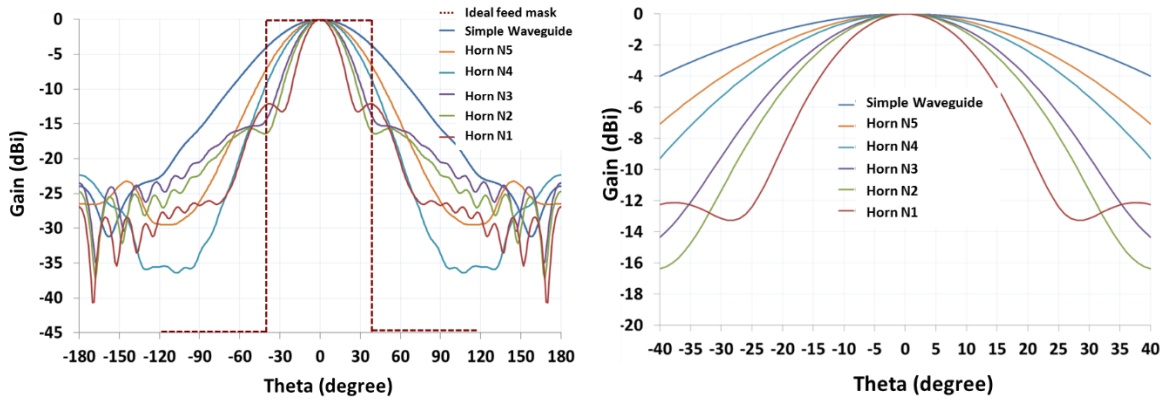

Figure 3-13: Normalized 60GHz simulated radiation patterns of different primary sources for edge taper parametric study.

Table 3-3 presents the numerical values of the edge taper of each simulated primary source for illumination angle $\theta_{Edge} = 36.9°$. It can be noted that by increasing the horn aperture and therefore increasing its directivity, the horn edge taper will increase as well : horn N1 has the largest aperture and therefore more directive radiation pattern.

Table 3-III: Different horns edge tapers for a fixed illumination angle.

Primary source	Edge Taper (dB)	HPBW (°)
Standard WR-15 waveguide aperture	3	38°
Horn N5	5.5	50°
Horn N4	7	45°
Horn N3	12	35°
Horn N2	15	32°
Horn N1	12*	25°

All these primary sources where simulated with the designed grooved FZP lens. Figure 3-14 presents the gain variation over the frequency of the FZP lens excited by each of these primary sources.

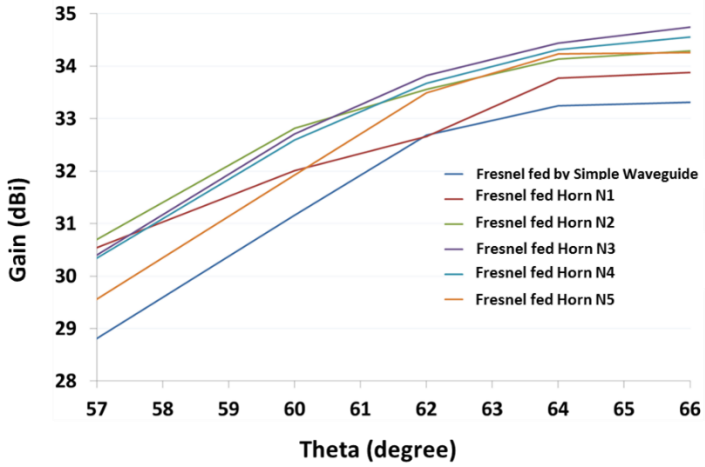

Figure 3-14: FZP lens gain variation over frequency for different edge tapers.

As we can see, the best gain result is for the horn labeled N3. This horn presented in figure 3-15, has an aperture of 7.2 mm × 9 mm, offering an edge taper of 12 dB for $\theta_{Edge} = 36.9°$. N3 horn offers the best compromise between illumination efficiency and spillover efficiency of the FZP lens.

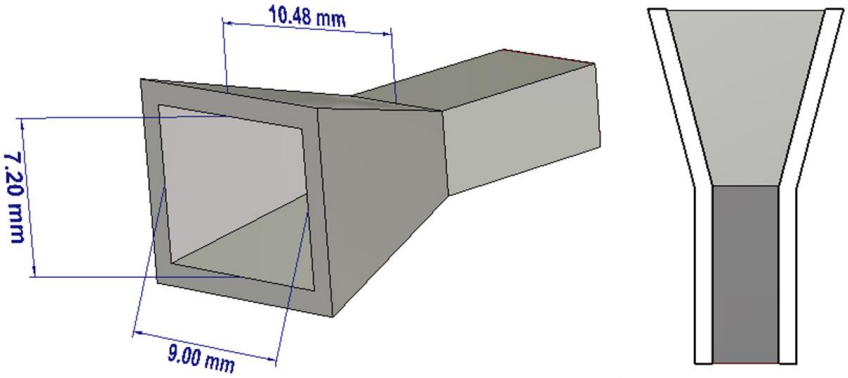

(a) (b)

Figure 3-15: Optimal edge taper horn N3 : (a) 3D perspective view, and (b) and cut-view.

3.2.1.1.5. Grooved FZP lens additional optimizations: Optimal focal point and centralized max gain

The grooved FZP lens used for parametric studies is a basic solution used as a reference. This lens is further optimized on two parameters:

- Real focal distance
- Centralizing gain variation over frequency around 60 GHz

Designing the FZP lens, we assume a certain theoretical focal distance (*F*) and we calculate the FZP parameters based on this value of *F*. But in reality, because of the discrete phase correcting behavior of the FZP lens and its phase error, the real focal point of the lens is displaced. To find the real position of the focal point of a designed FZP lens, the lens is exited using a plane wave and its field is observed in the focal axis (z-axis, see figure 3-16). As presented in figure

3-16, the real focal distance of our FZP lens is 84 mm instead of the assumed 80 mm. It should be noted that the obtained focal distance is between the FZP lens and the phase center of the primary source. This phase center is not always on the aperture of the source and could vary in function of the source type, and also in function of the frequency. The solution is to find the mean position of the phase center of the focal source over the frequency band of interest.

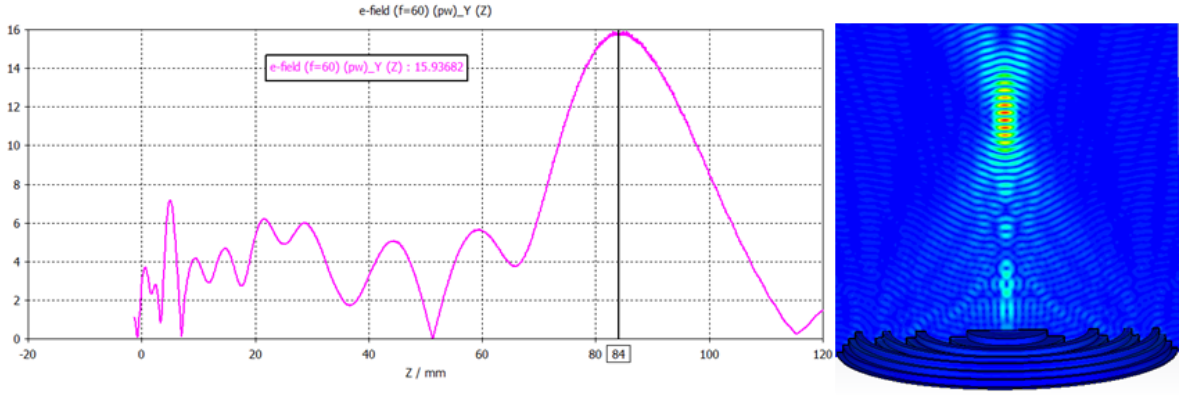

(a) (b)

Figure 3-16: E-field cartography of FZP lens excited by a plane wave at 60 GHz (a) 1-D on z-axis (b)2-D on z-x plane.

Regarding the simulated gain of the designed FZP lens, as it was illustrated in figure 3-8, the maximum gain is not around the central 60 GHz frequency but it's at upper-band of the frequency band, at 66 GHz. In order optimize the antenna performance over the frequency band it is preferred to have the maximum gain around the center of the frequency band. This can be achieved by applying minor modification in the FZP design equations. In fact, this happens by taking into account the thickness of each sub-zone when calculating its radius. Equation 5 presents the new calculation in order to centralize the gain variation over frequency band :

$$R'_s = \sqrt{\frac{2s\lambda_0(F+T_p)}{p} + (\frac{s\lambda_0}{p})^2}, \quad s = 1,2,\dots,N \times p \tag{5}$$

where T_p is the total thickness of the corrugation of the sub-zone *p:*

$$T_p = (p-1) \times t_c. \tag{6}$$

Figure 3-17 presents the comparison of the simulated gain variation between a FZP lens with centralized gain designed using corrected radius equation (6) and a typical FZP lens designed using non-corrected radius equation (2). The mention WG in the figure legend refers to the fact that FZP lens is illuminated using the simple waveguide aperture and not by the optimal edge taper horn N3. As can be seen the max gain is around 60 GHz instead of 66 GHz. Also the gain variation with the real focal point (84 mm) is presented in this figure, which illustrates much better gain for the frequencies over 60 GHz with a maximum gain of 33 dBi at 62 GHz.

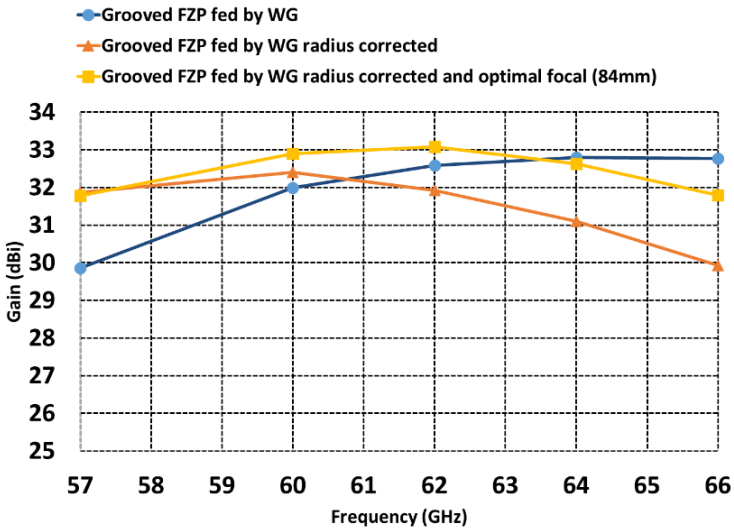

Figure 3-17: FZP lens gain optimization.

3.2.1.2. Conclusions on corrugated FZP lens

Different parametric studies on corrugated FZP lens were presented. Also some optimization techniques were proposed. To summarize, an optimal grooved FZP lens with form factor compromises shall have the following characteristics:

- Number of sub-zones: 4
- *F/D* = 0.66
- Illumination Edge taper: 12 dB

3.2.2. Focal source design

As mentioned earlier, the basic focal source of the FFZP lens is a basic waveguide aperture. We will see in the section 3 of this chapter that the basic waveguide aperture is replaced by the optimal edge taper horn N3 to obtain an optimal gain, or in the next chapter by printed microstrip patch elements for beam steering purposes.

Whatever the primary source is, the antenna access should be a standard WR15 rectangular waveguide to be compatible with the radio equipment at V-band. Therefore a transition from the antenna primary source to input waveguide is required. For the waveguide aperture source and the optimal edge taper horn, an integrated step-wise transition is implemented. Also, a novel waveguide-to-microstrip line transition is proposed in chapter 5.

3.2.2.1. Waveguide aperture (basic) with integrated transition to WR15

Figure 3-18 shows the 3D perspective and cut-view of the basic waveguide aperture with integrated transition to WR-15 waveguide. The external aperture dimensions of 6.5 mm × 5.5 mm takes into account the waveguide 1 mm wall thickness.

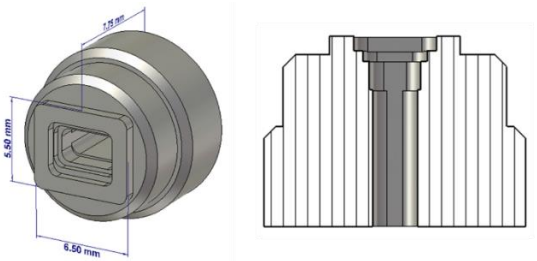

(a) (b)

Figure 3-18: Waveguide aperture with integrated transition to WR15: (a) perspective view, (b) cut-view.

This transition was optimized using *CST Microwave Studio* optimizer to minimize the reflection loss between the aperture and the WR15 waveguide input. As presented in figure 3-19, the simulated reflection coefficient is lower than -30 dB over the 57-66 GHz frequency band.

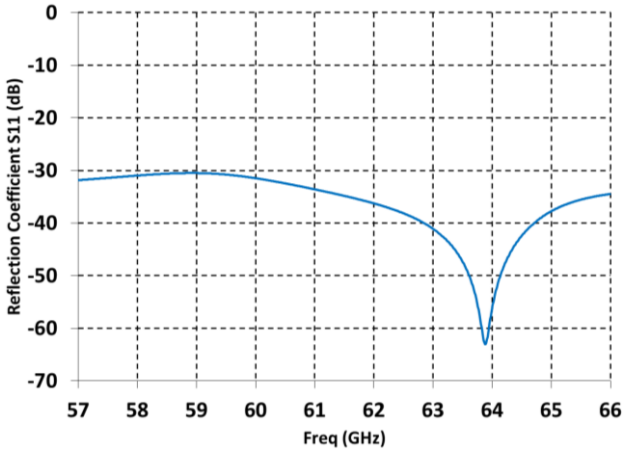

Figure 3-19: Simulation of the reflection coefficient of the waveguide aperture with integrated transition to WR15.

The radiation pattern of this source was presented previously in figure 3-7, illustrating an edge taper of only 5 dB.

3.2.2.2. Optimal edge taper horn (N3) with integrated transition to WR15

As discussed in section 2.1.1.4 of this chapter, the optimal edge taper of the designed FZP lens is 12 dB which is obtainable with a horn feed. This horn antenna (shown in figure 3-15) has an aperture of 7.2 mm × 9 mm, with a length of 10 mm until the WR15 input. The fabrication of this type of structure is complicated. In order to facilitate its realization, a step-wise transition from the horn aperture to WR15 input is implemented and presented in figure 3-20. In the rest of the document the optimal edge taper primary source will be referenced as horn N3 in order to avoid confusion with the basic waveguide aperture presented in the previous section.

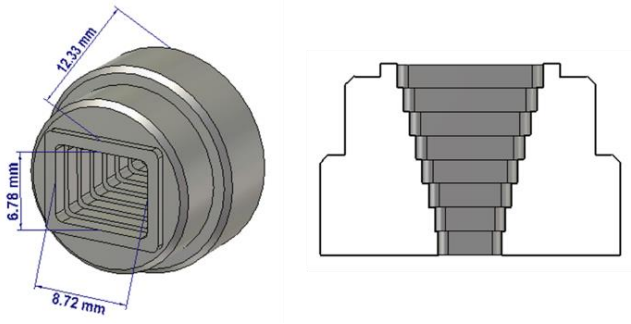

(a) (b)

Figure 3-20: Optimal Edge taper Stepped horn (N3) with integrated transition to WR15: (a) perspective view, (b) cut-view.

The reflection coefficient and normalized radiation patterns of the stepped horn are presented in figure 3-21, where the reflection coefficient is lower than -23.8 dB over the 57-66 GHz frequency band and the edge taper is around 13 dB for $\theta_{Edge} = 36.9°$.

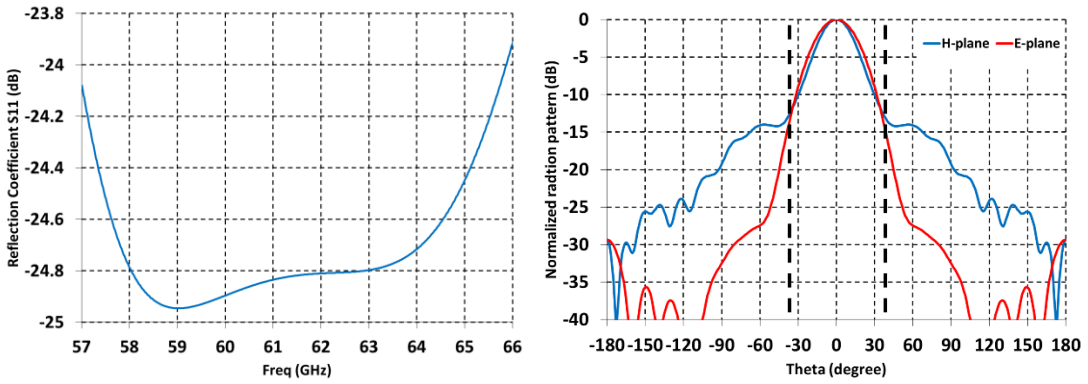

(a) (b)

Figure 3-21: Simulation results of the stepped horn: (a) reflection coefficient, (b) normalized radiation patterns.

3.2.3. Folded structure simulation and measurement

The folded structure was briefly presented in the introduction section and illustrated in figure 3-1. This structure, formed by a trans-reflector and a twist-reflector, is the key element to reduce the antenna form factor. A linearly-polarized field, with the E-field parallel to the strips of the trans-reflector, is radiated by the feed towards the trans-reflector, which reflects it back to the twist-reflector. Then, the twist-reflector reflects a 90° twisted E-field, now perpendicular to the initial incident field that will radiate through the trans-reflector. As illustrated in figure 3-1, this configuration allows tripling the electric path between the source and the FZP lens which results in a reduction of the physical focal distance by a factor of three.

In the following, the design and optimization technics of each building block of the folded structure are presented. The twist-reflector and the trans-reflector were simulated and optimized using *ANSYS HFSS*.

3.2.3.1. Trans-reflector

Also called polarizing grid, the trans-reflector is a polarization selective surface which is transparent to linear perpendicular polarized fields and reflects the linear parallel polarized fields [9]. The trans-reflector is typically made of printed parallel microstrip lines printed on a dielectric substrate with a thickness of half the guided wavelength in the dielectric ($\lambda g/2$). In order to have a maximum reflection for parallel polarized fields, and maximum transmission for perpendicular polarized fields, the width of the lines and gap between them were optimized using Floquet ports of *ANSYS HFSS*. As presented in figure 3-22, two Floquet ports with two orthogonal modes were positioned on both sides of the grid, in master-slave boundaries conditions.

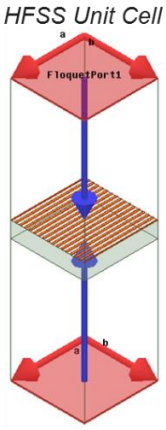

Figure 3-22: Trans-reflector unit-cell.

Figures 3-23(a) and 3-23(b) represent the simulated reflection and transmission coefficients of the optimized grid, with a strip width of $\lambda_0/40$ and a gap (side to side) of $\lambda_0/20$. The dielectric support is an Arlon AD350A substrate, with relative permittivity of 3.5, a loss tangent of 0.003 (at 10 GHz) and a thickness of 1.27 mm.

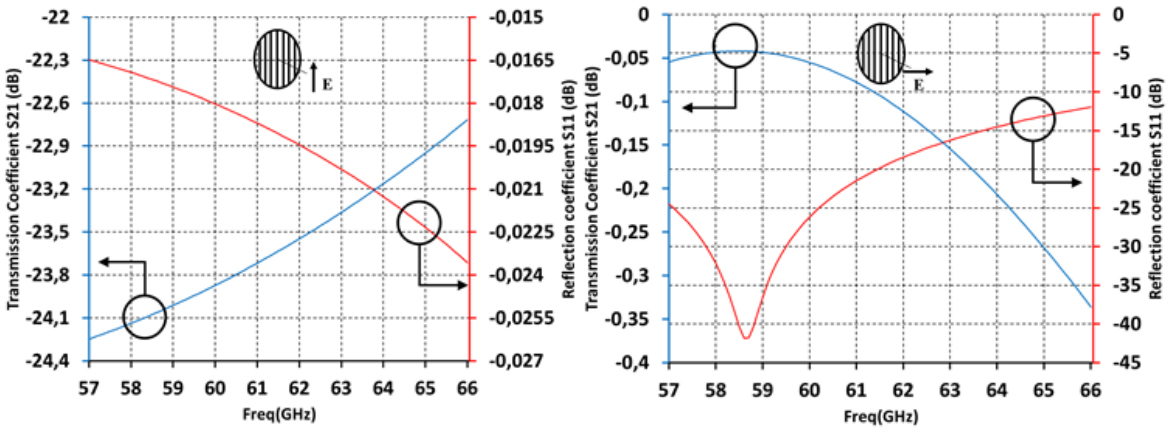

(a) (b)

Figure 3-23: Trans-reflector reflection and transmission simulated coefficients : (a) Parallel linear polarized incident wave, (b) Perpendicular linear polarized incident wave.

As shown by figure 3-23(b), maximum reflection of 0.03 dB and transmission loss of 0.33 dB for respectively parallel and perpendicular polarizations are obtained at 66 GHz, confirming the expected efficiency of the trans-reflector. Table 3-4 presents the final design parameters numerical values of the trans-reflector.

Table 3-IV: Trans-reflector design parameters.

Strips width	0.127 mm
Air gap	0.254 mm
Substrate thickness	1.27 mm
Substrate material	Arlon AD350A with $\varepsilon_r = 3.5$, $\tan\delta = 0.003$

The simulation results of the optimal trans-reflector are further verified by measuring its prototype. To do so, the trans-reflector was putted in middle of two 60 GHz horns and their transmission coefficient was measured. Figure 3-24 presents this measurement results compared to their simulation values for parallel and perpendicular incidents towards the trans-reflector strips. As expected, the transmission loss for a parallel incident is around 24 dB and for perpendicular incident is well around 0.1 dB, with variations due to the environment of the measurements.

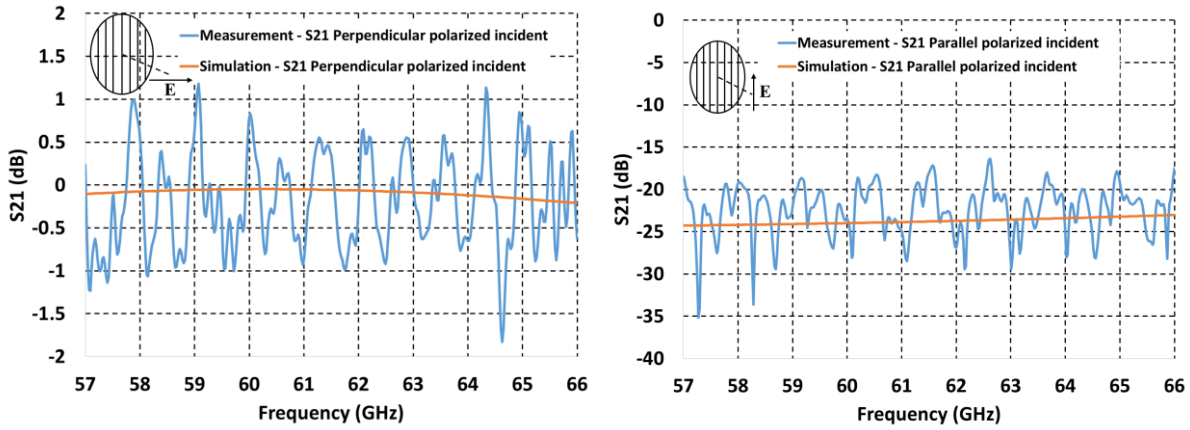

(a) (b)

Figure 3-24: Trans-reflector measured transmission coefficient compared with simulation : (a) perpendicular incident, and (b) parallel incident.

3.2.3.2. Twist-reflector

The twist-reflector typically consists of parallel microstrip lines oriented at 45° related to the incident field polarization, and printed on a grounded dielectric substrate with a thickness of $\lambda g/4$ [10]. There exists also other types of twist-reflector where meander lines are used instead of continuous lines for bandwidth increasing purposes [11]. The incident field is decomposed to two orthogonal components parallel and perpendicular to the microstrip lines. The parallel component is reflected directly by the microstrip lines, while the perpendicular one passes through the dielectric substrate and is reflected by its metallic ground plane with 180° phase shift. The addition of these two reflected components gives a field rotated by 90° compared to

the primary incident field. Figure 3-25 illustrates the twist-reflection functionality. The width of the microstrip lines and their spacing were optimized using Floquet ports of *ANSYS HFSS* where a Floquet port with two orthogonal modes is positioned on top of the strips.

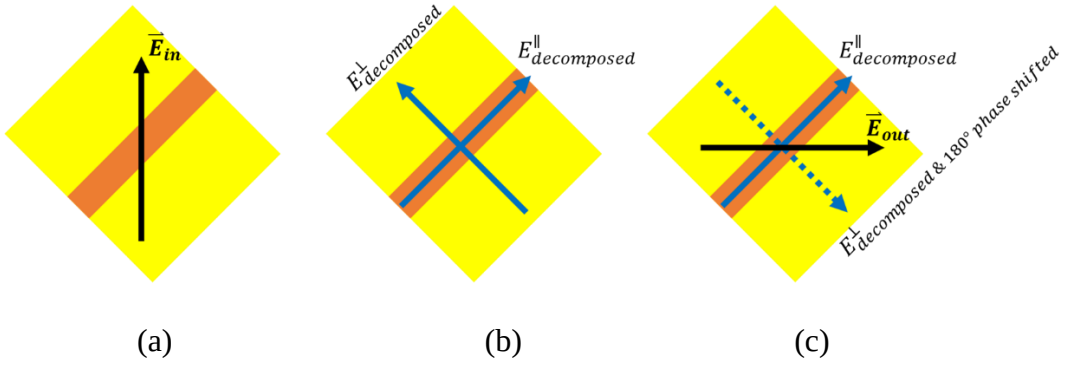

(a) (b) (c)

Figure 3-25: Twist-reflector functionality based on vector field decomposition: (a) Incident wave, (b) decomposition of incident wave into parallel and perpendicular components, and (c) Compostion of the parallel component reflected directly and perpendicular component reflected with 180° phase shift resulting in the reflected wave with 90° polarization twist.

Figure 3-26 presents the mode transmission coefficients of the optimized grid with a width of $0.1\lambda_0$ and a gap of $0.3\lambda_0$. The optimization goal is to reach a minimum transmission loss between the two orthogonal modes (S_{11}/S_{12}) and maximum transmission loss between the same modes (S_{11}/S_{11}). The substrate dielectric is Rogers RO4003C with relative permittivity of 3.66, a loss tangent of 0.004 (at 10 GHz) and a thickness of 0.762 mm. As illustrated the transmission loss between two orthogonal modes is less than 0.35 dB.

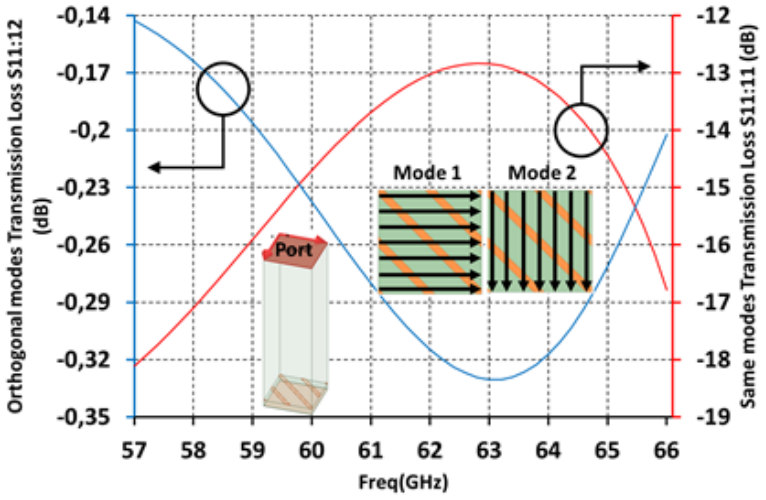

Figure 3-26: Twist-reflector modal simulated transmission coefficients. The HFSS unit-cell, the Floquet port, and the two orthogonal modes are shown in the inset.

Table 3-5 presents the final design parameters of the twist-reflector.

Table 3-V: Twist-reflector design parameters.

Strips width	0.45 mm
Air gap	1.7 mm
Substrate thickness	0.762 mm
Substrate material	Rogers RO4350B with $\varepsilon_r = 3.66$, $\tan\delta = 0.004$

In order to verify the Twist-reflector functionality by measurements, the transmission coefficient between the folded structure (Waveguide horn + Trans-reflector + Twist-reflector) and a 60 GHz horn antenna is measured. The waveguide horn exciting the folded structure and the receiving horn are in crossed polarizations, so if the folded structure is working properly, the transmission loss should be close to 0 dB. Figure 3-27 shows this measured transmission coefficient which is around -2 dB. Taking into account the Trans-reflector measured transmission loss (see figure 3-24) which is around 0.1 dB, the ideal case would be to have a transmission loss around –0.45 dB for the folded structure, but as the exciting waveguide and the receiving horn are not identical, part of the 2 dB measured loss might be because of this fact. But still comparing the measurement of the folded structure and simulation of the Twist-reflector (figures 3-27 and S11:12 of figure 3-26 respectively), a similar behavior of increased transmission loss around 62 GHz frequency can be observed.

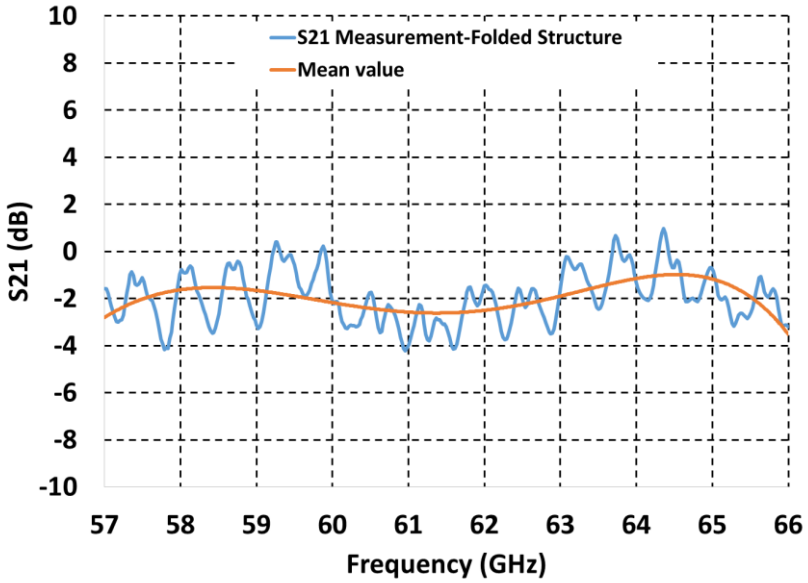

Figure 3-27: Twist-reflector measured transmission coefficients.

3.2.4. Conclusions on FFZP building blocks

The design and optimization methods of different building blocks of the Folded Fresnel Zone Plate (FFZP) were detailed in previous sections. This structure benefits from compact form factor and low cost manufacturing. In the following section of this chapter the complete FFZP antenna simulation results are presented. In this chapter only fix antennas (no beam steering) excited using the basic waveguide aperture and also the optimal edge taper horn (N3) are presented. For the later, an inversed FZP lens is used so it can act as a radome as well. For each case, the simulation results are compared with measurement results.

3.3.FFZP excited by basic waveguide aperture: simulation & measurement results

3.3.1. Antenna structure characteristics

In this sections, the simulation and measurements results for the FFZP antenna excited by the basic waveguide aperture are presented. As a reminder, main parameters of the simulated FFZP antenna are:

- FZP lens :
  - Diameter D = 124 mm
  - Focal distance F = 84 mm
    - In folded structure F' = 28 mm
  - F/D=0.67
    - In folded structure $F'/D=0.22$
  - 4 sub-zones → max phase error: π/2 → Quarter-wavelength Fresnel
  - Material: Poly Methyl Methacrylate(PMMA) with $\varepsilon_r = 2.53$
  - Base dielectric thickness t_b = 1.5 mm
  - FZP lens overall thickness t = 7.85 mm
  - Edge illumination angle θ_{Edge}= 36.9°
- Primary feed :
  - Waveguide aperture of 4.5mm×3.5mm
- Trans-reflector :
  - Strips: Width = 0.127 mm, gap = 0.254 mm
  - Substrate: $\varepsilon_r = 3.5$, thickness: $\lambda_g/2 \approx 1.27$ mm
- Twist-reflector :
  - Strips: Width = 0.45mm, gap = 1.7mm
  - Substrate: $\varepsilon_r = 3.55$, thickness: $\lambda_g/4 \approx 0.762$ mm

It should be noted that for the prototype, for technical reasons (lower cost), it was decided to realize the Fresnel lens with Poly Methyl Methacrylate (PMMA) instead of Polypropylene (PP). Therefore all the results, simulation as well as measurements, are with the Fresnel lens made with PMMA. The design parameters (sub-zones and zones radius and corrugation thickness) of the lens with PMMA are different form the lens with PP because of their different ε_r.

3.3.2. FFZP prototype structure

Before presenting the FFZP antenna structure simulation results, the prototype structure is presented, as it will be used in simulation to ensure an accurate comparison with measurement.

The antenna prototype structure was designed with the objective to assure measurement quality and reproducibility, and maintain the antenna robustness. As presented in figures 3-1 and 3-28, a metallic cylinder with integrated feed transition is used as the antenna support. In-house 3D printed plastic pins are used to fix the trans-reflector and twist-reflector substrates on metallic cylinder. The FZP lens is realized with extended leg so it can be positioned properly on the cylinder. A layer of 5 mm thickness carbonated foam absorber is pasted inside the cylinder to block perturbing field reflections inside the antenna structure.

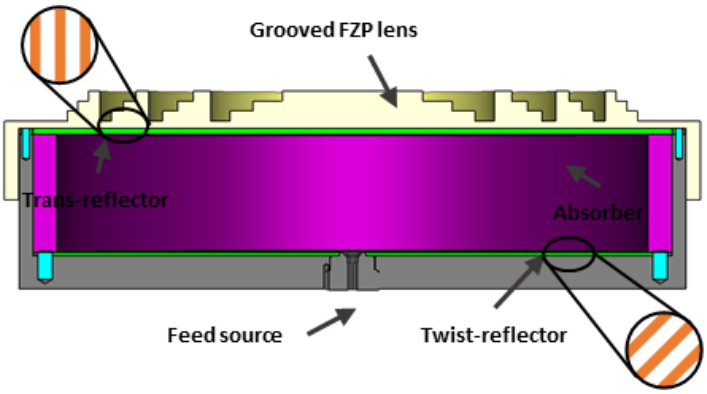

(a)

(b)

Figure 3-28: FFZP antenna fed by basic waveguide aperture (a) 3D schematic cut-view, and (b) prototype photos.

The total thickness of the antenna structure including the waveguide transition is $9\lambda_0$, and its diameter is $24.8\lambda_0$. The distance between the waveguide aperture and the bottom side of the FZP lens is $5.6\lambda_0$ which is three times smaller than the non-folded FZP lens focal distance of $16.8\lambda_0$.

3.3.3. Simulation and measurement results

The complete antenna structure was simulated using *CST Microwave Studio* Time domain solver, and the results are validated by measurements.

Figure 3-29 represents the superimposed calculated and measured reflection loss of the overall antenna. The measured S_{11} is better than -18.7 dB for the frequency range of 57-66 GHz and fits well the simulation results.

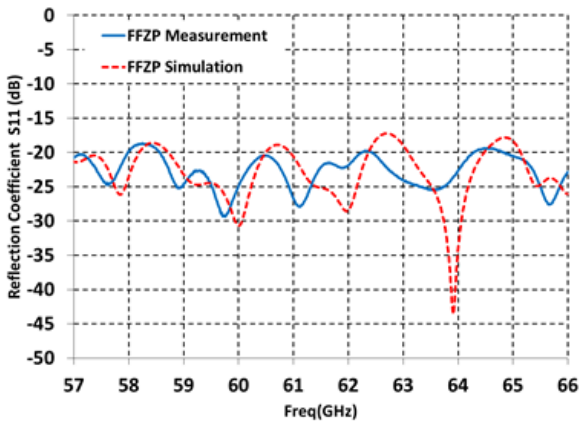

Figure 3-29: Measured and simulated reflection coefficient S11 of the compact folded FZP lens antenna.

The simulated and measured normalized radiation patterns of the complete antenna are plotted in figure 3-30 at 57, 60 and 66 GHz on co-polarization and cross-polarization. The ETSI V-band class 2 RPE is also provided to verify the antenna compliance. As it can be seen, the antenna is completely compliant with ETSI V-band class 2 RPE [1]. By comparing the first side lobe level of simulated and measured radiation patterns at the three frequencies, we can see that at 57 GHz the measured SLL is lower and in contrary, at 60 and 66 GHz, the simulated SLL are lower than measurements. This indicates a slight downwards frequency shift of the prototype. Also, relatively high SLL of measured and simulated patterns at 66 GHz shows the limited bandwidth of the FZP lens.

An important point to consider is that even if the physical distance between the feed and the grooved FZP is reduced by a factor of three in the folded structure, the illumination angle remains the same as the non-folded grooved FZP which is 36.9°. The measured Half Power Beam Width (HPBW) of the antenna is 3° in E-plane and 2.9° in H-plane at 60 GHz. Measured side lobe levels are less than -20 dB and the measured cross-polarization discrimination (*XPD*) is below -35 dB.

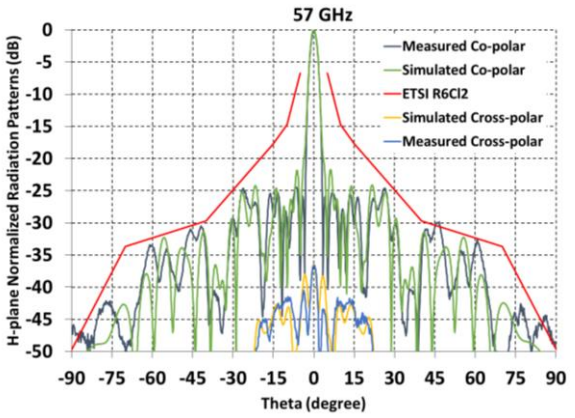

(a)

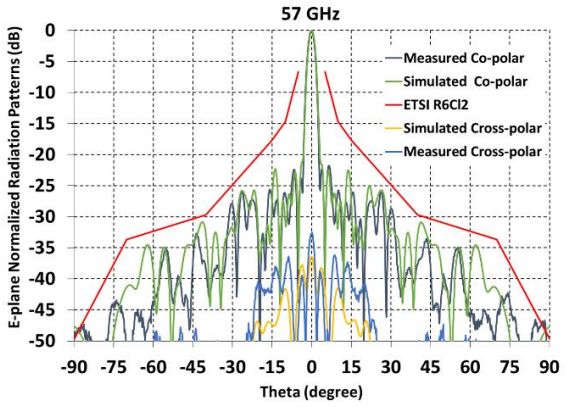

(b)

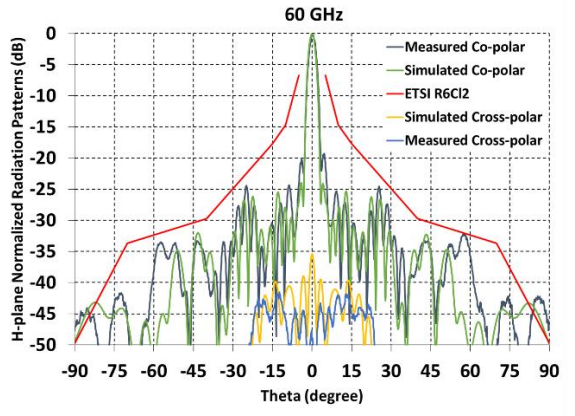

(c)

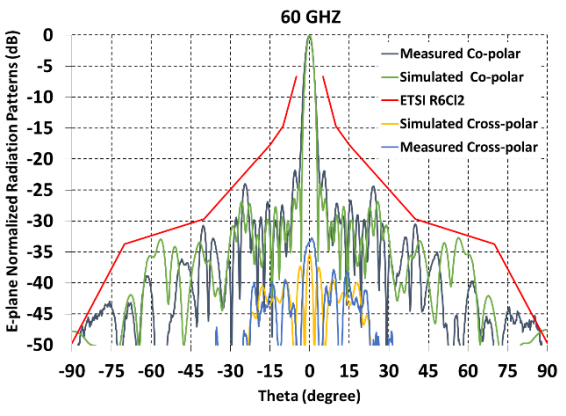

(d)

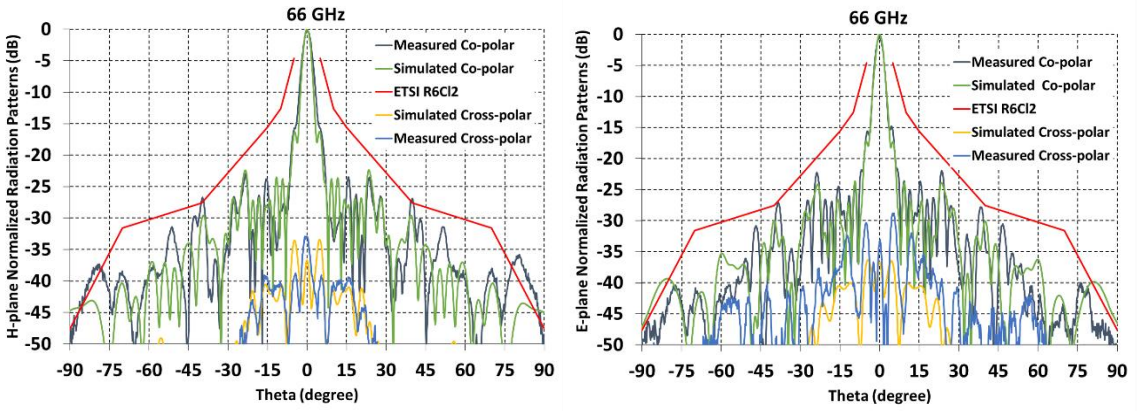

(e) (f)

Figure 3-30: Normalized simulated and measured antenna radiation patterns of the compact folded FZP lens antenna. (a) 57GHz H-plane, (b) 57 GHz E-plane, (c) 60 GHz H-plane, (c) 60 GHz E-plane, (e) 66 GHz H-plane, (f) 66 GHz E-plane.

In order to evaluate the Fresnel lens performance, independent from the folded structure (Trans & Twist reflectors), the non-folded FZP lens (Fresnel lens alone) was measured. For this a new cylindrical metallic box was realized to ensure the 84 mm focal distance between the lens and waveguide feed. Figure 3-31 presents the comparison between Fresnel lens alone and the folded FZP lens (FFZP) E-plane measured radiation patterns at 57 GHz, 60 GHz and 66 GHz. It's interesting that at 57 GHz the radiation pattern of lens alone is not as good as FFZP in terms of focalization and SLL. This can confirm that the downwards frequency shift is because of the folded structure. At other frequencies the radiation patterns are coherent.

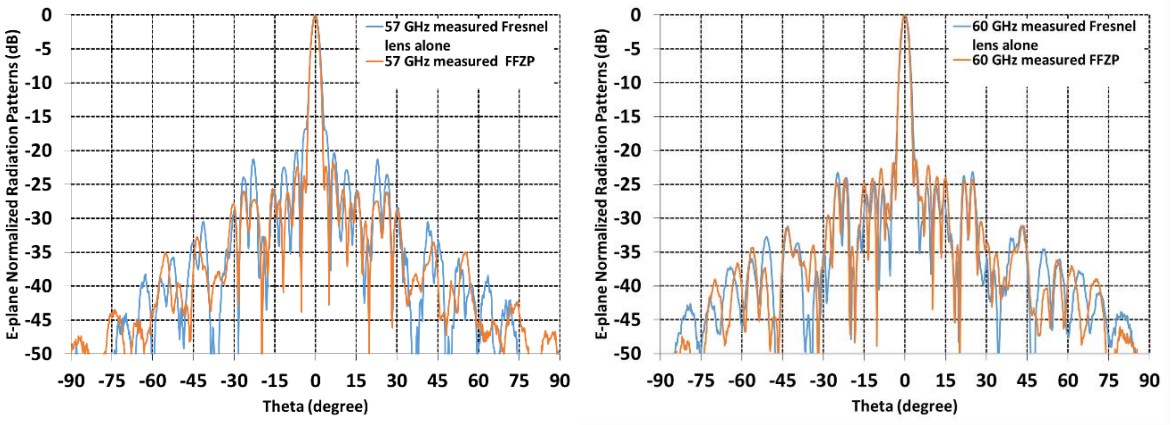

(a) (b)

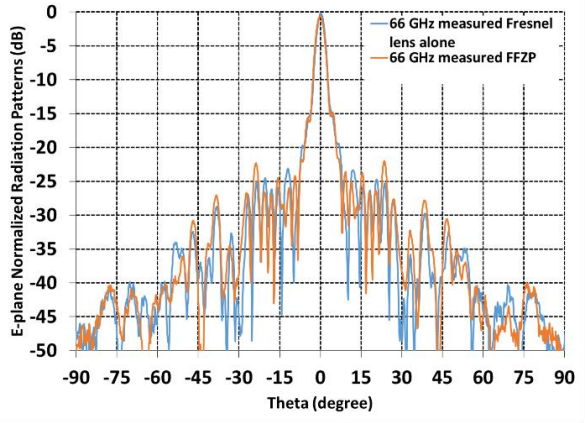

(c)

Figure 3-31: Normalized measured and simulated antenna radiation patterns of the non-folded FZP lens and folded FZP lens antennas: (a) at 57 GHz, (b) at 60 GHz, and (c) at 66 GHz.

Figure 3-32 shows the comparison of isotropic gain variation over frequency for measured non-folded FZP lens (Fresnel lens alone) and folded FZP lens (FFZP). For this one, it can be observed that for higher frequencies the gain shoot is almost 1 dB more than for Fresnel lens alone. Also the gain variation is more stable over the frequency band for Fresnel lens alone (2 dB for non-folded FZP and 3 dB for folded FZP).

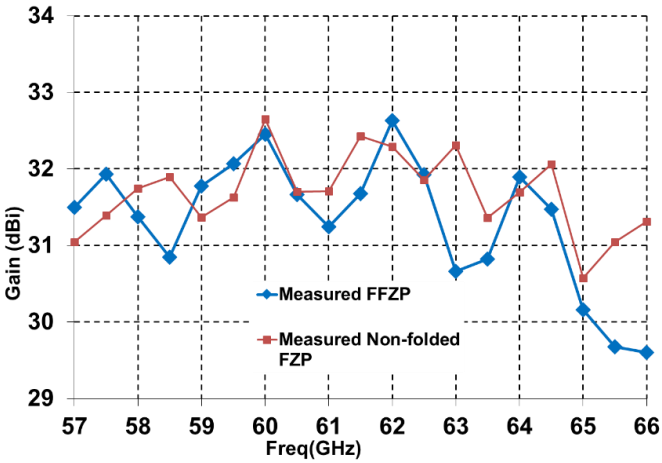

Figure 3-32: Measured gain variation over frequency comparison between non-folded and folded FZP lens.

Figure 3-33 represents the evolution of the simulated and measured isotropic gains and the radiation efficiency over the frequency band of interest for the FFZP antenna. The gain difference between measured and simulated FFZP may be explained by fabrication and alignment inaccuracies (Trans-reflector, Twist-reflector) and possibly under-estimated material loss. The antenna has a maximum measured isotropic gain of 32.7 dBi, with a maximum peak-to-peak variation of 1.5 dB in 57-64 GHz frequency range. As presented in figure 3-33, the simulated gain difference between FFZP and non-folded FZP is rather small. There is a 2 dB gain drop after 64 GHz for measured FFZP, 1.6 dB for simulated FFZP and 1 dB for simulated non-folded FZP. The common gain drop is mainly due to Fresnel lens limited bandwidth and the 0.6 dB gain drop delta between FFZP and non-folded FZP can be explained by the trans-reflector transmission loss increase after 64 GHz (see figure 3-23(b)). The antenna has a maximum radiation efficiency of 52.8% at 62 GHz and a minimum of 33.6% at 65 GHz.

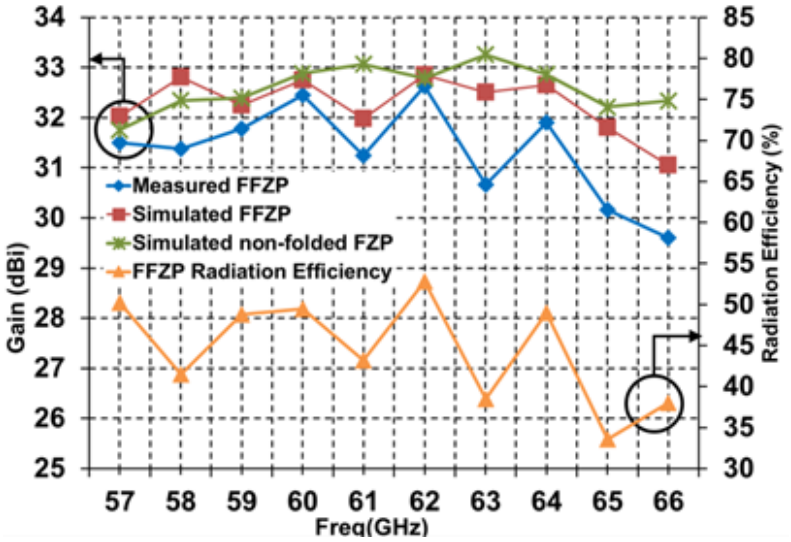

Figure 3-33: Variation of the measured and simulated FFZP gains, simulated non-folded FZP gain and FFZP radiation efficiency as a function of frequency.

3.3.4. Conclusions on FFZP excited by basic waveguide aperture

A new compact folded grooved FZP lens antenna excited by the basic waveguide aperture was presented. The proposed antenna has a maximum measured gain of 32.7 dBi, a 1.5 dB gain variation over the 57-64 GHz V-band and is compliant with ETSI standard [12] for point-to-point communications. The measured reflection coefficient of the antenna remains below -18.7 dB. The measured *XPD* is below -35 dB and the side lobe levels are below -20 dB. The antenna has approximately a diameter of $24\lambda_0$ and a total depth of $9\lambda_0$, offering a *F/D* of 0.22, which makes the antenna low profile, compatible with the growing market pressure of minimizing the visual impact of antennas in urban areas.

In the following section the optimized version of the presented FFZP antenna solution is discussed.

3.4. Radom integrated FFZP excited by optimal edge taper horn: simulation & measurement results

In the previous section, the basic Folded Fresnel Zone Plate (FFZP) antenna solution excited by the basic waveguide aperture was presented and validated by measurements. In this section, the FFZP antenna is optimized in terms of gain, bandwidth and form factor. To do so, following modifications are applied:

- The FZP is used inversely so it can be used as radome as well → radome integrated antenna → reduced form factor
- Optimized Twist-reflector → gain improvement
- The FZP lens material is changed to Polypropylene (PP) → hiding the antenna building blocks from external eyes
- The basic waveguide aperture primary source is replaced by the optimal edge taper stepped horn (N3) → gain improvement

3.4.1. Inversed Fresnel Concept verification

Firstly, the impact of inversing the Fresnel lens is shown by measurements. To do so, the FZP lens used for the prototype presented in figure 3-26 is inversed. Figure 3-34 shows the comparison between radiation patterns of the FZP lens with inversed and not-inversed Fresnel lens at 57 and 64 GHz. As shown, there are risen side lobes for $|\theta| > 30°$ ° which are mainly because of the extended legs of the inversed Fresnel which in this configuration (see inset of figure 3-34) are radiant and not covered by the cylindrical structure absorber. Other observation regarding the side lobe levels is that they are lower for the antenna with inversed Fresnel lens for $-30° < \theta < 30°$.

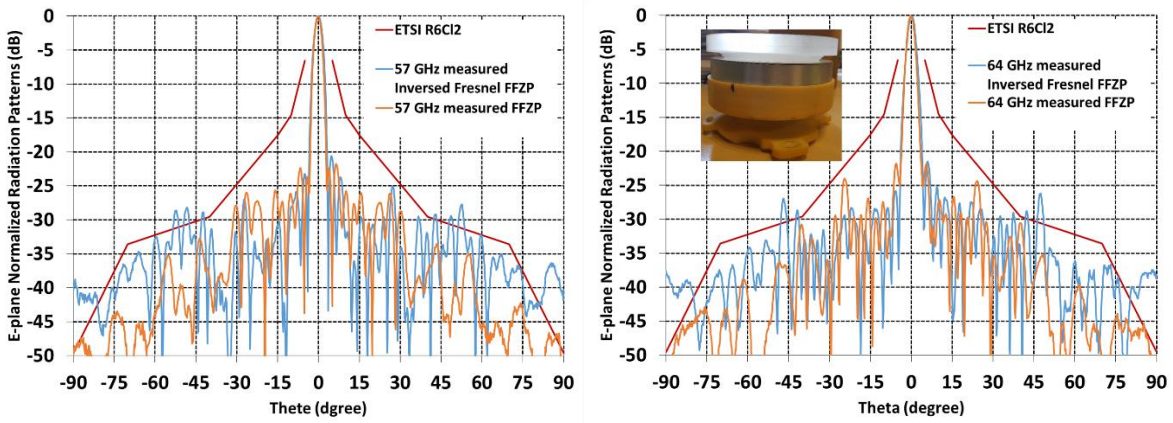

Figure 3-34: E-plane normalized measured radiation patterns of the FFZP antenna for Inversed and non-inversed FZP lens.

The HPBW for the FFZP antenna with inversed Fresnel is slightly higher (+0.2°) comparing to the basic FFZP antenna. This illustrates the gain losses caused by the increased side lobe levels.

Figure 3-35 shows the return loss comparison between the basic FFZP and inversed Fresnel FFZP antennas. As can be seen the fact of inversing the Fresnel lens doesn't have any major negative impact on the antenna returns loss and its remains well adapted with a minimum return loss of 18 dB.

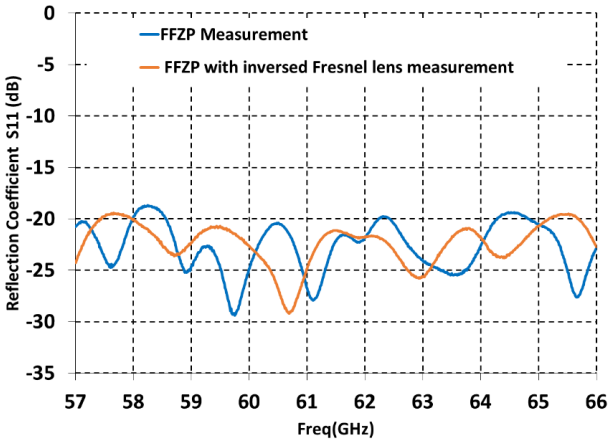

Figure 3-35: Reflection coefficient comparison between inversed Fresnel and non-inversed Fresnel FFZP antennas.

To conclude, the concept of using an inversed Fresnel lens in the FFZP antenna solution is verified. The main goal is to use the inversed Fresnel as a radome simultaneously to its functionality as the phase correcting aperture. This will reduce the final antenna system form factor as well as its cost.

3.4.2. Twist-reflector optimization

Other modification done for this prototype is the optimization of the twist-reflector. As presented in figure 3-26, the primary designed twist-reflector has a transmission loss of 0.32 dB at 63 GHz. In order to balance the twist-reflector performance over the frequency band and reduce its transmission loss, it was redesigned using the same substrate, Rogers 4350B with relative permittivity of 3.66, a loss tangent of 0.004 and thickness of 0.762 mm. Figure 3-36 presents the mode transmission coefficients of the optimized grid with a width of 0.4 mm and a gap of 1.78 mm. The optimization goal is to reach a minimum transmission loss between the two orthogonal modes (S11:12) and maximum transmission loss between the same modes (S11:11). As shown, the optimized twist-reflector offers a maximum transmission loss (between two orthogonal modes) of only 0.18 dB.

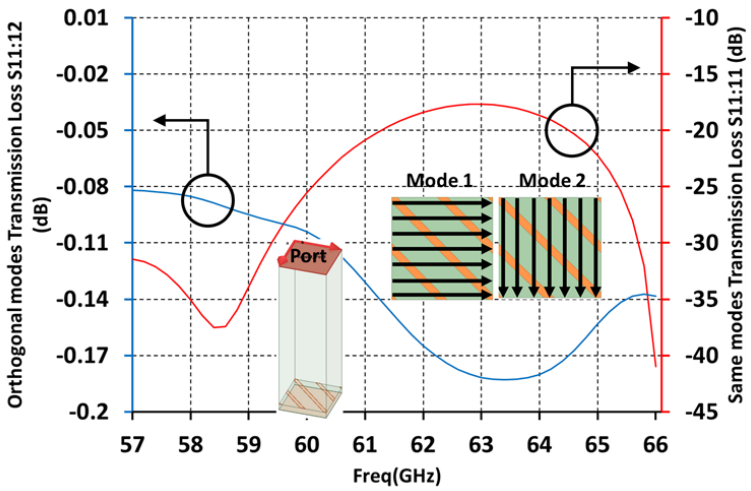

Figure 3-36: Optimized Twist-reflector modal transmission coefficients. The HFSS unit-cell, the Floquet port, and the two orthogonal modes are shown in the inset.

Table 3-6 presents the final design parameters of the optimized twist-reflector.

Table 3-VI: Optimized twist-reflector design parameters.

Strips width	0.4 mm
Air gap	1.78 mm
Substrate thickness	0.762 mm
Substrate material	Rogers RO4350B with $\varepsilon_r = 3.66$, $\tan\delta = 0.004$

3.4.3. Fresnel lens material change (from PMMA to PP)

All the parametric studies on Fresnel Zone Plate (FZP) lens were done using a FZP lens made of Polypropylene (PP). But for the first prototype it was decided realized the FZP lens with Poly Methyl Methacrylate (PMMA). The reason for this choice was the lower cost of PMMA comparing to PP. The 3D simulated structures (cut-view and full-view) of these two antennas is presented in figure 3-37. As the two structures are identical in shape, only one of the antennas is presented in the figure. To accelerate the simulation time, the antennas are simulated without mechanical structure of the prototype and the waveguide aperture is excited without transition to WR15.

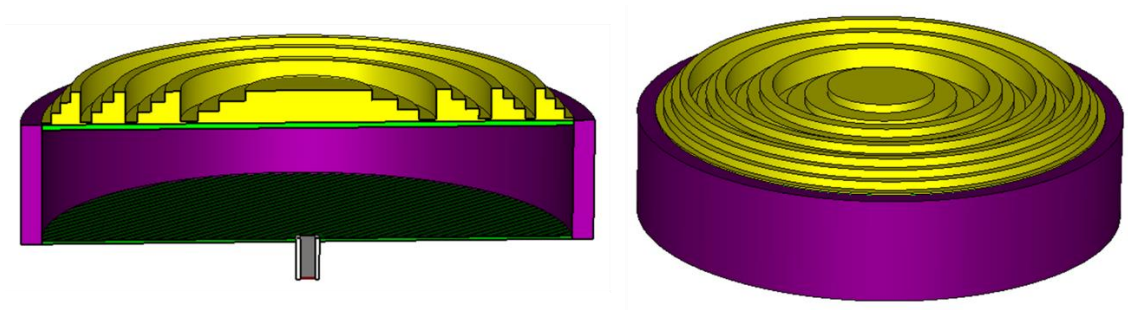

Figure 3-37: FFZP antenna simulation 3D structure with the lens (made of PP or PMMA).

Both antennas FZP lenses have the same number of zones and sub-zones, and the folded structure (Trans and Twist reflectors) is the same for both antennas. The FZP lens made of PP has a diameter of 124.74 mm and the FZP lens made of PMMA has a diameter of 124.16 mm and they both have a focal of 84 mm, meaning they have almost the same *F/D*. The two antennas are excited using identic basic waveguide apertures as presented in previous section.

Figure 3-38 compares the gain variation simulations of two FFZP antennas where their FZP lens is made of PP and PMMA. As can be seen there is no relevant difference between the two antenna gain performances.

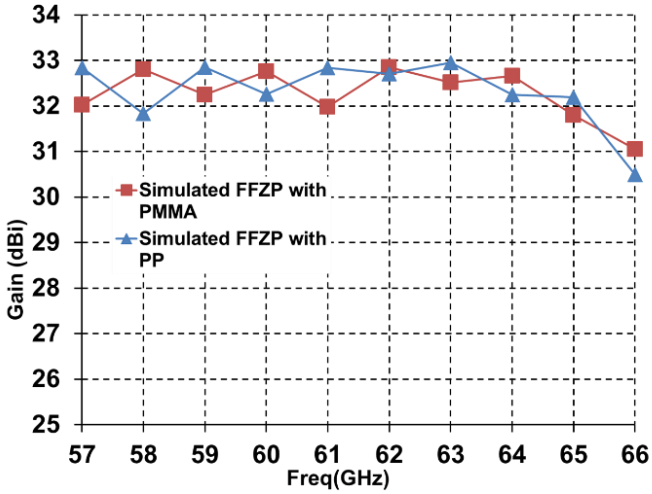

Figure 3-38: Comparison of gain variation over frequency for FFZP antenna with their lens made of PMMA and PP.

In terms of return loss, the minimum for FFZP made of PMMA is 14.3 dB and for the FFZP made of PP is 14.3 dB, meaning both are well adapted. This observation can be concluded from simulated reflection coefficients presented in figure 3-39.

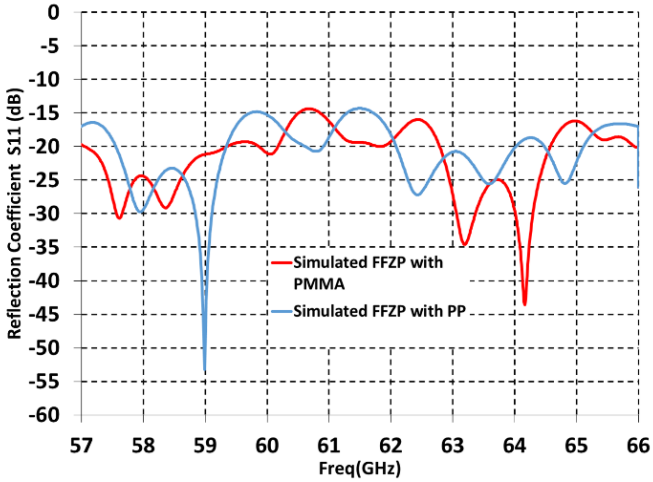

Figure 3-39: Comparison of reflection coefficients for FFZP antenna with their lens made of PMMA and PP.

The radiation patterns of these two antenna are also similar as it could be expected. However, PP is not a transparent material as PMMA and can hide the antenna building blocks from external eyes. Therefore, for this optimized prototype an inversed FZP lens made of PP is used.

3.4.4. Optimal edge taper primary source (N3)

The inversed FZP lens made of PP is excited by the primary source with an optimal edge taper. As discussed earlier, the optimal edge taper for our FZP lens is 13 dB and this can be obtained using a stepped horn previously introduced as horn N3 in section 2.2.2 of this chapter. The radiation pattern of this primary source was presented in figure 3-21. The photo of the manufactured prototype of this primary source is presented in figure 3-40.

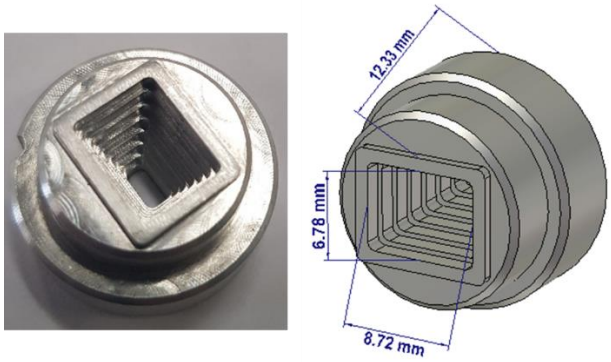

(a) (b)

Figure 3-40: Stepped horn (N3) : (a) Photo of manufactured prototype, and (b) 3D schematic.

3.4.5. Final Optimal solution

Different optimization elements applied to the primary FFZP antenna prototype were presented. These four modifications are:

- Inversing the Fresnel lens → Radome integrated antenna
- Optimizing the twist-reflector → Gain improvement
- Fresnel lens material change from PMMA to PP → Visual protection
- Using more directive primary source with optimal edge taper (N3) → Gain improvement

The above modifications resulted in an optimal antenna solution for fixed point-to-point communications. As presented in figure 3-41, the inversed FZP lens acts as a radome. Its physical dimension are similar to the previous prototype, meaning it has an overall diameter of 146 mm with a total height (primary source included) of 47.4 mm. It should be noted the lens radiating diameter is 124 mm and its physical focal distance in the folded structure is 84/3=28 mm which offers a *F/D* of 0.22.

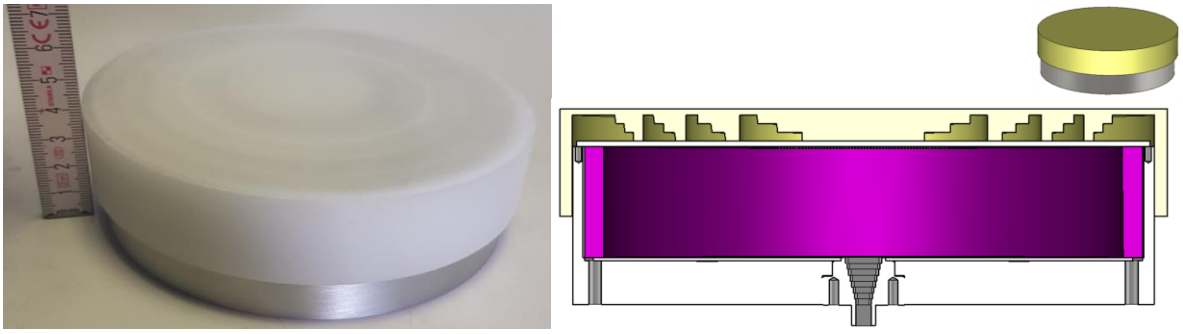

(a) (b)

Figure 3-41: Integrated FFZP antenna prototype: (a) photo of Radome, (b) 3D simulation schematic.

Figure 3-42 compares the reflection coefficient of the measured prototype and its simulation. A slight downwards frequency shift (0.3 GHz) can be observed in the measurement results, which might be due to FZP lens material and its dielectric constant deviation comparing to its datasheet nominal value. Comparing this antenna return loss with the previous prototype, we

can observe a lower return loss. There we had a minimum return loss around 18 dB and here it's around 10 dB. This is because in the first prototype a basic primary source with smaller aperture was used comparing to the stepped horn N3 used here. Larger aperture of the primary source results in more direct returned energy reflected from the trans-reflector into the primary source. This can be reduced by considering a small shadow zone in the center of the trans-reflector, without printed strips to avoid direct reflections into the feed.

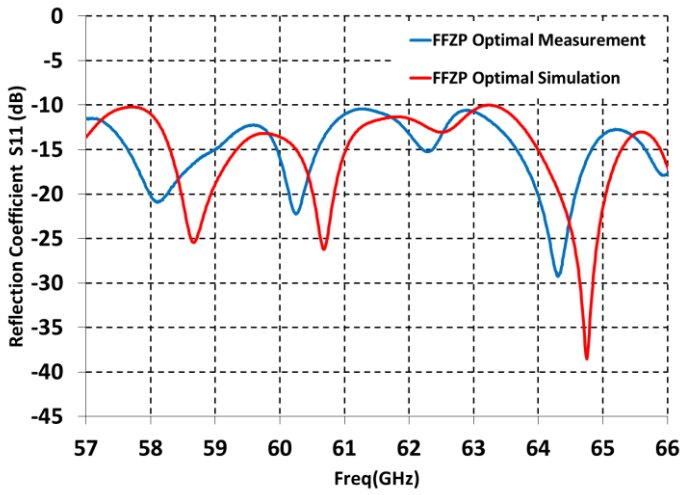

Figure 3-42: Measured and simulated reflection coefficient S11 of the radome integrated FFZP lens antenna.

The gain variation over frequency of this prototype is presented in figure 3-43. Minimum measured gain of this antenna is 31 dBi, 2 dB higher than the previous prototype. Maximum measured gain is 33.5 dBi at 61.5 GHz which is 1 dB higher than the previous prototype. The measured gain variation over the V-band (57-66 GHz) is 2.3 dB which is a little bit high, mainly because of the gain drop at 60 GHz, but it remains relatively acceptable as is less than 3 dB. Comparing with simulated gain variation, we can observe slight upwards shift. Also the maximum simulated gain is 34 dBi at 65 GHz which is slightly higher than maximum measured gain and this is because of underestimated material loss at mm-waves.

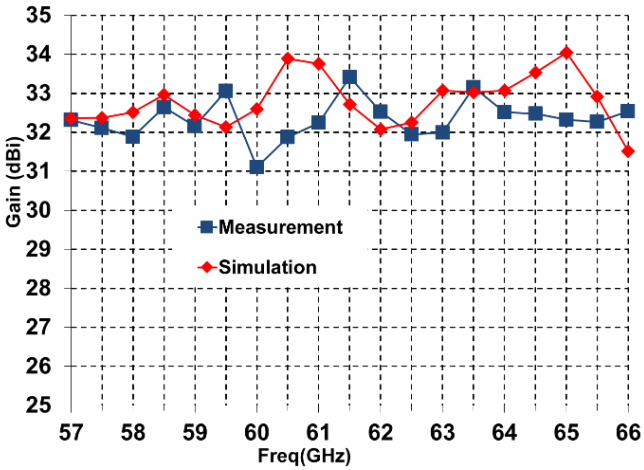

Figure 3-43: Variation of the measured and simulated gains of the radome integrated FFZP as a function of frequency.

Another phenomenon that can be observed in both measured and simulated gain variations over frequency presented in figure 3-43, is the sudden gain drops in middle of the frequency bands namely around 60 GHz and 62 GHz frequencies. In Figure 3-44, the simulated gain variations over frequency for different physical focal distances are presented. These important gain variations in function of the focal distance demonstrate the FZP lens limited bandwidth. As can be seen, by increasing the focal distance the middle frequency gain drops (or sudden picks) shift towards lower frequencies. The reason of this sudden drops (or picks), which were also present for the FFZP antenna with basic waveguide aperture feed (presented in section 3) are related to the folded structure, as this phenomenon is absent for non-folded FZP lens (see figure 3-33). In fact, the resonance nature of the trans-reflector and twist-reflector of the folded structure are causing this impact.

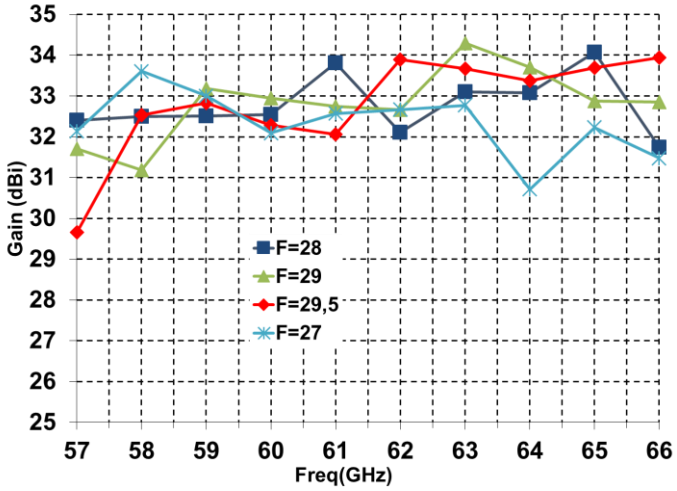

Figure 3-44: Simulated gain variation over frequency of the radome integrated FFZP antenna for different physical focal distances (mm).

The simulated and measured patterns of the radome integrated FFZP antenna at 57, 60 and 66 GHz frequencies are presented in figure 3-45. As presented in measured patterns, we can observe some increased side lobes for $|\theta| > 50°$ in lower and central side of frequency band (57 and 60 GHz) which are not compliant with ETSI RPE. It should be noted that the ETSI RPE is normalized taking into account the measured gain at the corresponding frequency. The reason for this increased slide lobe levels is the antenna prototype structure. As can be seen in the cut view presented in figure 3-41, there is a gap between the external side of the trans-reflector and the internal side of the inversed FZP lens and the absorber cannot cover the gap and block the radiation leakage from the lens extended legs of the FZP lens.

Moreover, comparing the simulated and measured radiation patterns presented in figure 3-45, we can observe that there is a good agreement for $|\theta| > 15°$ but there is some discrepancy in first side lobes levels. The reason for this is maybe because of the frequency shift observed in the antenna return loss (see in Figure 3-42), which might be due also to the FZP lens material characteristics discrepancy in mm-waves comparing to datasheet and simulations, especially dielectric constant.

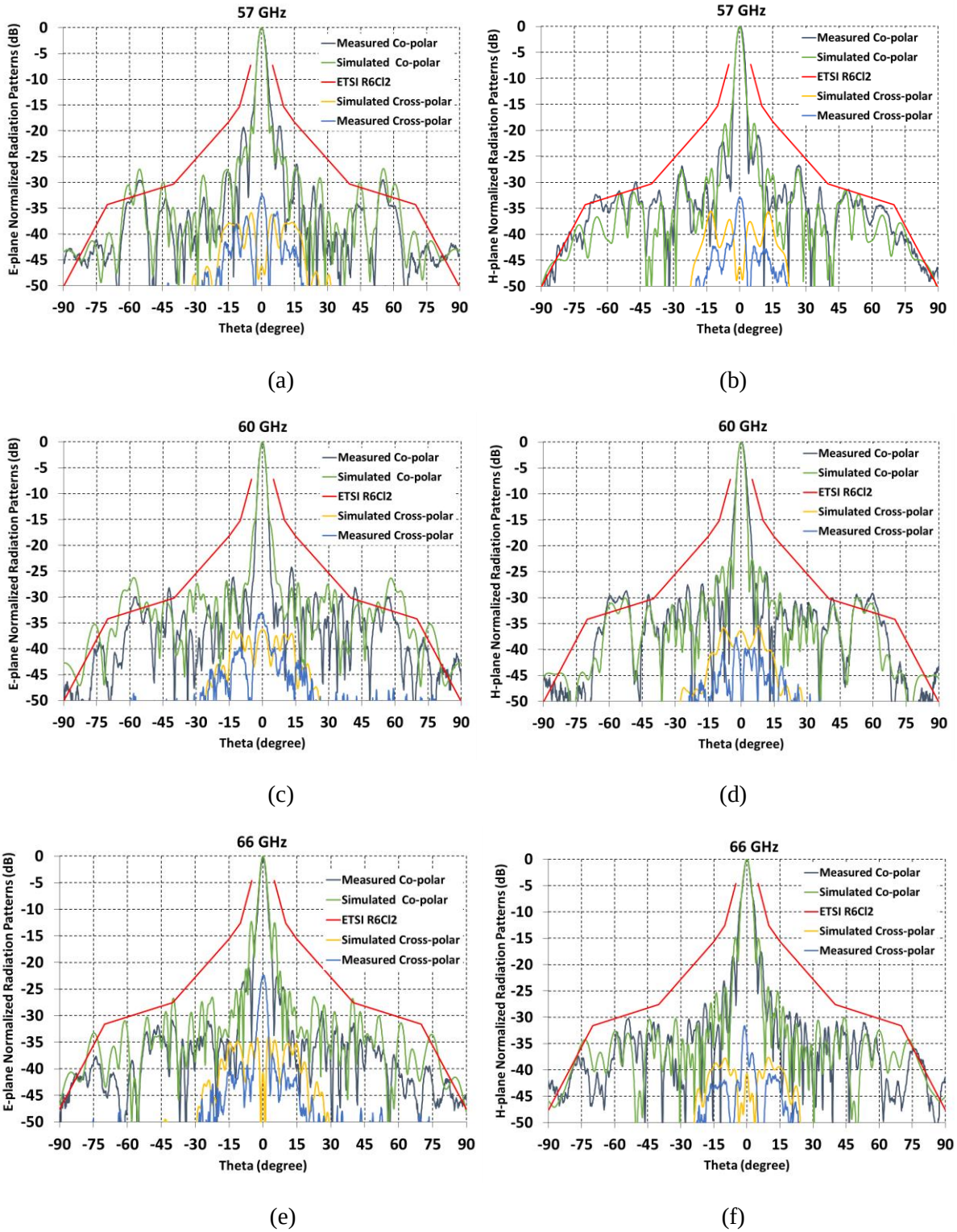

Figure 3-45: Normalized simulated and measured radiation patterns of the radome integrated FFZP antenna (a) 57 GHz E-plane, (b) 57 GHz H-plane, (c) 60 GHz E-plane, (d) 60 GHz H-plane, (e) 66 GHz E-plane, and (f) 66GHz H-plane.

The measured cross-polarization discrimination (*XP*D) of the radome integrated FFZP is mainly around -32 dB, which is 3 dB lower comparing to the previous FFZP antenna prototype where a feed with smaller aperture was used.

The measured HPBW of this antenna is 2.6° in H-plane and 2.8° in E-plane at 61 GHz, which is around 0.3° lower than the basic FFZP. This confirms the higher gain of the radome integrated FFZP antenna where a primary source with optimal edge taper is used.

3.4.6. Conclusions

The simulation and measurement results of the radome integrated FFZP antenna were presented in this section. In addition of using an inversed FZP lens with purpose of functioning as a radome integrated lens, the primary source was also optimized to offer optimal illumination edge taper. As presented, this antenna offers wide bandwidth of 18 % for 2.3 dB gain variation with maximum gain of 34 dBi. The antennas radiation patterns are compliant with ETSI RPE with some minor expectations because of the prototype structure which can be easily corrected by modifying its mechanical structure. The antenna is well matched with S11<-10 dB over the 57-66 GHz frequency band. Comparing to the basic FFZP presented in section 3, where the matching level was -18 dB, the reflection coefficient is less than -10 dB because of the wider aperture of the primary source used for this prototype.

Overall, this antenna offers good RF performances, specially radiation patterns compliant with ETSI, high gain, and large bandwidth as well a low form factor thanks to the folded structure and the radome integrated functionality of the inversed FZP lens. This low cost solution is a good candidate for mm-waves PtP links. Its only limitation is the fact of being only single polarization, depending on the application. However this is addressed in chapter 6 and an ultra-low cost solution is proposed to offer dual-polarization functionality for the FZP lens with similar compact form factor comparing with the folded FZP solution.

3.5.References

[1] D. N. Black and J. C. Wiltse, "Millimeter-wave characteristics of phasecorrecting Fresnel zone plates," *IEEE Trans. Microw. Theory Techn*., vol. MTT-35, no. 12, pp. 1122–1129, Dec. 1987.

[2] W. Menzel, D. Pliz, and M. Al-Tikriti, "Millimeter-wave folded reflector antennas with high gain low loss and low profile," *IEEE Antennas Propag. Mag*., vol. 44, pp. 24-29, Jun. 2002.

[3] D. R. Reid and G. S. Smith, "A full electromagnetic analysis of grooveddielectric Fresnel zone plate antennas for microwave and millimeterwave applications," *IEEE Trans. Antennas Propag*., vol. 55, no. 8, pp. 2138–2146, Aug. 2007.

[4] J. M. Rodriguez, H. D. Histrov, and W. Grote, "Fresnel zone plate and ordinary lens antennas: Comparative study at microwave and terahertz frequencies," *41st European Microwave Conference (EuMC)*, Manchester, UK, 2011.

[5] A. Petosa and A. Ittipiboon, "Design and performance of a perforated dielectric Fresnel lens," *IEE Proc., Microw., Antennas Propag.*, vol. 150, no. 5, pp. 309–314, Oct. 2003.

[6] X. Wang, M. Jenning, and D. Plettemeier, "60 GHz planar fresnel zone lens," *IEEE international Symposium on Antennas and Propagations*, 2015

[7] H. D. Hristov and J. M. Rodriguez, "Design equation for multidielectric fresnel zone plate lens," *IEEE Microw. Wireless Compon. Lett*. , vol. 22, no. 11, pp. 574–576, Nov. 2012.

[8] A. Petosa, A. Ittipiboon, "Shadow Blockage Effects of Aperture Efficiency of Dielectric Fresnel Lenses," *IEE Proceedings Microwave Antennas Propag*. , Vol. 147, No. 6, Dec. 2000, pp. 451454.

[9] E. A. Lewis and J. P. Casey, Jr., "Electromagnetic reflection and transmission by grating of resistive wires," *J. Appl. Phys*., vol. 23, no. 6, pp. 605-608, Jun. 1952.

[10] J. D. Hanfling, G. Jerinic, and L. R. Lewis, "Twist reflector design using E-type and H-type modes," *IEEE Trans. Antennas Propagat*., vol. 29, pp. 622–629, Jul. 1981.

[11] K.C. Hwang, "Optimisation of broadband twist reflector for Ku-band application," *Electron. Lett*., vol. 43, no. 2, pp. 608–610, 2004.

[12] ETSI EN 302 217-4- V2.1 (2017-05) -Fixed Radio Systems; Characteristics and requirements for point-to-point equipment and antennas; Part 4: Antennas, 2017.

4. Chapter 4 : FFZP Antenna Beam Steering characteristics and focal array design considerations

4.1. Introduction

As mentioned in the first chapter, the beam steering functionality is one of the requirements of antennas deployed in 5G networks. As illustrated in figure 4-1, the beam steering functionality for Point to-Point links (Backhaul/Fronthaul) is required for two main reasons. First for the antenna installation phase where automatic link alignment is required to ensure fast and low cost installation. This phase requires about ±15° beam steering range. Second for the antenna operational phase where compensating antenna swift and sways to ensure continuous high quality link connection is required. This phase requires about ±4° beam steering range.

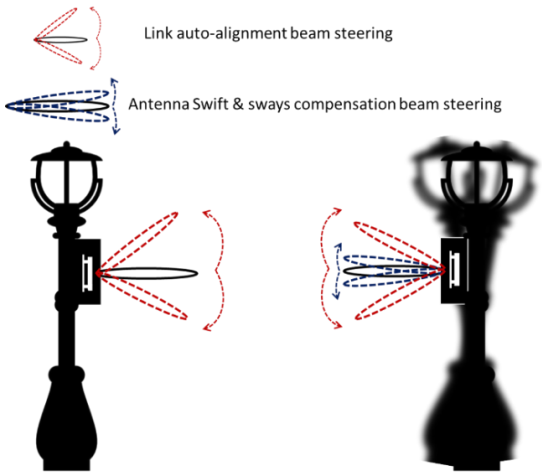

Figure 4-1: Backhaul antenna beam steering scenarios.

The antenna solution proposed in this thesis and presented in chapter 3, the Folded Fresnel Zone Plate (FFZP) antenna, is based on a lens antenna. As illustrated in figure 4-2, the direction of the beam of any lens antenna depends directly on the position of its primary source on the

focal plane. In other words, by displacing the primary source (or exciting a primary source displaced) from the focal point on the focal plane, the antenna beam will be steered. There is an almost-linear relation between the displacement distance from the focal point and the lens antenna beam direction. This relationship for the lens particularly used in the FFZP antenna will be detailed later in the next section.

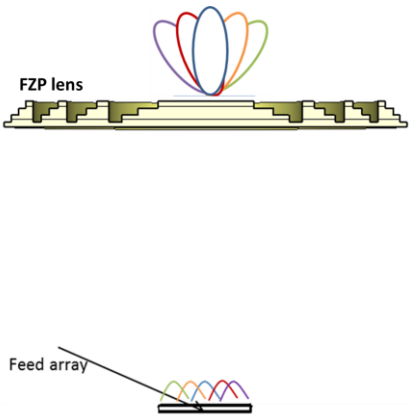

Figure 4-2: Lens antenna beam steering philosophy.

Any beam steering solution for a lens antenna will be based on this simple fact: steering the beam by displacing the focal source. In reality, it's more convenient to have multiple primary sources in the focal plane, i.e. a focal array, and at each time excite one of the focal array elements depending on the desired steering angle. Moreover, using a focal array, enables active solutions that enables switching between focal array elements in real-time.

There are two main parts in this chapter. First part goal is to study the FFZP antenna beam steering characteristics and define reference evaluation parameters. Second part covers all aspects and consideration regarding the focal array design, such as the primary source design and optimizations and the focal array coupling.

The beam steering capabilities of the FFZP antenna are studied and main evaluation parameters are defined in section 2 of this chapter. The beam steering performance of the FFZP antenna is studied using a waveguide aperture as primary source. We will see that using a waveguide aperture as primary source poses some limitations. To overcome these limitations, the waveguide primary source is replaced by a printed Aperture Coupled Microstrip Patch (ACMP) antenna in section 3. As the ACMP will be deployed in a focal array for active beam steering solutions, the coupling impact of the focal array on the antenna performance is studied in section 4.

Using the established characteristics of the FFZP antenna focal array in this chapter, two beam steering solutions are studied using measurement and simulation results in next chapter.

4.2.FFZP antenna beam steering characteristics

In this section the FFZP lens antenna beam steering capability is studied, and in order to evaluate it, some reference parameters are defined. For these studies, the antenna presented in chapter 3- section 3 is used. The antenna structure used for simulations of this section is presented in figure 4-3. As can be seen, contrary to the antenna presented in chapter 3, a simple waveguide aperture without transition is used to simplify the simulations. For the same reason

the mechanical structure is not included in the simulations as well. The simulations are done using *CST Microwave Studio* Time Domain Solver.

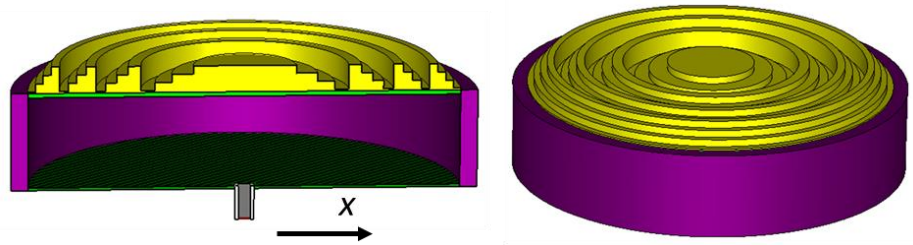

Figure 4-3: FFZP antenna with basic waveguide aperture as primary source.

As illustrated in figure 4-2, the lens antenna beam can be steered in the main planes by displacing its focal source along focal plane axes. There is a direct relationship between the primary source displacement distance and the steered beam direction (scan angle). In order to extract this relationship, the primary source was displaced along the horizontal *x*-axis (E-plane of the antenna) on the focal plane. As a reminder, the primary source is a waveguide with an overall aperture of 6.5 mm × 5.5 mm (*x*-*y* plane).

Figure 4-4 shows the FFZP antenna radiation pattern for different primary source positions along *x*-axis on the focal plane at 60 GHz.

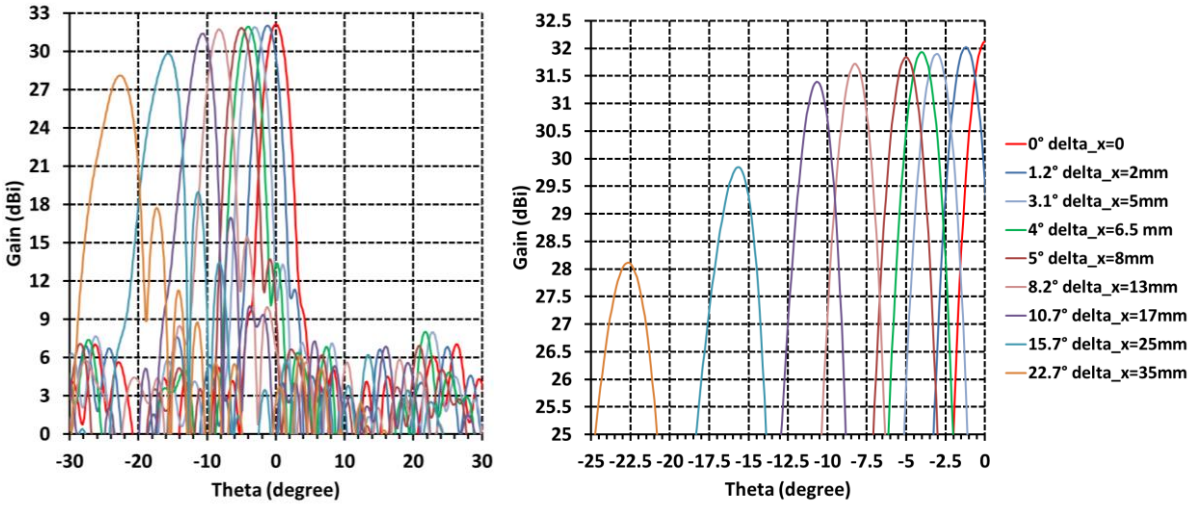

(a) (b)

Figure 4-4: FFZP antenna beam steering for different primary source (waveguide aperture) positions on x-axis of the focal plane at 60 GHz : (a) Wide angle view diagrams, (b) Zoomed view diagrams.

Figure 4-4 gives good information on beam steering characteristics of the FFZP antenna. To quantify these characteristics there evaluation parameters are defined. First parameter is Beam Crossing Level (BCL) or in some literatures known as beam crossover. Beam crossing level, as illustrated in figure 4-5, is the value of the gain loss of two adjacent beams crossing point (or nulls). The value of BCL is signal level loss when switching between two neighboring

beams and it's preferred to be the minimum value possible and not more than 3dB. For example, in figure 4-4, the BCL for the broadside beam and the one steered at 1.2°is 0.5 dB.

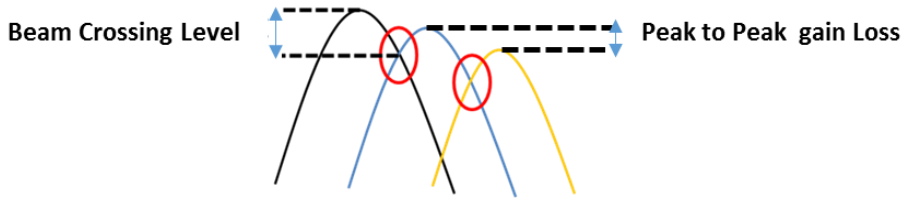

Figure 4-5: Beam Crossing Level (BCL) and Peak to Peak gain Loss (PPL) definitions.

Second parameter is Peak to Peak gain Loss (PPL) which is known also as the scanning loss. This parameter illustrated in figure 4-5, is antenna gain loss when moving from one beam peak to the other beam peak. For example in figure 4-4, the PPL for the broadside beam and the beam steered at 10.7° is only 0.7 dB. The variation of PPL in function of primary source displacement distance and beam scan angle is presented in figure 4-6.

Last parameter is the Beam Steering angle step Resolution (BSR). This parameter is defined for discontinuous beam steering, such as beam switching solutions for lens antennas, and allows to evaluate the beam steering resolution of the antenna. The less the beam steering angle step is, there will be lower peak to peak gain loss as well as less BCL and therefor more stability in the link connection when steering the beam. For example, if we assume that the BSR for our FFZP is 3.1°, then based on figure 4-4 its BCL is 4dB.

Figure 4-6, shows peak to peak gain loss as function of primary source displacement distance from the focal point along *x*-axis for the FFZP antenna. What is notable is the sudden PPL increase for scanning angles beyond 10 degrees. This is because the FZP lens used is a single focal lens and by distancing the primary source from its focal point, the lens illumination is no longer symmetrical and also lesser surface of the lens is projected and therefore its collimating performance degrades.

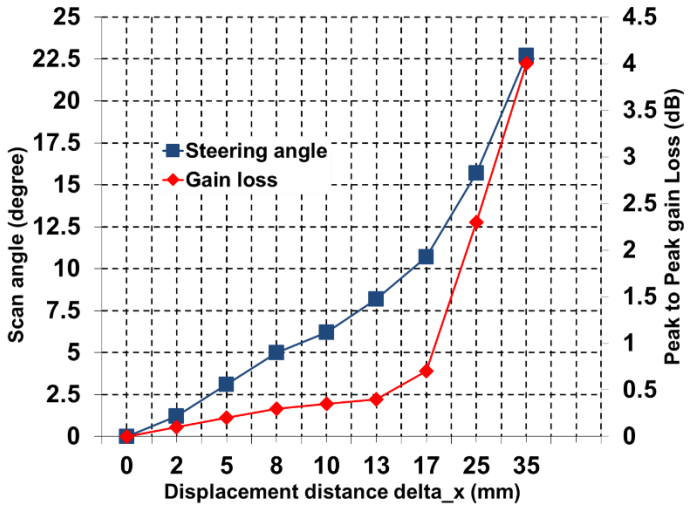

Figure 4-6: Scan angle and peak to peak gain loss (PPL) in function of primary source displacement distance from focal point along x-axis at 60GHz.

Figure 4-6 also represents the variation of the main beam direction as a function of the focal source displacement along *x*-axis at 60 GHz. This variation can be approximated as follows

$$\theta = 0.6 \times \sqrt{\Delta x^2 + \Delta y^2} \quad (1)$$

where Δx and Δy denote the source displacement along *x*- and *y*-axes. This equation allows predicting the main beam direction with an accuracy of ±0.5° for a maximum beam deviation of ±16°.

For our proposed antenna solution, the FFZP lens antenna which is a quasi-optical solution, one of the common beam steering technologies, relies on beam switching approaches [1, 2]. In this solution, switches are used to switch between the primary sources of the focal array. Beam steering using a beam switching approach has a major limitation: the discontinuous beam scanning caused by the minimum beam steering angle step imposed by focal source physical dimensions and the mandatory inter-element spacing. Furthermore, the minimum beam steering angle step resolution imposes the minimum obtainable beam crossing level value.

For the FFZP antenna, with a waveguide aperture (overall dimension of 5.5 mm × 6.5 mm) as the primary source and assuming no inter-element spacing in case of a focal array, the lowest feed phase center displacement from the focal point on *x*-axis would be 6.5 mm. According to figure 4-6 and equation (1), this displacement distance results in approximately 4° scanning angle. This BSR value of the FFZP antenna with 6.5 mm×5.5 mm aperture size primary source is an ideal value considering that no inter-element spacing was assumed. A beam steering resolution of 4° will result in 0.2 dB peak to peak gain loss and 7 dB beam crossing level (between the broadside beam and 4° steered beam). For a real life network, 7 dB loss is not acceptable as it will result in poor network quality.

In this section, the beam steering characteristics of the FFZP antenna were presented. To evaluate these characteristics three evaluation parameters were defined. It was demonstrated that in order to improve beam crossing level, small beam steering angle steps are required. This can be achieved by using primary sources with smaller physical dimensions comparing to waveguide apertures. Also, as mentioned, main beam steering technology used for quasi-optical antenna solutions is beam switching. This solution requires integrating RF circuit components (MMIC switches, Low Noise Amplifiers, Power amplifiers, etc.) with the primary source feeding network. This integration is much easier when using printed technology based radiating elements such as Aperture Coupled Microstrip Patch (ACMP) antennas. For these reasons, the waveguide aperture used as primary source for our FFZP antenna, is replaced by ACMP antenna as primary source from onwards.

4.3. ACMP antenna as primary source for FFZP antenna Focal Array

4.3.1. Introduction

A primary source based on PCB technology is preferred over waveguide technologies because of their compactness and compatibility with RF components (MMIC switches, etc.). An Aperture Coupled Microstrip Patch (ACMP) antenna is preferred to other type of microstrip patch antennas such as coaxial-fed or inset-fed microsstrip patches. This is because for the ACMP its feeding line is in a separate layer from its radiating element. As presented in figure 4-7, in an ACMP antenna, the microstrip patch is coupled to its microstrip feed line by a

coupling slot. This configuration avoids parasitic effects of the RF components and feed lines on radiating elements and facilitates integrating the RF and active components into the antenna structure.

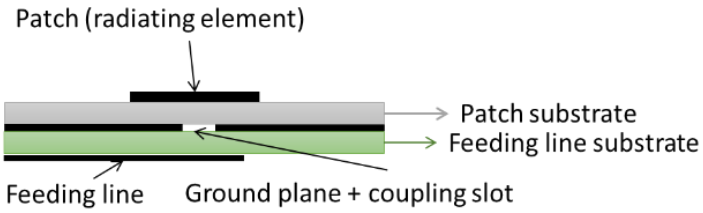

Figure 4-7: Aperture Coupled Microstrip Patch Antenna (ACMP) side-view schematic.

4.3.2. Simple ACMP design and simulation

At the first step, a simple ACMP is designed at 60 GHz to determine its characteristics as primary source for the FFZP antenna and identify improvement points. Figure 4-8 shows the simple ACMP layers, its materials and dimensions. As can be seen, the patch is rectangular and also the coupling aperture is a simple rectangular slot. The length of the adapting stub is $\lambda_g/4$ where is λ_g is the guided wavelength in the feeding line substrate. The feeding line width is calculated to have a 50-Ohm line.

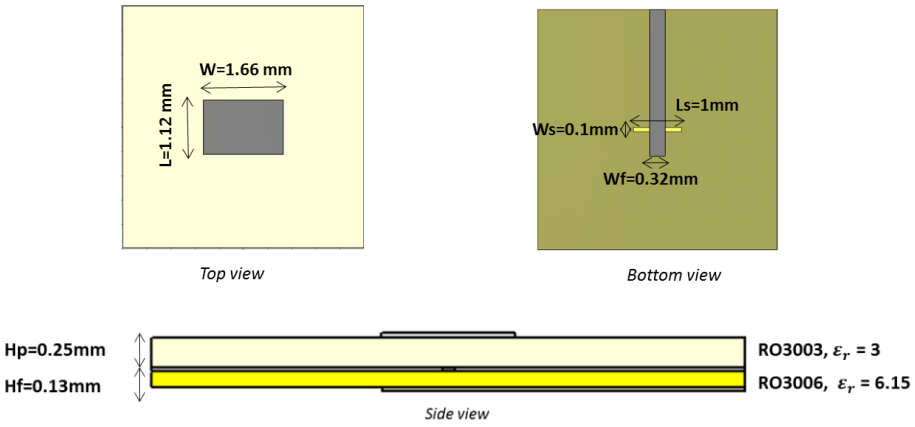

Figure 4-8: Simple ACMP structure with design dimensions at 60 GHz.

Figure 4-9 presents the reflection coefficient of the designed ACMP patch antenna simulated using *CST Microwave Studio*. As demonstrated, the -10 dB impedance bandwidth of this ACMP is only 6.6% (58-62 GHz) and doesn't cover all the 14.6% required for V-band (57-66 GHz). Limited bandwidth of microstrip patch antennas is their known drawback and it's because of their resonant nature.

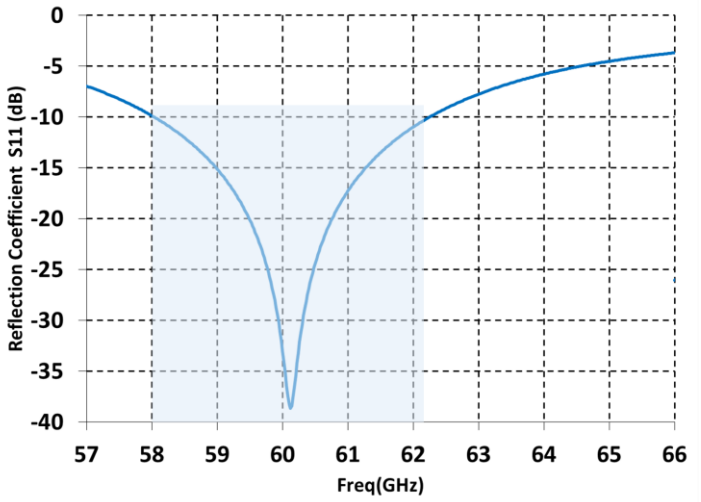

Figure 4-9: Refection coefficient of the simple Aperture Coupled Microstrip Patch antenna.

The simulated radiation pattern of the simple ACMP at 60 GHz is presented in figure 4-10. Its gain at 60 GHz is 7.26 dBi and its illumination edge taper for $\theta_{Edge} = 36.9°$ regarding our Fresnel Zone Plate (FZP) lens is 2.4 dB in both planes. As discussed in chapter 3, section 2 during the FZP lens parametric studies, the optimal edge taper of a primary source illuminating the FZP lens with illumination angle of $\theta_{Edge} = 36.9°$ is around 12 dB. This means by using this ACMP as primary source, the FFZP antenna will not offer its optimal gain.

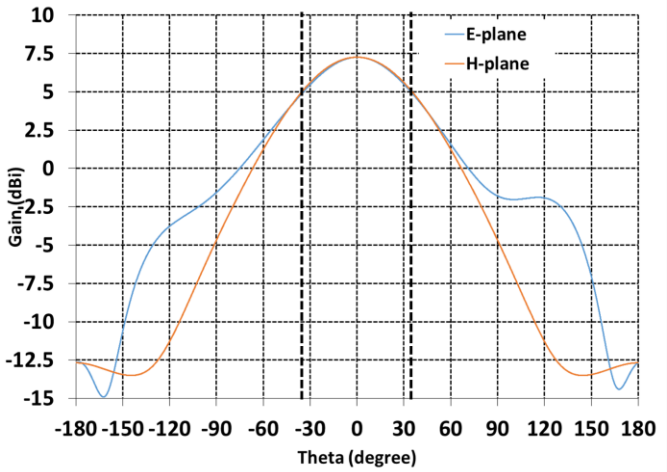

Figure 4-10: Simulated radiation patterns the simple Aperture Coupled Microstrip Patch antenna at 60 GHz.

The E-plane radiation pattern of the simple ACMP antenna (figure 4-10), is not completely symmetrical and the lobe for positive thetas has higher level compared to the other side. This asymmetry is caused by the feeding line stub, which is causing non-symmetrical coupling to the patch. As this asymmetry is outside our FZP lens edge illumination angle its impact is not noticeable and can be ignored.

As presented, the simple ACMP requires two main improvements. First is impedance bandwidth increase in order to cover all the V-band frequency band. Second is increasing its

radiation pattern edge taper, or in other words increasing its directivity. In following sections 4.3.3 and 4.3.4, alternative solutions to obtain the required improvements are proposed.

4.3.3. ACMP bandwidth enhancement

Microstrip patch antennas naturally suffer from limited impedance bandwidth due to their resonant nature. Their impedance bandwidth can be increased by creating a second resonance frequency in proximity with the first resonance frequency. The combination of two resonances will results in larger impedance bandwidth.

To create this second resonance and improve the impedance bandwidth, a parasitic patch is added on top of the main patch. Figure 4-11 shows the schematic presentation of the ACMP plus parasitic patch (ACMPP) antenna.

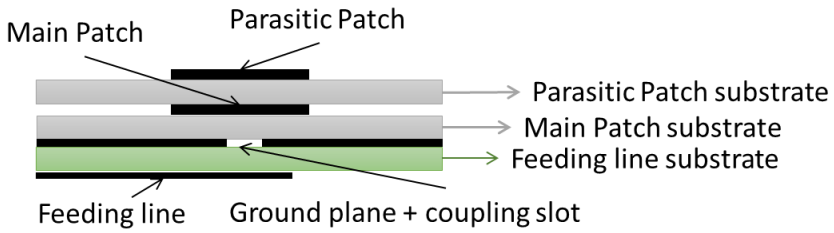

Figure 4-11: Aperture Coupled Microstrip Patch Antenna with parasitic patch (ACMPP) side-view schematic.

The designed ACMPP parameters are presented in figure 4-12. The feeding line and coupling slot dimension are the same as simple ACMP presented in figure 4-8.

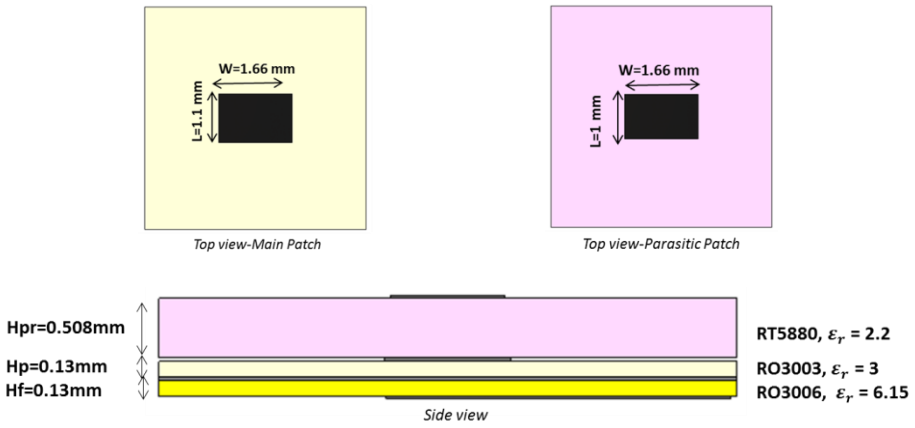

Figure 4-12: ACMP with parasitic patch structure with design dimensions at 60 GHz.

The reflection coefficient of the ACMPP antenna is presented in figure 4-13. This antenna offers a wide impedance bandwidth of 17% (55.5-66 GHz) for return loss better than 10 dB.

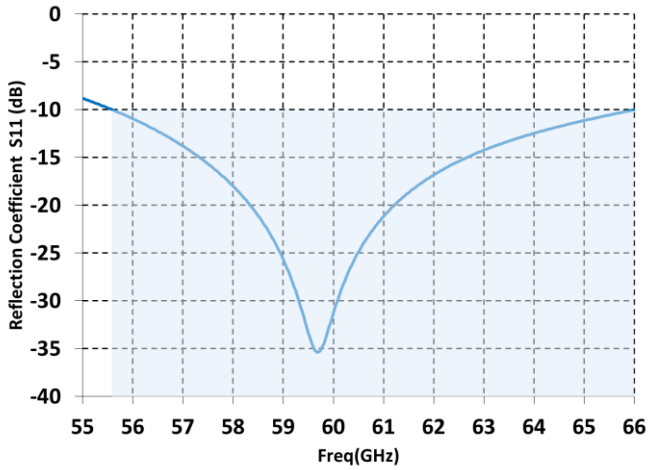

Figure 4-13: Refection coefficient of the ACMP with parasitic patch antenna.

In terms of directivity and edge taper, adding the parasitic patch doesn't have any impact. As shown in figure 4-14, ACMPP edge taper for edge illumination angle $\theta_{Edge} = 36.9°$ is 2.25 dB which is even slightly (0.15 dB) lower than the simple ACMP.

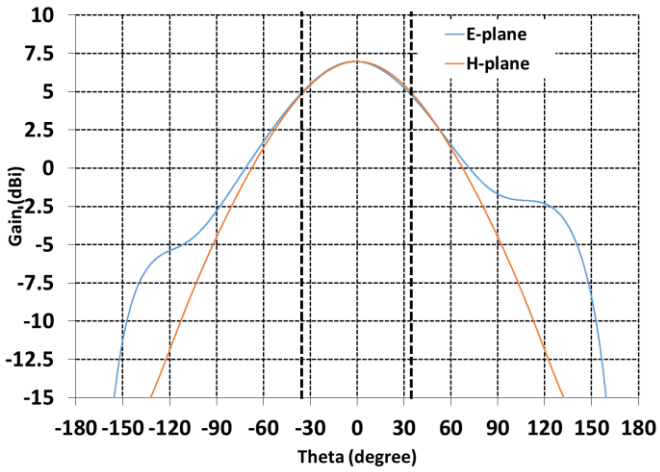

Figure 4-14: Simulated radiation patterns of the ACMP plus parasitic patch antenna at 60 GHz.

The non-symmetrical E-plane radiation phenomena is present here as well, and can be ignored as it occurs outside the FZP lens illumination angle.

The limited impedance bandwidth of the simple ACMP was solved by adding a parasitic patch on top of the main patch. This solution increases the ACMP impedance bandwidth from 6.6% to 17% which is more than enough for the target frequency band of V-band which requires 14.6% bandwidth. This solution did not improved the edge taper of the ACMP. In the following section, different solutions to improve the ACMP edge taper are discussed.

4.3.4. ACMP edge taper optimization

With regard to the parametric studies on the FZP lens that were presented in the previous chapter, the optimal edge taper of a primary source illuminating our FZP lens is around 12 dB. This optimal edge taper is required to obtain the maximum efficiency from the FZP lens and

reduce spillover losses. The simple ACMP source can only offer around 2 dB edge taper which is far from the optimal value. In the following, different solution along with their advantages and disadvantages to improve the ACMP directivity and therefore increase its edge taper are discussed. In all this solutions, the ACMP with the parasitic patch (ACMPP) is used as reference.

4.3.4.1. ACMPP plus cavity

One of the first solution that comes into mind to increase the directivity is to introduce a cavity inside the ACMPP structure. As presented in figure 4-15(c), this cavity is in fact a removed cylindrical part from the parasitic patch substrate. Several simulations where performed for various cavity diameters to obtain the optimal diameter of the cavity. The best edge taper is for a cavity with a diameter of 3mm. The edge taper as presented in figure 4-15(a) is 2.8 dB which is slightly 0.5 dB more than the ACMPP solution. The fact of removing the substrate under the parasitic patch, has a direct impact on the return loss. To re-obtain the desired impedance bandwidth, the design parameters of the ACMPP should be re-optimized. As the goal of this section is to optimize the radiation pattern edge taper, the design parameters are kept constant to be able to compare different solutions precisely.

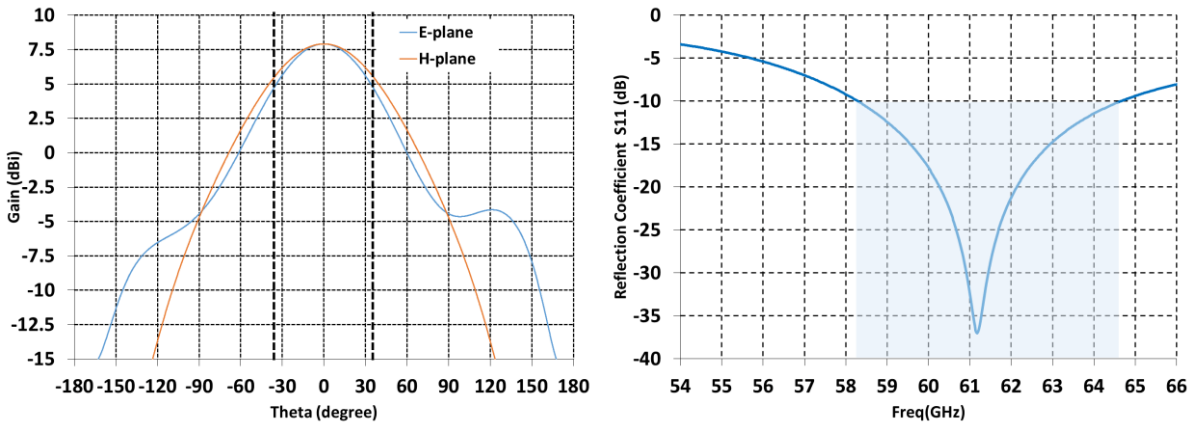

(a) (b)

(c)

Figure 4-15: ACMPP plus air cavity : (a) simulated radiation patterns at 60 GHz, (b) simulated reflection coefficient, and (c) 3D view.

4.3.4.2. ACMPP plus small dielectric lens

The aim is to benefit from lens directivity enhancement nature to increase the ACMPP edge taper. This solution is suitable for increasing a single ACMPP edge taper, but for beam steering solutions where an array of primary sources are required, there are two major issues. Main issue is increased inter-element coupling because of adjacent lenses, second inconvenient is manufacturing challenges.

Four different lenses are used to improve the ACMPP edge taper. These lenses are:

- Integrated Lens Antenna (ILA)
- Hyperbolic lens
- Elliptical lens
- Simple uniform dielectric slab

In the following, the impact of each one of these dielectric lenses on the ACMPP is presented.

4.3.4.2.1. ACMPP plus Integrated Lens Antenna

Figure 4-16 (c) shows the 3D schematic view of the ACMPP with Integrated Lens Antenna (ILA) on top of it. The ILA is constituted of a hemispherical lens with extended cylindrical section. The ILA material is Polystyrene (PS) with dielectric permittivity of 2.5. The length and diameter of the ILA are the two main parameters. The optimal value was found to be a diameter of 3mm, extended length of 3mm and overall height of 4.5mm. In should be noted that the lens diameter is kept at 3mm to avoid bulky structures and facilitate deploying this solution in focal arrays. The radiation pattern of the ACMPP plus ILA at 60 GHz is presented in figure 4-16(a). The edge taper of this solution is 8.2 dB in both E-plane and H-plane. As illustrated in figure 4-16(b), the ILA causes a frequency shift on the ACMPP reflection coefficient and limits its bandwidth. This can be resolved by re-optimizing the ACMPP parameters and also choosing a material with lower dielectric permittivity for ILA to reduce the patch-dielectric interface reflections.

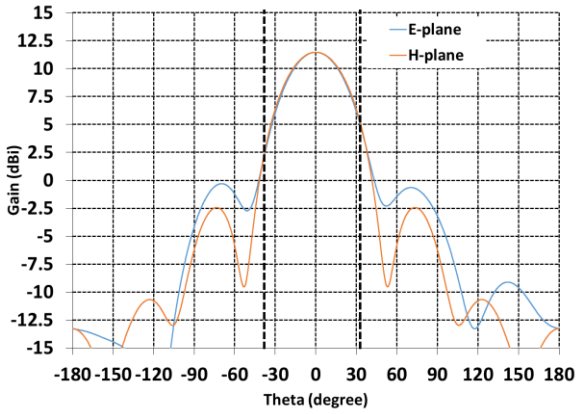

(a)

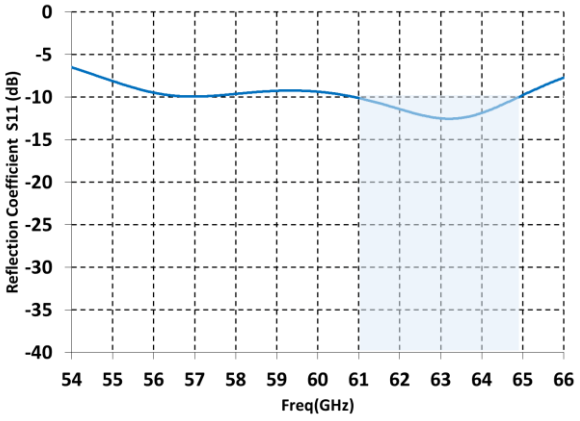

(b)

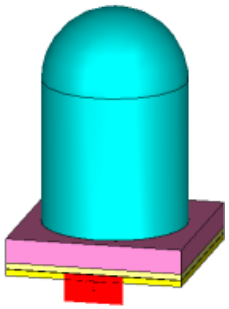

(c)

Figure 4-16: ACMPP plus ILA lens : (a) simulated radiation patterns at 60 GHz, (b) simulated reflection coefficient, and (c) 3D view.

4.3.4.2.2. ACMPP plus Hyperbolic lens

Other type of lens used to integrate on top of the ACMPP is hyperbolic lens (see figure 4-17(c)) which offers quite smaller profile comparing to integrated lens (extended hemispheric). Design equation form chapter 2 were used to design this lens. Same as the ILA, the diameter of the lens is 3mm and is made of Polystyrene (PS) with dielectric permittivity of 2.5. As presented in figure 4-17(a), the edge taper of this solution is 2.95 dB in H-plane and 5.5 dB in E-plane. Comparing to the solution where an ILA was used, this solution is less directive and this is mainly because of smaller volume of the hyperbolic lens comparing to ILA. The reflection coefficient of this solution is presented in figure 4-17(b). We can see that the ACMPP becomes totally dis-matched, meaning that the ACMPP parameters need to be re-optimized in order to have a matched solution.

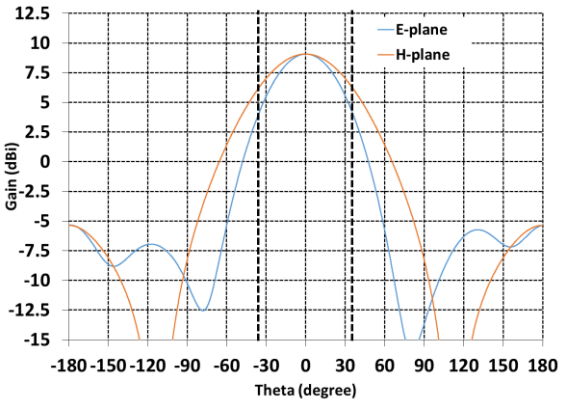

(a)

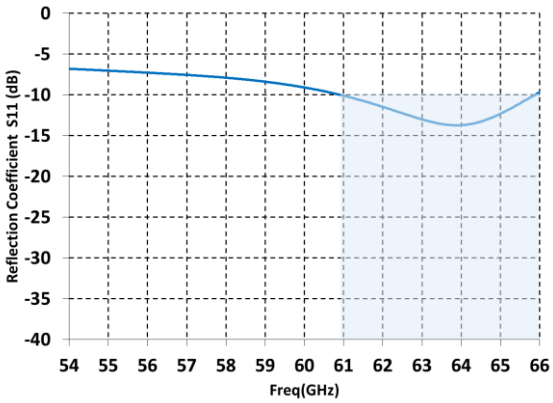

(b)

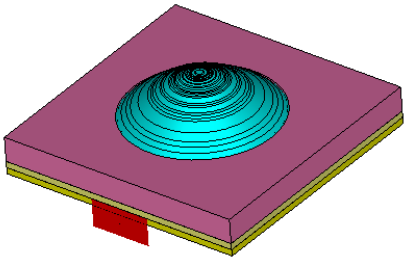

(c)

Figure 4-17: ACMPP plus hyperbolic lens : (a) simulated radiation patterns at 60 GHz, (b) simulated reflection coefficient, and (c) 3D view.

4.3.4.2.3. ACMPP plus Elliptical lens

The elliptical lens is also made of Polystyrene (PS) with dielectric permittivity of 2.5. The height of the lens is 4mm with a lower diameter of 1.42mm. Equations presented in chapter 2 are used for designing this lens. The 3D structure of this solution is shown in figure 4-18(c). As illustrated in figure 4-18(a), this solution offers an edge taper of almost 7 dB in both planes. The reflection coefficient of the ACMPP plus elliptical is presented in figure 4-18(b). It shows that the impact of the elliptical lens on S-parameters is less than previous solutions, but still the dielectric lens is causing some limited bandwidth reduction comparing to the reference ACMPP solution.

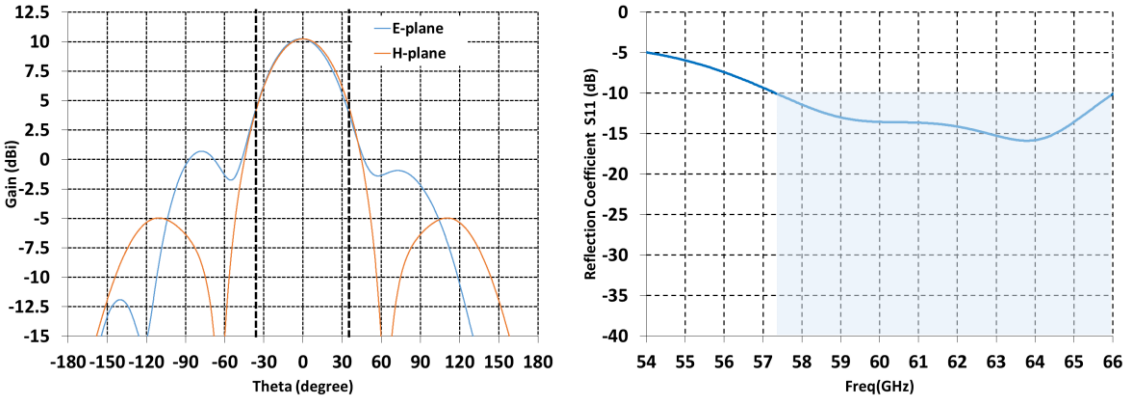

(a) (b)

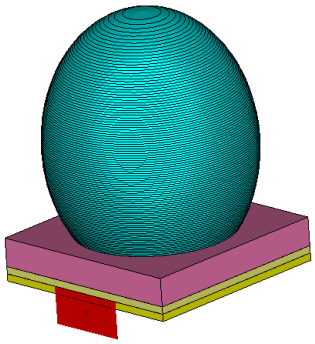

(c)

Figure 4-18: ACMPP plus elliptical lens : (a) simulated radiation patterns at 60 GHz, (b) simulated reflection coefficient, and (c) 3D view.

4.3.4.2.4. ACMPP plus dielectric slab

The main advantage of this solution comparing to the lens solutions is its manufacturing simplicity. Figure 4-19(c) presents the 3D presentation of this solution. The optimal thickness of this dielectric slab after several parametric studies is found to be equal to full wavelength λ_0 at free space at 60 GHz (5 mm). The dielectric slab material is Polystyrene (PS) with dielectric permittivity of 2.5. As illustrated in figure 4-19(a), the edge taper of this solution is 14 dB in both planes. This value is very close to the optimal 12 dB edge taper required for the FZP lens. The impedance adaption of this solution is illustrated by reflection coefficients presented in figure 4-19(b). The dielectric slab, similar to the elliptical lens, has less impact on the ACMPP matching comparing to the other lenses presented previously.

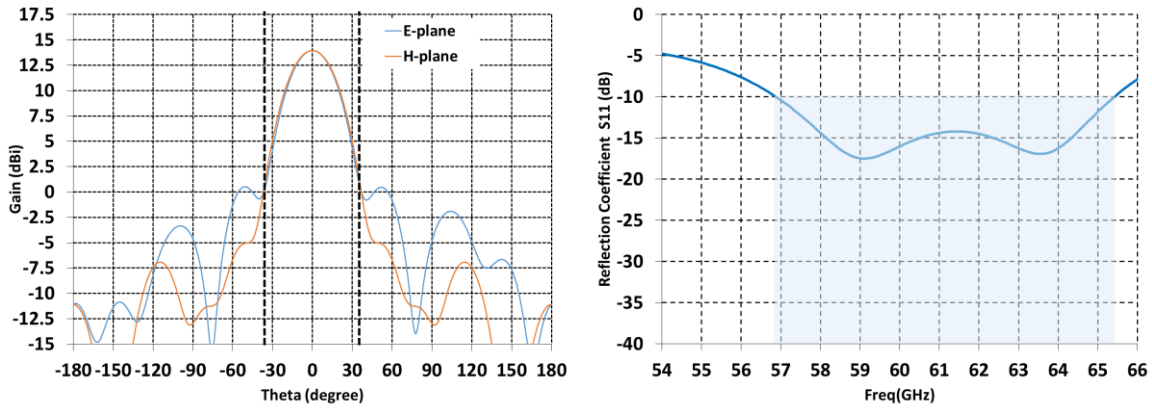

(a) (b)

(c)

Figure 4-19: ACMPP plus dielectric slab of λ_0 (5mm) thickness : (a) simulated radiation patterns at 60 GHz, (b) simulated reflection coefficient, and (c) 3D view.

4.3.4.3. 2×2 elements sub-array

Another technique to achieve a more directive radiation pattern is to benefit from the array factor. By using a sub-array of 2×2 ACMPP elements, higher edge taper values can be obtained comparing to a single ACMPP element. Depending on inter-element spacing of the 2×2 sub-array, variable edge tapers can be obtained. Figure 4-20 shows the 2×2 sub-array structure.

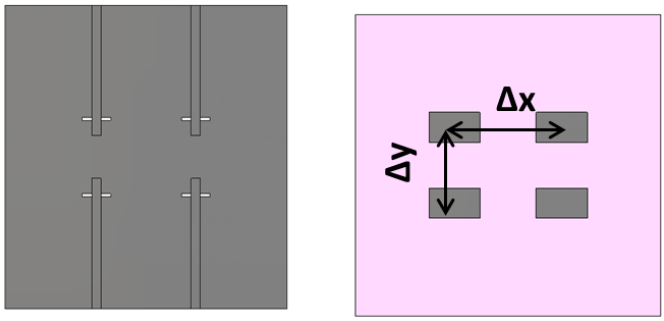

Figure 4-20: ACMPP 2×2 sub-array structure.

Table 4-1 shows the variation of the edge taper value as a function of the 2×2 sub-array inter-element distance (Δx and Δy). These values are obtained using *CST* array wizard, meaning the inter-element coupling is not taken into account and its only array factor calculations. As can be seen the inter-element spacing of 0.7λ offers an edge taper of 14.1 dB in both planes which is the closest value to the 12 dB optimal edge taper required.

Table 4-I: ACMPP 2x2 sub-array edge taper variation in function of sub-array inter-element spacing at 60 GHz.

2x2 array(Δx – Δy)	Gain Max (dBi)	Edge Taper in E-plane (dB)	Edge Taper in H-plane (dB)
0.4λ-0.4λ	10.2	5	5
0.5λ-0.5λ	11.7	7	7
0.7λ-0.7λ	13.6	14.1	14.1
0.8λ-0.8λ	13.6	25.4	25.4
0.7λ- 0.5λ	12.7	7	13.7

As mentioned, these calculations don't consider the coupling between the sub-array elements. To consider the inter-element coupling, the 2×2 sub-array presented in figure 4-20 is simulated completely. Figure 4-21 presents the 2×2 sub-array radiation pattern taking into account the couplings at 60 GHz. With considering the coupling, the edge taper for 0.7λ spacing array would be 11.92 dB in E-plane and 14.56 dB in H-plane and the maximum gain is 12.4 dBi. Due to E-plane coupling the directivity and therefore the edge taper is slightly reduced in this plane.

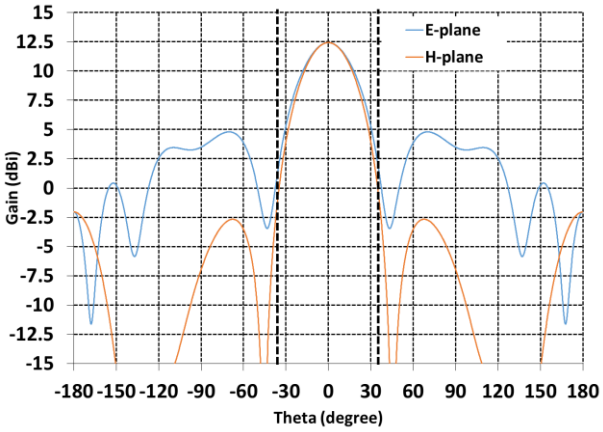

Figure 4-21: Radiation patterns of a 2x2 sub-array of ACMP elements with separate feeding line per element.

4.3.4.4. Conclusions on edge taper optimization solutions

Different solutions to increase the ACMPP edge taper were discussed in previous sections. Among them there exists only 2 solutions that enable obtaining the target edge taper of 12-14 dB. First solution is using a dielectric slab with a thickness of half guided wavelength and second is using a sub-array of 2×2 ACMPP elements as the primary source instead of a single ACMPPP. What differentiates these two solution, is their performance in the focal array and their behavior in presence of the focal array coupling. This is studied in details later in section 4.4.

To have a better understanding of these two solutions, their impact on the FZP lens is studied. Figure 4-22 presents the normalized radiation patterns of the non-folded FZP lens excited using: 1- Single ACMPP, 2- Single ACMPP plus dielectric slab, and 3- Sub-array of a 2×2 ACMPP elements. As the objective was to compare these solutions and to accelerate the simulation time the non-folded FZP lens (alone without the folded structure), without absorber, was simulated using *CST* Integral Equation (IE) solver. Also instead of simulating the FZP lens with each of the primary sources, it was simulated with their exported Fairfield at 60 GHz.

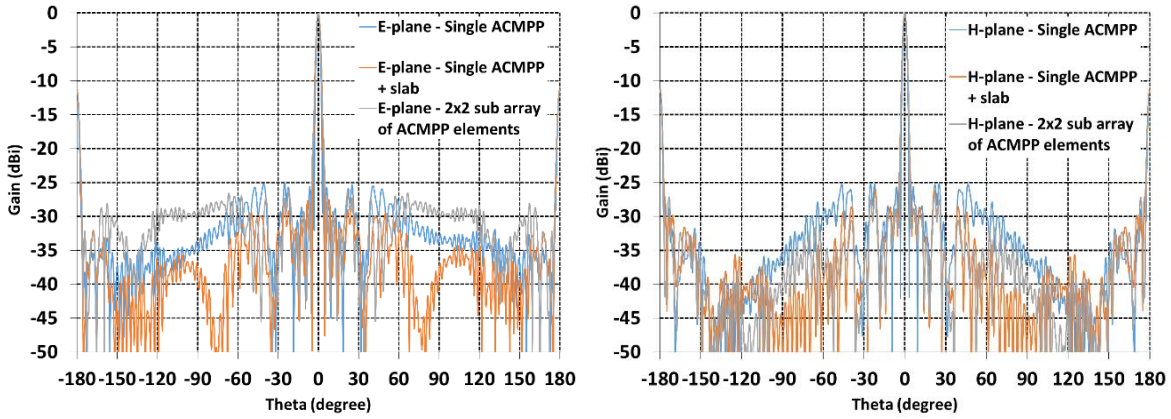

Figure 4-22: Primary source Edge taper optimization solutions impact on FZP lens at 60 GHz.

In addition to figure 4-22, Table 4-2 compares the maximum gain of these three cases at 60 GHz. It is demonstrated that for the case of the FFZP fed by an ACMPP plus dielectric slab, the highest gain and lowest side lobe levels are obtained.

Table 4-II: Comparison of primary edge taper optimization impact on FZP gain.

Solution	Gain (dBi) / E-plane & H-plane
Single ACMPP	31.6
Single ACMPP + slab	33.8
2×2 sub-array of ACMPP elements	33

4.3.5. Conclusions on ACMP as primary source for FFZP antenna

The primary source design and optimization for the FFZP antenna focal array was presented in this section. The Aperture Coupled Microstrip Patch antenna (ACMP) was chosen to be the primary source because of its small form factor and compatibility with RF circuits and component required for active beam steering solutions. Main limitations of this primary source are limited impedance bandwidth and low directivity (edge taper). Alternative solutions to

overcome this limitations were proposed. To enhance the bandwidth, the ACMPP solution, where a parasitic patch is stacked on top of the main patch is proposed. In order to increase the ACMP directivity, different solutions were studied and it was concluded that the best options are to use a 2×2 ACMPP elements sub-array as primary source instead of a single ACMPP or to use dielectric slab on top of the ACMPP. The behavior of these two solutions in a focal array are further studied in this chapter.

In the following section, the focal array coupling impact on the primary source performance as well as on the overall antenna solution is studied.

4.4. Couplings in the focal array

One of the major issues when using patch antennas in a focal array is the coupling between patches and between their feeding lines. In this section the impact of the coupling is studied using S-Parameters (transmission coefficients). In order to distinguish the coupling between patches and coupling between feeding lines two scenarios are considered:

- An array of ACMPP elements excited using discrete lumped ports (no feeding line) on their coupling slots
- An array of ACMPP elements where conventional microstrip feeding lines are used for excitation

The reference focal array is constituted by 4×4 ACMPP elements. The reason of using 4×4 elements is to have a symmetrical array and be able to study the coupling in case of using a 2×2 sub-array as primary source instead of a single ACMPP.

4.4.1. Coupling studies: Only radiating elements (without feeding lines)

To study the coupling of only the radiating elements, the 4×4 focal array is simulated without any feeding lines. The patches are excited using discrete lumped ports in their coupling slots. Figure 4-23 presents the focal array structure and its E-field when the patch number one is excited. The inter-element spacing here is 3.6 mm ($0.72\lambda_0$) in both directions. This value is chosen to offer the best beam steering angle resolution (BSR), 2.4°, and therefore lowest beam crossing level possible, 2 dB.

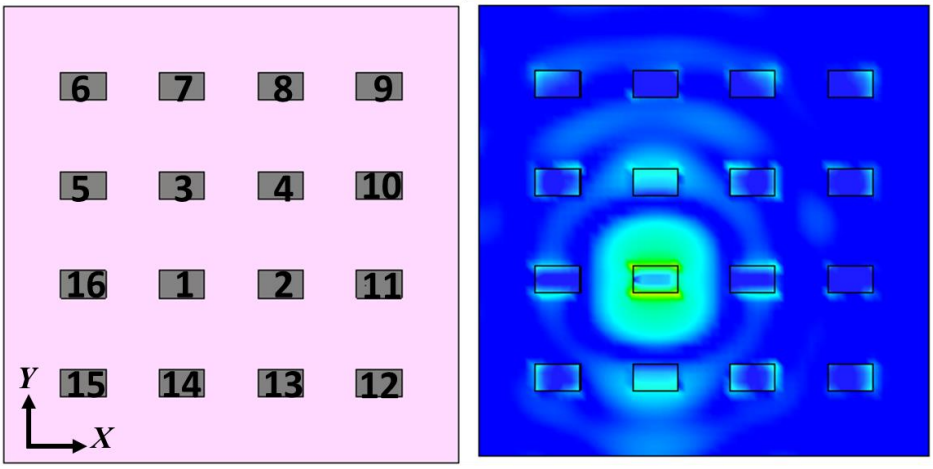

Figure 4-23: Focal array excited by lumped ports for coupling study of only radiating elements.

The transmission coefficients between the lumped port number one and the rest of the ports are presented in figure 4-24. It can be observed that worst coupling is between patch number one and its E-plane neighbor patch number fourteen. The maximum coupling, S_{14} is -22.3 dB at 57 GHz. The coupling between patch number one and its other E-plane neighbor patch number 3 is also higher than others and is -23.8 dB at 57 GHz. The higher E-plane coupling comparing to other planes can also be observed in E-filed presented in figure 4-23.

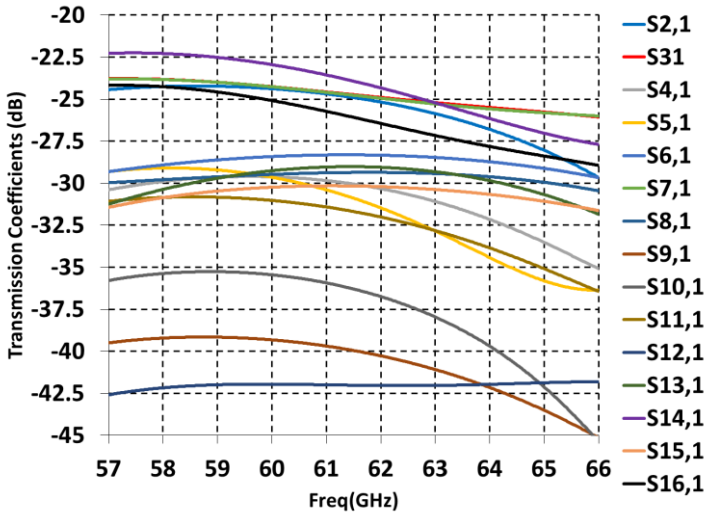

Figure 4-24: Transmission Coefficient between patch number 1 and its surrounding patches all excited using lumped ports on their slots.

The impact of the coupling without feeding lines on the patch radiation pattern is presented in figure 4-25. This figure shows the radiation pattern of the patch number one of the 4×4 array at 60 GHz. By comparing it with figure 4-14 where the radiation pattern of a single ACMPP with no surrounding elements is presented, it is observed that the focal array coupling degrades and deforms significantly the primary sources radiation pattern.

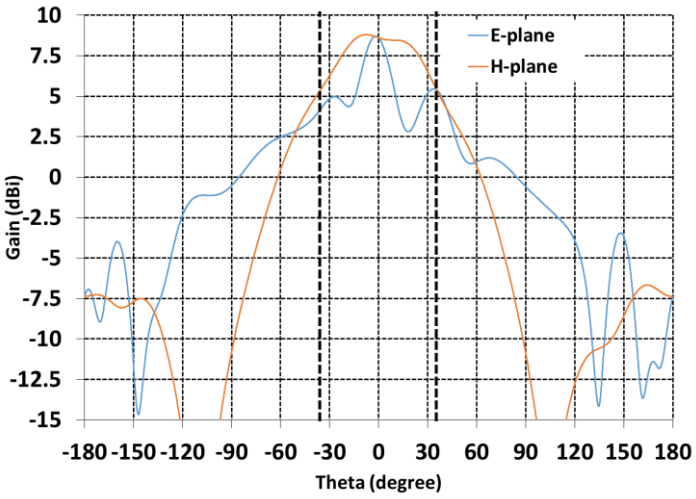

Figure 4-25: Impact of focal array elements coupling on the radiation pattern of a single ACMPP (number 1) excited by lumped port at 60 GHz.

In figure 4-25, it can be observed that the E-plane radiation pattern is more degraded. As presented with the transmission coefficients in figure 4-24, this corresponds to the stronger coupling in E-plane comparing to H-plane.

Other observation point in figure 4-25, is the slightly increased directivity of the ACMPP excited in an array comparing to the single ACMPP. This is due to the array effect of the neighboring elements. Table 4-3, compares the Half Power Beam Width (HPBW) and the edge taper values between the ACMPP excited alone and excited in the 4×4 array at 60 GHz.

Table 4-III: Coupling impact of only radiating elements of the focal array on primary source Edge taper.

ACMPP	HPBW (E-plane) degree	HPBW (H-plane) degree	Edge Taper in H-plane (dB)	Edge Taper in E-plane (dB)
Alone	85.1	85.2	2.25	2.25
In focal array	21.4	66.4	3.35	4.7

4.4.2. Coupling studies: Radiating elements and feeding lines

To study the impact of the feeding lines in focal array coupling, as presented in figure 4-26 a simple feeding network was designed to excite the ACMPP elements of the 4×4 array.

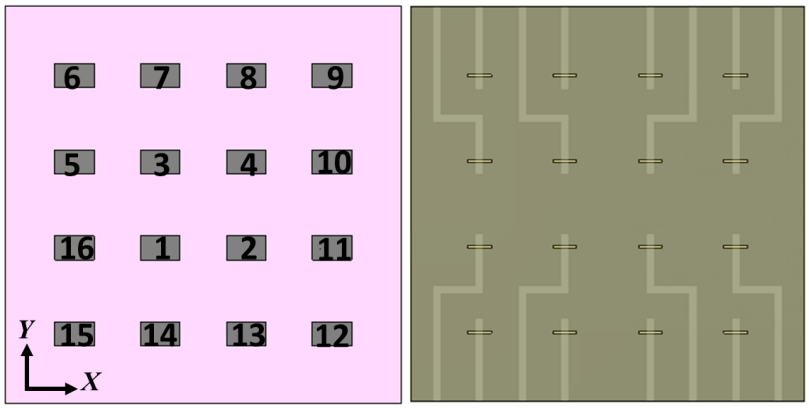

Figure 4-26: Focal array excited by feeding lines for coupling study of radiating elements and feeding lines.

In figure 4-27, the coupling impact, in presence of the feeding lines is presented by the transmission coefficients between patch number one and its neighbors in the focal array. It's noticeable that because of the coupling between the feeding lines, the overall coupling increases as well. In this case also most strong coupling for patch number one is with its E-plane neighbor, patch number fourteen which gives a S_{14} of -21 dB at 57 GHz. By comparing figure 4-27 and 4-24, we can conclude 2.8 dB more transmitted energy between patches number one and fourteen because of the feeding lines.

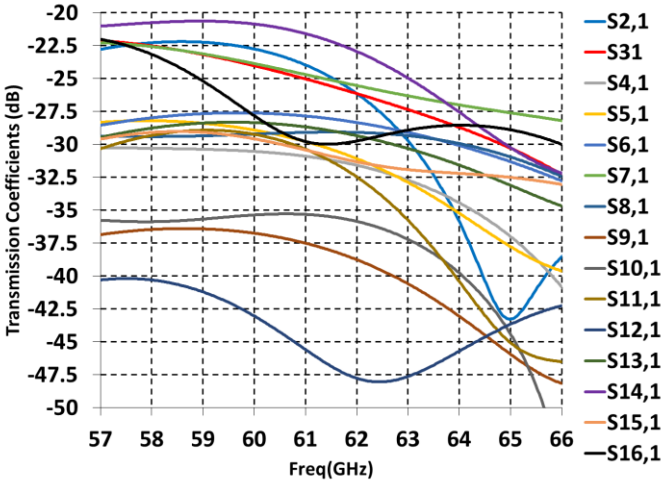

Figure 4-27: Transmission Coefficient between patch number one and its surrounding patches all excited using feeding lines.

The E-field for the case where only patch number one is excited is presented in figure 4-28. The E-field distribution confirms again the strong coupling in E-plane because of the patch natural E-field distribution on its surface.

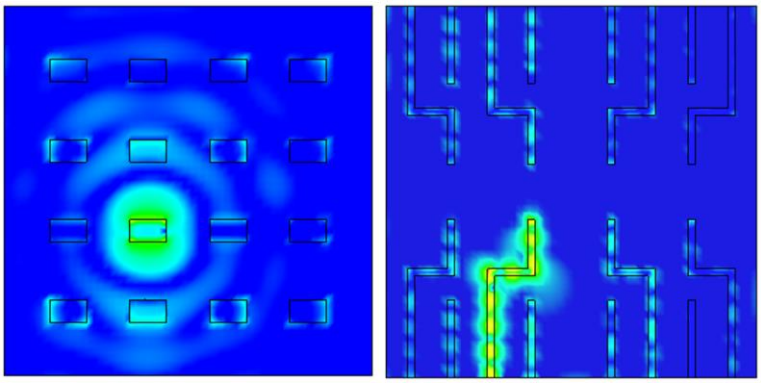

Figure 4-28: E-field distribution of the 4×4 array of ACMPP elements fed by feeding lines with only one element excited at 60 GHz.

The impact of this coupling is studied on the patch radiation pattern as well. As presented in figure 4-29, the patch radiation pattern in the focal array is strongly perturbed because of the coupling between array elements. Also as the patch number one is not in the middle of the array, it's suffering from unbalanced coupling which translates into unbalance radiation pattern. The impact of this perturbations on the antenna is studied and the results will be presented in following sections.

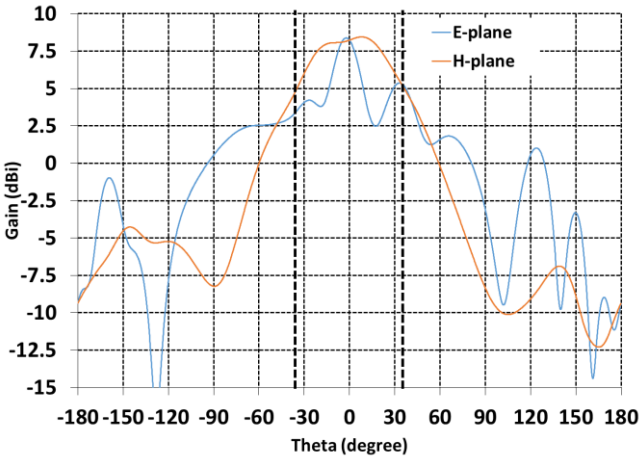

Figure 4-29: Impact of focal array coupling on the radiation pattern of a single ACMPP (number one) excited by feeding line at 60 GHz.

As presented in Table 4-4, similar to the previous case, the fact of exciting the ACMPP in an array increased its directivity and therefore its edge taper.

Table 4-IV: Coupling impact of focal array radiating elements and their feeding lines on single ACMPP.

ACMPP	HPBW (E-plane) degree	HPBW (H-plane) degree	Edge Taper in H-plane (dB)	Edge Taper in E-plane (dB)
Alone	85.1	85.2	2.25	2.25
In focal array	21	66.3	3.65	5.31

4.4.3. Coupling studies: Impact on the FZP lens

The focal array coupling for a single ACMP was studied in details. This coupling is mainly between the radiating elements of the focal array, but the feeding lines also increase the coupling. The focal array coupling has two main effects. First effect is radiation pattern perturbations and higher and unbalanced side lobe levels. And second impact is primary source directivity and therefore edge taper increase.

To quantify the impact of the focal array coupling on the antenna solution, the non-folded FZP lens was simulated with three different primary sources: 1- Single ACMP, 2- ACMP in 4×4 array without feeding lines, and 3- ACMP in 4×4 array with feeding lines.

In order to accelerate the simulation time, the FZP lens was simulated using Integral Equations (IE) solver of *CST*, and instead of simulating the primary sources with the FZP lens, their Fairfield pattern was exported and simulated with FZP lens.

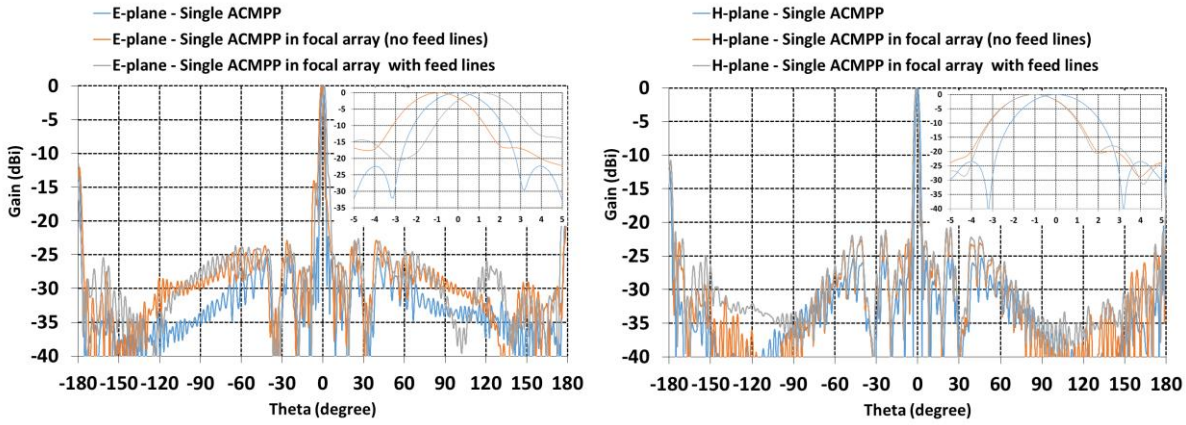

Figure 4-30: Focal array coupling impact on FFZP antenna.

As presented in figure 4-30, the coupling of the focal array that deformed the primary source radiation patters, perturbs the FFZP radiation pattern as well in E-plane where the coupling is the highest. Also we observe slight beam deviations around 1° in the zoomed diagrams. The beam deviation are caused by the primary source phase center displacement from the patch center due to the focal array couplings comparing to the single ACMPP case where the phase center is in the center of the patch.

Table 4-5 demonstrates that the focal array coupling impact will result in the antenna gain loss of 3.4 dB. To be more specific, 2.5 dB loss is because of the coupling between the focal array radiating elements and 0.9 dB is between the focal array feeding lines.

Table 4-V:Focal array coupling impact on FFZP antenna.

Solution	Gain (dBi) E-plane	Gain (dBi) H-plane
Single ACMPP	31.6	31.6
Single ACMPP in focal array without feeding lines	29.1	29.6
Single ACMPP in focal array with feeding lines	28.3	28.2

The coupling between the focal array radiating elements may be reduced by isolating each radiating element (main patch + parasitic patch) with via-holes.

4.4.4. Focal array coupling impact on primary source edge taper optimization solutions

Among the solutions presented to optimize the antenna primary (ACMPP) source edge taper, two of them offer the desired optimal edge taper of 12-14 dB. The dielectric slab on a single ACMPP and using a 2×2 sub-array as primary source. The objective of using the microstrip patch antenna (ACMPP) as the FFZP antenna primary source, is to integrate it in a focal array for beam steering solutions. Therefore the focal array impact on the edge taper optimization solutions radiation patterns are studied in this section.

4.4.4.1. Focal array coupling impact on ACMPP plus dielectric slab

Using a dialectic slab is one of the most efficient solution to obtain the desired edge taper and moreover it is the simplest solution as well. Therefore, the performance of this solution in case of an array of single ACMPP elements is studied. The 9×3 array is chosen for this study in order to be able to obtain a beam steering range ±8° in azimuth and ±2° in elevation in case of beam switching solution. This focal array characteristics for beam switching solution will be further detailed in next chapter. Moreover this array allows to have symmetrical coupling impact on central element of the 9×3 elements focal array. The array inter-element spacing is chosen to be a full guided wavelength at the parasitic patch substrate at 60 GHz, 2.88 mm, in order to minimize the natural inter-element coupling. This enables us to better evaluate the coupling occurred because of the dielectric slab. The E-field of a 9×3 ACMPP elements array with a dielectric slab on top is shown in figure 4-31. In this case only the central element is excited. As can be seen, there is a very strong coupling inside the dielectric slab that is perturbing the radiation of the primary source.

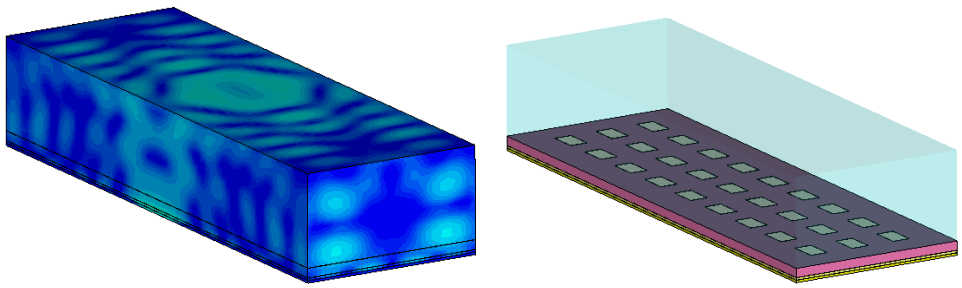

Figure 4-31: E-field cartography on an array of 9×3 ACMPP elements plus a dielectric slab (only central element excited).

Figure 4-32, compares the normalized radiation patterns of a 9×3 ACMPP elements array with and without the dielectric slab at both elevation and horizontal planes. As illustrated in figure 4-32, the dielectric slab perturbs the ACMPP radiation strongly when is being applied to an array. For the case without dielectric slab, the inter-element coupling and as wall larger substrate dimensions of an ACMPP in array comparing to single ACMPP, results in higher side lobe levels. For the case with dielectric slab, the increased side lobs levels of the ACMPP and also destructive interferences of coupled fields inside the slab (shown in figure 4-31), result in total deformation of the ACMPP radiation pattern.

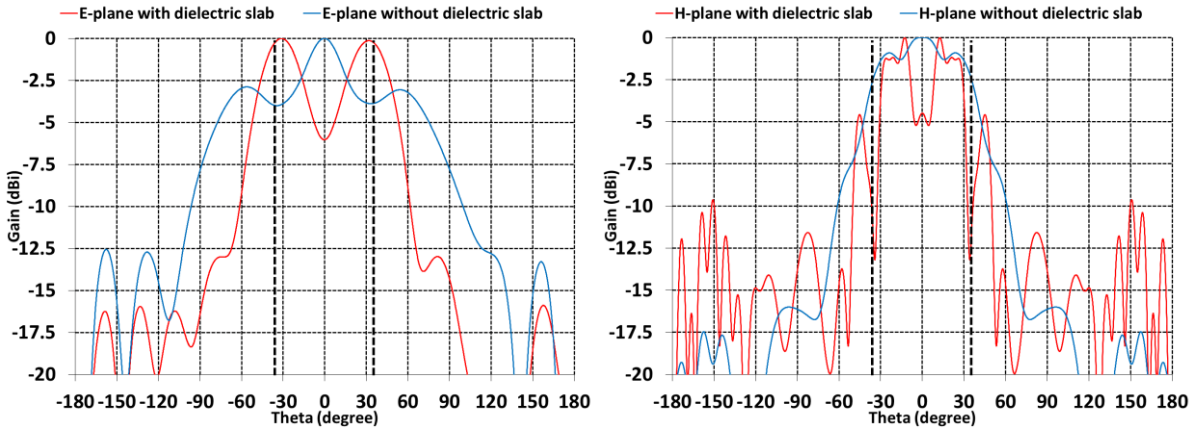

Figure 4-32: Normalized radiation patterns of a single ACMPP excited within a 9×3 ACMPP elements array with and without a λ_0(5mm) dielectric slab at 60 GHz : (a) E-plane (b) H-plane.

The main reason of this perturbation is high thickness of the dielectric slab and the fact that is not transparent. By reducing its thickness to half guided wavelength in the dielectric slab ($\lambda_g/2$), 1.58mm, the results presented in figure 4-33 are obtained. By using the half guided wavelength dielectric slab, an edge taper of 17 dB in E-plane and 7.5 dB in H-plane can be obtained. The reason of this asymmetry between the two planes is the non-symmetricity of the 9×3 elements rectangular array. By using symmetric array such, as circular array, this issue can be overcome and equivalent edge tapers in both planes can be obtained. However, the fact that the edge taper value depends on the focal plane array size, is an inconvenient and makes this solution exclusive and not a general solution to achieve a desired edge taper value independent from the focal plane array size.

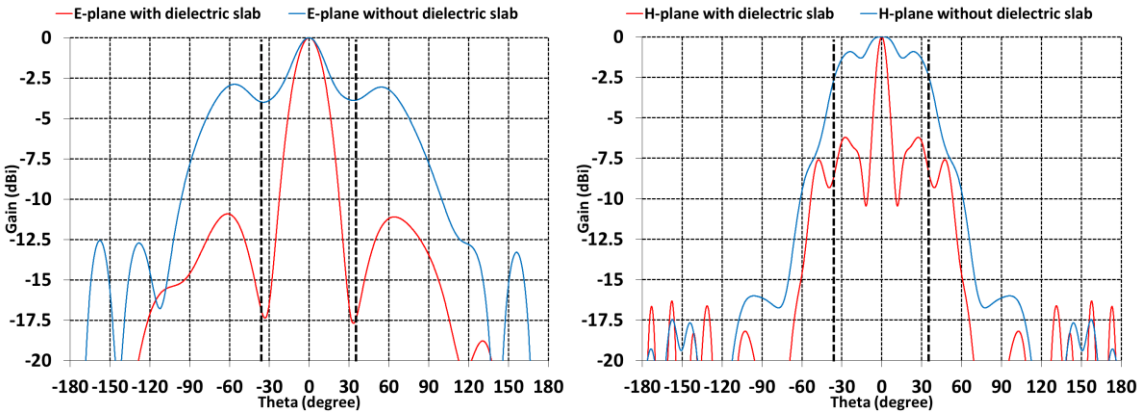

Figure 4-33: Normalized radiation patterns of a single ACMPP excited within a 9×3 ACMPP elements array with and without a $\lambda_g/2$ (1.58mm) dielectric slab at 60 GHz : (a) E-plane (b) H-plane.

To summarize, for a single ACMPP alone, when using a dielectric slab with thickness of λ_0 (5 mm at 60 GHz)) a suitable edge taper enhancement up to 14 dB is obtained. When deploying this solution in a focal array, strong E-field interferences in the dielectric slab perturbs the ACMPP radiation pattern strongly. However, by adjusting the dielectric slab thickness to $\lambda_g/2$ (1.58 mm at 60 GHz) this problem is solved. By comparing the radiation pattern of the ACMPP in a focal array for the two cases, with and without the dielectric slab (figure 4-33), edge taper enhancement is observed. This enhancement is not equal in both planes because of the non-symmetrical focal array (9×3 elements array), meaning that the edge taper of the primary source will depend directly on the focal array dimensions which makes this an exclusive solution and

not inclusive. Moreover, this solution suffers from limited frequency bandwidth, as the dielectric slab thickness is in function of guided wavelength. It was illustrated in simulations that the obtained edge tapers in figure 4-33 have a deviation of 13 dB over the V-band frequency range (57-66 GHz).

4.4.4.2. Focal array coupling impact on a sub-array of 2×2 ACMPP elements

As mentioned before, one other technique to improve the patch directivity and so its edge taper, is to use a sub-array of 2×2 ACMPP element instead of one single ACMPP as primary source. Figure 4-34, shows the E-field of a 2×2 sub-array excited in an array of 4×4 ACMPP elements. Contrary to the previous section where a 9×3 array was used to study the focal array coupling, a 4×4 array is used here. The reason is to be able to study a symmetrical coupling effect around the 2×2 sub-array.

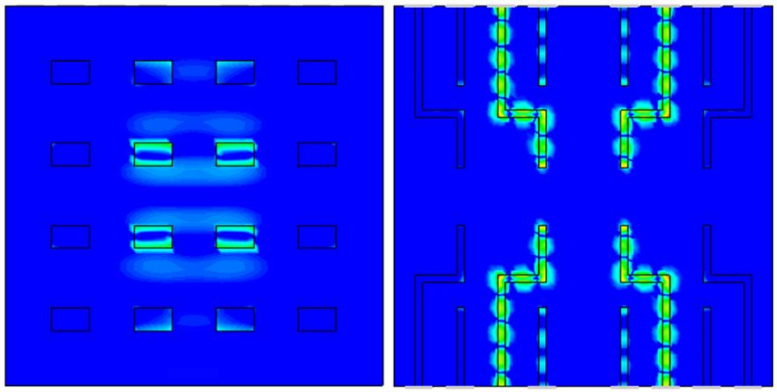

Figure 4-34: E-field distribution of the 4×4 array of ACMPP elements fed by feeding lines with a 2×2 sub-array excited at 60 GHz.

Figure 4-35, shows the radiation pattern of a 2×2 sub-array excited in the 4×4 array. Comparing with figure 4-21, where the 2×2 sub-array is excited alone without focal array elements, we observe some perturbations especially in E-plane where a side lobe is appearing around θ=30°. But comparing to the single ACMPP in a focal array, the fact of using the directive 2×2 sub-array reduces the coupling impact.

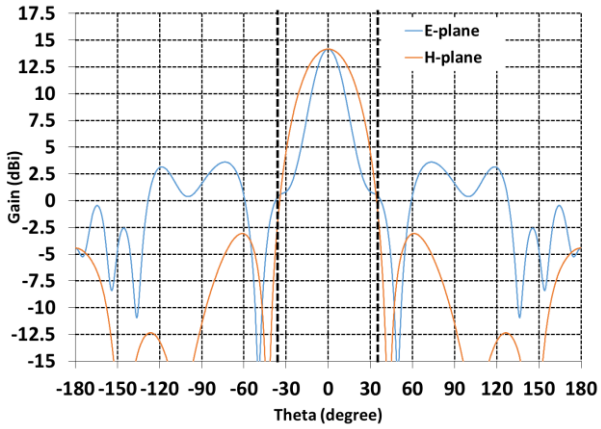

Figure 4-35: Radiation pattern of the 2×2 sub-array excited in a 4×4 focal array.

As presented in Table 4-6, other focal array impact on the sub-array is directivity and edge taper increase. Almost 3dB edge taper increase in both planes is observed. This means when designing the 2×2 sub-array and defining its inter-element spacing to obtain a desired edge taper, the focal array impact needs to be taken into account as well.

Table 4-VI:Coupling impact of focal array radiating elements and their feeding lines on 2×2 sub-array of ACMPP elements.

2×2 sub-array of ACMPPs	HPBW (E-plane)	HPBW (H-plane)	Edge Taper in H-plane (dB)	Edge Taper in E-plane (dB)
Alone	40.1°	37.4°	11.92	14.56
In 4×4 focal array	20°	36.7°	14.05	17.66

4.4.5. Conclusions on focal array couplings impact

The focal array coupling impact on the antenna performance was studied and quantified. It was observed that the focal array coupling has two main impacts on the primary source: 1- Radiation pattern perturbation, i.e. increased and unbalanced side lobes, 2- Directivity and therefore edge taper increase due to the array effect of the focal array. These focal array perturbation on the primary source, translates into almost 3 dB gain loss for the FFZP antenna solution fed by a focal array comparing to the FFZP fed by single ACMPP element.

Moreover, the focal array coupling on the best two edge taper optimization solutions, one using a dielectric slab on single ACMPP and other using a sub-array of 2×2 ACMPP elements as primary source, were studied. The results show that, when using sub-array of 2×2 ACMPP elements as primary source, the focal array coupling is not noticeable. What is impacting the primary source in this case is the array factor of the focal array. This effect increases the directivity and therefore the edge taper the 2×2 ACMPP elements sub-array. However it can be can be controlled by adjusting the sub-array inter-element spacing. For the other solution, where a dielectric slab is used, the focal array coupling can be controlled by adjusting the dielectric slab thickness. However this solution is exclusive as the obtained edge taper for the primary source depends on the focal array dimensions (slab aperture). Moreover it is frequency dependent and suffers from limited frequency bandwidth as the slab thickness depends strongly to the guided wavelength.

Main conclusion is when designing a lens based antenna solution fed by a focal array, the lens and the primary source design need to be adjusted accordingly taking into account the focal array coupling.

4.5. Conclusions

In this chapter, the beam steering characteristics of the FFZP antenna where defined in section 2. The immediate conclusion was that the waveguide aperture as a primary source is not suitable for beam steering solutions because of its large physical dimensions and non-compatibility with RF circuit components. Therefore a primary source based on PCB technology is required. To fulfill this requirement, an Aperture Coupled Microstrip Patch (ACMP) antenna as a primary source for the FFZP antenna was introduces in section 3. The ACMP performance as a single primary source as well as focal array element was studied. Some issues such as limited bandwidth and low directivity (edge taper) were detected and solutions to improve them where proposed. The focal array coupling impact was studied in details in section 4 and it was concluded that coupling impact is noticeable and should be taken into account during the antenna and its focal array design.

Based on the established beam steering characteristics of the FFZP antenna, and the focal array design consideration in this chapter, two beam steering solutions are proposed in the following chapter 5.

4.6.References

[1] J. Ala-Laurinaho, J. Aurinsalo, M. Kaunisto, A. Lamminen, J. Nurmiharju, A.V. Räisänen, J. Säily, P. Wainio, "2-D beam-steerable integrated lens antenna system for 5G E-band access and backhaul*," IEEE Trans. Microw. Theory Techn*., vol. 64, no. 7, pp. 2244–2255, Jul. 2016.

[2] J. Reinholdt, "Cylindrical Luneburg lens antenna for multi-beam small cell wireless backhaul applications," *M.S. thesis*, Luleå University of Technology, 2014.

5. Chapter 5 : FFZP Antenna Beam Steering Solutions: Simulations & Measurements

5.1. Introduction

The beam steering characteristics of the FFZP antenna were defined in chapter 4. The immediate conclusion was that the waveguide aperture as a primary source is not suitable for beam steering solutions because of its large physical dimensions and non-compatibility with RF circuit components. Therefore a primary source based on PCB technology is required. To fulfill this requirement, an Aperture Coupled Microstrip Patch (ACMP) antenna acting as a primary source for the FFZP antenna was introduced in chapter 4. The ACMP performance was studied as a single primary source as well as focal array element. Some issues such as limited bandwidth and low directivity (edge taper) were detected and solutions to improve them were proposed. It was demonstrated in section 3 of chapter 4 that by adding a parasitic patch on top of the ACMP, its bandwidth is increased enough to cover all V-band. Therefore in this chapter the ACMP plus Parasitic patch (ACMPP) is used as the as the primary source.

In this chapter two beam steering solutions are proposed for the FFZP antenna. These solutions are based on established beam steering characteristics and focal array design considerations in the previous chapter. These solutions are studied both by 3D model simulations and prototype measurements. Therefore, before discussing these solutions, realization considerations of the focal array radiating element, the ACMPP, and consequently required design modifications are presented in section 2. Also, as is preferred by the clients to have a single waveguide input for the final antenna solution, a novel wideband single layer microstrip-to-waveguide transition is proposed in section 3. This transition is tested in the beam steering solutions prototypes as well.

Two beam steering solutions are studied in sections 4 and 5. The first solution is based on switching between focal array elements (beam switching technology) [1]. To verify the FFZP antenna functionality with this solution, passive porotypes are realized and measured. The second solution, which offers a high resolution continuous beam steering, is based on focal array amplitude tapering when using a 2×2 sub-array as primary source [2-3]. For this solution as well, prototypes are realized to validate the concept.

To evaluate the beam steering solutions independent from the folded structure, two types of antenna structures are measured and simulated for each beam steering solution. In first case, the non-folded FZP (lens alone) is measured with the beam steering circuits as focal source (figure 5-1(a)). In the second case, the complete Folded FZP antenna structure (figure 5-1(b)) fed by the beam steering focal arrays is simulated and measured.

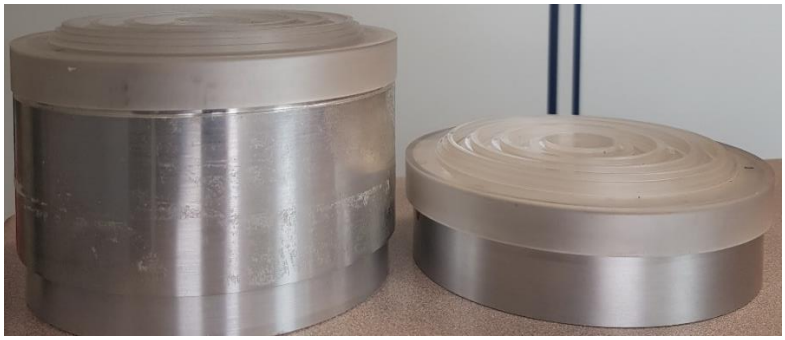

(a) (b)

Figure 5-1: Photograph of the (a) Non-folded FZP antenna structure prototype, and (b) Folded FZP (FFZP) antenna structure prototype.

5.2. ACMPP fabrication considerations

For manufacturing the ACMPP, some modifications in its design are required in order to optimize the manufacturing process as well as its cost. The complete structure layout of the modified ACMPP for manufacturing is presented in figure 5-2. One of the modifications is to consider bonding films between the substrates to stack them together. Until now, the simulations were done without considering these bonding layers. Moreover in order to reduce the manufacturing cost, after consultation with different PCB manufacturers, it was decided to change the substrates materials as well.

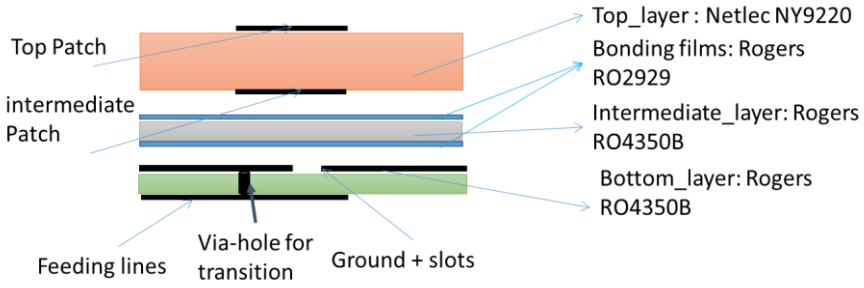

Figure 5-2: Structure layout of the ACMPP for manufacturing.

As illustrated in Figure 5-2, the bottom layer is a two-face printed substrate (microstrip feedlines and ground/slot), the intermediate layer is a dielectric substrate with two bonding films on two sides, so that the top layer has two metallic etched films (main patches and parasitic patches). The choice of substrate materials is important in terms of RF performance,

mechanical stability and cost. The chosen materials for the three substrate and bounding films are:

- Bottom substrates : Rogers RO4350B with ε_r=3.66 and $\tan\delta = 0.0037$ (at 10 GHz)
- Intermediate substrates : Rogers RO4350B with ε_r =3.66 and $\tan\delta = 0.0037$ (nominal at 10 GHz)
- Top substrate : Netlec NY9220 with ε_r =2.2 and $\tan\delta = 0.0009$ (at 10 GHz)
- Bonding films: Rogers RO2929 with ε_r =2.94 and $\tan\delta = 0.003$ (at 10 GHz)

The thickness of these layers are:

- Bottom Layer (RO4350B): 0.168 mm
- Intermediate Layer (RO4350B): 0.168 mm
- Top Layer (Netlec NY9220): 0.508 mm
- Bonding Films (RO2929) : 0.038 mm
- Metallic cooper etched films : 0.018mm.

The diameter of the via-holes are 0.36 mm. They contribute to the microstrip-to-waveguide transition, detailed in the next section.

Taking into account all modifications, the ACMPP design parameters were re-optimized in order to have an adapted wide band solution in the V-band frequency (57-66 GHz). The new ACMPP design dimension are presented in Table 5-1.

Table 5-I: ACMPP prototype dimesions.

Top patch dimensions	1.2 mm × 0.96 mm	Feed line width	0.34 mm
Intermediate patch dimensions	1.1 mm × 1.1 mm	Slot aperture	1.07 mm × 0.1 mm
Bottom layer thickness	0.168 mm	Intermediate layerthickness	0.168 mm
Top layer thickness	0.508 mm	Bonding layers thickness	0.038 mm

The reflection coefficient and the radiation pattern of the new ACMP are presented in figure 5-3. This ACMP offers a wide bandwidth of more than 35% for return loss better than 10 dB (30% for return loss better than 15 dB) and has a low edge taper of 2.56 dB at E-plane and 1.96 dB at H-plane.

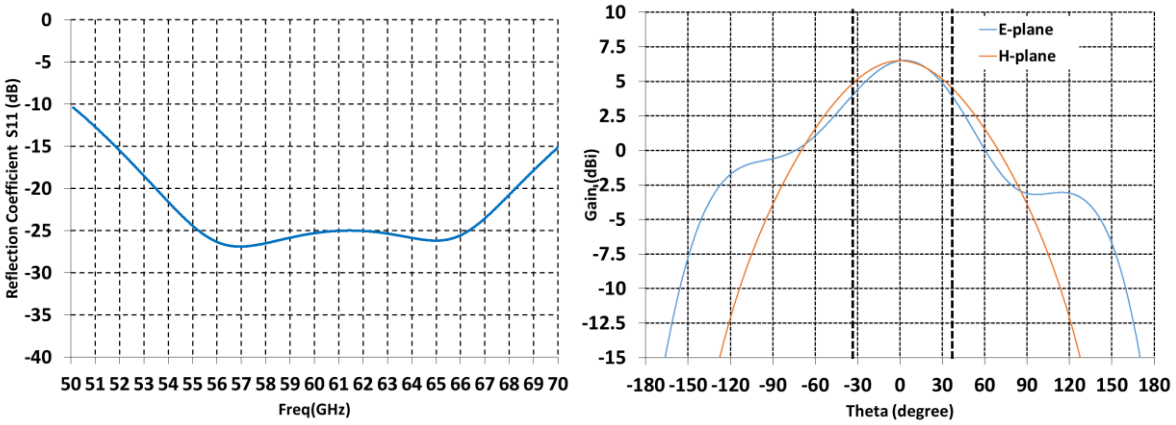

(a) (b)

Figure 5-3: ACMPP optimized for manufacturing (a) Reflection Coefficient, and (b) Radiation patterns at 60 GHz.

As mentioned in the coupling studies section in chapter 4, one solution to reduce the coupling between ACMPP elements in a focal array, is to use via-holes around the main and parasitic patches in order to isolate them from neighboring elements, presented in figure 5-4. After discussing with different PCB manufacturers, it was concluded that the manufacturers are not able to realize the metallized via-hole 1 because the ratio between via-hole height and diameter is larger than 1 and the bonding layer (RO2929) is thermoplastic and will become liquid with two stratifications.

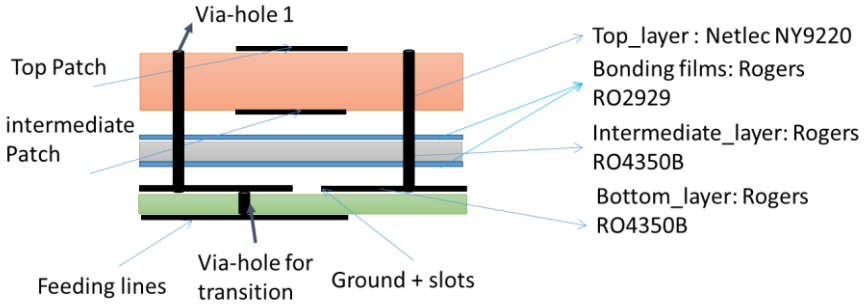

Figure 5-4: Primary design of ACMP with isolating via-holes layout.

So in order to integrate via-hole surrounding the patches in the two top layers (top layer and intermediate layer) the ACMPP structure needs to be changed. As a results of a collaboration with one of the PCB manufactures, the new structure in figure 5-5 is proposed for the cases where isolating via-holes are required.

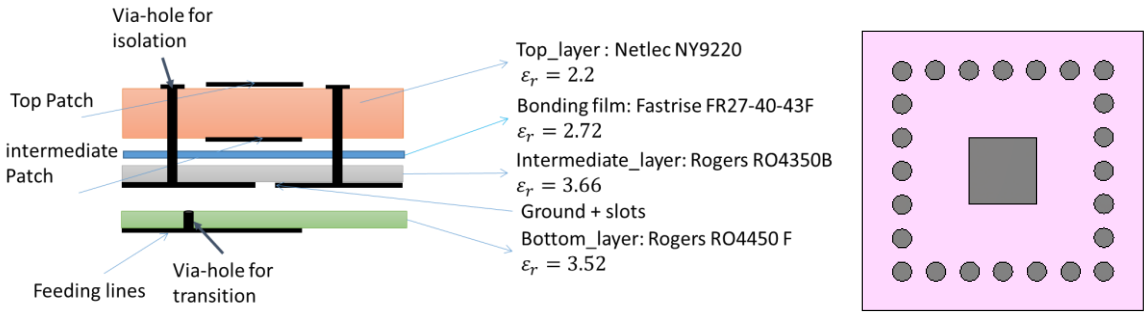

Figure 5-5: ACMPP final structure for integrating isolating via-holes structure layout and it top view.

The via-holes for isolation are placed with 1.8 mm distance from the center of the patch and have a diameter of 0.35 mm. The design parameters of this new ACMPP structure are presented in Table 5-2.

Table 5-II: ACMPP with isolating via-holes design dimensions.

Top patch dimensions	1.14 mm × 1 mm	Feed line width	0.42 mm
Intermediate patch dimensions	1.2 mm × 1.2 mm	Slot aperture	1.05 mm × 0.1 mm
Bottom layer thickness	0.2 mm	Intermediate layer thickness	0.168 mm
Top layer thickness	0.508 mm	Bonding layer (FR27) thickness	0.1 mm

The chosen materials for the three substrate and bonding film are:

- Bottom substrate : Rogers RO4450F with ε_r=3.52 and $\tan\delta = 0.004$ (at 10 GHz)
- Intermediate substrate : Rogers RO4350B with ε_r =3.66 and $\tan\delta = 0.0037$ (at 10 GHz)
- Top substrate : Netlec NY9220 with ε_r =2.2 and $\tan\delta = 0.0009$ (at 10 GHz)
- Bonding film: FR27-40-43F with ε_r =2.72 and $\tan\delta = 0.0017$ (at 10 GHz)

The reflection coefficient and radiation pattern of this ACMPP structure are presented in figure 5-6. This ACMPP with isolating via-holes offers an edge taper of 3.15 dB at E-plane and 2 dB at H-plane. Its bandwidth is 23% and it covers 53.6-68 GHz with return loss more than 10 dB.

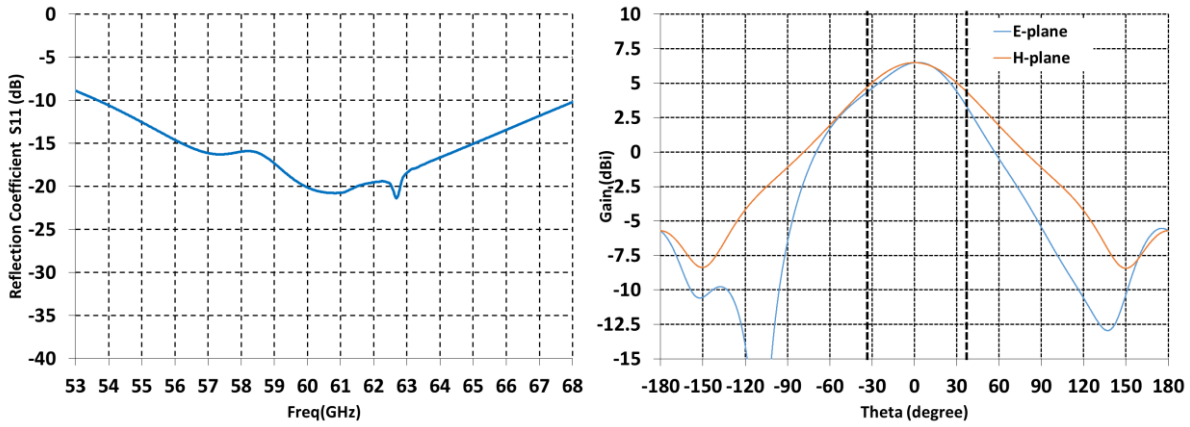

(a) (b)

Figure 5-6: ACMPP with isolating via-holes (a) Reflection Coefficient, and (b) Radiation patterns at 60 GHz.

Both of the structures presented in figures 5-2 and 5-5 are used in two different beam steering solutions and discussed in detail in section 4 and 5. But before that, in the following section a novel wide-band microtstrip to standard WR15 waveguide transition is proposed.

5.3. Microstrip line to waveguide transition

As has been said previously, the antenna access should be a standard WR15 rectangular waveguide to be compatible with the radio equipment at V-band. In order to feed a microstrip antenna by a standard waveguide, a transition between standard waveguide and the microstrip line is required. A transition is qualified based on its *S* parameters, S_{11} (return loss) and S_{21} (transmission loss). The lower the overall transmission loss is, the better is the transition. A good transition should have a S_{11} less than -12 dB in the operating bandwidth. Moreover, keeping a low form factor of the antenna structure is essential today as compact antennas are requested more and more by the customers.

The main issue of existing waveguide-to-microstrip line-transition (WMT) solutions is their limited bandwidth, because of the microstrip technology nature. Current solutions to improve the bandwidth are based on back ended (short circuited) waveguides on the other side of the circuit [4-5], or consist in adding additional substrate layers with coupling the transition probe to the microstrip line using coupling slots [6]. These solutions increase the dimensional structure, the manufacturing complexity and thus the cost. Also the integration of the first solution with the ACMPP is not possible without impacting the antenna radiating layers due to the additional short-circuit upper waveguide.

Moreover, in most cases, it is required that the WMT be physically vertical (see figure 5-7).

A specific solution must then be developed for our work. In this solution, the waveguide is vertically and directly coupled to the microstrip line using a probe without any additional substrate or cavities. Figure 5-7 present the overall 3D view of the vertical waveguide to single substrate microstrip line.

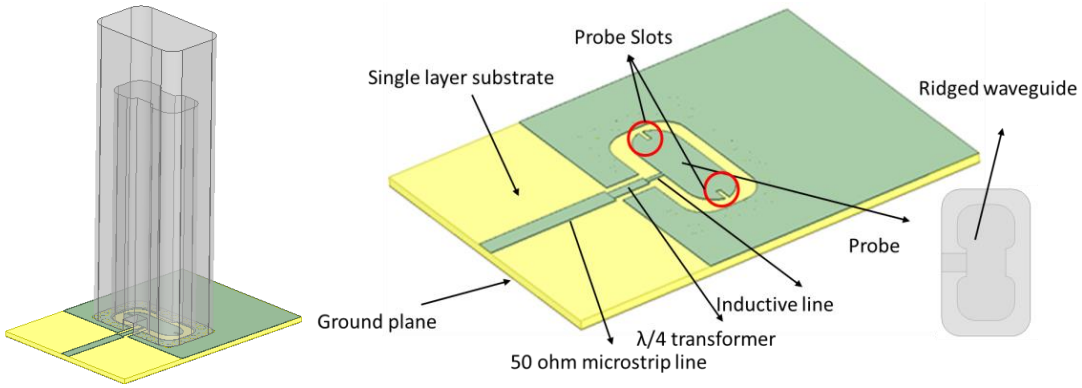

Figure 5-7: 3D overall view of the new waveguide-to-microstrip line transition.

To obtain a wide-band single layer WMT, different features are deployed. First of all, we use two slots in the probe, which help creating a second resonance frequency, resulting in an increased bandwidth. Also by varying the slots lengths and widths, one can easily tune the WMT operating frequency. The second feature consists on an impedance matching circuit using an inductive line and a $\lambda/4$ transformer. The cascade of these two lines between the probe and output microstrip line enables matching the probe between the waveguide and any microstrip line, depending on the application. The third feature uses a ridged waveguide (in E-plane), with integrated transition to standard waveguide, where the ridges act as parasitic short-end element for the probe to improve the bandwidth. Moreover, the probe is connected by its radiating side (E-plane) to the microstrip line which assures smooth mode conversion between microstrip quasi-TEM mode and waveguide TE_{10} mode avoiding no resonances and ripples in the S-parameters.

The achieved results of the new WMT for V-band (57-66 GHz) are presented in figure 5-8. For this transition the substrate dielectric is Rogers RO4450F with permittivity of 3.52 and loss tangent of 0.004. As we can see, the transmission loss is always better than 1.66 dB at V-band (57-66 GHz) and the return loss is better than 10 dB for 56.85 GHz – 67 GHz frequency range. This correspond to a frequency bandwidth of 16.4%. This solution permits to reduce the cost, realization complexity and form factor of the antenna.

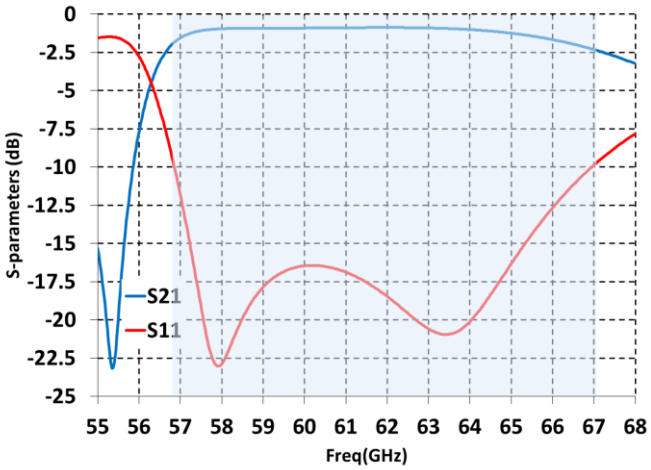

Figure 5-8: Transmission Loss (S12) and Reflection Loss (S11) of the Waveguide (WR15) to microstrip transition designed for V-band (57-66 GHz) with RO4450F substrate.

The substrate dielectric material can be any standard material, although the transition design parameters need to be adjusted regarding to it. The RO4450F used for simulations in figure 5-8, is used in bottom layer of the ACMPP presented in figure 5-5. This will be used in one of the beam steering solutions that will be presented in the following sections. The design parameters of the microstrip to waveguide transition are presented in Table 5-3 for the case where the RO4450F is used as substrate.

Table 5-III: Waveguide to microstrip line transition design dimension for RO4450F as microstrip line substrate.

Probe diemnsions	3.42mm×1.06mm	Feed line thickness	0.42mm
Probe bending	0.7 mm	Inductive line dimensions	0.1mm×0.42 mm
Probe slots dimensions	0.35 mm×0.1 mm	λ/4 line dimensions	0.25 mm×0.9 mm
Substrate thickness	0.2 mm	Waveguid ridge diemnsions	0.9 mm×0.3 mm
Waveguide blending	0.6 mm	Waveguid ridge blending	0.3 mm

The ACMPP presented in figure 5-2 will be deployed in another beam steering solution. As this microstrip element uses RO4350B with dielectric permittivity of 3.66 for its microstrip feeding line substrate, the WMT design is re-optimized and RO4450F is replaced by RO4350B. For this case also the same transition structure, but with adjusted design parameters is used. The waveguide to microstrip transition *S* parameters of this substrate are presented in figure 5-9. As presented in this figure, the insertion loss is always better than 1.8 dB at V-band (57-66 GHz) and the return loss is better than 10 dB for 56.78 GHz – 68 GHz frequency range. This corresponds to a frequency bandwidth of 18.4%.

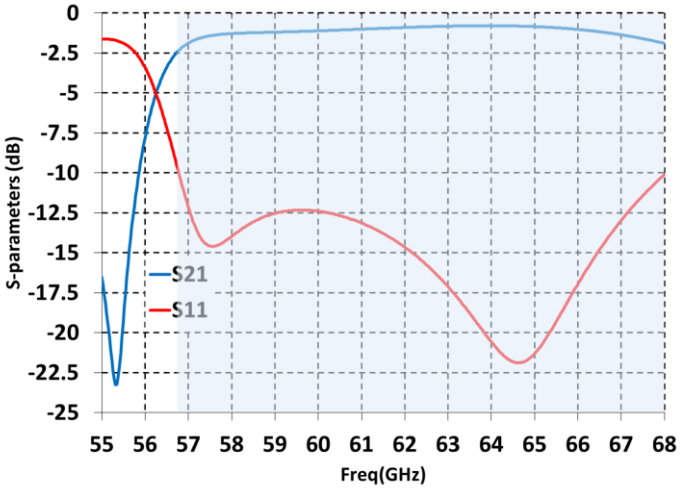

Figure 5-9: Transmission Loss (S12) and Reflection Loss (S11) of the Waveguide (WR15) to microstrip transition designed for V-band (57-66 GHz) with RO4350B substrate.

Table 5-4 presents the design parameters for substrate material RO4350B.

Table 5-IV: Waveguide to microstrip line transition design dimension for RO4350B as microstrip line substrate.

Probe diemnsions	3.2mm×1.05mm	Feed line thickness	0.34mm
Probe bending	0.7 mm	Inductive line dimensions	0.1 mm×0.5 mm
Probe slots dimensions	0.35 mm×0.1 mm	λ/4 line dimensions	0.2 mm×0.8 mm
Substrate thickness	0.168 mm	Waveguid ridge diemnsions	0.9 mm×0.3 mm
Waveguide blending	0.6 mm	Waveguid ridge blending	0.3 mm

Also a ridged waveguide to perfect WR15 step-wise transition is designed. This transition presented in figure 5-10, is required to minimize the losses when the antenna is excited by a standard WR15 input.

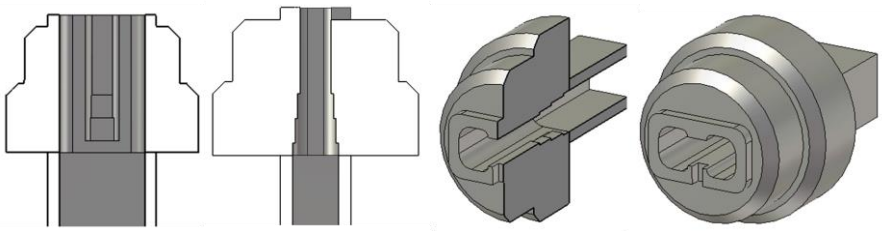

Figure 5-10: Ridged waveguide to standard WR15 step-wise transition in different views.

The transmission loss of this transition is less than 0.02 dB and its return loss is better than 24 dB. Figure 5-11 shows the S-parameters curves.

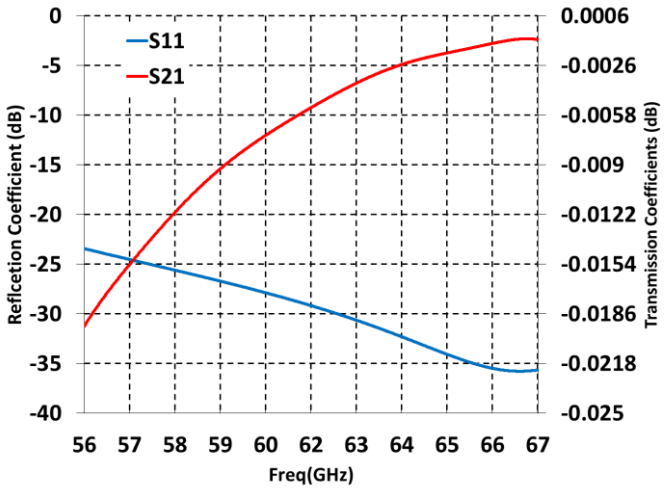

Figure 5-11: Transmission Loss (S12) and Reflection Loss (S11) of the Ridged waveguide to perfect WR15 transition.

A schematic representation of the new WMT and the photos of the fabricated components are presented in figure 5-12. The measured performance of this transition and its assembling within the antenna structure are presented in the following sections, dedicated to the beam steering antenna solutions.

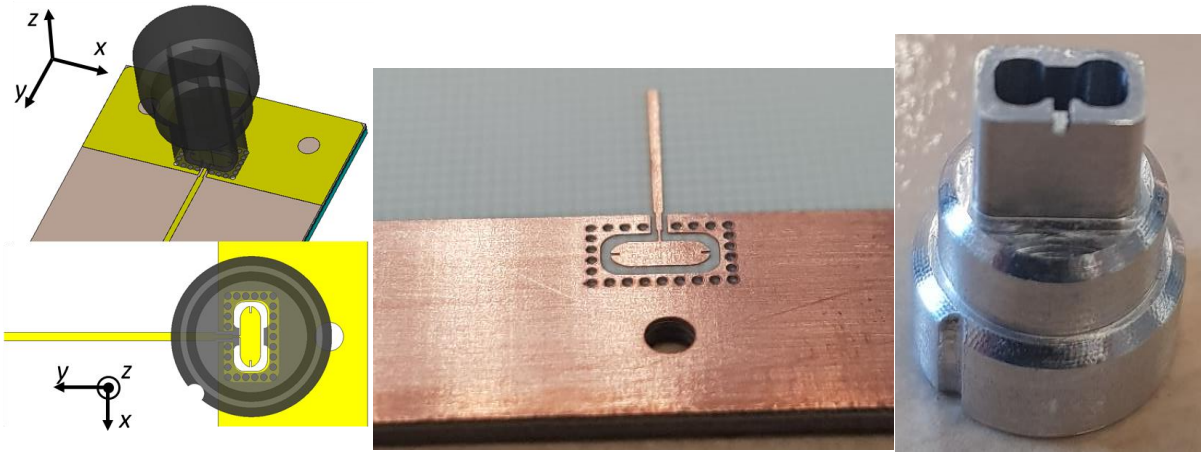

(a) (b) (c)

Figure 5-12: Assembling of the new WMT: (a) 3D schematic representation, (b) photograph of fabricated new WMT, (c) ridged waveguide with integrated transition to WR15.

Figure 5-13 present the simulated results of a study on the ridged waveguide and mirostrip probe alignment tolerance in all three direction of *x*, *y* and *z* axes. This study is done for WMT designed for the RO4350B substrate. It can be observed that in case of a gap on z-axis between the waveguide and the microstrip probe, the WMT transition remains matched up to 0.1 mm gap and then will be mismatched on the low band and remains matched only for upper side of the frequency band (> 64 GHz). In case of misalignment on the *x-y* plane, the WMT transition can tolerate only 0.1 mm displacement.

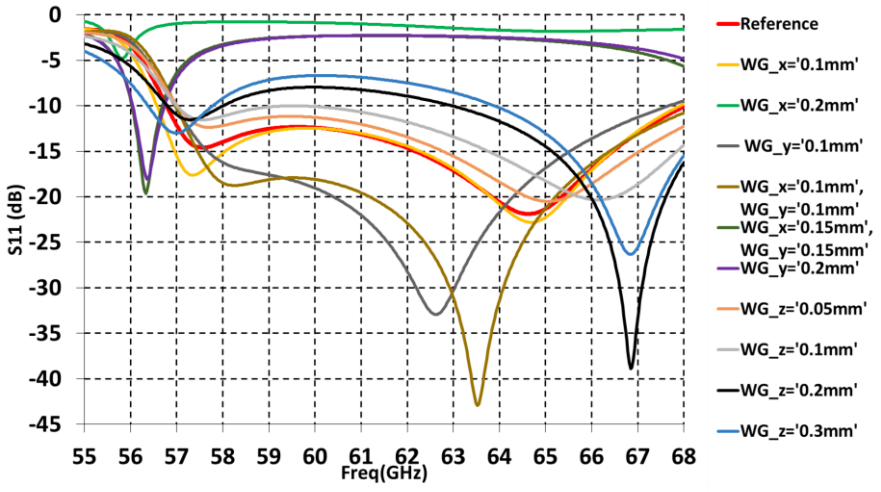

Figure 5-13: Alignment tolerance study of the ridged waveguide and microstrip probe.

To conclude, in this section, a novel wide-band single-layer waveguide-to-microstrip line transition is proposed. Depending on substrate dielectric material, this solutions offers bandwidth up to 18%. However, the proposed WMT requires very high precision alignment and can tolerate only up to 0.1 mm of displacement on either of 3D directions. This transition can be used in any antenna or RF circuit where a direct transition from a microstrip line to standard waveguide is required.

5.4.Beam steering solution: beam switching

5.4.1. Introduction

As presented in detail in chapter 4, the FFZP antenna main beam can be steered by displacing its focal source. Practically, it's more convenient to have focal array in the lens focal plane and switch between the focal array elements, for example from MMIC switches [1]. In order to verify this solution for the FFZP antenna, a 25 ACMPP element focal array is designed. Figure 5-14(a) presents the top view of this array.

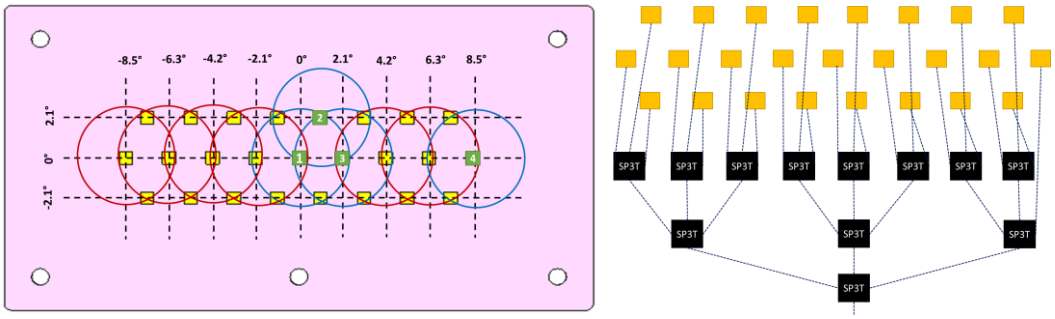

(a) (b)

Figure 5-14: 25 elements Beam switching focal array : (a) top view, (b) schematic representation of required switches.

As shown in figure 5-14(b), to have an active beam switching focal array, at least twelve 3-ports MMIC switches (SP3T) plus additional RF chains (namely dividers, filters, LNAs and PAs) are required for the focal array. However, as the circuit design was not an objective of this project, it was decided to realize passive prototypes without using MMIC switches. For this, 4 different focal arrays where designed and realized. For each circuit only one ACMPP element is excited and depending on the position of the excited ACMPP, the FFZP antenna beam will be steered. The radiating part of all 4 focal array circuits are identical to figure 5-14(a). In this figure, the four radiating elements are excited separately in four different focal arrays and are identified in green colors and are numerated. The focal array elements (ACMPPs) design parameters have already been presented in Table 5-1 in section 3 of this chapter.

On each of the three rows, the inter-element spacing is 3.6 mm, which corresponds to $0.72\lambda_0$. The substrate dimensions are 49 mm×27 mm and the five holes around the circuit are for fixing purposes. The meshing layout of the array is chosen to be triangular in order avoid nulls at 45°

planes. This can be verified by the 3 dB contours demonstrated by red circles around each focal array element in figure 5-14(a). The position and diameter of these contours are calculated knowing the HPBW of the FFZP antenna fed by the ACMPP and also knowing the relation between the main beam direction and primary source displacement from the focal point, both presented in chapter 4. In order to have a clear image for the 3 dB contours, they have been put only around the central raw of the array plus only one element on vertical direction. The 3 dB contours of the beam that will be measured separately using one of the circuits are in blue instead of red.

The four different focal arrays are exposed in figure 5-15. Their top side are all identical and same as figure 5-14(a) and what differentiates them is the microstrip feeding line design and the coupling slot position that depends to position of the excited patch. The numerations of the focal arrays circuits presented in figure 5-15 indicate the patch number that will be excited in figure 5-14. The microstrip feeding line of each circuit was designed and optimized separately to minimize transmission loss. The microstrip line to waveguide transition used is the same design presented in section 3 of this chapter.

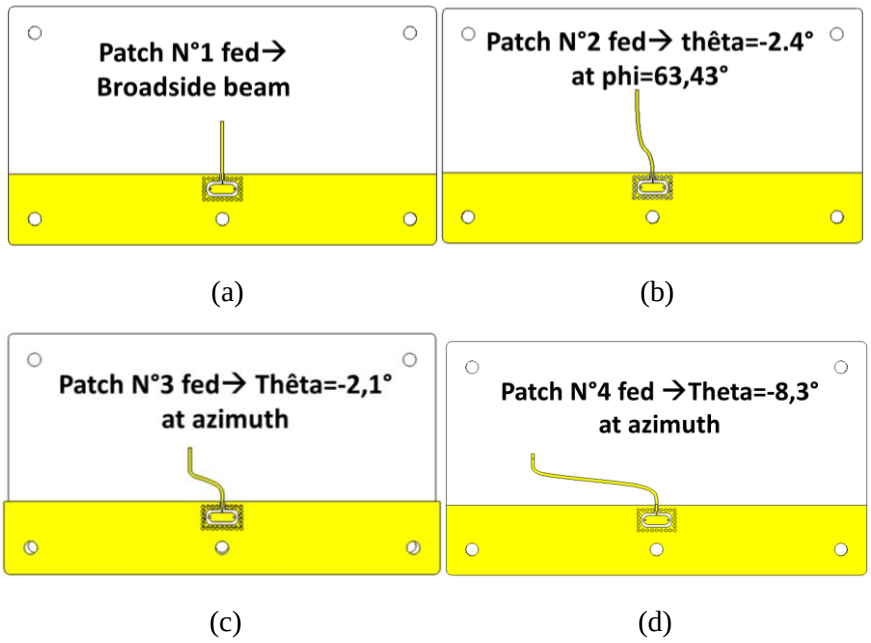

Figure 5-15: Beam switching passive circuits design : (a) BS N°1, (b) BS N°2, (c) BS N°3, and (d) BS N°4.

Figure 5-16 shows the photos of the realized prototypes with the switching circuits of figure 5-15. As can be seen, metallic screws are used to fix the circuits to the cylindrical structure in order to assure a good electrical contact between the input waveguide and the microstrip to waveguide transition.

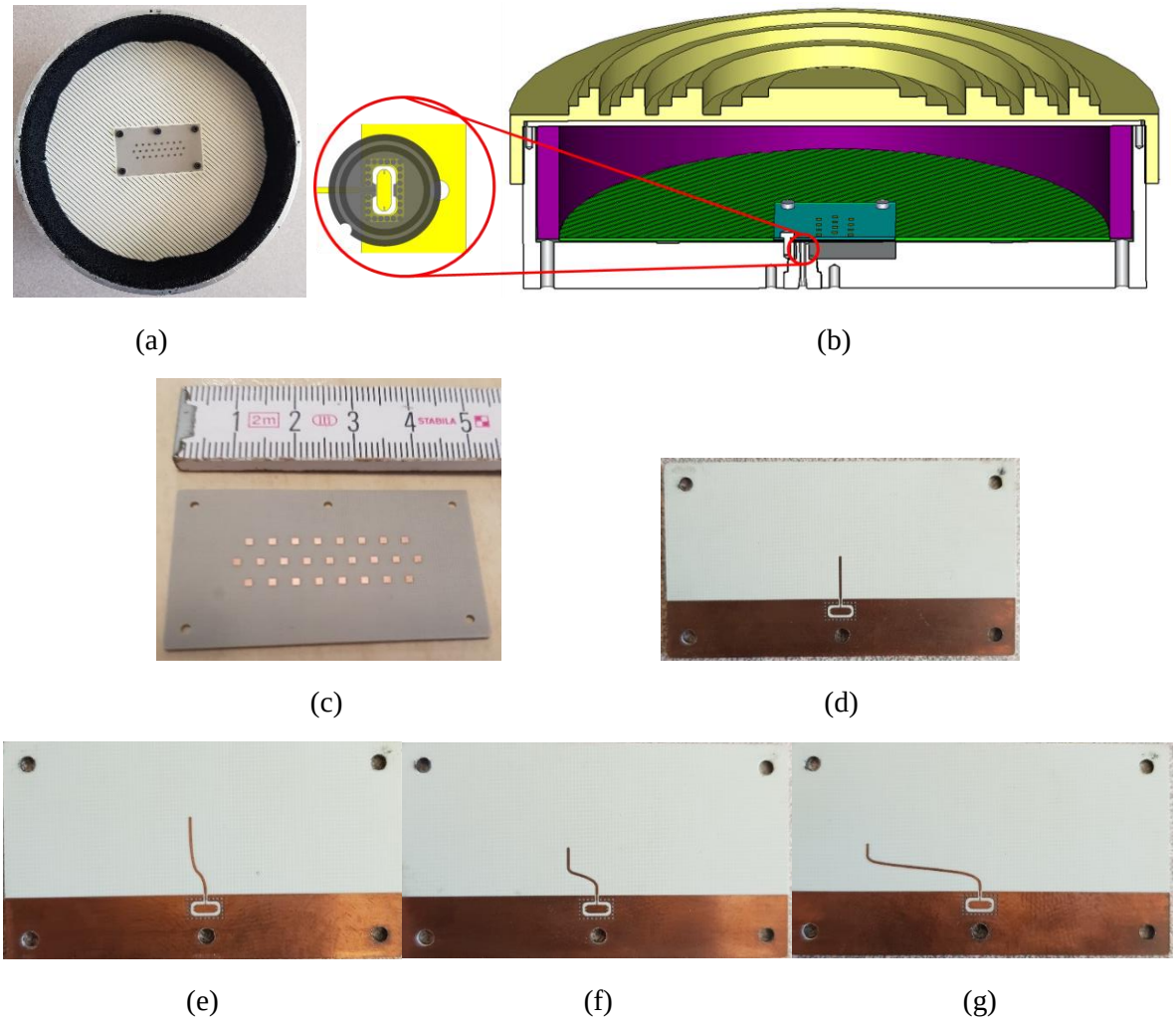

Figure 5-16: Photograph of the beam switching passive circuits prototypes : (a) Top-view of the circuit installation within the antenna structure, (b) schematic cut-view of the complete folded antenna structure (c) top view of the circuits, (d) bottom view of circuit BS N°1, (e) bottom view of circuit BS N°2, (f) bottom view of circuit BS N°3, and (g) bottom view of circuit BS N°4.

The measured and simulated reflection coefficient of all four circuits excited by their waveguide to microstrip transition are compared in figure 5-17. Then network analyzer was calibrated using calibration wizard for its V-band module for a WR15 output waveguide. As it can be observed, the circuits don't have a similar behavior. This is natural because they excite different ACMPP element and therefore they have different microstrip feed lines. The differences between simulation and measurement are due to the prototype structure where there may not be a perfect electrical contact between the circuits and the waveguide, and unfortunately this is not easily verifiable. Also, we should consider manufacturing inaccuracies that cause different results in measurement and simulation.

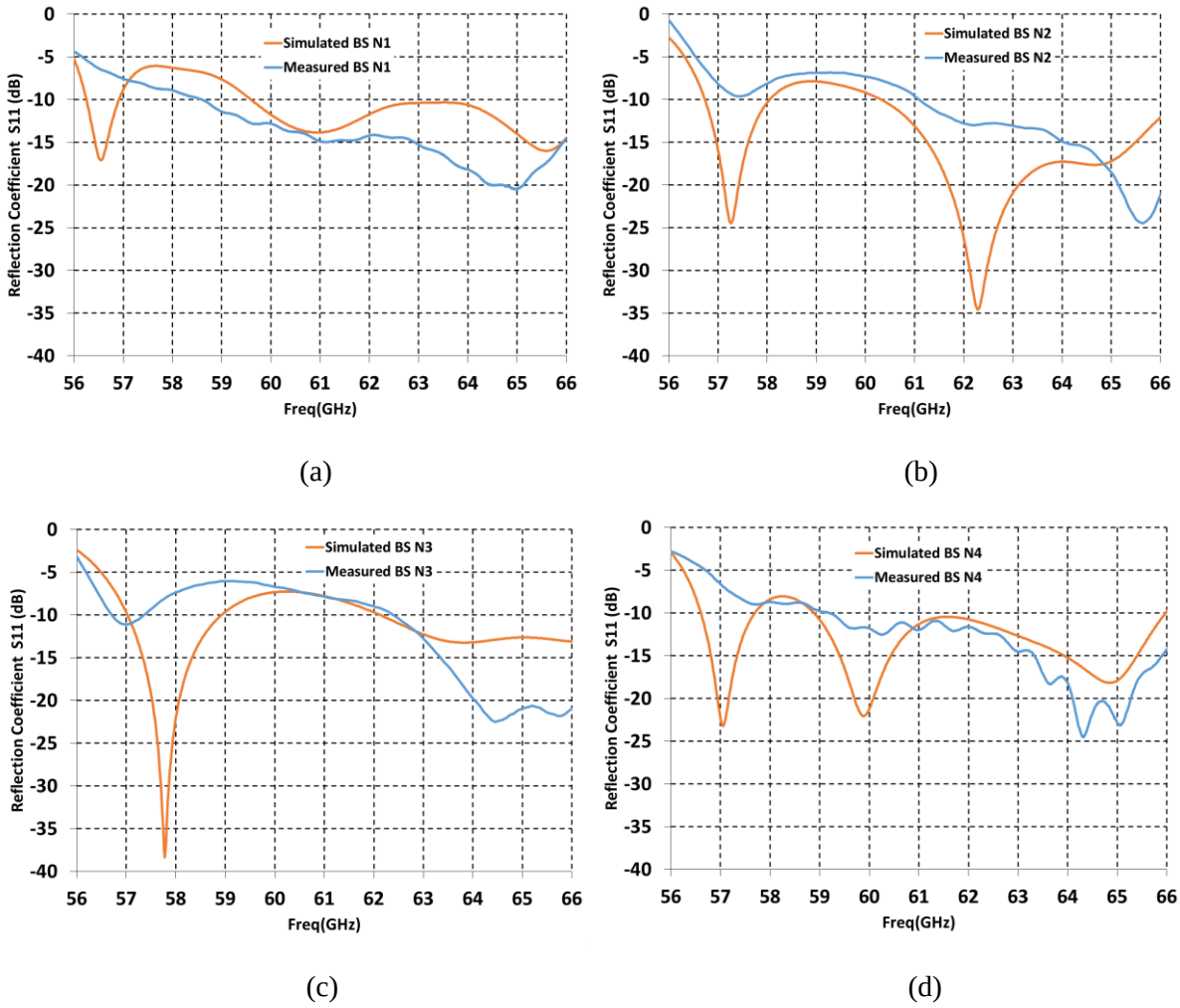

Figure 5-17: Measured and simulated reflection coefficients of beam switching focal arrays : (a) BS N°1, (b) BS N°2, (c) BS N°3, and (c) BS N°4.

The reflection coefficient results are not optimal neither in measurements nor in simulations over the targeted frequency V-band (57-66 GHz). However, the objective of these prototypes is to compare the radiation patterns of the FFZP antenna fed by these four circuits and measure the antenna beam steering characteristics. The circuits are functional and we were able to achieve this objective. For a future optimization, it will be necessary to re-optimize the circuit's impedance matching so they could cover all the V-band.

5.4.2. Non-folded FZP antenna and «beam switching»

In this section, in order to verify the beam switching circuits functionality, the non-folded FZP lens antenna is simulated and measured being excited by them. Figure 5-18 compares the simulated and measured radiation patterns for the non-folded FZP lens (figure 5-1(a)) at 60 GHz. As presented in this figure, there is a good agreement between simulation and measurement for broadside beam obtained by exciting the FZP lens using beam switching circuit BS N°1. For this comparison the complete structure of the prototype, meaning the circuit N°1, the FZP lens and the absorber is simulated using *CST* Time domain solver (simulation model presented in figure 5-18(g)). As this simulation is time consuming, for the rest of the

circuits the FZP lens is simulated without absorber and excited with the imported far field of the circuits and simulated using *CST* Integral Equations (IE) solver (simulation model presented in figure 5-18(h)). It is noticeable that for the circuits BS N°2, BS N°3 and BS N°4 the side lobe levels for $|\theta| > 36.9°$ are higher in simulation comparing to the measurements, because of the absence of the absorber in simulations. Beside this, simulations and measurements are in good agreement in terms of main beam direction, HPBW and first side lobe levels. It should be noted that for the patch N°2, the main beam direction is neither at E-plane nor at H-plane but is at phi=63.43° plane. Therefore, we could not trace its radiation pattern in measurement at its correct plane. For this reason, only its simulated radiation pattern at phi=63.43° plane is presented in figure 5-18(e). Also the H-plane radiation patterns for FZP fed by circuits N°3 and N°4 are not presented as well since we have beam steering only in one plane (E-plane). Moreover, it should be noted that radiation patterns are normalized regarding to the broadside beam (N°1) gain level so the scan loss is observable.

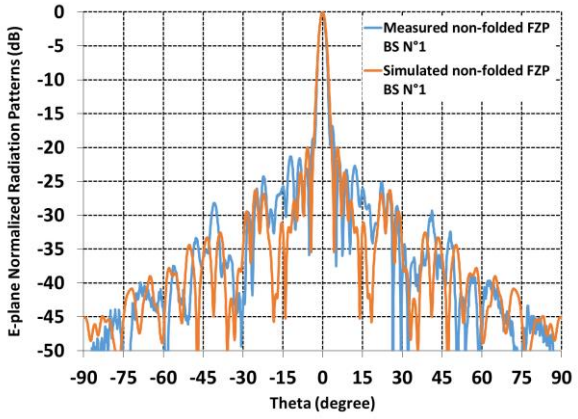

(a)

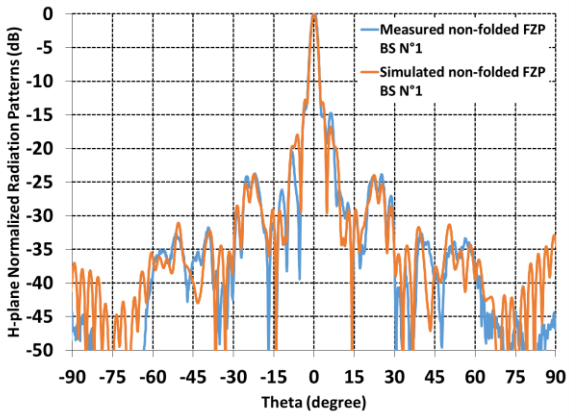

(b)

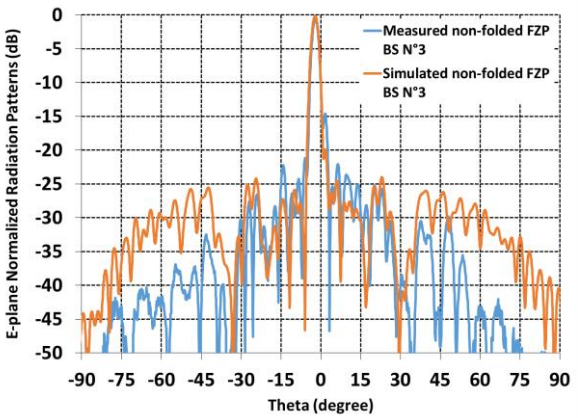

(c)

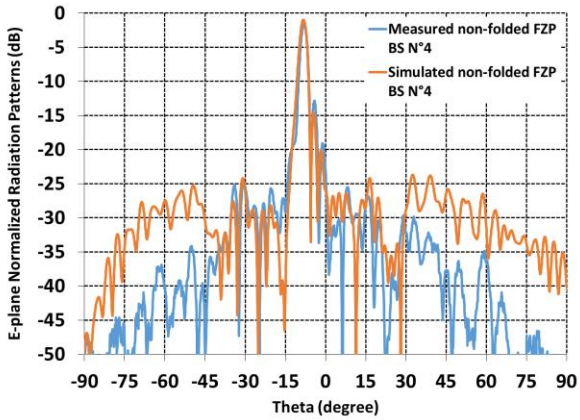

(d)

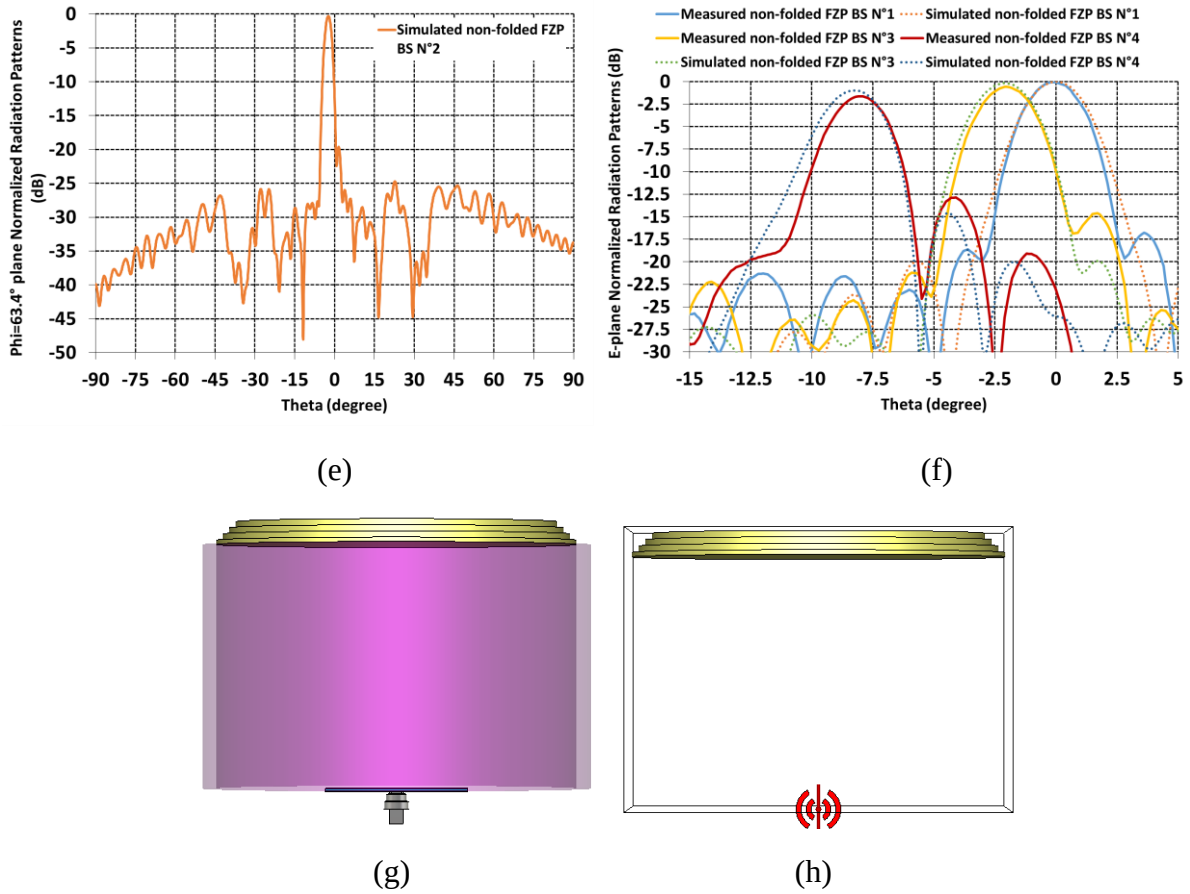

Figure 5-18: Measured and simulated radiation patterns of the non-folded FZP fed by beam switching focal arrays at 60 GHz : (a) E-plane by circuit N°1, (b) H-plane by circuit N°1, (c) E-plane by circuit N°3, (d) E-plane by circuit N°4, (e) Phi=63.4° plane by circuit N°2, (f) Superposition o E-planes by circuits N°1, 3 and 4, (g) CST time domain solver simulation model of the non-folded FZP and circuit N°1, and (h) CST IE solver simulation model of the non-folded FZP lens and imported far fields of circuits N°2 ,3 and 4.

Taking into account the measurement results in figure 5-18(f), the beam steering characteristics for non-folded FZP using the beam switching solution are the followings: 1- the beam crossing level (BCL) of the two adjacent sources (N°1 and N°3) is 2.3 dB, 2- the peak to peak gain loss (PPL) for the two adjacent sources is 0.6 dB and for the worst case (N°1 and N°4) is 1.64 dB, and 3- the beam steering angle step resolution (BSR) obtained using this focal array with inter-element spacing of 3.6mm is 2°.

As can be seen in figure 5-18(f), there is a little more scan loss in measurements compared to the simulations, especially for circuits N°3 and N°4. This can be explained by the fact that we could not remove the twist-reflector, present around the focal array circuits for both folded (figure 5-1(b)) and non-folded (figure 5-1(a)) measurements. Consequently, the presence of the twist-reflector caused additional coupling with the focal array circuit which resulted in more gain loss comparing to the simulation where the twist-reflector is absent.

Table 5-5 compares the measured values of beam direction and scanning loss of the non-folded FZP lens fed by each of the beam switching circuits.

Table 5-V: Non-folded FZP fed by beam switching focal array measured scanning angle and loss.

Non-folded FZP fed by circuit N°	Beam Direction (AZ / EL)	Scan loss (dB) - 60 GHz
N°1	0.1° / 0°	0
N°2	-1° / -2°	0.43
N°3	-2° / 0°	0.6
N°4	-8° / 0°	1.6

Figure 5-19 presents the measured gain of the FZP lens fed by each of the four circuits and the simulated gain of the FZP fed by central patch (N°1) in function of frequency over the V-band (57-66 GHz). The gain measurements are at the peak direction of each case. For the broadside beam (N°1), we observe almost up to 3dB gain difference between simulation and measurement. This 3dB gain difference is much more than the FFZP antenna fed by a waveguide presented in chapter 3 where there was almost no gain difference between measurement and simulation. A detailed power budget for the non-folded FZP lens fed by ciruit N°1 is presented in Table 5-6. Regarding the measured gain for different beam directions (different circuits), it is confirmed that for wider scanning angle there will more gain losses. Also for the measured gain, we can see that there is gain drop at the lower side of the frequency range, around 57-59 GHz, this correspond to the circuits mismatch at these frequencies (see Figure 5-17).

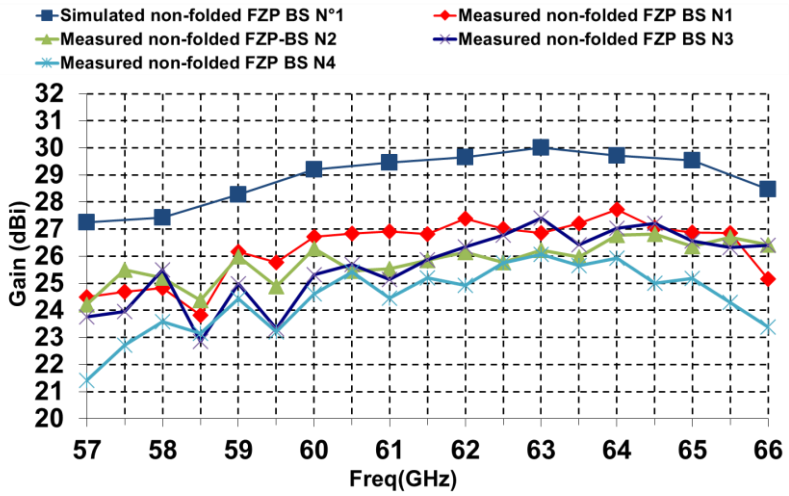

Figure 5-19: Measured and simulated gain variation over frequency for non-folded FZP fed by beam switching focal arrays.

A detailed power budget for the non-folded FZP antenna fed by the beam switching circuit N°1 at 60 GHz is presented in Table 5-6. The total loss of the antenna is 11 dB where, 5.8 dB is FZP lens losses such as illumination loss (spillover, apodisation) and focusing loss (phase correcting). There is 0.6 dB simulated reflection loss. Also, 1.25 dB is counted for the WMT insertion loss taking into account the simulated transmission coefficient presented in figure 5-9. There is 1.55 dB losses due to focal array circuit loss such as radiation loss. There remains 1.8 dB prototype loss. Unfortunately, due to some technical reasons we were not able to realize

the end-to-end transition prototype and measure its exact loss. However, based upon separate simulations of the FZP lens and the focal array circuit their material losses are estimated to be 0.1dB and 0.8 dB respectively. The remaining 0.9 dB loss might be due to the leakage between the waveguide and the microstrip probe and realization inaccuracies. Moreover, measurement errors should be considered as well.

Table 5-VI: Power budget of the non-folded FZP antenna fed by circuit BS N°1.

Parameter	Value at 60 GHz
Directivity - uniform aperture (dBi)	37.8
Directivity simulated (dBi)	32
Gain simulated (IEEE) (dBi)	29.2
Gain simulated (Realized) (dBi)	28.6
Gain measured (dBi)	26.8
Total loss (dB)	11
Microstrip line (5.95 mm) to waveguide transition transmission loss (simulated) (dB)	1.25
Focal array radiation loss (dB)	1.55
Reflection loss (simulated) (dB)	0.6
Prototype loss (material loss, leakage loss, realization tolerance loss and etc.)	1.8
Antenna non-perfection loss (focusing loss, illumination loss) (dB)	5.8

The non-folded FZP lens beam steering performance using beam switching technology was studied. There is a good agreement between the measurements and simulation radiation pattern and beam steering performances of the non-folded FZP which also confirms the focal arrays functionality (passive circuits). In the following, the performance of the Folded FZP (FFZP) antenna excited by the four beam switching focal arrays is studied.

5.4.3. Folded FZP (FFZP) antenna and «beam switching»

After verifying the beam switching circuits functionality in the previous section, their performance and compatibility with the Folded FZP (FFZP) lens are studied in this section. Figure 5-20 compares the simulation and measurement results of the FFZP antenna fed by circuit number one (BS N°1) at 60 GHz (simulation model presented in figure 5-16(b)). It should be noted that because of the folded structure and the twisting function, the E-plane of FFZP corresponds to the H-plane of the non-folded FZP. As the central patch is excited in circuit BS N°1, no beam steering is expected. Comparing this radiation patterns with the non-folded FZP fed by circuit N°1 (figures 5-20(a) and 5-20(b)), increased side lobe levels are noticeable especially in E-plane. This pattern degradation observed for the FFZP antenna, both in simulation and measurements is due to the masking effect caused by the focal array circuit on the twist-reflector (as the circuit is positioned inside the twist-reflector disc).

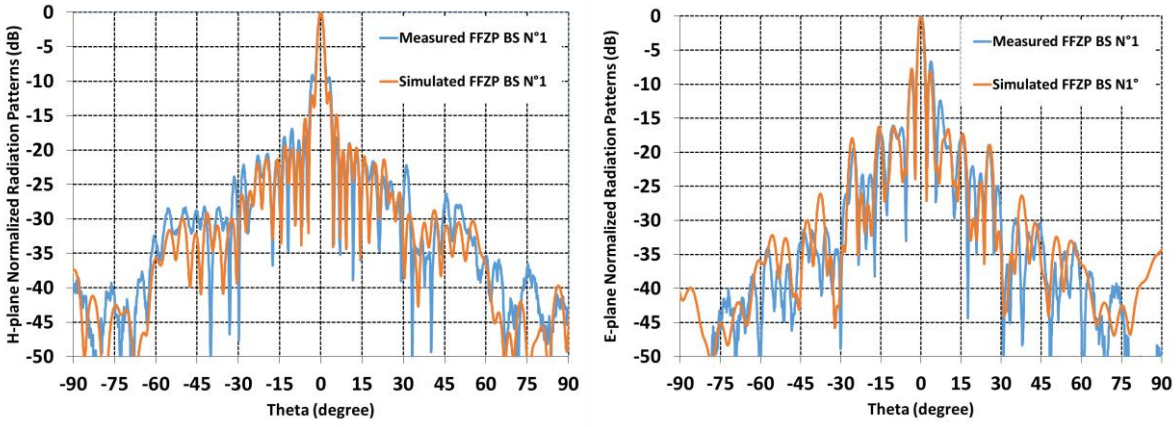

(a) (b)

Figure 5-20: Measured and simulated radiation patterns of the FFZP antenna fed by beam switching focal array circuit N°1.

In order to demonstrate the masking effect, the FFZP antenna is fed by a single ACMPP element (without the rest of the focal array elements) in a smaller substrate with dimensions of 5 mm × 7.15 mm. Figure 5-21(a) and (b), compares its simulated radiation patterns with FFZP fed by focal array circuit N°1 where the substrate dimension is 49 mm × 27 mm. In figure 5-21(d), a schematic representation of each circuit (blue rectangles) surrounded by the twist-reflector (green circular disc) is available for comparison. It can be observed that difference is quite noticeable and the case with smaller masking has a radiation pattern similar to non-folded FZP antenna fed by circuit N°1 in terms of side lobe levels. The masking effect has a dual impact : first there will be less effective surface for twist-reflector (less fields are twisted), and second is reflections by the focal array elements (copper surface of the patches) that will cause parasitic radiations.

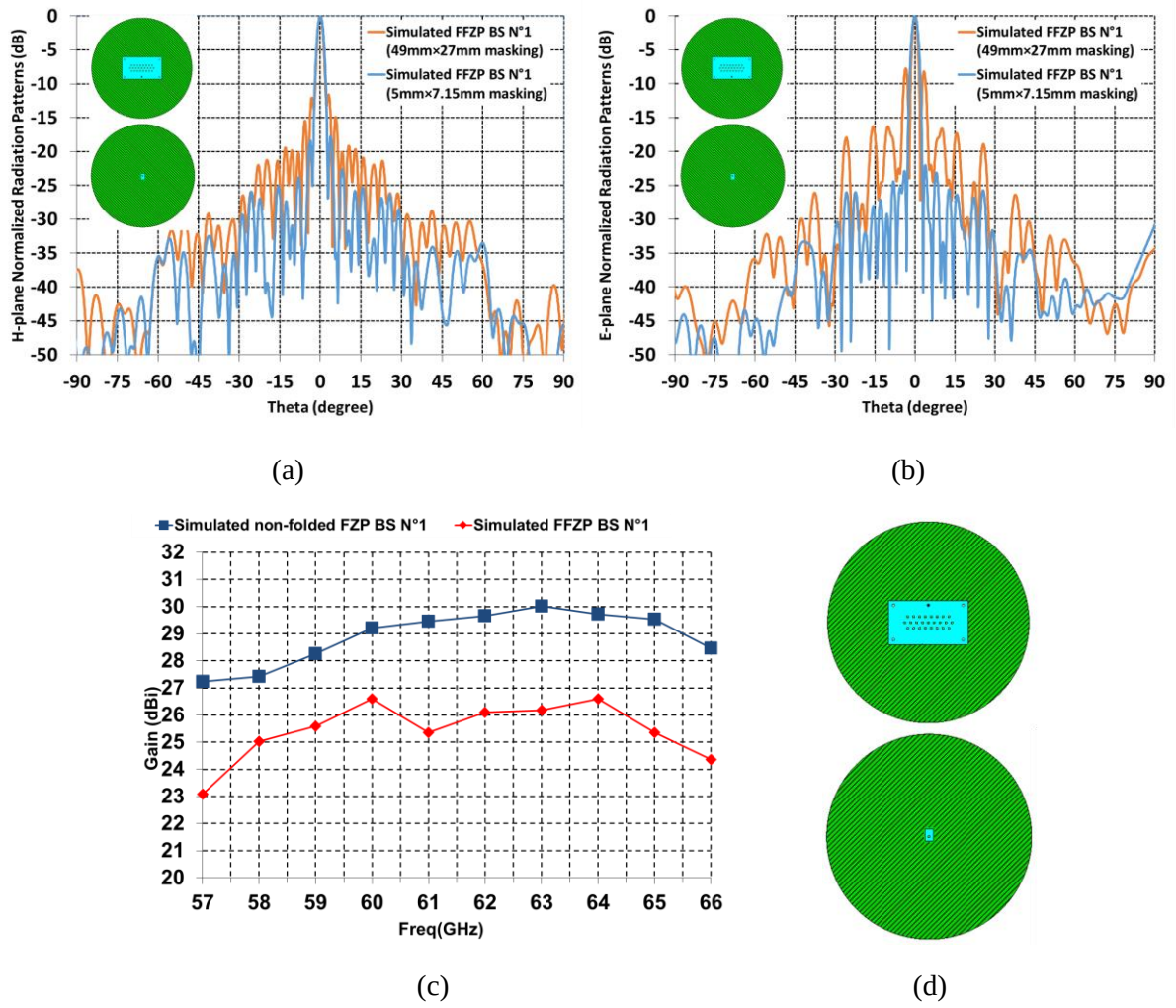

Figure 5-21: Beam switching focal array circuit masking effect on the FFZP antenna : (a) simulated H-plane radiation patterns of FFZP antenna fed by different size focal source at 60GHz, (b) simulated E-plane radiation patterns of FFZP antenna fed by different size focal source at 60GHz, (c) simulated gain variation over frequency comparison between Folded and Non-folded FZP antenna fed by circuit BS N°1, (d) Zoomed masking area of the focal source (blue) within the twist-reflector (green).

As illustrated in figure 5-21(c), the folded structure (Twist-reflector) masking effect introduces almost 4dB gain loss by comparing the simulated gain of the folded and non-folded FZP antenna fed by the central patch (circuit N°1).

The measured and simulated H-plane radiation patterns of the FFZP antenna fed by the rest of the beam switching circuits are presented in figure 5-22. It should be noted, for circuit N°2, as its beam is steered at phi=63.43° and not E-plane or H-plane, only the simulated result is presented for this circuit.

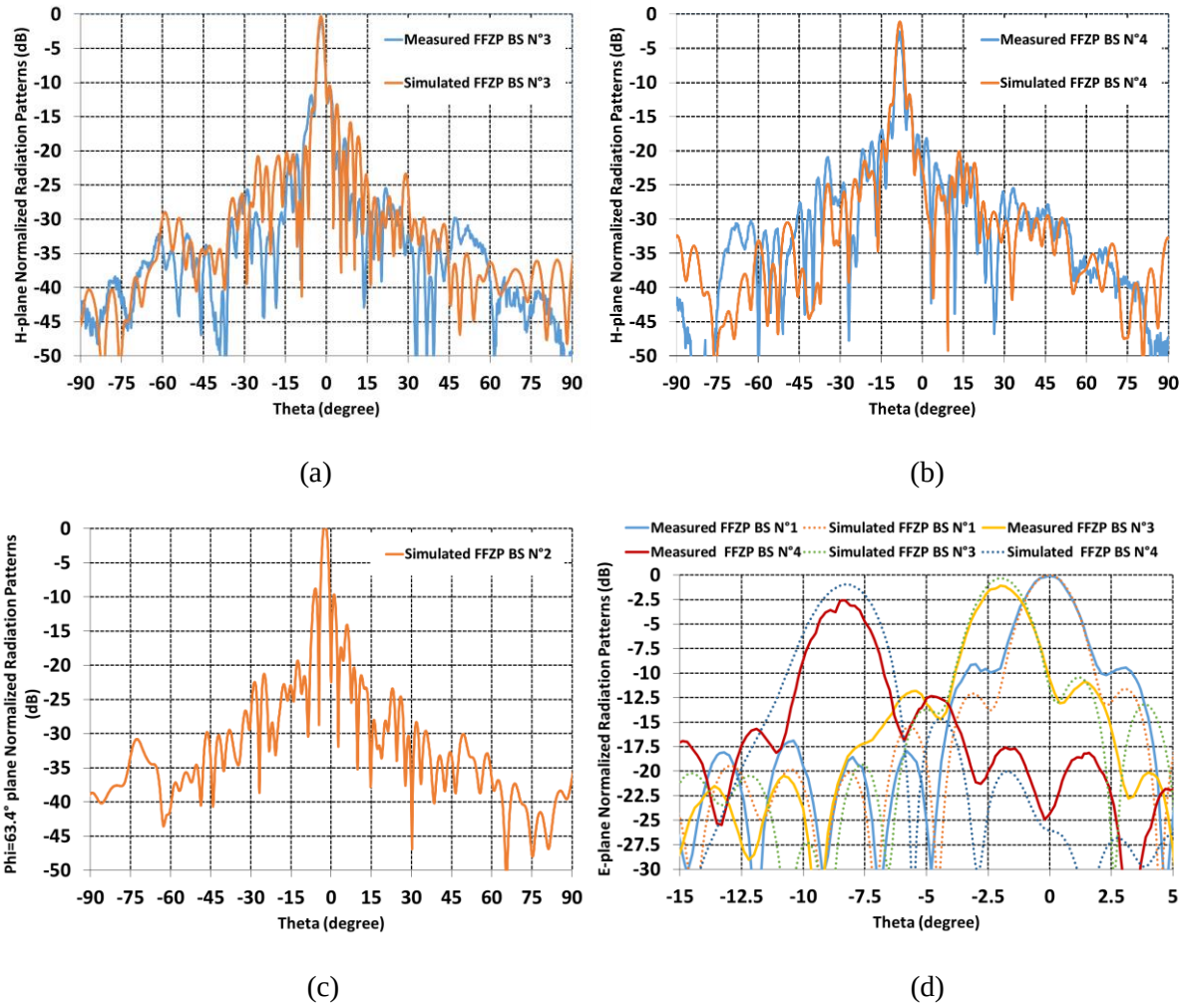

Figure 5-22: Measured and simulated radiation patterns of the FFZP antenna fed by beam switching focal array (a) circuit N°3, (b) Circuit N°4, (c) Circuit N°2, and (d) Ensemble of FFZP fed by N°1, N°3 and N°4.

From the measurement results in figure 5-22(d), we can extract the beam steering characteristics of the FFZP antenna using beam switching technology as follows: 1- the beam crossing level (BCL) of the two adjacent sources (N°1 and N°3) is 2.8 dB, 2- the peak to peak gain loss (PPL) for the two adjacent sources is 1.1 dB and for the worst case (N°1 and N°4) is 2.58 dB, and 3- the beam steering angle step resolution (BSR) obtained using this focal array with inter-element spacing of 3.6 mm is 1.9°.

Table 5-7 compares the measured scanning angle and the scan loss of the non-folded FZP and the Folded FZP (FFZP) fed by the beam switching focal arrays. As already observed with the radiation patterns, the folded structure degrades the FZP lens beam steering performances.

Table 5-VII: Measured scan angle and scan gain loss comparison between non-folded and folded FZP antennas.

Antenna fed by circuit N°	Non-folded FZP Beam Direction (AZ / EL)	Folded FZP Beam Direction (AZ / EL)	Non-folded FZP scan loss (dB) 60GHz	Folded FZP scan loss (dB) 60GHz
N°1	0.1° / 0°	-0.1° / 0°	0	0
N°2	-1° / -2°	na	-0.43	na
N°3	-2° / 0°	-1.9° / 0°	-0.6	1.1
N°4	-8° / 0°	-8.4° / 0°	-1.6	2.58

5.4.4. Conclusions on beam-switching beam-steering concept

By measuring the non-folded FZP antenna, the functionality of the design and realized multi-layer circuits with integrated transitions were confirmed. The non-folded FZP shows good beam steering performance in line with simulation results.

The measured results confirms the beam switching concept for the FFZP antenna in terms of beam steering characteristics. However, major issue is the circuit mask effect on the twist-reflector which results in gain loss (almost 4 dB) and increased side lobes. This effect will become even more important for the cases where higher beam steering ranges and therefore larger focal arrays are required. The conclusion, would be that there is a compromise between the FZP lens antenna compactness (using folded structure) and its beam steering performance and range (focal array dimension and masking effect).

Both for the folded and non-folded FZP antenna, using a beam switching technology results in a discrete beam steering solution forced by focal array inter-element spacing. As discussed in chapter 4, this spacing defines the beam steering resolution and therefore the beam crossing level. In this section, it was demonstrated by measurements that by using a focal array with inter-element spacing of 3.6 mm, 1.9° beam steering angle resolution is obtained. This will force a beam crossing level of 2.8 dB, meaning we will lose 2.8 dB gain if the target is in-between two adjacent switchable beams. In next section, a continuous beam steering solution is proposed to overcome this limitation.

5.5. Beam steering solution: Continuous beam steering by focal array tapering

5.5.1. Introduction

It was concluded previously that beam steering solution based on beam switching has a major limitation: the discontinuous beam scanning caused by the minimum beam steering angle step, imposed by focal source physical dimensions and the mandatory inter-element spacing. In this section, an alternative solution is proposed to overcome this major limitation and improve the antenna beam steering efficiency.

The proposed continuous beam steering solution consists on tapering the excitation of the focal plane array elements [2-3]. This approach offers a very simple solution to move the phase center of the focal array and thus steer the radiated beam.

In this approach by tapering the amplitude of a sub-array in the focal array, the phase center of the sub-array can be displaced. This phase center displacement is seen by the lens as a source displacement which results in the steering of the lens beam as a function of the phase center displacement form the center of the lens antenna. The size of the sub-array depends directly on the lens illumination edge taper. It was demonstrated in previous chapter that a sub-array of 2×2 ACMPP elements will result in an edge taper of 12-14 dB which is close to our FZP lens optimal edge taper of 12 dB. This means selecting a smaller or bigger sub-array will result in a non-optimal edge taper with increased spillover loss or reduced illumination efficiency respectively. For this reason a sub-array of 2×2 ACMPP elements is chosen for this solution. However, this sub-array can be a part of a bigger N×M elements focal array, where each time only a 2×2 sub-array will be active. The size of the N×M focal array depends directly on the desired beam steering range.

Figure 5-23 provides a schematic representation of the N×M elements array with a 2×2 elements sub-array used as a the primary source of the focal array.

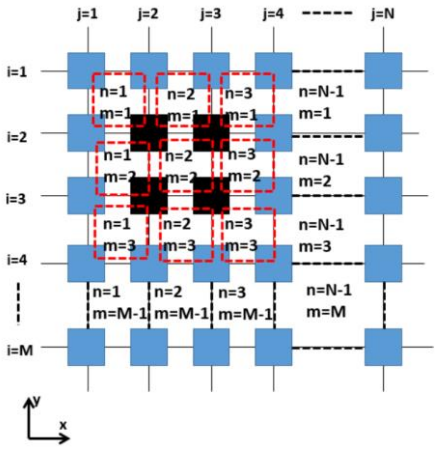

Figure 5-23: Schematic representation of the N×M elements array with a 2×2-elements sub-array used as a single focal array element.

As a general rule, based on equations from [3], the phase center position of the focal plane array on N×M elements along *x*- and *y*- axes can be computed as follows

$$\begin{cases} X_n = \frac{\Delta x}{2}\left(\sum_{\substack{i=m\\ j=n+1}}^{\substack{i=m+1\\ j=n+1}} \frac{A_{ij}}{A_\Sigma} - \sum_{\substack{i=m\\ j=n}}^{\substack{i=m+1\\ j=n}} \frac{A_{ij}}{A_\Sigma}\right) \\ Y_m = \frac{\Delta y}{2}\left(\sum_{\substack{i=m\\ j=n}}^{\substack{i=m\\ j=n+1}} \frac{A_{ij}}{A_\Sigma} - \sum_{\substack{i=m+1\\ j=n}}^{\substack{i=m+1\\ j=n+1}} \frac{A_{ij}}{A_\Sigma}\right) \\ A_\Sigma = \sum_i A_i \end{cases} \quad (1)$$

where *n* and *m* denote the sub-array number along x- and y-axes, A_{ij} is the amplitude coefficient of each radiating element. Δx and Δy are inter-element spacing along *x*- and *y*- axes.

For the specific case of having a 2×2 elements sub-array active at each time, its phase center can be calculated using the following equation

$$X = \frac{\Delta X}{2}\left(\frac{A_2+A_4}{A_\Sigma} - \frac{A_1+A_3}{A_\Sigma}\right)$$
$$Y = \frac{\Delta Y}{2}\left(\frac{A_1+A_2}{A_\Sigma} - \frac{A_3+A_4}{A_\Sigma}\right) \quad (2)$$
$$A_\Sigma = \sum_i A_i$$

where A_i is the amplitude excitation coefficients of each element of the 2×2 elements sub-array.

This solution can be deployed by associating Power Amplifiers (PA) or Low Noise Amplifiers (LNA) to each element of the focal array sub-arrays. However as realizing the RF circuits is not the objective of this project, passive prototypes are realized to verify this concept.

To this end, a 2×2 elements array fed by 3 different corporate feeding networks are designed. One prototype (N°1) will be with uniform amplitude corporate feeding network, other (N°3) will be with only 2 patches of 4 patches excited (A_1=A_2=1, A_3=A_4=0) and last one (N°2) will be a tapered corporate feeding network (A_1=1, A_2=0.4, A_3=0.4,A4=1). All these arrays are constituted with ACMPP elements with isolating via-holes presented previously in this chapter (see Table 5-2 and Figure 5-5 in section 2). The inter-element spacing is 3.6 mm. Figure 5-24 shows the schematics of these 3 focal arrays and their corresponding feeding networks. Each section of the feeding network, power dividers, blends, stubs, quarter wavelength transformers and etc. are optimized in terms of impedance matching, amplitude distribution and transmission loss.

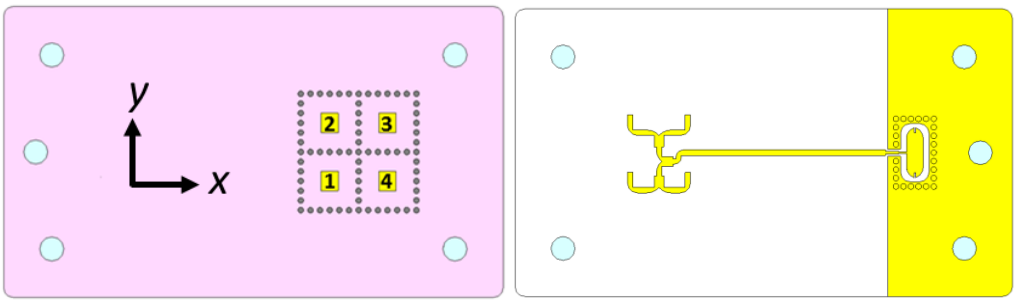

(a)

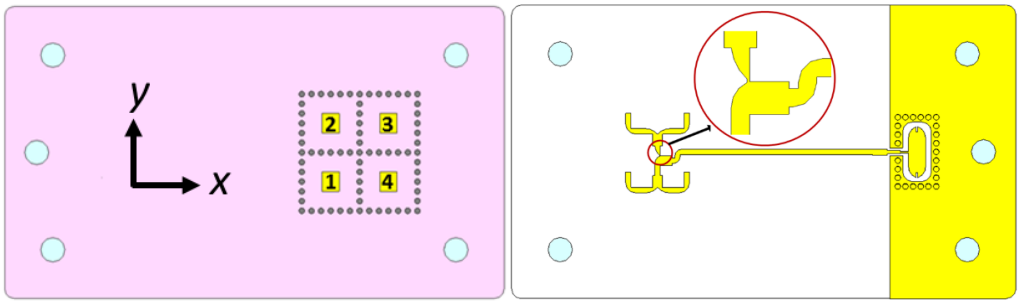

(b)

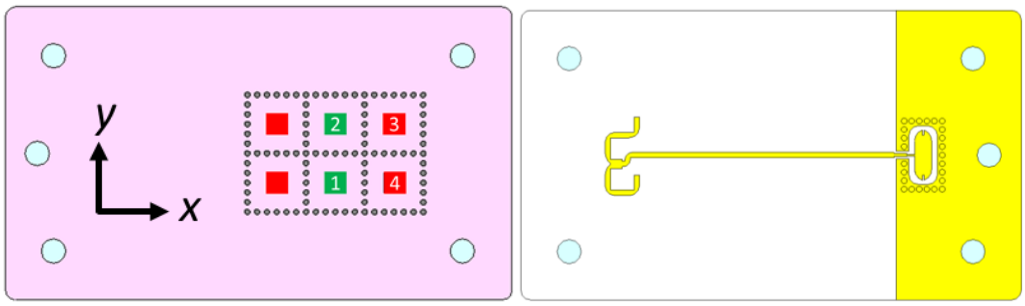

(c)

Figure 5-24: Continuous beam steering passive prototypes schematic view: (a) Circuit N°1: Uniform amplitude corporate feeding network, (b) Circuit N°2: Tapered amplitude feeding network (1-0.4), and (c) Circuit N°3: Tapered amplitude feeding network (1-0).

As presented in figure 5-24(c), for the 1-0 tapered 2×2 array, only 2 patches of the array are excited (green patches), also to balance the phase center displacement, 2 parasitic patches were added.

Table 5-8 presents the calculated phase center displacement according to equation (2) and the expected beam steering angle according to equation (1) of chapter 4 for each of the three focal arrays.

Table 5-VIII: 2×2 array phase center displacement and FZP beam direction in function of the 2×2 array amplitude coefficients.

Circuit number and its amplitude coefficient matrix $\begin{pmatrix} A_2 & A_3 \\ A_1 & A_4 \end{pmatrix}$	Phase center position-mm (x-axis / y-axis)	Ideal Beam Direction of the FZP lens (AZ / EL) °
N1 $\begin{pmatrix} \mathbf{1} & \mathbf{1} \\ \mathbf{1} & \mathbf{1} \end{pmatrix}$	0/0	0° / 0°
N2 $\begin{pmatrix} \mathbf{0.4} & \mathbf{0.4} \\ \mathbf{1} & \mathbf{1} \end{pmatrix}$	0/-0.771	0°/ 0.46°
N3 $\begin{pmatrix} \mathbf{1} & \mathbf{0} \\ \mathbf{1} & \mathbf{0} \end{pmatrix}$	-1.8/0	1.08° / 0°

These circuits are integrated to a cylindrical metallic box similar to the case for beam switching circuits. This mechanical structure is used for both non-folded and folded FZP antenna measurements.

Figure 5-25 shows the photos of the realized circuits.

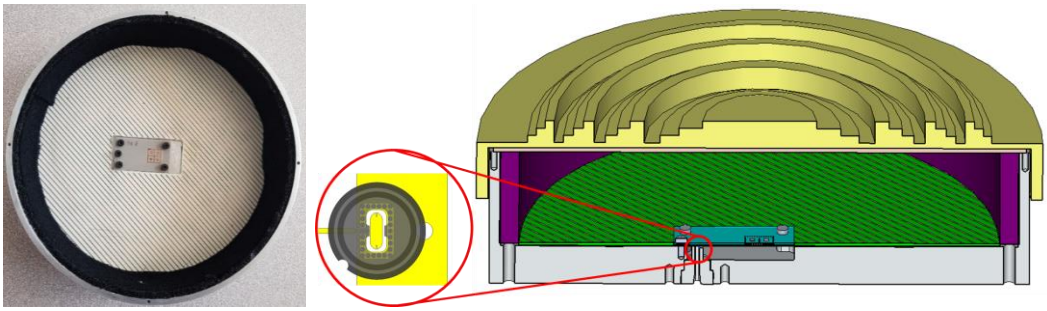

(a)

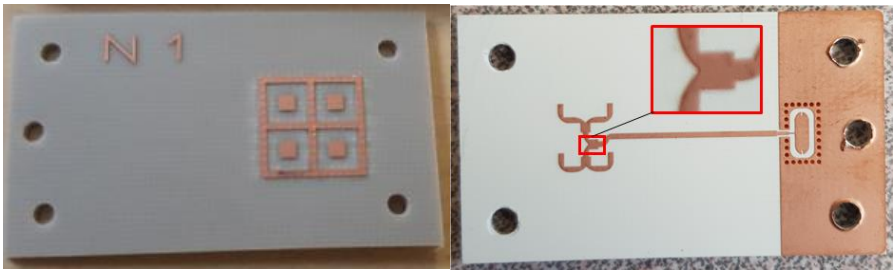

(b)

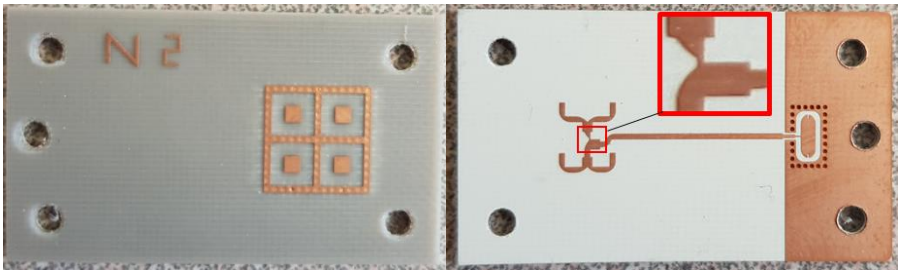

(c)

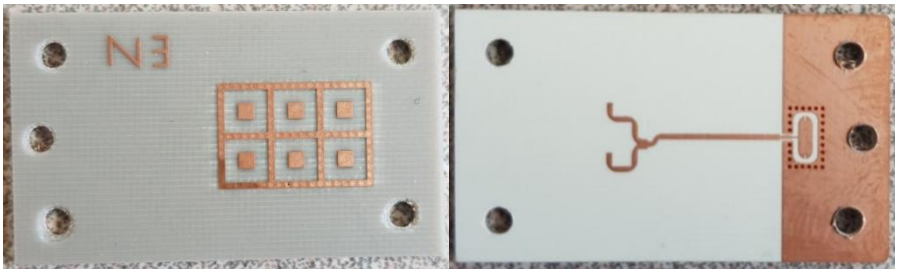

(d)

Figure 5-25: (a) focal array circuit installation into the FFZP antenna structure top view and schematic cut-view, (b) prototype of the uniform focal array circuit N°1, (c) prototype of the tapered focal array circuit N°2, (d) prototype of the tapered focal array circuit N°3.

The measured and simulated reflection coefficients of these three circuits are presented in figure 5-26. All three circuits are almost well matched for the 57-66 GHz frequency range. However, some frequency shift, especially for circuit N°3 about 2GHz, can be observed. This frequency shift may be due to the realization inaccuracies. Also, similar to the beam switching circuits, due to the mechanical structure it's not possible to have direct view on the microstrip to waveguide transition and verify if there is a perfect contact and/or good alignment. Despite

some minor differences, we can confirm that the realized prototypes of the focal array circuits are functional in terms of reflection coefficients.

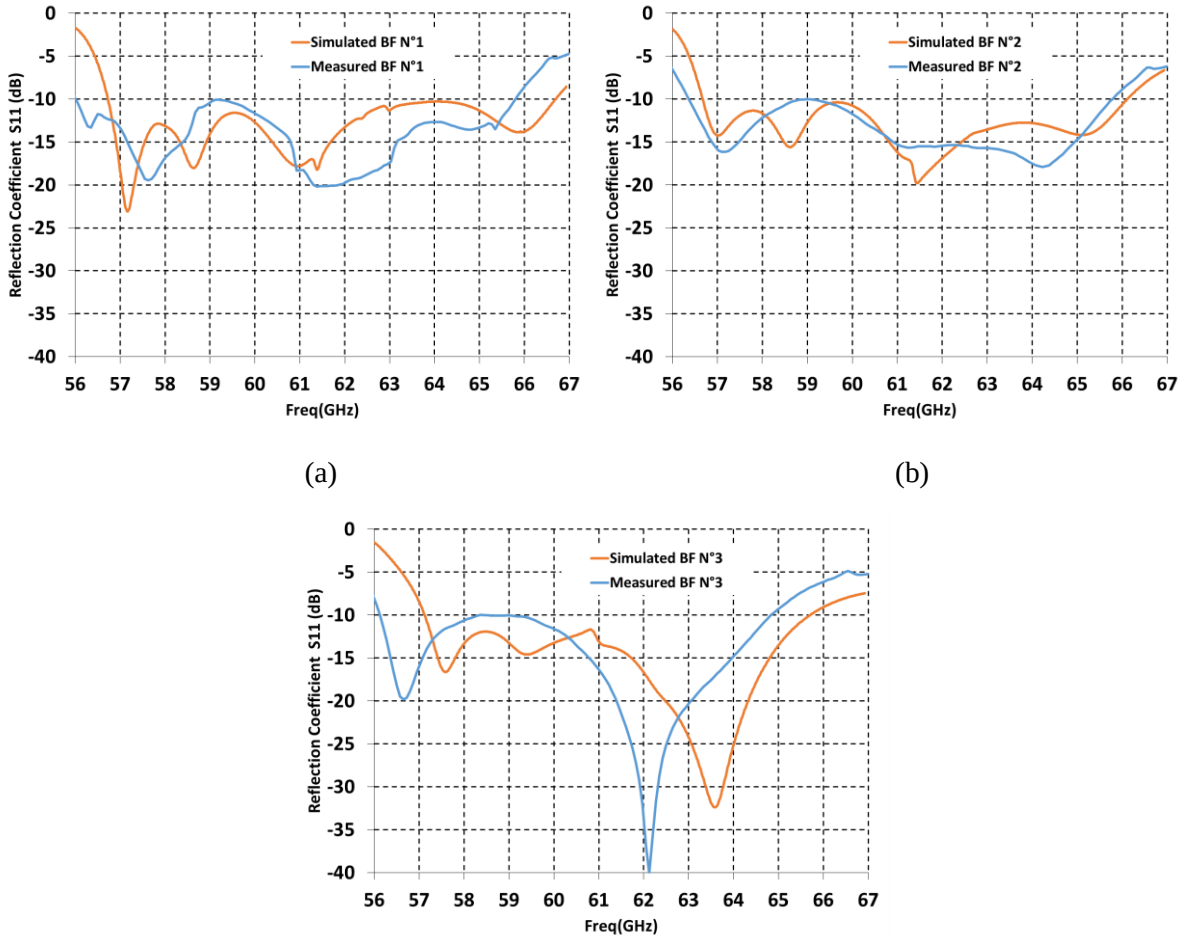

Figure 5-26: Measured and simulated reflection coefficients of continuous beam steering focal arrays : (a) BF N°1, (b) BF N°2, and (c) BF N°3

Similar to beam switching studies, first the non-folded FZP antenna fed by the tapered focal arrays is analyzed by simulations and measurements in order to verify the circuits functionality independent from the folded structure.

5.5.2. Non-folded FZP lens and continuous beam steering

Figure 5-26 presents the simulated and measured results of the non-folded FZP antenna fed by the uniform amplitude circuit number one (BF N°1). Good agreement between simulation and measurement is observed at both planes at 60 GHz. For the simulation of the non-folded FZP and fed by circuit BF N°1 and BF N°2, complete structure of the antenna including the absorber and the focal array circuit is simulated by *CST* time domain solver. However, as this simulation consumes a lot of time and machine memory, for the other circuit (BF N°3), the FZP lens is simulated with their exported far field using *CST IE* simulator. Simulation models for both cases are presented in figures 5-27 (c) and (d).

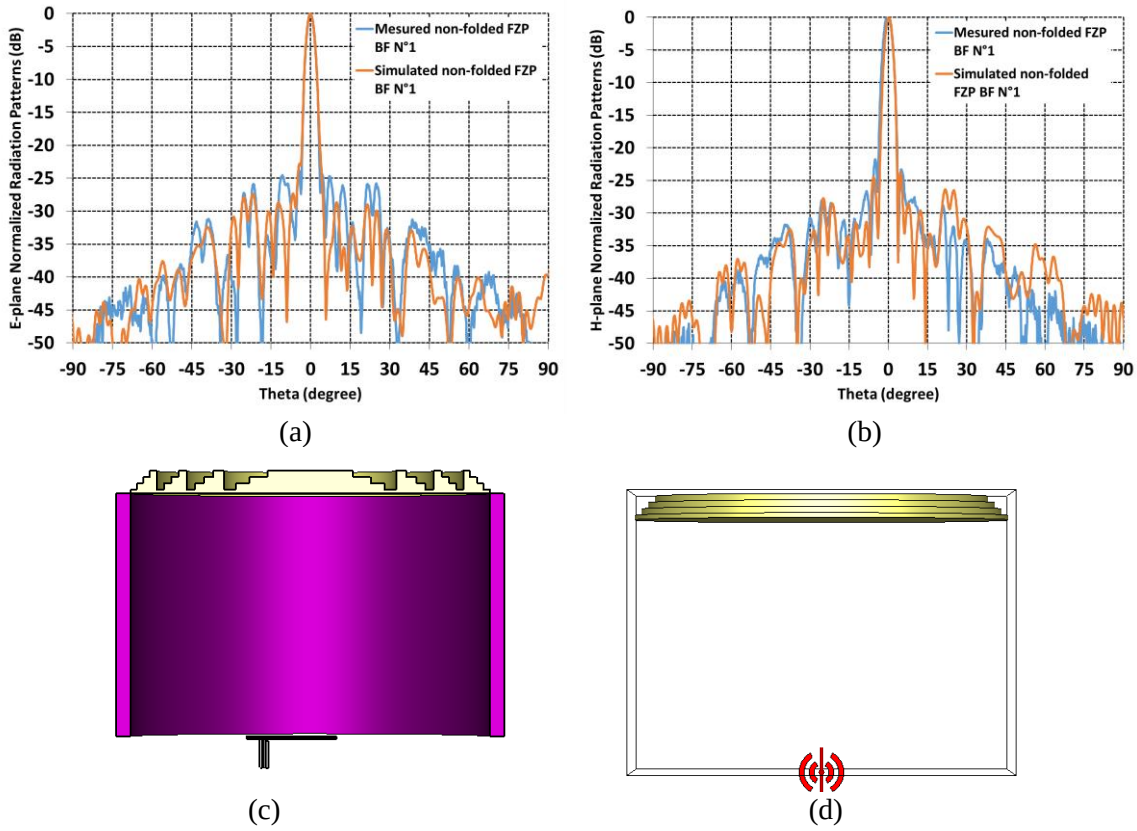

Figure 5-27: Measured and simulated radiation patterns of the non-folded FZP fed by uniform amplitude 2x2 focal array (N°1) (a) E-plane, (b) H-plane, (c) CST time domain solver simulation model of the non-folded FZP and circuit N°1 and N°2, and (d) CST IE solver simulation model of the non-folded FZP lens and imported far fields of circuits N°3.

Figures 5-28(a) and (b) present the simulation and measurement results of the FZP fed by the tapered focal arrays (circuits N°2 and N°3) at 60 GHz. It should be noted that the difference in side lobe levels between simulation and measurement at $|\theta| > 36.9°$ is because of the absence of the absorber in simulations. The normalization reference for both simulation and measurement radiation patterns is the simulated and measured gain of the non-folded FZP fed by circuit N°1 (uniform amplitude array). There is a difference between measurement and simulation in the scan loss level of the steered beams. The reason why we observe less scan loss for measurement compared to simulation might be due to the normalization error for the measured radiation patterns as the measurements for the broadband beam and steered beams were done at different days and probably resulting in different normalization references. Despite this, we can confirm the beam steering of the non-folded FZP using tapered arrays. This results also confirm the design and realization of the passive focal array circuits.

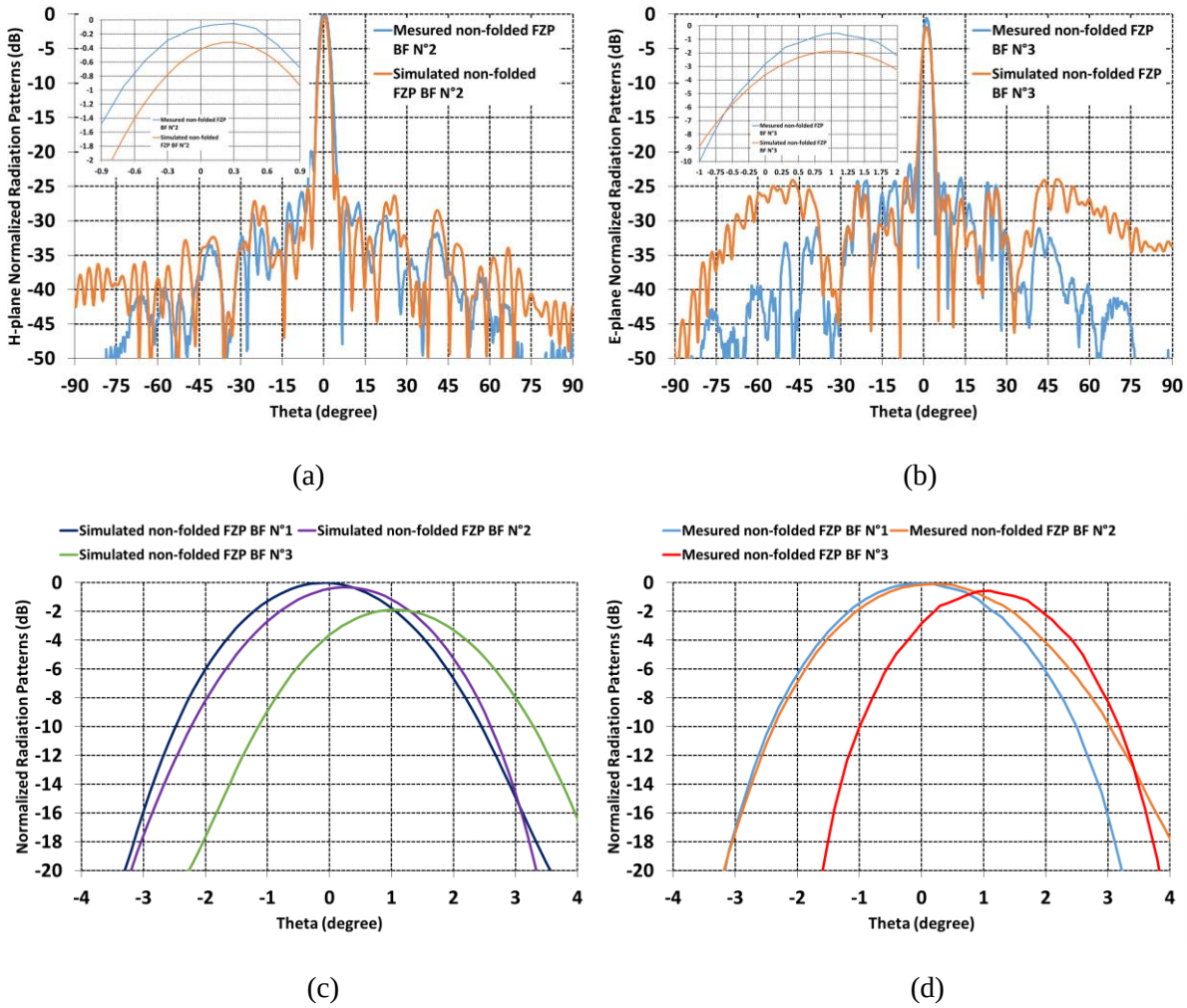

Figure 5-28: Measured and simulated radiatin patterns of the non-folded FZP (a) fed by tapered amplitude focal arrays circuit N°2, (b) fed by tapered amplitude focal arrays circuit N°3, (c) Superposition of all simulated patterns, and (d) superposition of all measured patterns at 60 GHz.

Table 5-9 compares the expected (by calculation) and obtained (by simulation and measurement) beam steering angles of the non-folded FZP antenna fed by the tapered focal arrays. As presented, there is a difference between the ideal targeted steering angles and the real steering angles obtained in simulation and measurement. This is because the position of the phase canter of the sub-array is impacted by other factors than the sub-array elements amplitude coefficients. One of this factors is the inter-element coupling of the sub-array. However, by using isolating via-holes around each element of the array, it was tried to minimize this coupling and its impact on the array phase center position.

Table 5-IX: Measured, simulated and ideal beam direction of the non-folded FZP antennas fed by continous beam steering focal arrays.

Circuit number and its amplitude coefficient matrix $\begin{pmatrix} A_2 & A_3 \\ A_1 & A_4 \end{pmatrix}$	Ideal Beam Direction (AZ / EL) °	Simulated Beam Direction (AZ / EL)	Measured Beam Direction (AZ / EL)
N1 $\begin{pmatrix} \mathbf{1} & \mathbf{1} \\ \mathbf{1} & \mathbf{1} \end{pmatrix}$	0° / 0°	0° / +0.1°	0° / 0°
N2 $\begin{pmatrix} \mathbf{0.4} & \mathbf{0.4} \\ \mathbf{1} & \mathbf{1} \end{pmatrix}$	0°/ 0.46°	0°/0.3°	-0.1° /+ 0.3°
N3 $\begin{pmatrix} \mathbf{1} & \mathbf{0} \\ \mathbf{1} & \mathbf{0} \end{pmatrix}$	1.08° / 0°	+1.1°/ 0 °	+1.1° / +0.3°

The presented beam steering approach enables a continuous beam steering with high resolution. A beam steering angle step resolution (BSR) of 0.3° was demonstrated with the passive prototype, but in real life the BSR depends on each sub-array element connected amplifier or the attenuator resolution. Smaller BSR means smaller beam crossing levels (BCL), in our case a BSR of 0.3° gives a BCL of 0.2 dB. The maximum achievable beam steering angle within the presented 2×2 sub-array is ±1.1°. The maximum peak to peak gain loss (PPL), between the broadside beam the extreme beam at 1.1° is demonstrated to be less than 1 dB in measurements.

Figure 5-29, shows the measured and simulated gain variations over the frequency for the non-folded FZP lens excited by the uniform amplitude focal array (circuit N°1). Also the measured gain variations over frequency for the tapered focal arrays (circuits N°2 & N°3) are presented as well. Comparing with the gain variation over frequency for the non-folded FZP excited by beam switching circuits (figure 5-19), almost 3dB gain increase is observed for the broadside beams in both simulation and measurements. This is because, in beam switching circuits, the primary source was a single ACMPP with an edge taper around 2dB. However, in this case for the tapered focal arrays, the primary source is a 2×2 array that offers an edge taper around 12 dB which is the FZP lens optimal edge taper. In figure 5-29, similar to the beam switching circuits in figure 5-19, up to 3dB gain difference between simulation and measurement is noticeable. A detailed power budget is presented in Table 5-10 to explain this 3dB loss. The gain of the non-folded FZP excited using circuit N°1(uniform) and circuit N°2(tapered) are very close and slightly higher for the latter at some frequencies. This might seem irregular, and usually we would expect less gain for the case with steered beam, but we should consider that firstly the scanning angle is very small for the non-folded FZP fed by circuit N°2 (0.3°), meaning very small scan loss, and secondly these are two separate circuits and there might be some realization inaccuracies within the prototypes.

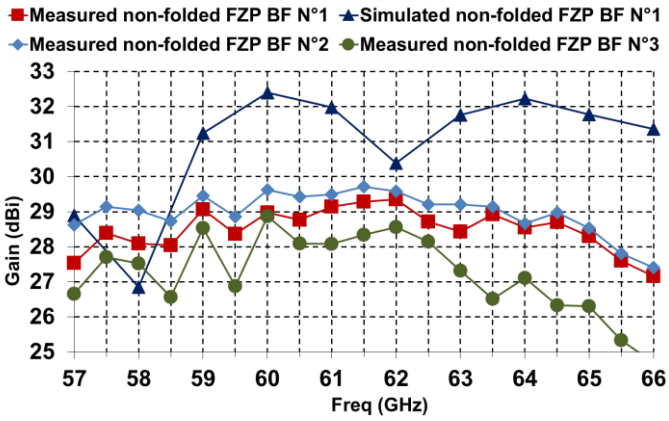

Figure 5-29: Measured and simulated gain variation over frequency for non-folded FZP fed by continuous beam steering tapered focal arrays.

Table 5-10, presents a detailed power budget for the non-folded FZP antenna fed by circuit BF N°1 estimated based on simulation and measurement results. This antenna solution has a total loss of 8.8 dB where 4.3 dB of it is related to the FZP lens losses such as illumination loss (spillover, apodisation) and focusing loss. The reflection loss of the antenna is 0.1 dB. There is 0.9 dB loss due to microstrip to waveguide transition transmission loss and 0.3 dB loss related to corporate 2×2 feeding network (Magic T, corner blend) loss. There is 3.3 dB prototype loss where based on separate simulations of the FZP lens and the focal array circuit 0.1 dB and 1.1 dB can be related to their material losses respectively. The remaining 2.1 dB might be due to power leakage between the waveguide and the micrstrip probe of the transition and also manufacturing inaccuracies of the prototype. Measurement errors should be considered a possibility as well, however this estimated power budget gives a good overview of the antenna performance.

Table 5-X: Power budget of the non-folded FZP antenna fed by circuit BF N°1.

Parameter	Value at 60 GHz
Directivity of uniform aperture (dBi)	37.8
Directivity Simulated (dB)	33.5
Gain simulated (IEEE) (dBi)	32.3
Gain simulated (Realized) (dBi)	32.2
Gain measured (dBi)	29
Total loss (dB)	8.8
Microstrip line to waveguide transition loss (simulated) (dB)	0.9
Corporate 2×2 microstrip feeding network loss (simulated) (dB) (Magic T+ Corner blends)	0.3
Reflection loss (simulated) (dB)	0.1
Prototype loss (material loss, leakage loss, realization tolerance loss and etc.)	3.3
Antenna non-perfection loss (focusing loss, illumination loss) (dB)	4.3

In the following section the performance of the Folded FZP (FFZP) antenna excited using the tapered focal arrays is studied.

5.5.3. Folded FZP (FFZP) lens antenna and continuous beam steering

Measurements and simulations results of non-folded FZP antenna fed by tapered focal arrays enabled us to validate the concept as well as the passive circuits functionality independent from the folded structure and its limitations. In this section, the measurement and simulation results for the compact folded FZP (FFZP) antenna are discussed. The schematic model of this antenna was presented in figure 5-25(b). Taking into account the results obtained for the FFZP antenna and beam switching circuits, degraded performances comparing to the non-folded case are expected. This is because of the masking effect of the focal array circuits in the Twist-reflector of the folded structure.

Figure 5-30 compares the E-plane measured and simulated radiation patterns of the FFZP antenna fed by the uniform amplitude array (circuit N°1) at 60 GHz. Similar to the case of the FFZP antenna fed by beam switching circuits, we can observe the masking effect of the focal array circuits in the twist-reflector. Comparing to the non-folded FZP fed by the circuit N°1, up to 15 dB side lobe level increase is observed. Also, we can see that the radiation patterns are not symmetrical in figure 5-30 because of the non-symmetrical dimensions of focal array and its position in the twist-reflector (see figure 5-29(a)). The reason that the measured side lobe levels are higher than the simulations, is that in the prototype realization, there was an error in cutting the twist-reflector in order to fit in the focal array circuit (see figure 5-29(a)). As a result, bigger portion of the twist reflector was cut and this mean bigger mask effect on the twist twist-reflector.

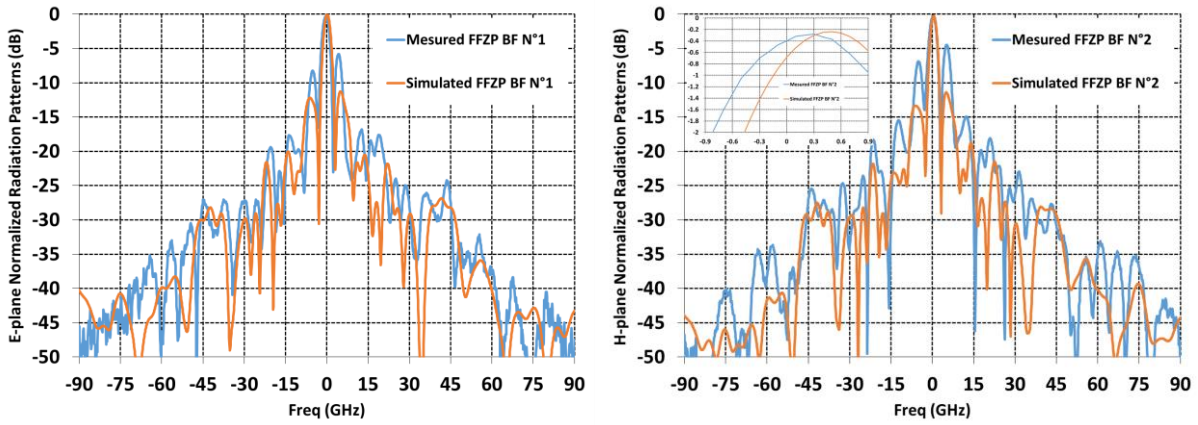

(a) (b)

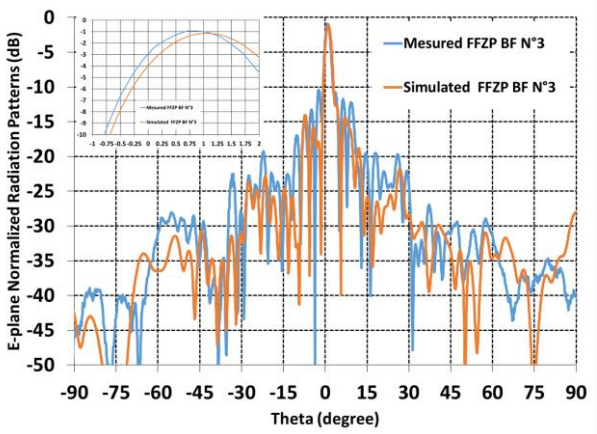

(c)

Figure 5-30: Measured and simulated radiation patterns of the Folded FZP (FFZP) fed by : (a) uniform amplitude focal array (N°1), (b) tapered focal array (N°2), and (c) tapered focal array (N°3) at 60 GHz.

Figure 5-31 compares the simulated gain variation over frequency between the folded and non-folded FZP fed by the uniform focal array (N°1). We can observe almost 3dB gain loss due to the masking effect in the Folded FZP (FFZP) antenna.

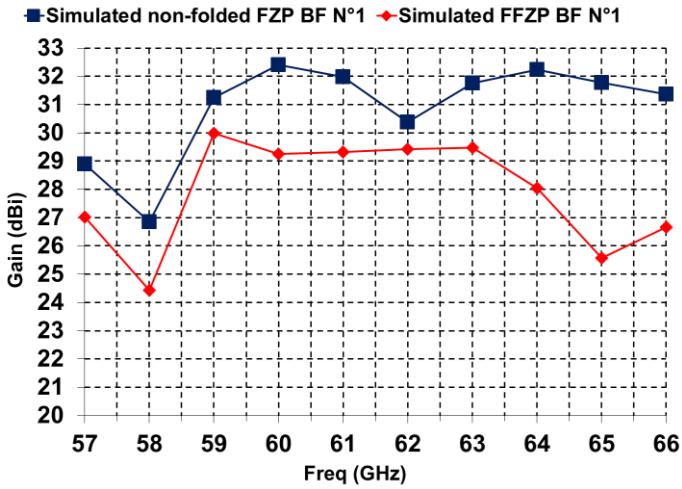

Figure 5-31: Simulated gain variation over frequency comparison between folded and non-folded FZP antenna fed by continuous beam steering foal array.

Table 5-11 compares the ideal (calculated), simulated and measured beam steering angles of the Folded FZP (FFZP) lens antenna fed by the tapered focal arrays.

Table 5-XI: Measured, simulated and ideal beam direction of the Folded FZP (FFZP) antennas fed by continuous beam steering tapered focal arrays.

Circuit number and its amplitude coefficient matrix $\begin{pmatrix} A_2 & A_3 \\ A_1 & A_4 \end{pmatrix}$	Ideal Beam Direction (AZ / EL) °	Simulated Beam Direction (AZ / EL)	Measured Beam Direction (AZ / EL)
N1 $\begin{pmatrix} \mathbf{1} & \mathbf{1} \\ \mathbf{1} & \mathbf{1} \end{pmatrix}$	0° / 0°	0° / +0.1°	0° / 0°
N2 $\begin{pmatrix} \mathbf{0.4} & \mathbf{0.4} \\ \mathbf{1} & \mathbf{1} \end{pmatrix}$	0°/ 0.46°	0°/0.5°	NA/0.3°
N3 $\begin{pmatrix} \mathbf{1} & \mathbf{0} \\ \mathbf{1} & \mathbf{0} \end{pmatrix}$	1.08° / 0°	1.1°/0°	0.9°/NA

The beam steering characteristics of the folded FZP (FFZP) antenna fed by the tapered focal arrays are similar to the non-folded FZP antenna fed by the same focal arrays. In the folded FZP case, we observe a beam steering angle step resolution of 0.3° with beam crossing level of 0.2 dB. For the 2×2 sub-array used in the prototypes, a beam steering range of ±0.9° with maximum peak to peak gain loss of 1 dB is obtained.

5.5.4. Conclusions on continuous beam steering concept

By simulating and measuring both the folded and non-folded FZP antenna with the tapered focal arrays we were able to verify first the functionality of the focal array circuits prototypes and secondly prove the concept of beam steering by tapering the focal array. For the main antenna solution, the compact folded FZP (FFZP) antenna, using a focal array has a masking effect on the twist-reflector and this result in antenna performance degradation in terms of gain (almost 3dB), efficiency and higher side lobe levels. However the masking effect does not have an important impact on the beam steering performances of the FFZP antenna.

5.6. Conclusions

In this chapter, two beam steering solutions for lens based antenna solutions were proposed and the concepts were verified by measuring them using the Folded Fresnel Zone Plate (FFZP) lens antenna. In order to realize the proof of concept prototypes, the focal arrays radiating element (the ACMPP) structure, was modified taking into account the realization consideration of each solution. Moreover, a novel single layer wide-band waveguide-to-microstrip line (WMT) transition was introduced and deployed within the focal arrays prototype circuits.

The first beam steering solution was based on beam switching concept. By realizing passive prototypes, it was demonstrated that this solution can offer a discontinuous beam steering with beam steering angle resolution of 1.9°. This results in a beam crossing level of 2.8 dB and peak to peak gain loss of 1.1 dB for two adjacent beams. The maximum peak-to-peak gain loss between the broadside beam and the most steered beam will depend on its steering angle. For this case where the maximum steering angle is ±8°, the maximum measured gain loss is 2.6 dB.

To improve the antenna beam steering characteristics obtained in the first solution, a continuous beam steering concept, based on focal array amplitude tapering, was proposed. In this solution, the primary source is a 2×2 ACMPP elements sub-array which its phase center is displaced by tapering its elements amplitude coefficients. This solution offers a beam steering angle resolution of 0.3°, a beam crossing level of 0.2 dB and a maximum peak to peak gain loss of 1dB. Moreover, in this solution, as the primary source is a 2×2 ACMP elements sub-array which offers an optimal edge taper of 12 dB, higher overall antenna gain (almost 3dB) is obtained comparing to the first beam steering solution.

5.7.References

[1] J. Ala-Laurinaho, J. Aurinsalo, M. Kaunisto, A. Lamminen, J. Nurmiharju, A.V. Räisänen, J. Säily, P. Wainio, "2-D beam-steerable integrated lens antenna system for 5G E-band access and backhaul*," IEEE Trans. Microw. Theory Techn*., vol. 64, no. 7, pp. 2244–2255, Jul. 2016.

[2] S. Romisch, D. Popovic, N. Shino, R. Lee, and Z. Popovic, "Multi-beam discrete lens arrays with amplitude-controlled steering," in 2003 *IEEE MTT-S int.Microwave symp*. Dig., Philadelphia, PA, Jun. 2003, pp. 1669-1672.

[3] A. Artemenko, A. Mozharovsky, S. Tikhonov, A. Myskov, and R. Maslennikov "Multiple-feed integrated lens antenna with continuous scanning range," *11th European Conference on Antennas and Propagation (EuCAP 2017)*, Mar. 2017.

[4] K. Sakakibara, M. Hirono, N. Kikuma, and H. Hirayama, "Broadband and planar microstrip-to-waveguide transitions in millimeter-wave band," *in Proc. Int. Conf. ICMMT'08*, Apr. 2008, pp. 1278–1281.

[5] Y.-C. Shih, T.-N. Ton, and L. Bui, "Waveguide-to-microstrip transitions for millimeter-wave applications," in *IEEEMTT-S Int. Dig*., May 1988, pp. 473–475.

[6] W. Grabherr, W. Huder, and W. Menzel, "Microstrip to waveguide transition compatible with mm-wave integrated circuits," *IEEE Trans. Microw. Theory Tech*., vol. 42, no. 9, pp. 1842–1843, Sep. 1994.

6. Chapter 6 : Perspective Solutions

6.1. Introduction

In this chapter three perspective solutions are proposed. These solutions add further properties to the base antenna solution of this thesis, the Folded Fresnel Zone Plate (FFZP) antenna, introduced in chapter 3.

First proposed solution consists on integrating dual-frequency functionality within the FFZP antenna. In order to obtain this, a dual-frequency band folded structure, twist-reflector and trans-reflector, are proposed. It should be noted that this solution has been filed for a patent application.

One major limitation of the FFZP solution is that it's a single polarization solution, meaning one cannot have two polarizations at the same time because of the trans-reflector that will only block one polarization. An alternative solution based on Cassegrain antennas is proposed to reduce the Fresnel lens focal distance by a factor of three (same as the folded structure) but meanwhile this solution is compatible for dual-polarization functionality. A patent application has been filed for this solution as well.

Finally, a solution based on [1] is proposed to further reduce the focal distance of the Fresnel lens by a factor of 5 instead of 3 using a triple-folded structure.

Each of these solutions are presented in the following sections. It should be noted that due to the limited time at last year of the thesis, we were not able to porotype these solutions. However, the concepts were validated by full-wave simulations of the complete antenna structure.

6.2. Dual-Frequency Band Folded Lens Antenna

The ability to combine a low frequency band that has good propagation properties and the higher frequency with greater capacity will allow carriers to leverage the benefits of both bands supporting higher capacities and broader availability over longer distances. Carrier aggregation with a single dual band antenna has been demonstrated to reduce total cost of ownership (TCO)

and result in CAPEX/OPEX savings by minimizing transportation needs, installation time, and tower loading and rental fees.

A compact solution for Point-to-Point communications at V-band (57-66 GHz) was proposed in chapter 3. This solution which is a folded lens antenna is limited to only one frequency because of the resonant nature of its Twist-reflector and also its trans-reflector. The lens part of the antenna, which can be any type of lens antenna can be easily configured for dual frequency depending the lens type. So the blocking point to have a dual-frequency folded lens antenna is the folded structure (twist-reflector and trans-reflector). In this section we try to solve this blocking point by introducing a dual-frequency twist-reflector and trans-reflector. This solution presents a dual-frequency band folded structure applicable to any kind of lens antenna (Fresnel lens, transmit-array, discrete lens, hemispherical lens and etc.). Figure 6-1, illustrates a folded structure being applied to different lens antennas.

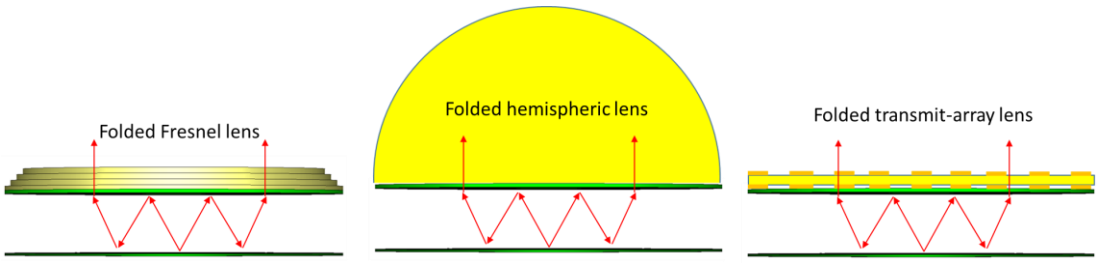

Figure 6-1: Folded structure applied to different lens antennas.

As an example, the two frequency bands were targeted to be V-band (57-66 GHz) and 28 GHz (27.5-29.5 GHz). Both of these frequencies are candidates for 5G backhauling, first one is intended for short range backhauling (small cell) and second one is intended for long range backhauling (macro cell).

6.2.1. Dual-Frequency Twist-reflector

As presented in chapter 3, a typical single frequency twist-reflector is made of parallel continuous metal strips printed on a single layer grounded dielectric substrate with $\lambda_g/4$ thickness and oriented at 45° with regard to incident wave (see figure 6-2(a)). The proposed dual frequency twist-reflector is constructed of a single layer dielectric substrate (as same as the single frequency twist-reflector). To have dual-frequency functionality, two resonance are created using rectangular printed patterns with vertical and horizontal gaps between them (see figure 6-2(b)).

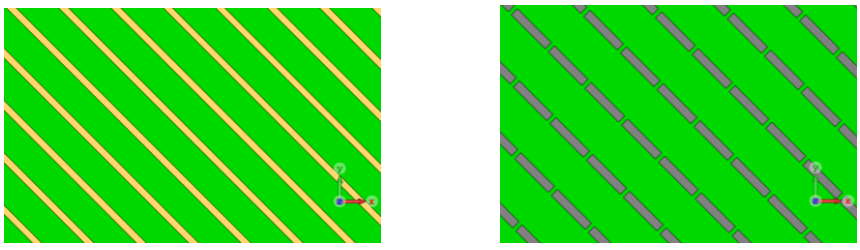

(a) (b)

Figure 6-2: Twist-Reflector : (a) single Frequency (60GHz) (b) Dual-frequency (28 & 60 GHz).

A typical solution for a dual-band twist-reflector would be having a dual layer stacked substrates with continuous strips printed on each layer, as its unit-cell is presented in figure 6-3.

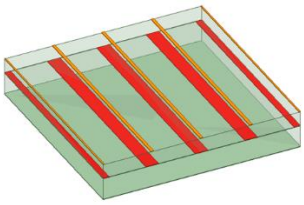

Figure 6-3: Dual-frequency Twist-reflector with 2 layers stacked substrates.

The drawback of this solution is the need of two layer stacked substrates which will increase the antenna RF loss and manufacturing cost. But the dual-frequency solution proposed in this invention has only one layer substrate same as a single frequency solution. To achieve dual-frequency functionality, our proposed solution uses discontinuous parallel strips instead of continuous parallel strips. The unit-cell of the proposed solution in figure 6-2(b) is presented in figure 6-4(a). As illustrated in figure 6-4(b), the tuning parameters of this solution are the width of the printed strip (W_t), vertical gap between them (G_{up}), horizontal gap between them (G_{side}) and the substrate thickness (H_t). These parameters will allow us to create and tune two resonant frequencies and therefore have a dual-frequency twist-reflector. The main parameter that creates the second resonance at 28.5GHz is G_{up} which is adding a capacitance (additional resonant element) to the twist-reflector equivalent circuit.

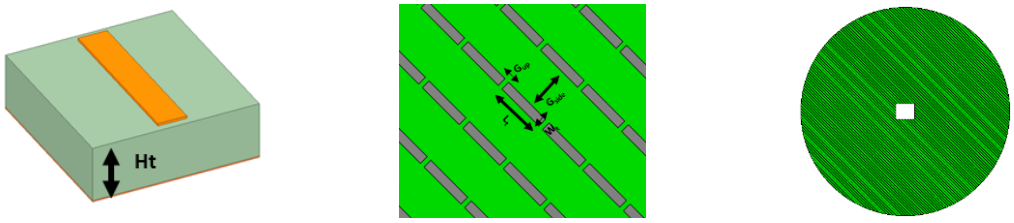

(a) (b) (c)

Figure 6-4: Proposed Dual-frequency Twist-reflector : (a) unit-cell, (b) partial zoomed view of the grid, and (c) complete view.

Figure 6-5 presents the proposed dual-frequency twist-reflector *S* parameters. The goal of the twist reflector is to turn the polarization of the incident wave by 90°. It's optimized using Floquet ports of *Ansys HFSS* where a Floquet port with two orthogonal modes is positioned on top of the strips. The optimization goal was to reach a minimum transmission loss between the two orthogonal modes (*S11:12*) and maximum transmission loss between the same modes (*S11:11*). The substrate dielectric material is the same as the one used for the single frequency twist-reflector presented in chapter 3, Rogers RO4003C with a relative permittivity of 3.66, a loss tangent of 0.004 (nominal for 10 GHz) and thickness of 0.762 mm. With regard to figure 6-5, the working frequency bands of the proposed twist-reflector are 25.9-29.75 GHz and 43.72-67.74 GHz which cover perfectly the targeted frequency bands of 28 GHz and V-band. The reference criteria for acceptable frequency bands are *S11:12* >-0.5 dB (blue region) and *S11:11*<-10 dB (red region).

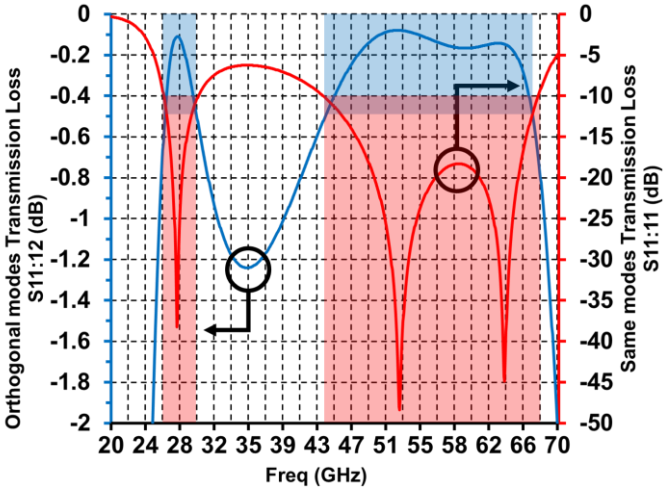

Figure 6-5: Dual-band Twist-reflector optimal value S-parameters.

Table 6-1 presents the optimal design parameters of the dual-frequency twist-reflector.

Table 6-I: Dual-frequency twist-reflector design parameters.

Parameter	Optimal value
H_t	0.762 mm
W_t	0.4 mm
L_t	2.2mm
G_{side}	1.9 mm
G_{up}	0.15 mm
Substrate material	Rogers RO4350B with $\varepsilon_r = 3.66$, $\tan\delta = 0.004$

In next section the design of the dual-frequency trans-reflector is presented.

6.2.2. Dual-Frequency Trans-reflector

The trans-reflector also called the polarizing grid, is a polarization selective surface which is transparent to linear perpendicular polarized fields and reflects the linear parallel polarized fields. Its evaluation criteria is to have a maximum reflection for parallel polarized fields, and maximum transmission for perpendicular polarized fields. The trans-reflector is typically made of printed parallel microstrip strips printed on a dielectric substrate. Its design parameters are the width of the strips and the gap between. The thickness of the substrate should be $\lambda_g/2$ in order to be transparent for the passing fields. Figure 6-6 shows a schematic of the trans-reflector.

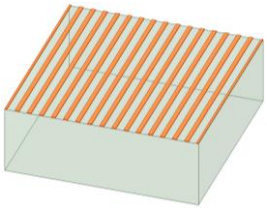

Figure 6-6: Trans-reflector schematic.

Instead of designing a dual-frequency trans-reflector, we try to benefit from the higher harmonics of the simple trans-reflector. In fact, the simple trans-reflector is transparent to perpendicular waves, for substrate thicknesses of $n\lambda_g/2$ with n=1, 2,… . The point is that in our case, the higher frequency band (60 GHz) is almost double the lower frequency band (30 GHz), so the substrate thickness that is set to $\lambda_g/2$ at 30 GHz and will become λ_g at 60 GHz and therefore transparent to the incident waves in both frequencies. Figure 6-7 shows perfectly this phenomenon for trans-reflector designed with λ_g being the guided wavelength at 30 GHz. In this Figure the transmission loss and reflection loss for perpendicular polarized incident waves are presented. As the trans-reflector should be transparent in face of perpendicular polarized waves, the optimization goal was to minimize than transmission loss (*S11:21*>-0.5 dB, blue regions) and maximize reflection loss (*S11:11*<-10 dB, red regions). As demonstrated, this trans-reflector covers our targeted frequency bands 28 GHz (27.5-29.5 GHz) and V-band (57-66 GHz).

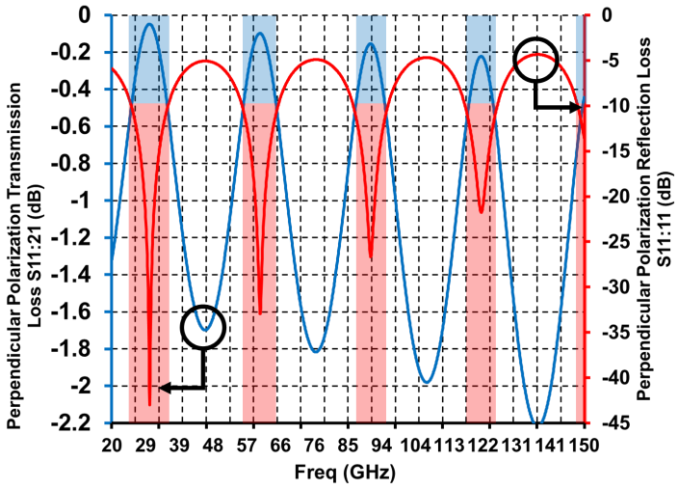

Figure 6-7: Trans-reflector harmonics of reflection loss and tranmission loss for perpendicular polarized incident waves.

Table 6-2 presents the design parameters of the trans-reflector functional at our targeted frequency bands. Comparing to the trans-reflector used in chapter 3, the substrate thickness of this trans-reflector is $\lambda_g/2$ with λ_g being the guided wavelength at 30 GHz whereas for other one λ_g was the guided wavelength at 60 GHz.

Table 6-II: Dual-frequency trans-reflector design parameters.

Strips width	0.127 mm
Air gap	0.254 mm
Substrate thickness	2.54mm
Substrate material	Arlon AD350A with $\varepsilon_r = 3.5$, $\tan\delta = 0.003$

In the following section, both the dual-frequency twist-reflector and trans-reflector will be applied to the FFZP antenna structure

6.2.3. Dual-Frequency Folded Fresnel Zone Plate Antenna

In the previous sections, a novel dual-frequency twist-reflector was proposed. Also, it was demonstrated that the trans-reflector can be used at both our targeted frequency bands (28 GHz, V-band) by calculating its substrate thickness at 30 GHz because of its harmonics. This dual-frequency folded structure can be applied to any lens antenna functioning in the two frequencies. In order to demonstrate the functionality of the dual-frequency folded structure, it was applied to Fresnel Zone Plate (FZP) lens where its design parameters where calculated at 28 GHz but it is functional at V-band as the lens will function at each $n\lambda$. The complete antenna structure is simulated using *CST Microwave Studio* time domain solver. As at this stage we did not design a dual-frequency primary source, the antenna is simulated separately at 28GHz and V-band using simple waveguide apertures adapted to each frequency band. For V-band the same basic waveguide aperture of chapter 3 is used and then it's scaled by a factor of two for 28 GHz frequency band. Apart from the primary sources, all other antenna components are identic in both 28 GHz and V-band simulations.

The diameter of the designed lens is 235 mm, almost double the 120 mm diameter lens at 60 GHz in chapter 3. The real focal distance of this lens for 28 GHz is 145 mm, but after simulating it at 60 GHz slight focal variation was observed. Finally a compromise between optimal focal distances at 28 GHz and 60 GHz lead to choosing a focal distance of 152 mm.

The superimposed radiation patterns of the dual-frequency FFZP antenna are presented in figure 6-8. The gain of the antenna at 60 GHz is 35.2 dBi and at 28GHz is 30.7 dBi. It's demonstrated that even with increased side love levels at 60 GHz due to the large electrical size of the lens, both radiation patterns are compliant with class 2 ETSI RPE.

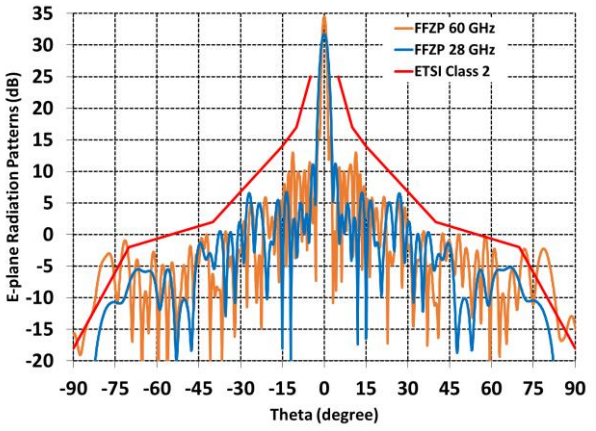

Figure 6-8: Superimposed radiation patterns of the dual-frequency FFZP antenna at 28 GHz and 60 GHz.

Figure 6-9 compares the gain variation over frequency of the dual-frequency FFZP antenna at 28 GHz (27.5-29.5) and V-band (57-66 GHz) frequency bands. As the FZP lens was optimized for 28 GHz frequency band, the antenna gain is more stable at this frequency band with having

only 1 dB variation over 28 GHz frequency band whereas it has almost 3.7 dB gain variation at V-band. However, as the FZP lens has a larger electrical dimension in V-band, up to 5dB higher gain is obtained at this frequency band.

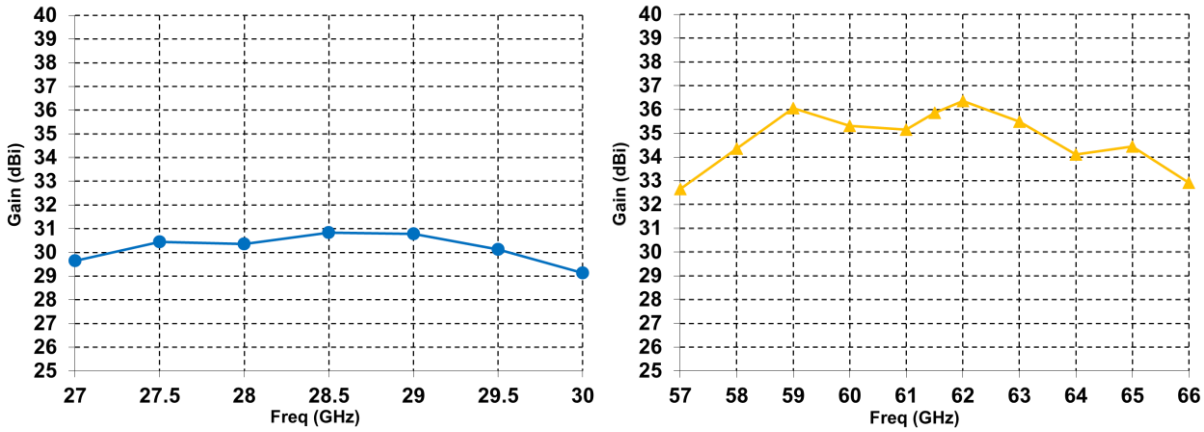

(a) (b)

Figure 6-9: Dual-frequency FFZP antenna gain variation over (a) 28 GHz frequency band, and (b) V-band.

To conclude, the concept of the dual-frequency band structure was validated by applying it to a FZP lens. It should be noted that the presented simulation result are not optimal, but good enough to validate the concept. To improve the antenna performance, especially in V-band, it would be better to use a dual-frequency lens structure such as a dual-frequency transmit-array. A patent application is filed for this dual-frequency band folded structure.

6.3. Compact Dual-Polarization Folded Lens Antenna

The solution proposed in chapter 3, the Folded Fresnel Zone Plate (FFZP) lens antenna, uses a Fresnel lens as the phase correcting aperture and by using a folded structure (a dielectric substrate based twist-reflector and trans-reflector) triples the electrical path between the lens and its focal source and therefore reduces the antenna form factor by factor of 3. The drawback of this antenna is that it's single polarization because of the trans-reflector which always blocks one polarization. Also the dielectric substrates of its folded structure increase the antenna RF losses as well as realization cost.

The alternative solution proposed in this section replaces the dielectric substrate based twist-reflector by a simple reflector plate and the dielectric substrate based trans-reflector by a simple Cassegrain or Gregorian sub-reflector implemented directly on the Fresnel Zone Plate (FZP) lens. This allows to still reduce the lens antenna physical focal by a factor of 3 and meanwhile being compatible with having two polarizations at the same time (dual-polarization folded lens antenna) by using a dual-polarization focal source. Moreover this solution avoids additional RF loss and higher cost because of the dielectric substrate based Twist and Trans reflectors. Figure 6-10 illustrates the focal reduction obtained by our novel folded structure. In this figure the FZP lens is inversed so it can act as a radome as well to offer a radome integrated folded lens antenna.

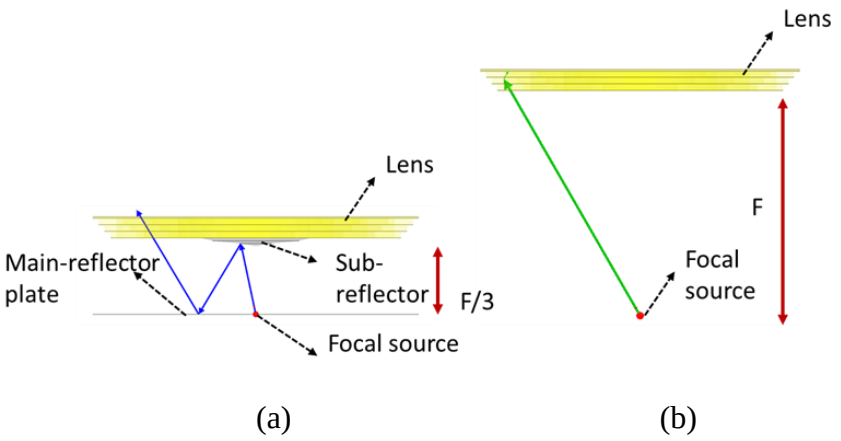

Figure 6-10: (a) Proposed dual-polarization folded lens antenna solution, (b) conventional non-folded lens antenna solution.

The ray tracing in figure 6-10 illustrate how the electrical path is tripled between the focal source and the phase correcting aperture (FZP lens here). Because of using simple reflectors, a dual-polarization folded lens antenna and not single-polarization is obtained. The idea of using a sub-reflector is similar to Cassegrain and/or Gregorian fed parabolic antennas. The difference is that in those antennas the phase is corrected at the parabola reflector and thus the focal is reduced by a factor less than two. Also the form factor of the parabola is much bigger than a lens.

It should be noted that in the proposed solution, the sub-reflector can have different shapes. These shapes can be convex (Cassegrain fed lens) or concave (Gregorian fed lens). It's better not to use a plate sub-reflector in order to avoid direct reflections towards the primary source.

In order to validate this solution, the complete antenna structure presented in figure 6-11 is simulated using *CST Microwave Studio* time domain solver. This antenna uses the same FZP lens designed for V-band that was used for the FFZP solution in chapter 3. The antenna is fed by the optimal edge taper horn antenna (N3) with integrated transition to WR15 waveguide (presented in chapter 3) and the structure is surrounded by an absorber to avoid side lobes. As shown in figure 6-11, the antenna components are the FZP lens, the horn, a convex sub-reflector pasted on the interior side of the FZP lens and a simple plate reflector around the horn.

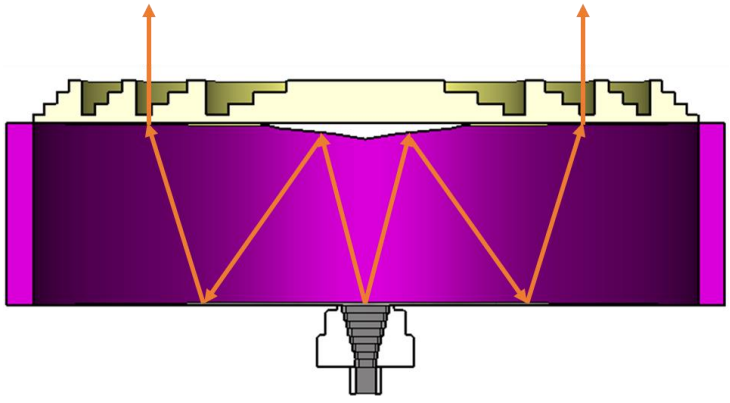

Figure 6-11: Dual-Polarization Folded FZP lens antenna schematic cut-view.

The diameter and the shape of the Cassegrain sub-reflector is calculated in order so its reflections can cover a sufficient portion of the main reflector surface. This was done by

parametric studies and comparing the antenna gain for different sub-reflector design parameters. The lens and the main reflector dimeters are 124 mm and the sub reflector diameter is 40 mm. Another matter is the focal distance of this antenna comparing to FFZP antenna with twist and trans-reflectors. Because of the ensemble of the sub-reflector and the main reflector the phase center of the primary source is displaced which results to a bigger focal distance, 34 mm (F=102 mm) instead of 28 mm (F=84 mm). However, it should be noted that due to lack of time at the end of the thesis, these are not optimal design values and there is still space for further optimizations. However, these results are good enough to prove the proposed concept.

Figure 6-12 presents the simulated radiation patterns of the antenna at 60 GHz and also its gain variation over frequency. It's illustrated that the antennas radiation patterns are almost compliant with class 2 ETSI RPE. The antenna offers a maximum gain of 33.2 dB with 2.1 dB variation over the V-band (57-66 GHz) frequency range. The gain variation over frequency is compared with optimal FFZP antenna from chapter 3. Almost 1.5 dB gain reduction is observed for the dual-polarization solution which is mainly due to masking of the sub-reflector on the lens surface.

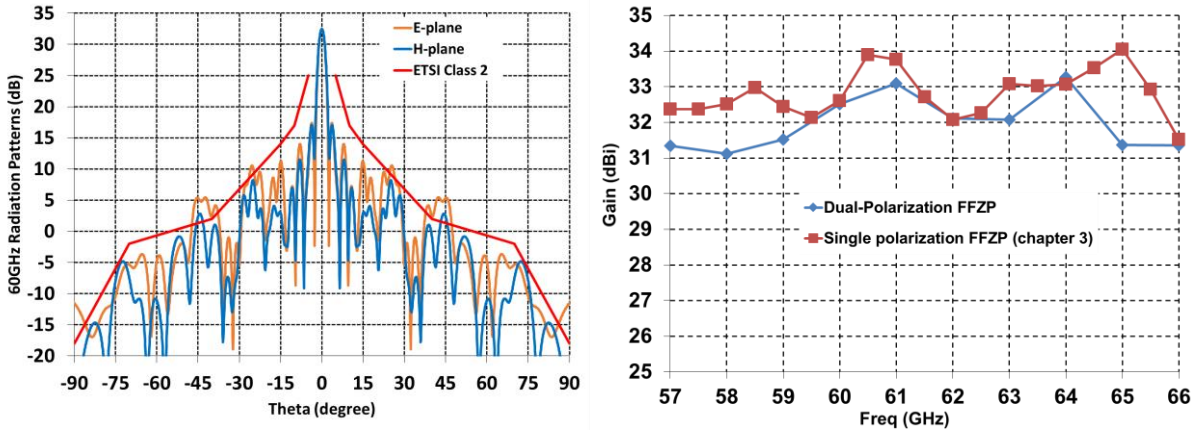

(a) (b)

Figure 6-12: Dual-polarization Folded FZP lens antenna simulated : (a) radiation patterns at 60 GHz, and (b) gain variation over frequency compared with simulated single polarization FFZP (chapter 3).

Main drawback of this solution would be its compatibility for beam steering. Because of the sub-reflector shape (optimized for centralized feed) and its smaller diameter comparing to FZP lens, this solution is not compatible for beam steering solutions based on focal source displacement form the lens focal point. As this concept is applicable to any kind of lens apertures, by replacing the FZP lens by other type of lenses such as transmit-arrays, one can integrate beam steering solution based on phase shifting within the lens aperture.

A patent application is filed for this dual-polarization folded lens antenna concept.

6.4. Triple Folded Fresnel Zone Plate Antenna

The proposed solution in this section makes the FFZP solution proposed in chapter 3 even lower profile. This solution which is inspired form [1], called triple folded structure, reduces the physical focal distance of the Fresnel Zone Plate (FZP) lens by a factor of 5 instead of 3 comparing to the FFZP solution. As presented in figure 6-13, this is achieved by multiplying the electrical path between the focal source and the FZP lens by a factor of 5 by adding a sub-reflector in middle of the trans-reflector.

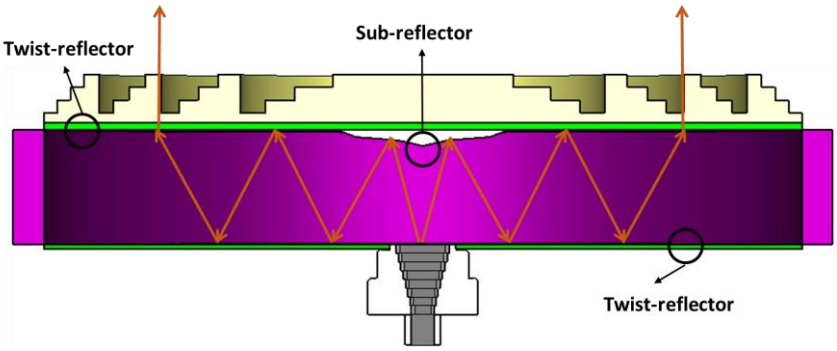

Figure 6-13: Cross-section of the Triple Folded FZP lens antenna structure.

Important design parameters of this structure are the sub-reflector shape and diameter so it can have wide enough reflections to cover sufficient surface of the twist-reflector. These parameters need to be optimized taking into account the primary source directivity and the FZP lens diameter. In order to have a primary verification on the concept, the antenna presented in figure 6-13 was fully simulated using *CST Microwave Studio* Time domain solver. The lens diameter is 124 mm and the sub-reflector diameter is 13.9 mm. The physical distance between the FZP lens and the primary source is 20 mm translating to a focal distance of F=20×5=100 mm for the FZP lens. Comparing to the FZP solution in chapter 3 where the physical distance was 28 mm, this solution reduces the antenna height by 8 mm. The primary source is the optimal edge taper horn N3 (introduce in chapter 3) with integrated transition to standard WR15 waveguide.

Figure 6-14 presents the simulated radiation patterns of the triple FFZP antenna at 60 GHz and its gain variation over frequency. It can be observed that the antenna has higher side lobe levels comparing with the results presented in chapter 3 but meanwhile it's almost compliant with class 2 ETSI RPE. The antenna has a maximum gain of 33.2 dBi with 3.2 dB variation over the V-band (57-66 GHz) frequency range. Comparing to the FFZP antenna, the triple FFZP solution has about 2dB less gain which is mainly due to sub-reflector masking impact on the FZP lens. Moreover, as the electrical path is multiplied by a factor of 5, the FZP lens is 5 times more sensible to the primary source phase center variation over the frequency comparing to a non-folded FZP (1× sensible) and FFZP (3× sensible).

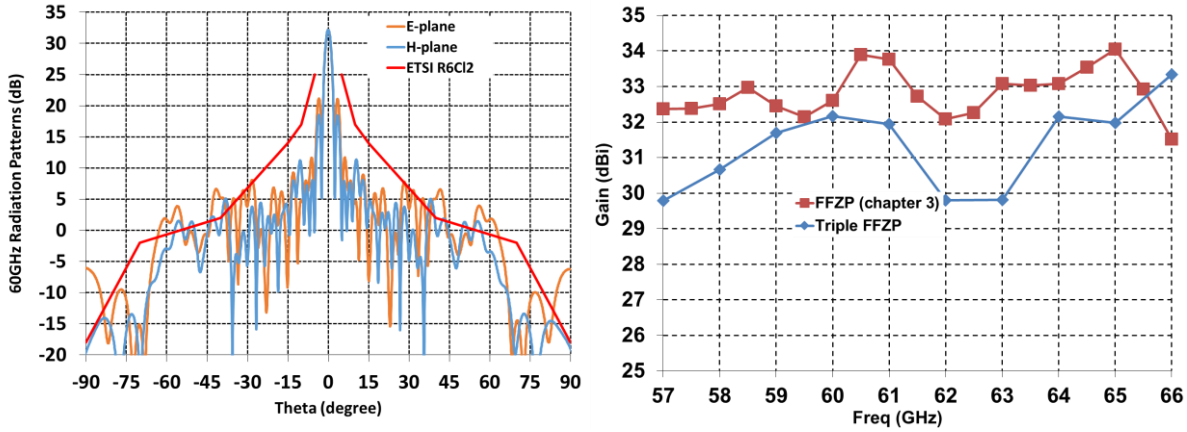

(a) (b)

Figure 6-14: Triple Folded FZP lens antenna simulated : (a) radiation patterns at 60 GHz, and (b) gain variation over frequency compared with simulated FFZP (chapter 3).

The gain performance of this solution in weaker comparing the FFZP solution but it remains acceptable whereas regarding the defined datasheets (in chapter 1) a minimum 30 dBi gain is required for V-band. In terms of realization this solution is more sensible to manufacturing tolerances especially for the physical distance between the FZP lens and the focal source.

The Triple Folded FZP antenna solution offers a more compact structure comparing to the FFZP antenna solution. However its main drawback is being non-compatible for beam steering solutions based on primary source displacement from the lens focal point. This is because of the sub-reflector limited diameter comparing to the FZP lens diameter and its shape that is optimized for a centralized focal source. Similar to the dual-polarization solution, by replacing the FZP lens by other type of lenses such as transmit-arrays, one can integrate beam steering solutions based on phase shifting within the lens aperture.

6.5. Conclusions

In this chapter, there alternative solutions were proposed to integrate additional feature within the FFZP antenna. These concepts are more as perspective solutions for further development which have been validated by primary simulations.

First solution proposes a dual-frequency folded structure compatible with any dual-frequency lens antenna including the FZP lens antenna.

Second solution proposes a dual-polarization folded structure using cassegrain reflectors in contrary to the single polarization typical folded strictures constructed with twist and trans reflectors. In addition to dual-polarization feature, this solution benefits from lower RF loss and realization cost comparing to the typical folded structures. Its main drawback is not being compatible for beam steering solutions based on focal source displacement from the focal point. However, it is compatible with beam steering solution based on phase shifting within the lens aperture. Other inconvenient of using a sub-reflector is its masking impact on the FZP lens antenna.

Third solution is based on triple folded structure offering a yet more compact solution comparing to the typical FFZP antenna solution. By integrating a cassegrain sub-reflector within the trans-reflector, the electrical path between the focal source and the FZP lens is multiplied by a factor of 5 resulting in the physical focal reduction by a factor 5 instead of 3 obtained by typical FFZP solution. Similar to the dual-polarization solution, the triple folded FZP lens antenna main drawback is not being compatible for beam steering solutions based on focal source displacement from the focal point. However, it is compatible with beam steering solution based on phase shifting within the lens aperture. The masking impact of the sub-reflector on the FZP lens antenna should be taken into account as well.

Two of the solutions, Dual-polarization FFZP and Dual-frequency FFZP, have been filed for separate patent applications.

6.6. Reference

[1] W. Menzel, D. Pilz and M. Al-Tikriti, "60 GHz triple folded reflector antenna," in *Electronics Letters*, vol. 38, no. 19, pp. 1075-1076, 12 Sept. 2002.

General conclusions

This thesis work was dedicated to the design, realization and experimental characterization of a new compact Folded Fresnel Zone Plate (FFZP) antenna for 5G point-to-point communications in V-band. This work stands out for the compatibility of the antenna with active beam steering solutions, based on standard PCB technology confirmed by both simulations and measurements.

In Chapter 1, the context of 5G point-to-point communications was presented. The main characteristics of potential frequency bands for 5G backhauling and fronthaluing links were identified and main antenna requirements were set to be : low-profile, low-cost, high gain and beam steerable. Detailed antenna specifications for this application taking into account the regulators standards were developed, and provisional technical datasheet per potential frequency band was proposed.

In Chapter 2, different directive antenna technologies were presented. Advantages and inconvenients of each solution were illustrated, either by theoretical calculations (for array antennas), or analyzing existing academicals and/or commercialized solutions. A decision matrix was proposed to evaluate the conformity of each antenna technology with the defined datasheets in first chapter. As a result of this evaluation, a Fresnel Zone Plate Lens antenna with a quasi-optical feeding system was chosen as the base antenna technology, basically due to its easy manufacturing (i.e. low cost) and compatibility for beam steering solutions.

In Chapter 3, a compact focal Fresnel Zone Plate (FZP) lens antenna solution was proposed for V-band (57-66 GHz). A folded structure applied to the FZP lens, resulting in a Folded FZP (FFZP) antenna solution, enabled reducing the physical focal distance of the FZP lens by a factor of three. The design and optimization of the different building blocks of the FFZP antenna were presented and complete antenna structure, in compliance with the defined datasheet, was validated by both simulations and measurements. The FFZP solution offers wide bandwidth of 18% and a maximum gain of 34 dBi for a 2.3 dB gain variation. The antenna radiations pattern are compliant with class 2 ETSI mask.

In Chapter 4, beam steering characteristics of the proposed FFZP antenna solution were determined. Also, focal array design considerations for beam steering solutions based on microstrip technology were studied. Alternative solutions were proposed to overcome some limitations such as microstrip technology impedance bandwidth, directivity and focal array coupling. These solutions consist on adding a parasitic element on top of the main radiating element (to increase the bandwidth), using a 2×2 sub-array as primary source (to increase directivity) and isolating the focal array element by via-holes (to reduce coupling).

In Chapter 5, two new beam steering solutions were proposed based on microstrip based focal arrays, and characterized by both simulations and measurement. The first solution, based on beam switching, allows a beam steering range of ±8° in azimuth and ±2° and elevation with an angle step of 2°. The second solution offers a continuous beam steering range of ±1.1°in both planes, for an angle steps of 0.3°. However, it was shown that due to masking effect of the focal array circuit on the folded structure, a compromise between the antenna performance (gain and side lobe levels) and beam steering range is required.

Finally in Chapter 6, three perspective solutions were proposed and verified by full-wave simulations. The first solution overcame the FFZP antenna major drawback, being only single polarization, by proposing a novel folded structure compatible for dual-polarization solutions. The second solution suggests a dual-frequency folded structure enabling also the FFZP antenna for dual-frequency applications. The third solution, based on a triple folded structure, makes the FFZP antenna solution even more compact. These solutions can be applied to any type of phase correcting apertures, and not only the FZP lenses.

In addition to the perspective evolutions presented in chapter 6, there exists short-term and long-term perspectives for the antenna solution proposed in this thesis.

Among short-term perspectives for the FFZP solution, we can refer to optimization of the focal arrays design in terms of reflection coefficients and the antenna mechanical structure re-design to ensure a perfect electrical contact for waveguide to micro strip line transition.

Main long-term perspective will result in replacing the FZP lens by other types of phase correcting apertures such as transmit-arrays or discrete lenses. This is mainly to be able to integrate beam steering solutions based on reconfigurable phase correcting apertures within the folded structure and overcome the folded structure masking effect on focal arrays. Other reason is to ensure a larger bandwidth solution comparing to the FZP lens. This reconfigurable folded transmit-array solution may result in a high gain, low side levels, reduced focal and beam steerable whose cost will be a challenge to meet.

List of Publications

International Journals

M. R. Dehghani Kodnoeih, Y. Letestu, R. Sauleau, E. Motta Cruz and A. Doll, "Compact Folded Fresnel Zone Plate Lens Antenna for mm-Wave Communications," in *IEEE Antennas and Wireless Propagation Letters*, vol. 17, no. 5, pp. 873-876, May 2018. DOI: 10.1109/LAWP.2018.2820420

G. Liu, **M. R. Dehghani Kodnoeih**, K. T. Pham, E. Motta Cruz, D. González-Ovejero and R. Sauleau, "A Millimeter Wave Transparent Transmitarray Antenna at Ka-band," *IEEE Antennas and Wireless Propagation Letters,* (under review)

International Conferences

M. R. Dehghani Kodnoeih, Y. Letestu, R. Sauleau, E. Motta-Cruz, A. Doll, "Compact Folded Fresnel Zone Plate Lens Antenna for 5G Point-to-Point Communications," *12th European Conference on Antennas and Propagation (EuCAP*), London, UK, 9-13 April, 2018. (oral presentation)

M. R. Dehghani Kodnoeih, R. Négrier, E. Motta-Cruz, Y. Letestu, R. Sauleau, L. Ferro-Famil, "Adaptive Continuous Beam Steering in Quasi-optical Antenna Solutions," *12th European Conference on Antennas and Propagation (EuCAP*), London, UK, 9-13 April, 2018. (poster presentation)

UNIVERSITE BRETAGNE LOIRE / MATHSTIC

UNIVERSITÉ DE NANTES

Titre : Développement de nouvelle génération d'antenne 5G dans la bande millimétrique

Mots clés : 5G, millimétrique, antenne directive, point-à-point, Lentille de Fresnel

Résumé : Etre compacte, avoir un faible coût, un gain élevé et être compatible avec dépointage électronique sont quatre des principales caractéristiques requises pour les antennes point à point 5G dans la bande millimétrique. Les bandes millimétriques ont attiré beaucoup d'attention ces dernières années car elles sont capables de fournir une communication à haut débit (jusqu'à 10 Gbits/s) en raison de leur large bande passante (jusqu'à 20%).
Différentes technologies d'antenne ont été proposées pour telles applications, avec leurs avantages et leurs inconvénients. Ce sont soit des solutions coûteuses, telles que des réseaux d'antennes directement alimentés (réseaux de cornets, réseaux de fentes, etc.), soit des solutions volumineuses telles que les antennes avec alimentation quasi-optique (lentilles, réseaux transmetteurs et réseaux réflecteurs).
Dans cette thèse, une antenne compacte, faible coût et directive basée sur des solutions quasi optiques est proposée pour la bande V (57-66 GHz). Une solution d'antenne à faisceau fixe optimisée avec une distance focale réduite est d'abordconçue puis validée par des mesures en champ lointain. Par la suite, la compatibilité de cette solution d'antenne pour le dépointage électronique est étudiée, et deux solutions de dépointage sont proposées. Ces solutions sont caractérisées à la fois par des simulations et des mesures. Enfin, en perspective, des solutions possibles pour intégrer des propriétés telles que le fonctionnement bi-fréquence ou en double-polarisation sont proposées.

Title : Development of next-generation 5G directive antennas at millimeter waves

Keywords : 5G, mm-waves, directive antennas, point-to-point, Fresnel Lens

Abstract : Low-profile, low cost, high gain and beam steerable are four of the key features required for 5G point-to-point antennas at millimeter waves. Millimeter-wave bands gained a lot of attention recently as they are capable to provide high data rate communication (up to 10 Gbps) due to their large bandwidth (up to 20%).
In the recent years, different antenna technologies have been proposed for such applications, with their advantages and weaknesses. They are either costly solutions, such as directly fed antennas arrays (horn arrays, slot arrays, etc.), or bulky ones such as quasi-optical antenna solution (lenses, transmit-arrays and reflect-arrays).
In this thesis, a compact, low cost and high gain antenna based on quasi-optical solutions is proposed in V-band (57-66 GHz). At first an optimized fixed beam antenna solution with reduced focal distance is designed and validated by outdoor measurements. Afterwards, the compatibility of this antenna solution for electronic beam steering is studied, and two beam steering solutions are proposed. These solutions are characterized by both simulations and measurements. Finally, perspective solutions to integrate properties such as dual-frequency and dual-polarization into the antenna solution are proposed.